

# **The Interplay Between Massive Stars and their Associated Nebulae within the Milky Way and Large Magellanic Cloud**

Emile Ignacio Doran

Department of Physics & Astronomy  
The University of Sheffield

*A dissertation submitted in candidature for the degree of  
Doctor of Philosophy at the University of Sheffield*

*March 2014*



# **Declaration**

I declare that no part of this thesis has been accepted, or is currently being submitted, for any degree or diploma or certificate or any other qualification in this University or elsewhere.

This thesis is the result of my own work unless otherwise stated.



# Acknowledgements

I must begin by thanking my supervisor Paul Crowther. His committed support, invaluable guidance and endless patience have all been crucial over the course of my PhD. This thesis would never have existed without his dedicated help - thank you Paul.

A warm thanks goes to my fellow colleagues, both past and present, at the Sheffield Astronomy Department. They helped me feel at home from the day I started, and rescued me from countless problems throughout my research. A special mention must go to Paul “Pablo” Kerry who ensured my computer was always running at full capacity. I was often oblivious to the numerous maintenance jobs he carried out, but knew things would never had worked without him - thanks Pablo. I would also like to thank all my collaborators within the VFTS. They gave me invaluable advice during the preparation of my journal paper and we enjoyed great times on our consortium meetings. I am grateful to all my friends, near and far, who always kept my spirit up and got me through the tough times. I’m so happy to have known you all.

No thanks is big enough for my Mum and Dad who were with me every step of the way. From observing the stars in our garden as a child, up to my final thesis submission, your support and encouragement was tireless - I love you. Finally my brother, Temujin. No-one was more excited about the research I carried out during my PhD, or had more faith that I could achieve it - this one is for you.



# Abstract

This study seeks to enhance our understanding of the relationship between massive stars and their environment.

New William Herschel Telescope (WHT) imaging and spectroscopy of 13 outer Milky Way H II regions is presented in Chapter 2. Properties of the nebulae and stars were separately determined and compared for consistency. Results showed that the ionising photons from the star were not accounted for by some nebulae, by as much as  $\sim 85\%$  in some cases. This fraction depended on the age of the region and indicated that photons were either escaping the region or being absorbed by dust.

The VLT-FLAMES Tarantula Survey (VFTS) is introduced in Chapter 3 with analyses of the emission line stars. Spectroscopic variabilities were investigated to improve understanding of their binary nature. In comparison to O2 stars, their spectral lines were found to be less reliable for determining radial velocities. Further derivations of their stellar properties were made via a series of template model atmospheres.

A census of the hot luminous stars within 30 Doradus of the LMC is compiled in Chapter 4, based on literature results, largely drawn from the VFTS. They were selected through specific photometric criteria of which 500 stars had spectroscopic classification while a further 222 were classified via their photometry. The spectroscopic completeness of hot luminous stars was estimated at  $\sim 85\%$  although this fell towards the central cluster due to crowding.

In Chapter 5, the integrated ionising output and wind luminosity of the stellar population was determined with the most massive stars ( $> 100 M_{\odot}$ ) found to make the highest contributions, and just ten stars providing 28% of the integrated value in both cases. Comparisons to the population synthesis code *Starburst99* showed significant underestimates in the integrated feedback if such massive stars were omitted. The stellar ionising output of 30 Doradus exceeded that derived from the nebula, indicating that  $\sim 6\%$  of ionising photons were escaping the region

A brief summary and potential avenues for future work are presented in Chapter 6.



# Contents

<b>1</b>	<b>Introduction</b>	<b>1</b>
1.1	Massive Stars . . . . .	1
1.1.1	Spectral classification . . . . .	3
1.1.2	Physical properties . . . . .	6
1.1.3	Atmospheric modelling . . . . .	12
1.1.4	Stellar winds . . . . .	13
1.1.5	Stellar evolution . . . . .	19
1.1.6	Binary systems . . . . .	22
1.1.7	The formation of massive stars . . . . .	23
1.2	H II Regions . . . . .	26
1.2.1	Properties of H II regions . . . . .	26
1.2.2	Sizes of H II regions . . . . .	28
1.2.3	Ionising stars . . . . .	29
1.2.4	Star formation rates . . . . .	30
1.3	Relations to extragalactic studies . . . . .	30
1.4	The Focus of this Study . . . . .	33
<b>2</b>	<b>A Study of H II Regions with Single Ionising Stars in the Outer Galaxy</b>	<b>35</b>
2.1	Introduction . . . . .	35
2.2	Observations . . . . .	36
2.3	Spectroscopy . . . . .	37
2.3.1	Data reduction . . . . .	39
2.3.2	Stellar spectroscopy . . . . .	43
2.3.3	Nebular spectroscopy . . . . .	53
2.4	Imaging . . . . .	66
2.4.1	Data reduction . . . . .	68
2.4.2	Image analysis . . . . .	68

2.5	Relating the Ionising Stars and the Nebulae . . . . .	73
2.6	Comments on Individual Regions . . . . .	75
2.7	Discussion . . . . .	78
2.8	Summary . . . . .	79
<b>3</b>	<b>Studying the Emission Line Stars of 30 Doradus with the VLT-FLAMES Tarantula Survey</b>	<b>81</b>
3.1	Introduction . . . . .	81
3.2	The VLT-FLAMES Tarantula Survey . . . . .	82
3.3	Classification of Emission Line Stars . . . . .	85
3.3.1	WN stars . . . . .	86
3.3.2	WC stars . . . . .	87
3.3.3	Of/WN stars . . . . .	89
3.4	Spectral Variation . . . . .	90
3.4.1	Radial velocities . . . . .	92
3.4.2	Binaries . . . . .	99
3.5	Special Cases . . . . .	112
3.5.1	Spectral variations in VFTS 002 . . . . .	112
3.5.2	VFTS 147 . . . . .	116
3.5.3	VFTS 682 . . . . .	118
3.6	The Significance of the VFTS on Emission Line Stars in 30 Doradus . . . . .	118
3.7	Properties of Emission Line Stars . . . . .	120
3.7.1	Photometry of W-R stars . . . . .	120
3.7.2	W-R binaries . . . . .	123
3.7.3	Templates stars . . . . .	127
3.7.4	Stellar modelling . . . . .	127
3.7.5	Discussion . . . . .	131
3.8	Summary . . . . .	132
<b>4</b>	<b>A Census of the Hot Luminous Stars in 30 Doradus</b>	<b>135</b>
4.1	Introduction . . . . .	135
4.1.1	The giant HII region of 30 Doradus . . . . .	136
4.1.2	The VLT FLAMES Tarantula Survey . . . . .	138
4.2	Photometry . . . . .	140
4.2.1	Photometry for the 30 Dor Region . . . . .	140
4.2.2	Photometry for the R136 Region . . . . .	143

4.2.3	Overlapping photometric sources . . . . .	145
4.2.4	Photometry of W-R stars . . . . .	145
4.3	Extinction in R136 and 30 Dor . . . . .	146
4.4	Candidate Selection . . . . .	148
4.5	Spectroscopy . . . . .	153
4.6	Spectroscopic Completeness . . . . .	160
4.6.1	Spectroscopic completeness in the MEDUSA region . . . . .	162
4.6.2	Spectroscopic completeness in the R136 region . . . . .	162
4.6.3	Stars that are unaccounted for . . . . .	167
4.6.4	Correcting for unclassified stars . . . . .	167
4.6.5	Queries with candidate selection . . . . .	170
4.7	Spectral Types and Distribution . . . . .	171
4.8	Summary . . . . .	174
<b>5</b>	<b>The Mechanical and Radiative Stellar Feedback of 30 Doradus</b>	<b>175</b>
5.1	Introduction . . . . .	175
5.2	Stellar Properties . . . . .	177
5.2.1	Modelling of early O-type stars . . . . .	177
5.2.2	O-type star calibrations . . . . .	183
5.2.3	B-type stars . . . . .	192
5.2.4	Uncertainties in calibrations . . . . .	197
5.2.5	Binary systems . . . . .	198
5.2.6	Wolf-Rayet and Of/WN Stars . . . . .	198
5.2.7	Census of hot luminous stars with spectroscopy . . . . .	198
5.3	Stellar Census . . . . .	201
5.4	Integrated Stellar Feedback . . . . .	204
5.4.1	Ionising photon rate . . . . .	207
5.4.2	Stellar wind luminosity and momentum . . . . .	209
5.4.3	Feedback from additional sources . . . . .	209
5.5	Comparison with Population Synthesis Models . . . . .	212
5.6	Star Formation Rates . . . . .	214
5.6.1	Lyman continuum from census . . . . .	216
5.6.2	Far-UV continuum . . . . .	217
5.6.3	Lyman continuum from $H\alpha$ . . . . .	217
5.6.4	Far-infrared continuum . . . . .	219
5.6.5	Combined $H\alpha$ and mid-IR . . . . .	219

5.6.6	Star formation rate comparison . . . . .	223
5.7	Photon Escape Fraction . . . . .	223
5.8	Summary . . . . .	225
<b>6</b>	<b>Summary and Future Work</b>	<b>227</b>
6.1	A summary of this study . . . . .	227
6.2	Expanding on this Study . . . . .	229
6.2.1	Selection of stellar sources . . . . .	229
6.2.2	New stellar properties . . . . .	230
6.2.3	Nebula comparisons . . . . .	231
6.3	Application to Other Star Forming Regions . . . . .	231
6.3.1	Synthetic modelling . . . . .	233
6.4	Ongoing and Future Observations . . . . .	235
<b>A</b>	<b>ISIS slit orientations and ACAM H<math>\alpha</math> aperture positions</b>	<b>239</b>
<b>B</b>	<b>The VFTS MEDUSA Observational Epochs</b>	<b>247</b>
<b>C</b>	<b>W-R star Spectral Fits</b>	<b>251</b>
<b>D</b>	<b>Spectral Fits of the O2 Star Models</b>	<b>261</b>

# List of Figures

1.1	HRD . . . . .	2
1.2	Spectral classification of O-dwarfs . . . . .	5
1.3	Effective temperature as a function of spectral type for OB stars . . . . .	9
1.4	Distribution of rotational velocities . . . . .	10
1.5	Schematic of P Cygni profile . . . . .	16
1.6	$H\alpha$ as mass-loss rate diagnostic . . . . .	18
1.7	Massive star evolutionary tracks . . . . .	22
1.8	Contamination of single and binary stars . . . . .	24
1.9	Nebular spectrum of a H II region . . . . .	27
1.10	The evolution of $\eta_0(t)$ . . . . .	31
2.1	A 2-D spectrum in the R158R grating . . . . .	39
2.2	Defining extraction apertures with IRAF . . . . .	41
2.3	Wavelength calibration of an arc frame . . . . .	42
2.4	Classification of the ionising stars . . . . .	45
2.5	Classification of BD +60° 2522 . . . . .	46
2.6	Convolutions of $B$ and $V$ -band filters . . . . .	49
2.7	Galactic distribution of the H II regions . . . . .	51
2.8	Comparing H II region distances with literature . . . . .	52
2.9	Gaussian fitting of $H\alpha$ line . . . . .	54
2.10	Comparison of the $E(B - V)$ . . . . .	56
2.11	Energy level diagram for O III . . . . .	62
2.12	Gaussian fitting of the O III lines . . . . .	63
2.13	Energy level diagram for S II . . . . .	64
2.14	$H\alpha$ image of Sh2 158 . . . . .	69
2.15	Comparison of ‘on- $H\alpha$ ’, ‘off- $H\alpha$ ’ and net images of Sh2 158 . . . . .	70
2.16	Comparison of $Q_0^*$ and $Q_0^{\text{neb}}$ . . . . .	74

3.1	The VFTS MEDUSA targets . . . . .	83
3.2	A spectral montage of the VFTS WN 3-WN 5 stars . . . . .	88
3.3	A spectral montage of the VFTS WN 6-WN 8 stars . . . . .	88
3.4	A spectral montage of the VFTS WC and WN/C stars . . . . .	89
3.5	The changing morphology of the $H\beta$ line . . . . .	90
3.6	A spectral montage of the VFTS Of and Of/WN stars . . . . .	91
3.7	A spectral montage of the LMC O2 stars . . . . .	96
3.8	Plot of observed vs synthetic radial velocities . . . . .	98
3.9	Gaussian fits to W-R star emission lines . . . . .	100
3.10	Spectral variations in VFTS 019 . . . . .	105
3.11	Spectral variations in VFTS 402 . . . . .	106
3.12	Orbital radial velocity plot of VFTS 402 . . . . .	106
3.13	Crowding around VFTS 507 . . . . .	107
3.14	Spectral variations in VFTS 509 . . . . .	109
3.15	Orbital radial velocity plot of VFTS 509 . . . . .	109
3.16	Spectral variations in VFTS 542 . . . . .	110
3.17	Orbital radial velocity plot of VFTS 542 . . . . .	110
3.18	Spectral variations in VFTS 695 . . . . .	111
3.19	VFTS MEDUSA spectrum of VFTS 002 . . . . .	112
3.20	Variations in LR03 spectra of VFTS 002 . . . . .	114
3.21	Contamination of the VFTS 002 spectra . . . . .	115
3.22	MEDUSA fibre pointings during the observation of VFTS 002 . . . . .	117
3.23	Spectral variations in VFTS 147 . . . . .	119
3.24	Comparison between broad and narrow-band filters . . . . .	121
3.25	The dilution of the W-R spectrum in a binary system . . . . .	124
3.26	Comparing WN star properties of this work with contemporary models . . . . .	133
4.1	The Tarantula Nebula . . . . .	137
4.2	The 30 Doradus nebula and star cluster . . . . .	139
4.3	Offsets in the CTIO astrometry . . . . .	142
4.4	Spatial and photometric coverage of the census . . . . .	144
4.5	Comparison of extinction values from different extinction laws. . . . .	149
4.6	Determination of $R_V$ in 30 Dor . . . . .	150
4.7	Colour magnitude diagram of VFTS OB stars and selection criteria cuts . . . . .	152
4.8	Classification of VFTS B-type stars . . . . .	155
4.9	Spatial coverage of hot luminous stars in 30 Dor . . . . .	158

4.10	Spatial coverage of hot luminous stars in R136 . . . . .	159
4.11	Colour magnitude diagrams of stars meeting the selection criteria . . . . .	161
4.12	Spectroscopic completeness in the MEDUSA region . . . . .	164
4.13	Spectroscopic completeness in the MEDUSA region without contaminants . .	165
4.14	Spectroscopic completeness in the R136 region . . . . .	166
4.15	Radial distribution of all hot luminous stars . . . . .	172
4.16	Radial distribution of O-type and W-R stars . . . . .	173
5.1	Model spectral energy distributions of O2 stars . . . . .	179
5.2	Evolutionary tracks of O2 stars . . . . .	184
5.3	$T_{\text{eff}}$ as function of SpT and $Z$ . . . . .	186
5.4	$BC_V$ as a function of $T_{\text{eff}}$ . . . . .	187
5.5	$q_0$ as a function of $T_{\text{eff}}$ for O-type stars . . . . .	189
5.6	$L_{\text{EUV}}/L_{\text{Bol}}$ as a function of $T_{\text{eff}}$ . . . . .	190
5.7	$q_0$ as a function of $T_{\text{eff}}$ for B-type stars . . . . .	194
5.8	The Wind luminosity relation in B-supergiants . . . . .	196
5.9	An H-R diagram of the census . . . . .	202
5.10	Mass luminosity relations . . . . .	203
5.11	Present day mass functions of the 30 Dor and R136 . . . . .	205
5.12	Cumulative ionising photon rates for 30 Dor and R136 . . . . .	208
5.13	Cumulative stellar wind luminosities for 30 Dor and R136 . . . . .	210
5.14	Comparing the R136 to <i>Starburst99</i> . . . . .	213
5.15	UIT image of 30 Dor . . . . .	218
6.1	The star forming nebula NGC 3603 . . . . .	232
6.2	Comparing NGC 3603 to <i>Starburst99</i> . . . . .	234
A.1	Sh2 99 . . . . .	240
A.2	Sh2 100 . . . . .	240
A.3	Sh2 101 . . . . .	241
A.4	Sh2 112 . . . . .	241
A.5	Sh2 128 . . . . .	242
A.6	Sh2 148 and Sh2 149 . . . . .	242
A.7	Sh2 152 . . . . .	243
A.8	Sh2 156 . . . . .	243
A.9	Sh2 158 . . . . .	244
A.10	Sh2 162 . . . . .	244

A.11	Sh2 170 . . . . .	245
A.12	Sh2 206 . . . . .	245
C.1	Model fitting of O2 If*/WN 5 template star . . . . .	252
C.2	Model fitting of O3.5 If*/WN 7 template star . . . . .	253
C.3	Model fitting of WN 3 template star . . . . .	254
C.4	Model fitting of WN 5 template star . . . . .	255
C.5	Model fitting of WN 6 template star . . . . .	256
C.6	Model fitting of WN 7 template star . . . . .	257
C.7	Model fitting of WN 8 template star . . . . .	258
C.8	Model fitting of WN/C template star . . . . .	259
C.9	Model fitting of WC 4 template star . . . . .	260
D.1	Spectral fitting in the UV . . . . .	262
D.2	Spectral fitting in the far-blue . . . . .	263
D.3	Spectral fitting in the blue . . . . .	264
D.4	Spectral fitting in the yellow-red . . . . .	265

# List of Tables

1.1	Physical properties of O-type stars . . . . .	8
1.2	Physical properties of W-R stars . . . . .	12
1.3	Stellar wind parameters of OB and W-R stars . . . . .	20
1.4	Properties of H II regions . . . . .	28
2.1	Target H II regions . . . . .	37
2.2	Spectral coverage of the ISIS gratings . . . . .	38
2.3	ISIS observing log . . . . .	38
2.4	Standard stars . . . . .	43
2.5	Properties of the ionising stars . . . . .	47
2.6	Nebular line fluxes and intensities . . . . .	57
2.7	Nebular line fluxes and intensities . . . . .	59
2.8	Spectroscopically derived properties of the H II regions . . . . .	61
2.9	ACAM observing log . . . . .	67
2.10	Photometrically derived properties of the H II regions . . . . .	72
3.1	The VFTS observing setup . . . . .	84
3.2	Classification of the VFTS emission line stars . . . . .	85
3.3	Classification criteria for WN stars . . . . .	86
3.4	The LMC O2 stars . . . . .	93
3.6	A comparison between observed and synthetic radial velocities . . . . .	97
3.7	Observed radial velocities of the VFTS Of/WN and WN stars . . . . .	102
3.8	Orbital parameters of WN binaries . . . . .	104
3.9	Photometry of W-R stars in 30 Dor . . . . .	125
3.10	Equivalent widths and binary corrections for W-R stars in 30 Dor . . . . .	126
3.11	The template emission lines star spectra . . . . .	129
3.12	The template emission line star models . . . . .	130
4.1	Relative scales of 30 Doradus and its associated regions . . . . .	138

4.2	Breakdown of photometric candidates and spectroscopically confirmed stars . . . . .	146
4.3	Census of the candidate hot luminous stars . . . . .	154
4.4	VFTS B-dwarfs and giants classified for the census . . . . .	156
4.5	Breakdown of candidate spectral types . . . . .	160
4.6	The spectral type distribution in the MEDUSA region . . . . .	163
4.7	The spectral type distribution in the R136 region . . . . .	163
4.8	The average absolute magnitudes of census O and B0 stars . . . . .	169
4.9	<i>Swift</i> UVOT sources not identified in the census . . . . .	170
5.1	Photometry of the O2 stars. . . . .	181
5.2	Model parameters of the O2 stars . . . . .	181
5.3	Comparison of O2 star models with literature . . . . .	182
5.4	Calibrations for O-dwarfs . . . . .	191
5.5	Calibrations for O-giants . . . . .	191
5.6	Calibrations for O-supergiants . . . . .	192
5.7	B-type star parameters . . . . .	195
5.8	The SB2 systems corrected in the census . . . . .	199
5.9	Stellar parameters of the spectroscopically confirmed hot luminous stars . . . . .	200
5.10	Cumulative properties of the census at increasing projected radii . . . . .	206
5.11	Stars with the highest ionising photon rates, wind luminosities and masses . . . . .	215
5.12	Comparison of SFR tracers . . . . .	222
5.13	Comparison of $Q_0$ tracers . . . . .	225
B.1	The VFTS MEDUSA observing epochs . . . . .	247

# Chapter 1

## Introduction

### 1.1 Massive Stars

Massive stars represent the most luminous stars in the Universe. Their high mass determines their eventual fate and this separates them from the rest of the stellar population. Whilst a star with similar mass to the Sun will ultimately fade away as a white dwarf, a more violent ending awaits more massive stars. Stars with initial masses  $M_{\text{init}} > 8 M_{\odot}$  are capable of producing iron cores and are expected to end their lives via a core-collapse supernova (CCSN) and leave a neutron star or black hole (BH) (Smartt 2009). In some cases, the CCSN may be accompanied by a long gamma ray burst (GRB) or the star may collapse to a BH without an associated supernova (SN) explosion. These eventual outcomes are thought to arise from different progenitors but all will have originally been massive stars.

In this work, due to their associated properties, massive stars will concern all stars with  $M_{\text{init}} \gtrsim 12 M_{\odot}$ . The Hertzsprung-Russell (H-R) diagram (Figure 1.1) connects two main stellar properties, temperature and luminosity. Being luminous and initially hot, massive stars predominantly occupy the extreme upper left region of the H-R diagram. The upper right region is comparatively empty. Only a few Luminous Blue Variable (LBVs) occasionally stray into the area, while cooler red supergiants (RSGs) are found below a particular luminosity, the Humphreys & Davidson (1979) limit. These positions are used to connect the individual phases with multiple evolutionary scenarios.

The narrow diagonal band on the H-R diagram marks the ‘main sequence’ where stars fuse H in their cores. As in lower mass cases, massive stars are expected to spend most of their time on the main sequence burning H. They are able to fuse H more efficiently in their cores than low mass stars by using C, N, O as catalysts. As H begins to diminish, they expand and cool, leaving the dwarf phase and evolving to become blue giants and supergiants. Where fusion

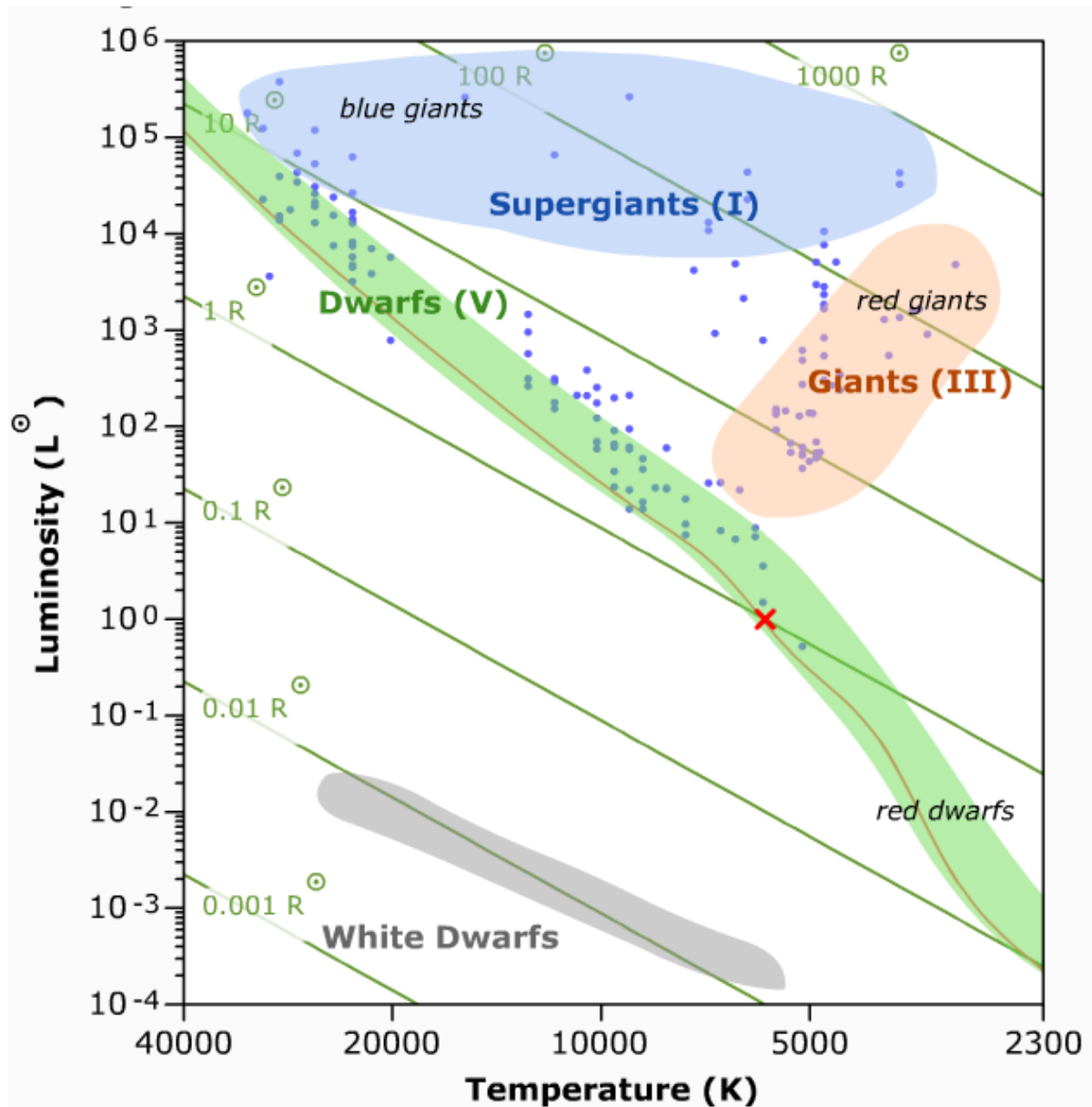


Figure 1.1: The Hertzsprung-Russell diagram. The regions occupied by the main luminosity classes are highlighted and isoradius lines are plotted in red. Blue dots mark the positions of luminous stars in the Yale Bright Star Catalog and the red cross represents the the Sun. Created using the Hertzsprung-Russell Diagram Explorer - <http://astro.unl.edu/naap/hr/animations/hrExplorer.html>

would be halted after He burning resulting in C+O nuclei in low mass stars, it can continue as far as Si burning in high mass stars, resulting in Fe/Ni cores. The products of fusion are exposed during supernovae (SNe), but also during the extreme phases beforehand. Severe mass-loss is experienced across the lifetime of the star which can alter its evolution and affect the surrounding interstellar medium (ISM). This is particularly noted during the Wolf-Rayet (W-R) phase, a period thought to follow supergiants where the outer layers are stripped away to reveal products of core H and He burning in the stellar interior.

Stars are believed to be born in clusters. Measuring their initial mass function shows stars of  $0.1 - 1 M_{\odot}$  make up the vast majority of the numbers and overall mass of the stellar population. Nevertheless, massive stars dominate the bolometric luminosity of star forming regions and galaxies. Their high luminosities also allow them to be studied individually at extragalactic distances, demonstrating how different metallicity environments can impact on stellar evolution. They play a crucial role on the structure and evolution of the ISM. Through different forms of stellar feedback, they are capable of ionising gas (to form H II regions, see Section 1.2) and changing its chemistry and dynamics. These effects can be observed and related to the massive stars responsible, even in extragalactic cases when the stars themselves may be unresolved.

We therefore rely on relatively nearby massive stars, particularly in the Milky Way and Magellanic Clouds (MCs), to form the basis of our understanding for other massive stars in the Universe. As we continue to study them and the relations with their associated H II regions, we can attempt to unravel details on their distribution, their stellar evolution and star formation history (SFH) as well as obtain a template for extragalactic star forming regions.

### 1.1.1 Spectral classification

The hot dense interior of a star produces a bright continuous spectrum across a wide range of wavelengths: the stellar continuum. As photons pass through the cooler and less dense atmosphere they are absorbed at specific wavelengths relating to the discrete excitation energy levels in an atom. This overlays a series of absorption lines on the continuum. The different lines observed are determined by the degree of ionisation, which in turn is a function of the temperature and density of the gas. For stars with dense atmospheres, emission lines can form as radiation leaving the stars is scattered back into view. This variety of spectra offers an ideal method for classifying different stars as well as determining their properties.

All stars can be assigned to a particular spectral type (SpT), a classification based on the spectroscopic lines, designed to group stars with similar properties. These are further divided into subtypes (typically running from 0-9 but with exceptions), where cooler stars are assigned

higher (later) subtypes. A luminosity class is also given according to the stellar gravity with gravity declining as a star moves from dwarf to giant to supergiant (V  $\rightarrow$  III  $\rightarrow$  I). Whilst on the main-sequence, massive stars occupy the O and early B spectral types (SpTs). Collectively they can be referred to as OB-type stars - including all O subtypes and running through to B2 dwarfs, later type B-giants and the latest B-supergiants (Gray & Corbally 2009). A spectrum dominated by emission lines is what defines W-R stars. They can be divided into nitrogen-rich (WN) and carbon-rich (WC) stars, and their classification criteria are discussed in Section 3.3.

Historically, classification of most SpTs has been concentrated in the blue spectral region where sensitivity has been greatest. The first classification schemes for O-type stars made use of the He I and He II lines. With He II lines being more dominant in earlier subtypes, the ratio He II  $\lambda 4541$ /He I  $\lambda 4471$  was set to equal unity for an O7 and He II  $\lambda 4200$ /He I+II  $\lambda 4026$  equalling unity at about O6 (Plaskett & Pearce 1931), see Figure 1.2. As the technique was combined with improving data quality, Walborn (1971b) introduced Si lines to help recognise the subtypes O9.7, B0.2 and B0.7. The earliest O subtype was extended to O3 by Walborn (1971a) and then again to O2 by Walborn et al. (2002b) on the basis of the N V  $\lambda 4603 - 20$ , N IV  $\lambda 4057$  and N III  $\lambda 4634 - 41$  lines. Conti & Alschuler (1971) offered a more quantitative approach based on the ratios of the equivalent widths ( $W_\lambda$ ) with both methods giving relatively consistent classifications.

Spectral lines from OB stars are primarily in absorption as particular atoms interact with the star's light at its photosphere. However, some lines can be seen in emission as the mass-loss rates in stars increases and their stellar wind becomes denser. This led to a subclass of "Of" stars based on the appearance of the N III  $\lambda 4634 - 41$  and He II  $\lambda 4686$  lines. Split into further subtypes, an O((f)) star indicated N lines in emission and He in absorption while an O(f) star showed the He line to be much weaker or absent. Both N and He would be in emission for an Of star. The behaviour of the He II  $\lambda 4686$  lines would be related to the luminosity of the star, Walborn (1971b) classifying O-type stars as OV, OIII and OI when the line was in absorption, absent or in emission, respectively.

Subsequent spectroscopic surveys (e.g. Walborn & Fitzpatrick 1990; Sota et al. 2011) have helped to categorise further unusual spectral features in massive stars. They offer a spectroscopic atlas that other massive star samples can be classified against, although they still predominantly fall into the optical wavelengths. Ultraviolet (UV) data has been limited to space-based observations from instruments such as the International Ultraviolet Explorer (IUE), the Far Ultraviolet Spectroscopic Explorer (FUSE) and Hubble Space Telescope (HST). Equivalent UV atlases (Walborn et al. 2002a; Pellerin et al. 2002) have highlighted metallic lines, such as C IV  $\lambda\lambda 1548, 1551$  and Si IV  $\lambda\lambda 1394, 1403$  to vary with different SpTs, but their analysis can be hampered by even moderate interstellar extinction.

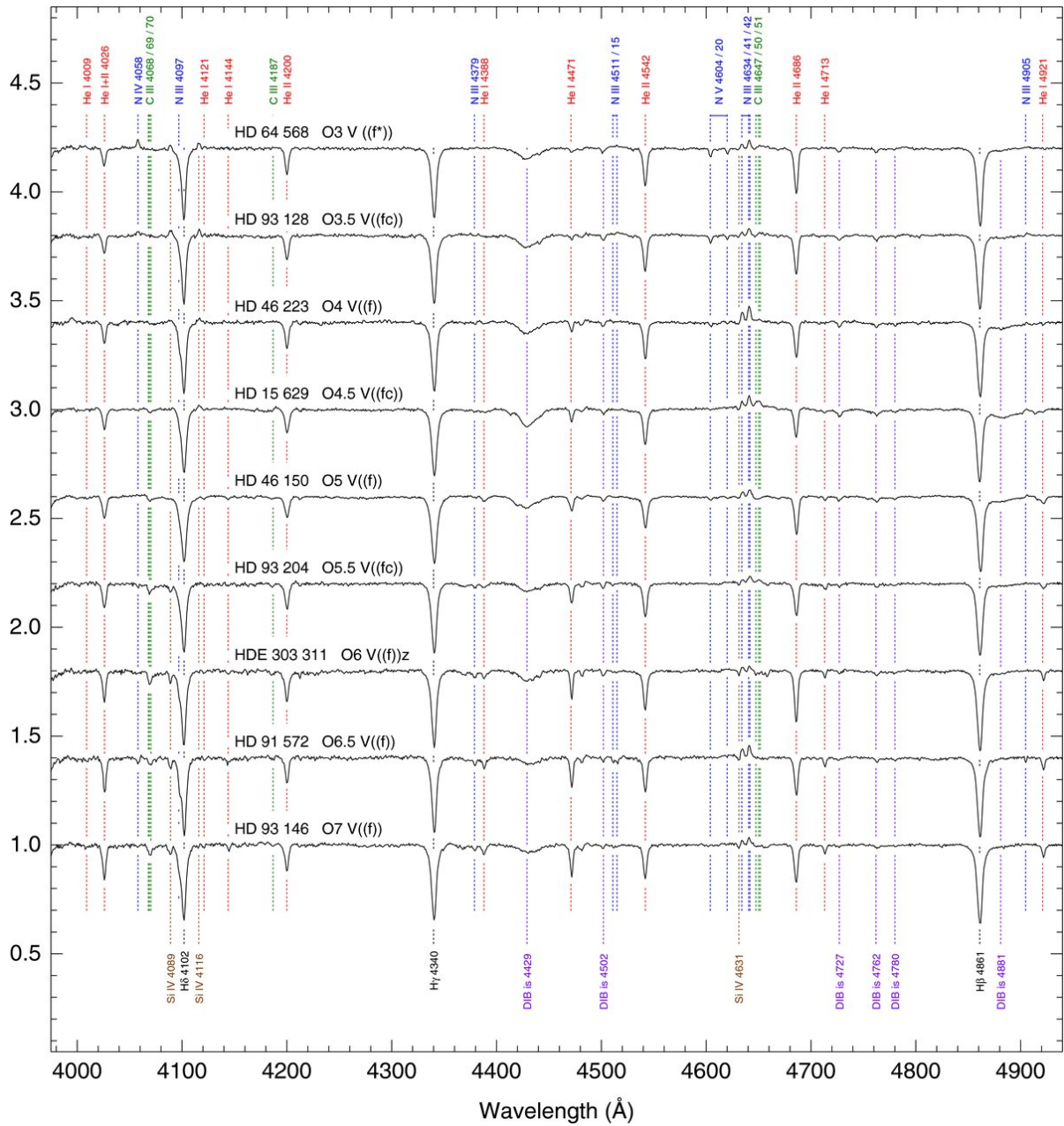


Figure 1.2: A spectral montage of O-dwarfs highlighting their key diagnostic lines. Taken from Sota et al. (2011).

Observations therefore also extended into the infrared (IR) wavelengths where extinction is greatly reduced, even compared to the optical, making it ideal for studying regions of star formation or those visually hidden near the Galactic Centre. However, the flux of OB stars is notably weaker in the IR, so that spectra require good signal-to-noise (S/N) ratios to reveal photospheric features. The number of spectral lines is also limited compared to the optical, which can make classification more uncertain, but He I  $\lambda 2.1120 \mu\text{m}$  and He II  $\lambda 2.18852 \mu\text{m}$  are strong enough to serve as the key diagnostics (Hanson et al. 1996).

### 1.1.2 Physical properties

Stars span a wide range of physical properties during their lifetimes. It is essential to determine these properties in order to understand their relation to the stars' evolution and feedback to the ISM. They are governed by two fundamental parameters: the effective surface temperature ( $T_{\text{eff}}$ ) and surface gravity ( $g$ ) of the star.  $T_{\text{eff}}$  can be defined by the relation:

$$L_* = 4\pi R_*^2 \sigma_{\text{sb}} T_{\text{eff}}^4, \quad (1.1)$$

which takes the star to radiate like a black-body and where  $L_*$  is the stellar luminosity,  $\sigma_{\text{sb}}$  is Stefan Boltzman's, constant and  $R_*$  is the stellar radius. More luminous stars will hence be hotter, as is seen in the H-R diagram by moving up the main sequence. Alternatively, physically larger stars of the same  $T_{\text{eff}}$  will be more luminous, as is the case for supergiants which may have sizes several times greater than their dwarf equivalents, or even thousands of times larger in the case of M-type stars. Table 1.1 lists typical properties for a range of O-type stars

Observationally,  $T_{\text{eff}}$  can be estimated from the star's continuum. Observing the flux of the star at  $4400 \text{ \AA}$  through a *B*-band filter and equivalently at  $5500 \text{ \AA}$  through a *V*-band filter provides the *B*–*V* colour index. *B*–*V* is negative for hotter blue stars and positive for cooler red stars with the star Vega (A0 V) defining the zero point of the magnitude scale. However, *B*–*V* is insensitive to temperature changes in hot stars, and more accurate values can be obtained from the stellar spectra. The most commonly used is the method of ionisation balance, which takes advantage of the fact that elements in the atmosphere will be more ionised at a higher  $T_{\text{eff}}$ . Therefore, spectral lines of the same element but at different ionisation states will also depend on  $T_{\text{eff}}$ . Synthetic spectra are produced from atmospheric models. By comparing observed lines to these synthetic lines, a star's  $T_{\text{eff}}$  can be derived. This method of analysis was individually applied to a sample of O-type stars and the results adopted by Martins et al. (2005). The values in Table 1.1 show the mean relations they derived between SpT and  $T_{\text{eff}}$ ,

as well as a number of other properties.

In the case of O-type stars, He I and II are the most reliable diagnostic lines, He I  $\lambda 4471$  and He II  $\lambda 4542$  being the most widely used, and lines such as He I  $\lambda 4026$ , He I  $\lambda 4388$ , He II  $\lambda 4200$  and He II  $\lambda 5412$  serving to compliment them (e.g. Herrero et al. 1992; Repolust et al. 2004). Ionisation states of N may be favoured in the hottest stars (e.g. Rivero González et al. 2012b), as used for a sample of O2 stars in Section 5.2.1. Only neutral He is found at lower  $T_{\text{eff}}$ , meaning that in B-type stars, the ionisation balance of Si is the favoured indicator. Lines such as Si II  $\lambda 4124 - 31$ , Si III  $\lambda 4552 - 67 - 74$ , Si IV  $\lambda 4089$ , Si IV  $\lambda 4116$  can be used depending on the  $T_{\text{eff}}$  involved (e.g. Trundle et al. 2007).

The surface gravity is defined as  $g = GM_*/R_*^2$ , where  $M_*$  is the stellar mass and  $G$  is the gravitational constant. It can also be derived from spectroscopy due to a process called Stark broadening. This collisional effect broadens spectral lines and is greater in a denser atmosphere i.e. one with a higher gravity. In O-dwarfs,  $\log(g) \approx 4$  (cgs), dropping to  $\log(g) \approx 3.5$  in O-supergiants and even lower at later SpTs. The surface gravity can therefore be used to determine  $M_*$  but care is needed in hot stars as their radiation and winds are capable of overcoming the gravity (see Section 1.1.4). An alternative estimate of  $M_*$  is to match a star's properties to those provided by stellar evolutionary models (see Section 1.1.5). However, a discrepancy has been found between evolutionary ( $M_*^{\text{evol}}$ ) and spectroscopically ( $M_*^{\text{spec}}$ ) derived masses, with  $M_*^{\text{spec}} < M_*^{\text{evol}}$  (Herrero et al. 1992), indicating that one or both of the methods remains incomplete.

It is clear from Table 1.1 that more massive stars are also more luminous. A mass-luminosity relation can be drawn for H burning stars whereby  $L_* \propto M_*^\alpha$ . However, this relation changes with the mass of a star such that  $\alpha \approx 4.5$  for solar type stars, dropping to  $\alpha \approx 2.5$  for massive stars and  $\alpha \rightarrow 1$  in the most massive cases. In turn this relation dictates the lifetime,  $\tau$ , of a star. Since  $\tau \propto M_*/L_*$ , for low mass stars  $\tau \propto M_*^{-3.5}$  whereas in high mass stars  $\tau \propto M_*^{-1.5}$ .

Also included in Table 1.1 is the Lyman continuum ionising photon rate of the star ( $Q_0$ ). This is defined as the number of photons capable of ionising a H atom, emitted by the star every second. Radiation from hotter stars peaks at shorter wavelengths, and so they emit a larger proportion of higher energy photons.  $Q_0$  is thus higher for earlier stars and in turn they are the primary ionising sources for H II regions.

The values in Table 1.1 are nevertheless averages, with any one SpT spanning a range of properties. Furthermore, metallicity is equally as important as  $T_{\text{eff}}$  and  $\log(g)$  in defining a star's parameters. For example, Mokiem et al. (2007a) found the  $T_{\text{eff}}$  of their OB star sample to increase by  $\sim 2$  and  $\sim 4$  kK when moving from the Milky Way to the progressively metal poorer Large and Small Magellanic clouds (LMC and SMC), respectively (see Figure 1.3 along with further study in Section 5.2.2). This was thought to arise due to a process known as "line

Table 1.1: Physical properties of Galactic O-type stars.

Spectral Type	$T_{\text{eff}}$ [K]	$\log(g)$ [cm s <sup>-1</sup> ]	$M_V$ [mag]	$\log L_*$ [L <sub>⊙</sub> ]	$R_*$ [R <sub>⊙</sub> ]	$M_*^{\text{spec}}$ [M <sub>⊙</sub> ]	$\log Q_0$ [ph s <sup>-1</sup> ]
O3 V	45000	3.92	-5.79	5.84	13.8	58	49.6
O6 V	39000	3.92	-4.92	5.32	10.1	31	49.0
O9 V	33000	3.92	-4.05	4.77	7.5	17	48.1
O3 I	42000	3.73	-6.35	5.99	18.6	68	49.8
O6 I	37000	3.48	-6.32	5.81	20.0	44	49.5
O9 I	31000	3.23	-6.29	5.61	21.8	30	49.1

**Notes.** Values are taken from the “observational scale” study of Martins et al. (2005).

blanketing” (discussed in the following section) which depends on the metallicity. The relation of  $T_{\text{eff}}$  with SpT, as well as other properties in Table 1.1, might be expected to continue on into the O2 subtype introduced by Walborn et al. (2002b). But the small number of O2 stars has limited their study with previous work drawing few differences with O3 stars (Massey et al. 2004, 2005). Section 5.2.1 revisits this new subtype with contemporary spectral modelling to determine whether their properties and feedback are notably different.

Stellar properties may see further variation in a star which is rotating. Rotation is typically a signature of a star’s formation, as the angular momentum from its natal cloud is conserved. The rotational velocity ( $v_r$ ) can be detected via broadening in the spectral lines, although as each star is viewed at a random inclination angle ( $i$ ), what is observed will only be a projection ( $v_r \sin i$ ) of the actual rotational velocity. However, for large samples, the rotation axis is assumed to be randomly distributed, allowing  $v_r$  to be estimated (as in Figure 1.4). Early type stars have been shown to rotate at a range of velocities reaching in excess of  $\sim 600 \text{ km s}^{-1}$  (Dufton et al. 2011a; Ramírez-Agudelo et al. 2013), with supergiants showing slower rotation rates than dwarfs, again reflecting the conservation of angular momentum during stellar evolution (Penny & Gies 2009; Ramírez-Agudelo et al. 2013). All stars also have a critical or break up velocity:  $v_{\text{crit}} = \sqrt{2GM_*/3R_p}$ , which marks the point at which the centrifugal force balances gravity. In this case, the star is flattened with the polar radius,  $R_p$ , being two thirds of the equatorial radius.

The effects of rotation can be observed through “gravity darkening” whereby the brightness of a star is not uniformly distributed (as would be the case for a non rotating star) but found to be brighter and hotter at the poles and fainter and cooler toward the equator (von Zeipel 1924). Rotation is thought to induce mixing within the star; helping to replenish the fuel in the core and giving a more homogenous star. This not only affects stellar properties but can greatly control the evolutionary path of a star (see following Section 1.1.5). However, rotation

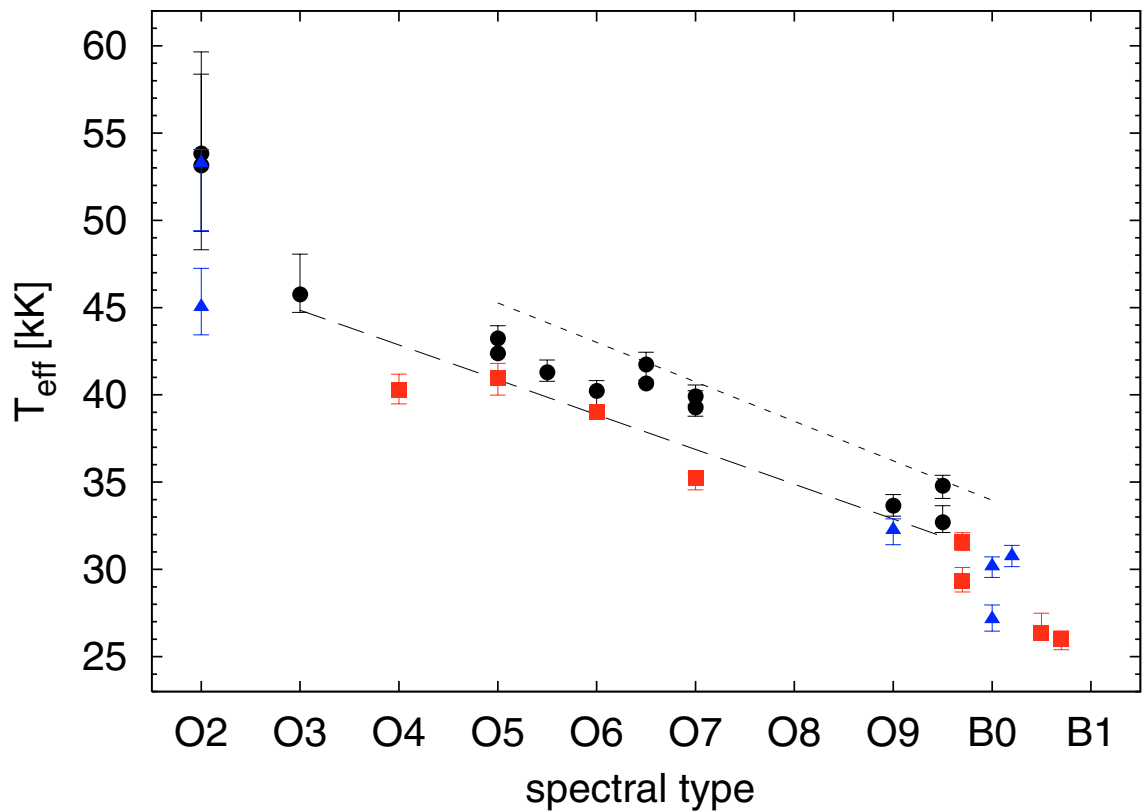


Figure 1.3: The effective temperature as a function of spectral type. Dwarf stars (black circles), giants (blue triangles) and supergiants (red squares). The dashed line represents the SpT- $T_{\text{eff}}$  calibration of Martins et al. (2005) while the dotted line marks the average  $T_{\text{eff}}$  of SMC dwarfs. LMC dwarfs are expected to lie between the two lines. Taken from Mokiem et al. (2007a).

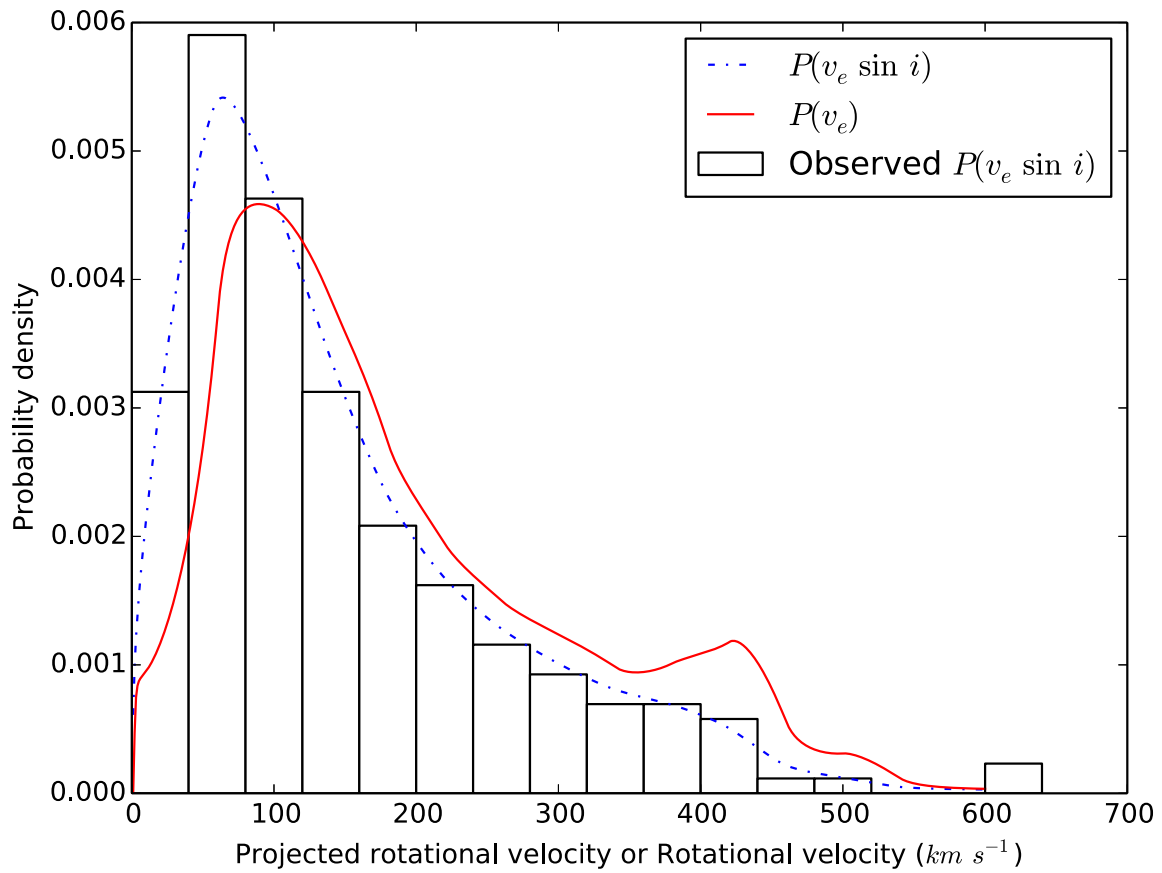


Figure 1.4: The distribution of rotational velocities for single O-type stars in 30 Doradus. Observations are represented by a solid black line. The dot-dashed blue line and solid red line are estimates of the probability density function for the projected and actual rotational velocities, respectively. Taken from Ramírez-Agudelo et al. (2013).

is only likely to be significant for a small proportion of early type stars where  $v_r$  is notably high. Perhaps more important will be the effect of binary interactions (see Section 1.1.6).

### W-R stars

Studying the properties of W-R stars is complicated by their strong stellar winds and requires a different approach to OB stars. Their extended atmospheres mean radiation escapes at a range of radii.  $R_*$  is the inner boundary of the star with an associated temperature of  $T_*$ , but lies at large optical depths, invisible to direct study. The optical continuum is taken to originate at a Rosseland optical depth of  $2/3$ . The corresponding radius and temperature at this point being  $R_{2/3}$  and  $T_{2/3}$ , respectively. In order to derive values for  $R_*$  and  $T_*$  deep within the atmosphere, it is assumed that the velocity laws that apply to  $R_{2/3}$  and  $T_{2/3}$  remain consistent throughout the wind. As with O-type stars, the temperatures of W-R stars is derived using an ionisation balance method. The emission lines of adjacent He or N ions are used for WN stars, while lines of C ions serve the WC stars. Given their high wind densities, temperatures and mass-loss rates must be determined simultaneously using atmospheric models, because the atmospheres are highly stratified (Crowther 2007).

From Table 1.2 it is clear that W-R stars can span a wide range of temperatures. These values exclude the envelope of the stars and are generally higher compared to the preceding OB stars, as mass-loss via stellar winds has revealed their hotter interiors. Their luminosities can be obtained by modelling the atmosphere or by associating them with stellar clusters. Determining an initial mass of a W-R star depends heavily on the mass-loss it has previously undergone. Potential evolutionary paths are discussed in Section 1.1.5. A current mass is easier to derive, as the W-R star is believed to be burning He and a much stronger correlation is found between their masses and luminosities, in comparison to O-type stars (Schaerer & Maeder 1992)

Exceptions are made in the case of some late-type WN stars (WNLs) that are still seen to be rich in H. They are typically found in high mass clusters and are very luminous,  $\log L/L_\odot \sim 6$  (Martins et al. 2009; Crowther et al. 2010). Their ionising photon rates can exceed even the hottest O-type stars, while classical W-R stars will produce only a fraction of the output of an O-type star. Given these properties and their abundance, Smith & Conti (2008) suggested these H-rich WNLs had originated from the most massive stars and only recently evolved on from the O-dwarf and O-supergiant phases. Several are present in the massive 30 Doradus region, and their role with respect to the other SpTs is investigated in Chapter 5.

Table 1.2: Physical properties of W-R stars.

SpT	$T_*$ [kK]	$\log L_*$ [ $L_\odot$ ]	$\log Q_0$ [ph s <sup>-1</sup> ]
WN 3-WN 6	85 – 60	5.34 – 5.2	49.2 – 49.0
WN 7-WN 9	50 – 32	5.54 – 5.7	49.4 – 48.9
WC 4-WC 6	90 – 80	5.22 – 5.06	49.0 – 48.9
WC 7-9	75 – 50	5.34 – 4.94	49.1 – 48.6
WO	150	5.22	49.0

**Notes.** Values taken from Crowther (2007).

### 1.1.3 Atmospheric modelling

The morphologies of spectral lines are determined by the properties of a star and processes which occur in its atmosphere where the lines are formed. By modelling these parameters, synthetic spectra can be generated and fit to observations to provide information on the fundamental properties discussed in Section 1.1.2.  $T_{\text{eff}}$  can be obtained from the ionisation balance of certain elements, He I and He II lines being the most common indicators. The stellar gravity can be derived by measuring the amount of Stark broadening lines have experienced, the Balmer lines being the main diagnostics. Meanwhile,  $L_*$  can be found by fitting the dereddened spectral energy distribution (SED). Synthetic models are scaled according to observed spectrophotometry and the extinction to the star is simultaneously derived. Chemical abundances and parameters of a star’s stellar wind will also be reflected in the stellar spectra so these too will be modelled.

When using model atmospheres to reproduce observations the main difficulty is modelling the opacity of the spectral lines, along with the continuum opacity, that blankets the emerging flux. Early models were developed (e.g. Kurucz 1979) to treat this “line blanketing” by accounting for millions of the bound-bound opacities of the lines. They were applied to a range of SpTs from O-type stars holding numerous resonance lines especially in the UV, through to K-type stars where line blanketing is dominated by molecules. This approximation was made possible by taking the atmospheres to be in local thermodynamic equilibrium (LTE). This assumes that the density of particles is high, ensuring high collision rates so they behave as in thermal equilibrium. Photons will also have a small mean free path so there is a balance in radiative processes and mean local conditions are held.

However, LTE does not apply in hot early stars where radiative rates will dominate over collisional rates. Photons will escape easier, particularly from low density atmospheres such as in hot supergiants. A non-LTE model atmosphere is required in such cases, but line blanketing must still be accounted for, particularly the increased opacities from metal lines. These were

found to scatter radiation down to lower layers in a backwarming effect (Repolust et al. 2004; Herrero et al. 1992) which resulted in modifications to O-type star calibrations (Martins et al. 2005; Repolust et al. 2004). Auer & Mihalas (1972) were amongst the first to model the departure from LTE but creating a fully line blanketed atmosphere requires knowledge of the atomic data and is computationally very demanding. The atomic level populations are a function of the radiation field, which are in turn a function of the populations, and so the two must be derived simultaneously. Things are further complicated by adopting a spherical, rather than plane-parallel, geometry. This is necessary in early stars with extended atmospheres, as they are no longer a thin layer with respect to the stellar radii.

Significant progress has been made to incorporate these factors into the latest atmospheric models. The most widely used include TLUSTY (Hubeny & Lanz 1995), WM-Basic (Pauldrach et al. 2001), FASTWIND (Santolaya-Rey et al. 1997), Po-WR (Hamann & Gräfener 2004) and CMFGEN (Hillier & Miller 1998). TLUSTY addresses non-LTE line blanketing although within a plane-parallel atmosphere, so is best suited to OB stars with weak winds. WM-Basic and FASTWIND extend this to a spherical geometry and with approximate treatment of the blanketing effects, calculations are still performed on a short timescale. Only lines from key elements will be modelled, H and He receiving most attention, along with N (Rivero González et al. 2012a), as FASTWIND continues to be updated. Meanwhile, Po-WR and CMFGEN have largely focussed on W-R stars. As many lines as possible are modelled in a co-moving frame to achieve an accurate line blanketing but this comes at the cost of considerably longer execution times. CMFGEN particularly benefits from being able to model the stellar radiation emitted from the UV through to the IR. Fitting to this whole spectrum subsequently gives better constraints on any properties derived.

### 1.1.4 Stellar winds

Stellar winds describe the continuous outflow of material from the stellar surface. In the case of massive stars, they can remove a substantial fraction of the initial stellar mass, helping to reveal nuclear processed material as well as impact its evolution. The winds help to transfer energy to the surroundings, capable of shaping bubbles into the ISM, as well as chemically enriching it. Shocks can form in stronger winds to generate sources of X-ray radiation, while the ejected material can go on to create circumstellar disks around the host star.

The radiative acceleration associated with the outward radiation pressure ( $g_{\text{rad}}$ ) continually acts against the inward gravitational acceleration ( $g$ ) of the star. For a star to produce a stellar wind,  $g_{\text{rad}} > g$ . When considering the acceleration produced by free electrons ( $g_{\text{rad}}^e$ ), it will be

proportional to the electron opacity. The ratio of  $g_{\text{rad}}^e/g$  can be written as:

$$\Gamma_e = \frac{g_{\text{rad}}^e}{g} = \frac{\kappa_e L_*}{4\pi c G M_*}, \quad (1.2)$$

where  $\kappa_e$  is the opacity due to electron scattering and  $\Gamma_e$  is known as the classical Eddington parameter. In low mass stars  $\Gamma_e \ll 1$  but in massive stars  $\Gamma_e \rightarrow 1$  because of their different mass-luminosity relation. A maximum (Eddington) luminosity can hence be derived for a star of any given mass following:

$$L_{\text{Edd}} = \frac{4\pi c G M_*}{\kappa_e}. \quad (1.3)$$

However, in hot stars, the opacity from both electron scattering and line scattering contribute to  $g_{\text{rad}}$ , and it is the spectral lines that are the main driving force, as their bound-bound transitions are intrinsically stronger (Puls et al. 2008). Radiation also peaks in the UV for hot luminous stars which is home to many absorption lines. The resulting line opacity exceeds the continuum opacity generated by electron scattering by a factor of  $10^6$  (Lamers & Cassinelli 1999). But the spectral lines are only capable of driving the wind due to the expansion of the atmosphere. For a static atmosphere, radiation from the photosphere would just be absorbed at the lowest layers but the velocity gradient means the outer layers view the radiation to be red-shifted as a result of the Doppler shift. The outer atmosphere can thus absorb photons that have been unattenuated by the layers below.

Castor et al. (1975) provided early concepts to explain the line driving process in hot star winds, later known as the CAK theory. Elements such as C, N and O along with those in the Fe-group provide the primary driving force. UV radiation is absorbed from the ground state in ‘resonance lines’ allowing energy and momentum to be transferred from the photons to the ions. This becomes shared amongst the rest of the plasma wind, that is predominantly made of electrons and  $\text{H}^+$  and  $\text{He}^+$  ions, thanks to Coulomb coupling. As more momentum continues to be transferred, the wind reaches a terminal velocity,  $v_\infty$ , far from the stellar surface. The terminal velocity, along with the mass-loss rate,  $\dot{M}$ , are two of the most important parameters to help explain the mechanisms involved in stellar winds.

The stellar wind analysis of hot massive stars occurs over a variety of wavelengths, using two main diagnostic methods. ‘Approximate’ methods determine wind parameters by focussing on a single process. The approach is simplified by only considering the wind physics, and adopting additional information from external photospheric diagnostics. Alternatively, non-LTE model atmospheres can be used to simultaneously derive stellar and wind parameters. Their synthetic spectra and SEDs are fitted to observations at a range of wavelengths,

providing diagnostics on a variety of processes (Puls et al. 2008).

### Wind velocities

In the UV, key resonance lines are formed by the C iv and N v ions where they can appear as P Cygni line profiles, presenting a blue-shifted absorption component alongside a red-shifted emission component (see Figure 1.5). P Cygni profiles are a direct result of the outflowing wind. The blue-shifted component is formed by the material between the star and observer, scattering photospheric radiation out of the region to create the absorption component. A symmetric emission component is produced as the surrounding sides of the star scatters radiation in all directions. The combined effect gives an asymmetric line but the strength of the different components also depend on the relative sizes of the star and its wind. If the star is large compared to the wind region, a notable fraction of photons will be scattered back into the star giving a smaller emission component. As the wind region increases, less radiation is back-scattered and the emission component will dominate as in a W-R star.

P Cygni profiles are the primary indicators for  $v_\infty$  in hot massive stars. Figure 1.5 shows the line flux making an asymptotic fall to zero (becoming saturated) as the wind is accelerated to  $v_\infty$ . A sharp return to the continuum would then be expected at this point,  $v_{\text{black}}$ , but in reality stars display a finite absorption region up to  $v_{\text{edge}}$ , as in Figure 1.5. Prinja et al. (1990) showed  $v_{\text{black}}$  to be a reliable measure of  $v_\infty$  and that their difference compared to  $v_{\text{edge}}$  arose from microturbulence.

Table 1.3 lists the typical  $v_\infty$  of OB stars, which exceeds  $3000 \text{ km s}^{-1}$  for the earliest stars. A star will also have an escape velocity from its surface,  $v_{\text{esc}} = (2gR_*)^{0.5}$ . However, the stellar gravity has a reduced effect as a result of the electron scattering. It must be corrected via the Eddington parameter to give the effective gravity:

$$g_{\text{eff}} = \frac{GM_*}{R_*^2}(1 - \Gamma_e), \quad (1.4)$$

such that  $v_{\text{esc}} = (2g_{\text{eff}}R_*)^{0.5}$ .

The relationship between  $v_\infty$  and  $v_{\text{esc}}$  therefore provides information on the radiative acceleration in the stellar wind. A ratio of  $v_\infty/v_{\text{esc}} = 2.36$  is observed in O-type stars (Prinja et al. 1990). The ratios are lower in cooler stars with a decrease close to the B1.5 subtype (Lamers et al. 1995; Crowther et al. 2006). Uncertainties in  $M_*$  and  $T_{\text{eff}}$  mean the region in which this “bi-stability” jump takes place remains unclear. It is thought that variations close to these temperatures, influence the ionisation of the lines driving the wind. These lines will also be dependent on the metallicity of the star. As Fe-group elements are the key drivers, stars with a

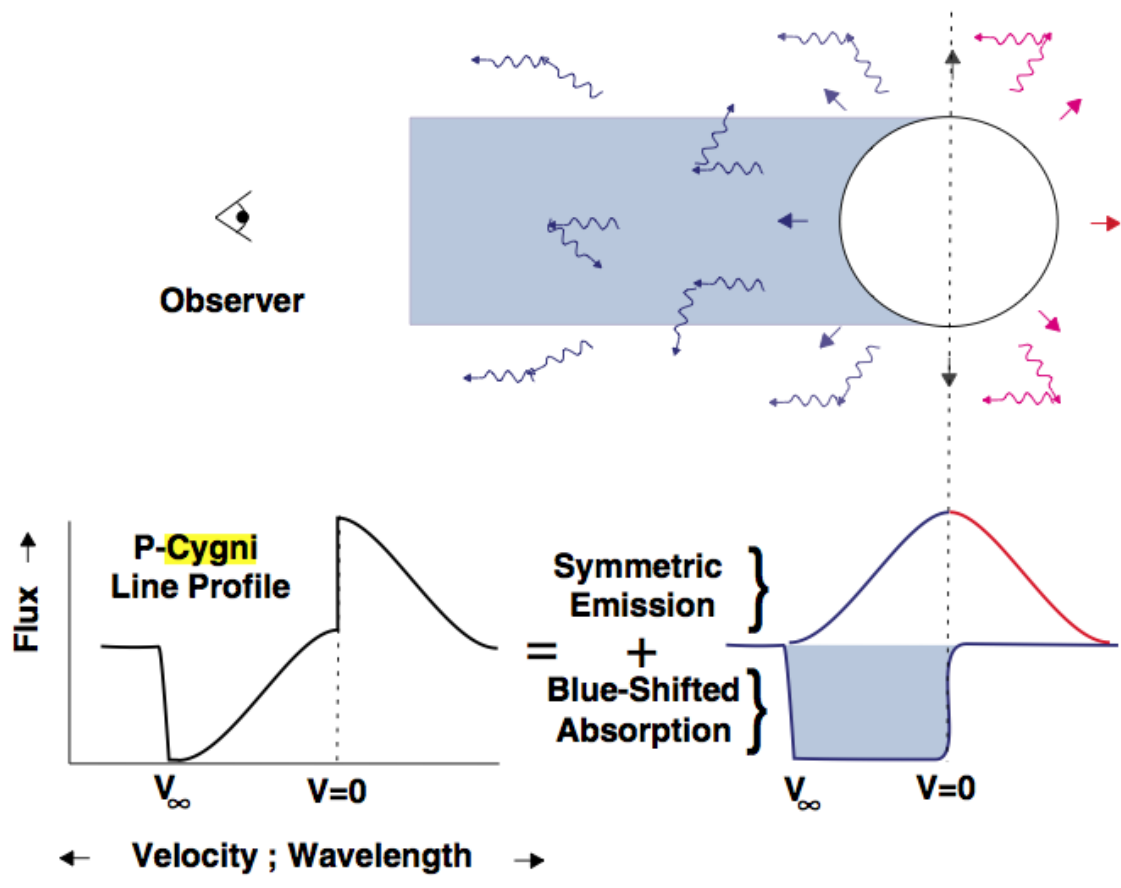


Figure 1.5: Schematic showing the formation of a stellar P Cygni profile. Taken from Dessart (2004).

higher metallicity accelerate their winds to a higher  $v_\infty$ , a relation of  $v_\infty \propto Z^{0.13}$  being derived by Leitherer et al. (1992).

### Mass-loss rates

The mass-loss rates of massive stars can be determined at a range of wavelengths. In the UV, P Cygni profiles from metal resonance lines are the common diagnostic. The profiles are sensitive to a product of the wind density and the ionisation fraction of the ion responsible for the line. The mass-loss rate can be derived since it is directly related to the density, and is achieved by comparing observations and theoretical predictions of the profiles. However, this requires accurate knowledge of the ionisation fraction of the specific ion, as well as its abundance, both of which depend on what radius the line is being formed at. The potential effects of shocks and X-rays embedded in the wind can make estimates of the ionisation fraction particularly uncertain. Nevertheless, the strength of the P Cygni profiles means the UV approach is sensitive down to mass-loss rates of  $10^{-10} M_\odot \text{yr}^{-1}$  (Martins 2011).

A more widely adopted technique is based in the optical using the  $H\alpha$  line (e.g. Puls et al. 1996). In this case, the  $H\alpha$  line forms via recombination, and as such, its strength depends on the square of the density (rather than just the density, as in the case of P Cygni profiles). For stars with progressively stronger winds,  $H\alpha$  will appear in emission upon a background of photospheric absorption, growing in strength until it is completely in emission. Emission will drop rapidly with density and therefore mass-loss rate (see Figure 1.6) meaning that the  $H\alpha$  line is only a practical diagnostic for stars where  $\dot{M} \gtrsim 10^{-8} M_\odot \text{yr}^{-1}$  (Puls et al. 2008). However, there is no concern over the ionisation of fraction of the ion since H will be almost completely ionised in massive stars. When determining the mass-loss rates of W-R stars supplementary indicators such as other Balmer lines or the He II  $\lambda 4684$  line can be particularly useful, as they too are in emission.

Alternatively, one can move to even longer wavelengths and determine mass-loss rates using the IR-radio continuum. The method avoids the complications of modelling spectral lines, and instead follows the principle that the emission (predominantly thermal emission) from free-free and bound-free processes will create an excess flux relative to photospheric models. This excess flux increases at longer wavelengths due to a  $\lambda^2$  dependence of the corresponding opacities and this corresponding increase in effective IR/radio-photosphere can be used to measure the mass-loss rate (Puls et al. 2008). Wright & Barlow (1975) were amongst the first to use the approach and showed that the continuum flux,  $S_\nu$ , would form the relation

$$S_\nu \propto \left(\frac{\dot{M}}{v_\infty}\right)^{4/3} \frac{\nu^{0.6}}{D^2}, \quad (1.5)$$

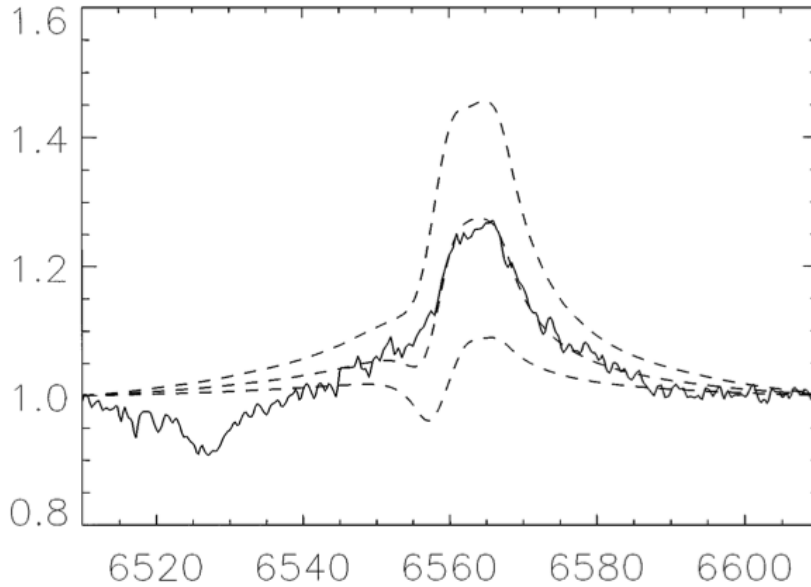


Figure 1.6: The  $H\alpha$  line profile of O5 Iaf+ HD 14947 compared with line fits as outlined by Puls et al (1996), adopting mass-loss rates of 10, 7.5 and  $5.0 \times 10^{-6} M_{\odot} \text{yr}^{-1}$ , respectively. Taken from Kudritzki & Puls (2000).

where  $\nu$  is the observed frequency, and  $D$  is the distance to the star. As the excess emission comes from a region in the wind which has already reached terminal velocity, the method is not dependent on a velocity law and only the terminal velocity must be known. The star's distance can often be the most uncertain factor and with OB stars typically being weak radio sources, recent observations have often been limited to Galactic targets.

Attempts have been made to describe mass-loss rates as a function of stellar properties. In particular, Vink et al. (2000) introduced a theoretical mass-loss recipe in good agreement with observations. The mass-loss rates in Table 1.3 adopt the Vink calibration showing typical O-type stars to range between  $10^{-6} - 10^{-5} M_{\odot} \text{yr}^{-1}$ . Vink et al. (2001) later improved the recipe to account for the expected metallicity dependence ( $\dot{M} \propto Z^{0.69}$ ), as a higher metal abundance would help drive more material.

The same dependence is reflected in the wind-momentum luminosity relation (WLR). The WLR (Kudritzki et al. 1999) demonstrated how the modified wind momentum,  $D_{\text{mom}} = \dot{M} v_{\infty} R_*^{0.5}$  scales with the stellar luminosity and can potentially be used to determine extragalactic distances. Mokiem et al. (2007b) observed the metallicity dependence of mass-loss rates of OB stars through the Galaxy and MCs. However, they noted empirical WLRs to be higher than those predicted from theory. Neither approach may be completely accurate but inconsistencies are believed to arise as the flow of material in the stellar wind is clumped rather than smooth. Evidence for such inhomogeneities have been revealed as they produce variable spectroscopic

features in the wind lines (Eversberg et al. 1998; Lépine & Moffat 2008). With wind clumping effects the empirical mass-loss rates of massive star might need to be scaled down by factors of  $\sim 3$ . In contrast, the theoretical mass-loss rates for mid-late B-supergiants can exceed observations by factors of 10 – 100, the so-called ‘weak wind problem’, underlining the difficulties in understanding hot stellar winds.

One can adopt the same techniques used on OB stars and apply them to W-R stellar winds. UV P Cygni lines allow an estimate of  $v_\infty$  as before, although a wealth of emission lines often makes it hard to identify the continuum of W-R stars (Prinja et al. 1990). However, alternative diagnostics such as He I P Cygni lines do become available in the optical and IR (Howarth & Schmutz 1992). Empirical results indicate a smaller  $v_\infty$  in later W-R subtypes. Some of fastest winds are recorded in WO types but W-R winds are otherwise similar to OB stars.

Conversely, W-R mass-loss rates easily supersede those of OB stars by factors  $> 10$  and can extend to several times the stellar radii. Momentum transfer is thus more efficient in W-R stars, again thought to source from their high wind densities. Equating the wind momentum to the total momentum of photons that leave an OB star:  $\dot{M}v_\infty = L/c$ , delivers the ‘single scattering limit’ whereby each photon is scattered once in the wind. But this will not apply to a W-R star which has more lines available to transfer momentum so a photon becomes trapped and undergoes multiple scattering (Puls et al. 2008). Nugis & Lamers (2000) connected these mass-loss rates to empirical W-R parameters. Effects of wind clumping are even more apparent in W-R stars. A so called volume filling factor,  $f$ , was introduced to describe the clumping of the wind such that a typical value of  $f \sim 0.1$  related to 10% of the wind being occupied. Therefore, with  $\dot{M} \propto f^{-0.5}$ , clumping reduces W-R star mass-loss rates by similar factors to OB stars. Mass-loss rates of LBVs and RSGs are less constrained but the observation of circumstellar shells suggest they too will influence evolution, despite their brief phase.

### 1.1.5 Stellar evolution

Massive stars are distributed across the upper H-R diagram but their positions are not random. The various SpTs show correlations in their properties indicating that they are connected by an evolutionary process. Where the massive stars in a young cluster will predominantly be dwarfs, older regions host the more evolved supergiants and W-R stars. The popular scenario linking the different evolutionary phases was put forward by Conti (1975). It suggested that the high mass-loss rates of massive stars were capable of stripping the outer layers to reveal the products of H and He burning such that  $O \rightarrow Of \rightarrow WR$ . More phases were incorporated by considering the amount of material stripped from the star as a function of its initial mass. Higher mass-loss would be necessary to form a WC star ( $\gtrsim 40 M_\odot$ ) while red supergiants (RSG) are only

Table 1.3: Stellar wind parameters for OB and W-R stars.

Spectral Type	$T_{\text{eff}}$ [kK]	$\log \dot{M}$ [ $M_{\odot} \text{ yr}^{-1}$ ]	$v_{\infty}$ [ $\text{km s}^{-1}$ ]
O3 V	45	-5.43	3200
O6 V	39	-6.15	2500
O9 V	33	-6.94	1500
B0 V	29.5	-7.15	< 1500
O3 I	42	-5.26	3200
O6 I	37	-5.42	2300
O9 I	31	-5.88	2000
B0 I	27.5	-5.98	1500
WN 3-WN 6	85-60	-5.3 - -4.8	2200-1800
WN 7-WN 9	50-32	-4.8 - -4.7	1300-700
WC 4-WC 6	90-80	-4.6 - -4.9	2750-2200
WC 7-WC 9	75-50	-4.7 - -5.0	2200-1200
WO	150	-5.0	4100

**Notes.** OB star mass-loss rates are predicted using the Vink et al. (2001) prescription and wind velocities are taken from Prinja et al. (1990). W-R star parameters are taken from Crowther (2007) and the mass-loss rates assume a volume filling factor of  $f = 0.1$ .

observed at a lower luminosity limit (Humphreys & Davidson 1979) which traces them back to lower masses ( $\sim 30 M_{\odot}$ ). The following scenarios are taken from Crowther (2007):

$M_{\text{init}} \gtrsim 75 M_{\odot}$ :

O  $\rightarrow$  WN (H-rich)  $\rightarrow$  LBV  $\rightarrow$  WN (H-poor)  $\rightarrow$  WC  $\rightarrow$  SN Ic

$40 M_{\odot} \lesssim M_{\text{init}} \lesssim 75 M_{\odot}$ :

O  $\rightarrow$  LBV  $\rightarrow$  WN (H-poor)  $\rightarrow$  WC  $\rightarrow$  SN Ic

$25 M_{\odot} \lesssim M_{\text{init}} \lesssim 40 M_{\odot}$ :

O  $\rightarrow$  LBV/RSG  $\rightarrow$  WN (H-poor)  $\rightarrow$  SN Ib

The LBV role is debatable, but the few that have been observed indicate extreme mass-loss. The mechanism is unclear but is thought to relate to the star evolving close to its Eddington limit. The resulting mass ejections not only prevent evolution onto the RSG phase but help reveal the W-R star underneath. The final stages in each scenario represent a type I core-collapse SNe both with He (SN Ib) and without He (SN Ic) in its spectrum. Substantial effort has recently gone into connecting supernovae with their predicted progenitors (Smartt 2009;

Maund et al. 2014). While some RSGs have been identified as the source of SNe, W-R star candidates remain elusive. The presence of circumstellar shells around type II core-collapse SNe has suggested that LBVs may even be the likely progenitors in some cases (Smith et al. 2011).

Alternative scenarios and mass limits demonstrate how the evolutionary sequences of massive stars remains uncertain. WNLs are linked to some of the most massive and luminous stars observed, yet Hamann et al. (2006) found no overlap in the luminosities of WNL ( $\log L/L_{\odot} > 6.0$ ) and early WN (WNE) stars ( $\log L/L_{\odot} < 5.8$ ), making a large transformation difficult to explain on such a small timescale. WNL stars might therefore avoid the other W-R phases altogether (Martins et al. 2009; Crowther et al. 2010) and end their lives via a different route. Meanwhile, atmospheric modelling of Galactic WC stars by Sander et al. (2012) led them to favour 20 – 45  $M_{\odot}$  progenitors. A favoured method for testing these scenarios is to compare the observed number ratios of stars (e.g. O/W-R, RSG/W-R, WN/WC) with those created by the different evolutionary sequences. For example, the W-R/O ratio helps to constrain the minimum initial mass needed for a star to evolve to the W-R phase. The metallicity dependence of these ratios means that some caution is required. However, extragalactic stellar surveys, particularly of W-R stars remain in their infancy (Shara et al. 2012).

Despite these complications, a number of models have been devised to predict the evolutionary paths of massive stars, see Figure 1.7. These have primarily been led by groups based in Geneva (e.g. Schaller et al. 1992), Padova (e.g. Bertelli et al. 1994) and Bonn (e.g. Brott et al. 2011). They attempted to reproduce observed stellar number ratios while adopting new estimates for mass-loss rates and metallicity dependence into their models. Recently, more attention has gone towards the effects of stellar rotation and attempting to incorporate them into models (Maeder & Meynet 2000; Brott et al. 2011; Vázquez et al. 2007; Levesque et al. 2012).

Understanding stellar evolution allows better estimates of the age of a region. The life spans of the separate evolutionary phases are connected to their relative numbers; the scarcity of yellow supergiants indicating that it is a very brief phase in comparison to the time spent as a blue supergiant. A series of evolutionary tracks can also be conveniently combined and inverted to provide isochrones to estimate the age of a stellar population. Ultimately the aim is to confidently model the evolution of a star of any mass from birth to death. A combination of all of these evolutionary paths permits stellar population synthesis (SPS), with the ability to model entire populations from stellar clusters to galaxies.

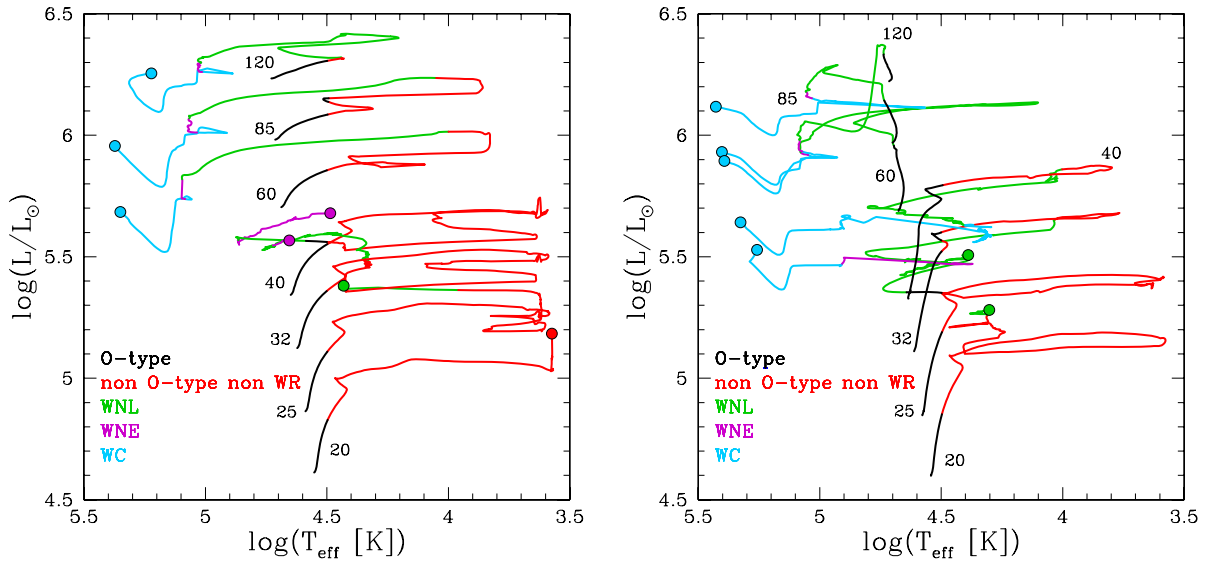


Figure 1.7: Evolutionary tracks of various mass models showing the different stellar phases. End points are marked with a circle. Left: non-rotating models. Right: rotating models. Taken from Georgy et al. (2012).

### 1.1.6 Binary systems

Observations suggest that a majority of stars are actually formed as part of multiple systems. The gravitational relation between the stars provides one of the most reliable methods for estimating stellar mass. Furthermore, if their orbits are close, the stars can undergo interaction that will significantly affect their evolution. Understanding multiple systems is therefore an essential component in the study of massive stars.

Spatially resolving multiple systems requires high quality optics, for even the widest binaries. Eclipsing binaries are an alternative method which makes use of the reduction in flux as one star passes in front of another. Spectroscopy can also be used to measure the radial velocity shifts displayed by the stellar lines as the stars move in their orbits, and is applied in Section 3.4.1. These methods offer a wealth of information on the stellar system including the orbital period and inclination, the radii of the stars, and ultimately their masses.

Mermilliod & García (2001) found the massive star binary fraction in Galactic open clusters to range from 0.14 to 0.8. Sana & Evans (2011) compared the different environments of clusters and associations and arrived at an average binary fraction of  $\sim 0.44$ . However, these studies have concentrated on spectroscopic techniques which reveal only close binaries. Wider binaries are expected, and indeed being discovered in these regions (e.g. Caballero-Nieves et al. 2014) to further boost the binary fractions.

In the case of a binary, the more massive of the two stars is designated as the primary,

and the less massive the secondary. The evolution of the system will depend on a number of variables. Those with a large separation and long period will likely evolve as independent stars. But in a close binary, interaction is determined by the surrounding regions that are gravitationally bound to each star, the Roche lobes. The first Lagrangian point marks where the Roche lobes meet and any material from the primary star extending beyond this point will fall into the gravitational well of the secondary, and vice versa. This mass exchange can occur as a star expands, leading to Roche lobe overflow (RLOF), and consequently refuelling the receiver. Depending on orbital parameters, the stars can share a common envelope or even merge. In turn, the class of SN expected to be observed for each star is affected by the changes in evolution. However, SNe occurring in binary systems also offer clues to the origin of stars moving at high velocities (runaway stars), the SN providing a kick to the ejected star. Binaries which survive the SN will be left with a companion neutron star or BH. This provides the scenario for X-ray binaries, as mass is transferred onto a compact object, forming an accretion disk and high X-rays luminosities.

Classically, stars showing binary effects have been withdrawn from samples to avoid contamination. Yet, de Mink et al. (2014) warn how this method can be counter productive as it favours the removal of binaries which have had an opportunity to interact. Figure 1.8 shows how their simulations predict a large fraction of apparently single stars are in fact likely to be binaries or have been binaries in the past. In some cases, mass is transferred between stars or they merge. Alternatively the radial velocity of the primary star ( $K_*$ ) falls below the detection limit of  $\sim 10 \text{ km s}^{-1}$ . Even stars that are detected as binaries are expected to be composed of systems that have undergone or are currently undergoing mass transfer.

Additional mass transfer can also occur from stellar winds, although does not compare to that from RLOF. Wind collisions will take place between two OB stars with a cone forming around the star with the weaker wind. The resulting shocks are also capable of producing X-rays, although less luminous than those from accretion disks. It is also noted that stellar winds in binaries are linked to dust formation. The effect is observed to be episodic and limited only to late WC stars. However, the process remains unclear, the results for some stars suggests that they are constantly producing dust, despite variations in the temperature and density of WC winds not being suited to its formation.

### 1.1.7 The formation of massive stars

Giant molecular clouds (GMCs) are the birth place of low and high mass stars alike. They are huge accumulations of cold (10 – 20 K) gas and dust that can span 10s of parsecs with masses between  $10^3 - 10^5 M_{\odot}$  (Zinnecker & Yorke 2007). Star formation begins when a re-

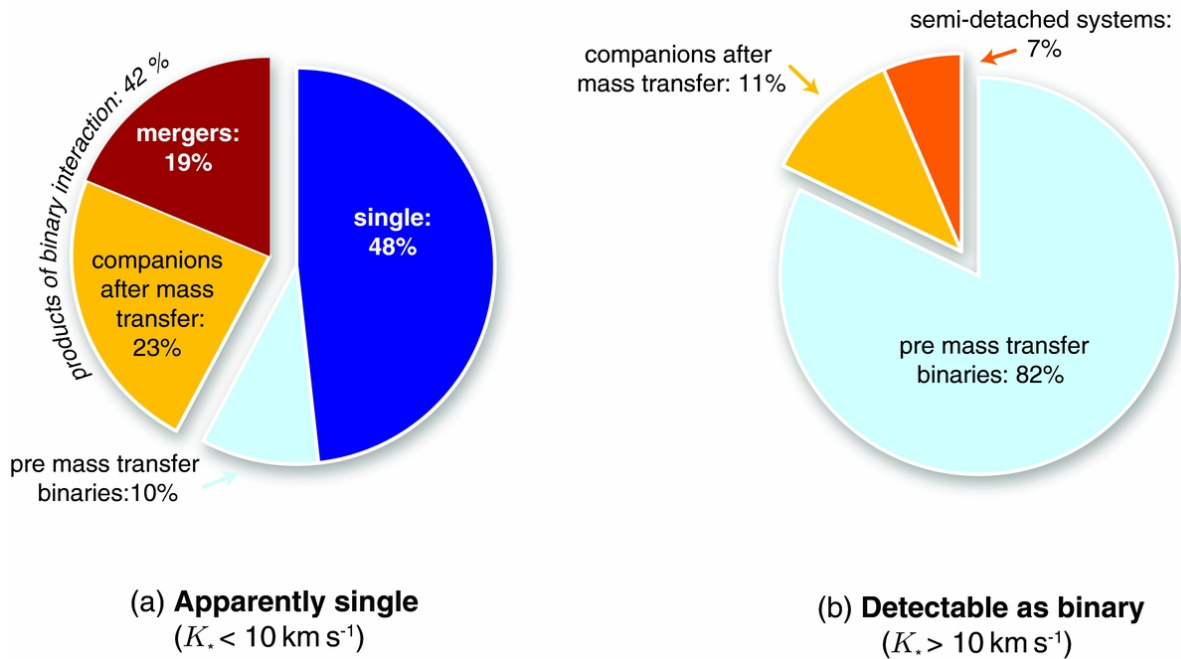


Figure 1.8: Expected contamination fractions for stars detectable as single and binary. Taken from de Mink et al. (2014).

gion collapses due to a gravitational instability, potentially triggered by a nearby SN. Material is accreted on to the centre, but the surrounding dust is optically thick to the resulting radiation. This heats the object to give a hot molecular core, bright in the mid and far-IR. If temperatures are sufficiently high, the closest regions of H gas can be ionised in what is known as a ultracompact H II region. This is a reliable indication of the presence of an OB star, yet its observation is often still restricted by remaining dust as defined for a young stellar object (YSO).

Whilst this same basic process is thought to apply to all stars, there are complications explaining how massive stars achieve their initial mass, suggesting that their formation differs from that of low mass stars. Problems arise as massive stars will commence H-burning at  $\sim 10 M_{\odot}$  and generate an opposing radiation pressure to any accreted material. Yet, further accretion is evident, since stellar masses are observed in excess of  $100 M_{\odot}$  (Schnurr et al. 2008a). This is thought to be feasible with material falling on to an accretion disk whilst radiation escapes perpendicularly through polar jets (Kuiper et al. 2011).

The idea of an accretion disk is held by the two current leading models of massive star formation, but how this accretion comes about is disputed. The ‘monolithic collapse’ model (e.g. McKee & Tan 2003) forms a star from a single hot core that accretes all the available surrounding mass. The mass of the core determines the mass of the eventual star. Alternatively,

the ‘competitive accretion’ model (e.g. Bonnell & Bate 2005) suggests that a GMC fragments to form a number of ‘seeds’ around which accretion occurs. Each seed competes with its neighbour so that those in favourable locations will be able to obtain more material and at a faster rate. The two approaches hold different pros and cons which are most distinct when trying to address the formation of star clusters as a whole.

Lada & Lada (2003) concluded that up to 90% of stars formed in clusters, with most GMCs going on to form star clusters containing at least 100 members. Bressert et al. (2010) discuss how these fractions are dependent on the adopted definition of a cluster, as selected densities can range from tightly bound clusters of  $\sim 80$  YSOs  $\text{pc}^{-2}$  to  $\sim 3$  YSOs  $\text{pc}^{-2}$  as used by Lada & Lada (2003). Nevertheless, high mass stars are rarely found in isolation, and those that are are often runaway stars with their origin being traced back to a cluster. Those observed within clusters are predominantly located towards the centre with lower mass stars further out: a state of mass segregation. This is problematic for the monolithic collapse model which should allow isolated massive stars to form. It predicts large dense cores avoiding fragmentation to produce massive stars with further dynamics required to segregate the masses. The competitive accretion model naturally favours a cluster environment as well as mass segregation, as the seeds at the centre with the deepest gravitational potential wells will become the most massive. However, the feedback from a growing seed could limit the amount of accretion itself and neighbours receive.

Further clues are obtained by studying star clusters as a whole where fewer stars fall into increasingly higher mass bins. This probability distribution of stars is a mass function,  $\phi(M_*)$ , such that  $\phi(M_*)dM$  is the number of stars between masses  $M_*$  and  $M_* + dM$ . A relation was first demonstrated by Salpeter (1955) according to the power law:

$$\phi(M_*)dM \propto M_*^{-\alpha} \quad (1.6)$$

to describe the initial mass function (IMF) of a cluster. While refinements have been made to account for the observations in low mass bins (Kroupa 2001), the value of  $\alpha \sim 2.3$  has been found to be relatively consistent in all instances (Bastian et al. 2010). This uniformity suggests a cluster formation process that is independent of the density or metallicity of the original GMC. Even with cluster age, and without accounting for binaries,  $\alpha$  appears to hold steady.

The fixed IMF can be extrapolated to estimate the number of stars at different masses. A shortage of stars in higher mass bins led Figer (2005) to draw an upper mass limit at  $150 M_\odot$  but some findings have exceeded this, reaching over of  $300 M_\odot$  (Crowther et al. 2010). Larson

(2003) related the most massive star in a cluster,  $M_{\text{up}}$ , to the total cluster mass,  $M_{\text{clu}}$  by:

$$M_{\text{up}} = 1.2M_{\text{clu}}^{0.45}. \quad (1.7)$$

Given its high mass-loss rate, a  $M_{\text{init}} > 150 M_{\odot}$  star may only be found in a massive enough cluster, and only if the cluster is observed at a young enough age.

## 1.2 H II Regions

Once massive protostars grow hot enough, their photons will be capable of ionising the surrounding gas to produce a H II region. A large fraction of the photon energy is needed to overcome the ionisation potential of the atoms, while the remainder supplies kinetic energy to the free electrons and provides a heat source for the gas. Due to its abundance, the most common ion is  $\text{H}^+$  (hence H II), and the optical spectra of gaseous nebulae are particularly dominated by the Balmer lines. Other emission lines are also prominent from elements such as O, N and S (see Figure 1.9). These emission lines equally extend to the UV, the IR and into the radio bands. They are overlaid upon a weak continuum predominantly caused by free-bound transitions in the Paschen continuum at  $\lambda > 3646 \text{ \AA}$  and the Balmer continuum at  $912 < \lambda < 3646 \text{ \AA}$ . Dust may be present in the nebula, which will further add to the continuum through thermal radiation, while the free-free emission of electrons dominates the radio continuum. In particular, the 21 cm radio H I line is used to map their distribution, and in turn their hot stars. It reveals a concentration along the spiral arms of the Milky Way, with similar instances for extragalactic galaxies.

### 1.2.1 Properties of H II regions

Emission lines are the primary tool for obtaining information on H II regions. For physical properties, methods make particular use of intensity ratios of atoms at different ionisation stages, e.g.  $\text{O}^+$  and  $\text{O}^{2+}$ , many of which are applied in Chapter 2. They can be used to estimate the electron temperature of the gas,  $T_e$ , which shows little variation from  $5 \times 10^3 - 10^4 \text{ K}$  (Osterbrock & Ferland 2006). This is observed despite the associated OB stars ranging  $T_{\text{eff}} = 2 - 5 \times 10^4 \text{ K}$ , and occurs due to the efficient cooling mechanisms in the nebula. If  $T_e$  is increased by a higher  $T_{\text{eff}}$  of a star, this is counteracted as the recombination rate falls, and so there is less neutral H for the star to ionise and heat. Furthermore, the cooling rate of ions such as  $\text{O}^+$  also increases with  $T_e$ , helping to maintain a steady temperature. The opposite applies should  $T_{\text{eff}}$  decrease.

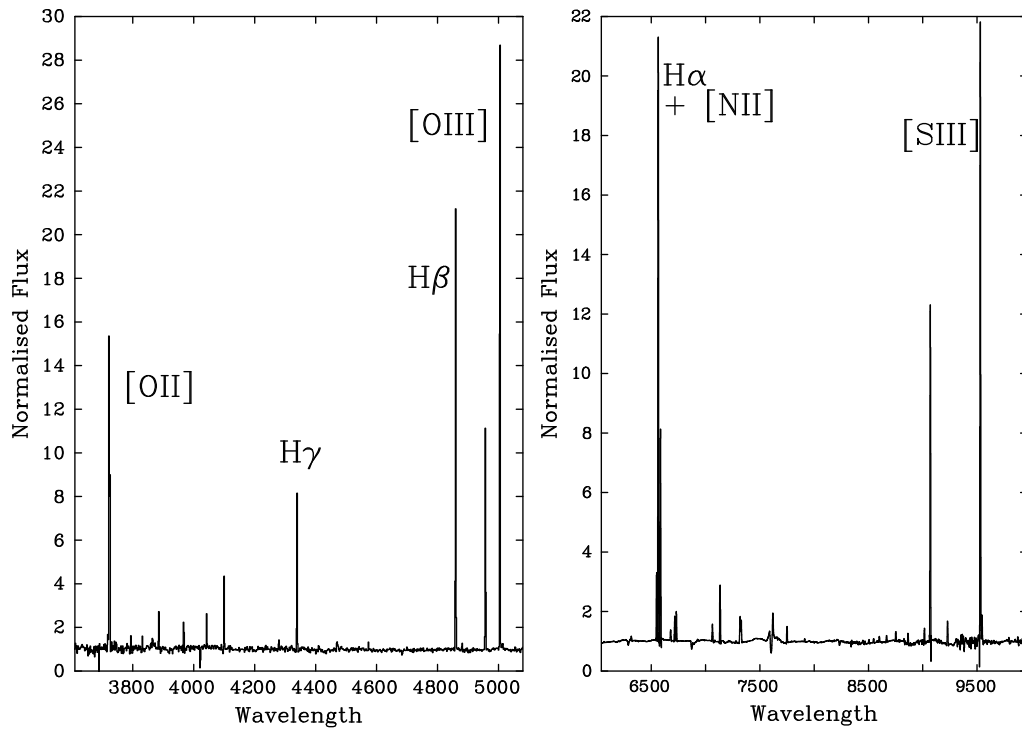


Figure 1.9: Prominent nebular lines in the optical spectrum of a H II region. Taken from ISIS observations presented in Chapter 2.

The density of the gas varies between nebulae and even within a region itself the structure can change from tight knots to more diffuse clouds. The density can also be estimated by measuring the relative intensities of emission lines. Radio recombination lines are commonly used since the recombination rate depends on the gas density and  $T_e$ . For other lines, collisional de-excitation can play an important role and their strengths are less dependent on  $T_e$ , as shown for the [S II]  $\lambda 6716/\lambda 6731$  ratio in Chapter 2.

Nebulae give further information on the chemical abundances of the region. This is important for determining the initial metallicity of the associated stars as it will have changed during evolution. They can be used to trace metallicity gradients over larger scales, Searle (1971) and Zaritsky et al. (1994) finding abundances to radially decrease along the disks of spiral galaxies. Work for the Milky Way is hindered by the obscuring dust in the Galactic plane. However, IR studies have allowed abundances in central H II regions to be estimated (e.g. Afflerbach et al. 1997), and combined with optical observations of the outer Galaxy (e.g. Deharveng et al. 2000) they indicate a similar gradient.

Table 1.4: Properties of H II regions.

Class	Size [pc]	Density [cm <sup>-3</sup> ]	Ionised Mass [ M <sub>⊙</sub> ]
Hypercompact	≲ 0.03	≳ 10 <sup>6</sup>	~ 10 <sup>-3</sup>
Ultracompact	≲ 0.1	≳ 10 <sup>4</sup>	~ 10 <sup>-2</sup>
Compact	≲ 0.5	≳ 10 <sup>4</sup>	~ 1
Classical	~ 10	~ 100	~ 10 <sup>5</sup>
Giant	~ 100	~ 30	~ 10 <sup>3</sup> – 10 <sup>6</sup>
Supergiant	> 10	~ 10	~ 10 <sup>6</sup> – 10 <sup>8</sup>

**Notes.** Based on values from Kurtz (2005).

### 1.2.2 Sizes of H II regions

The overall scale of an H II region is ultimately determined by its ionising source. At a given volume, the rate at which ionising photons are emitted will be balanced by the rate of recombination. This volume of gas is a Strömgen sphere with a radius known as the Strömgen radius,  $R_s$ :

$$R_s = \left( \frac{3}{4\pi} \frac{Q_0}{n^2 \beta_2} \right)^{1/3}, \quad (1.8)$$

where  $n$  (m<sup>-3</sup>) is the number density of H nuclei, and  $\beta_2 = 2 \times 10^{-16} T_e^{-3/4}$  (m<sup>3</sup> s<sup>-1</sup>) is the total recombination coefficient which depends on the electron temperature,  $T_e$ . For a single star,  $R_s$  will therefore be larger around a O3 star compared to an O9 since its  $Q_0$  is higher. Equally, a lower gas density would mean fewer recombinations and thus give a larger  $R_s$ .

H II regions can span a range of sizes, the smallest being the hypercompact H II (HCH II) and ultracompact H II (UCH II) regions, where the gas is observed to be densely packed within less than 0.1 pc and buried deep within a molecular gas cloud. As a result, their detection has been restricted to the IR and radio wavelengths (Wood & Churchwell 1989; Kurtz 2005). Other regions extend to the scales of hundreds of parsec, with the gas being more dispersed and clearly observable in the visible. Table 1.4 gives a summary of the types of H II regions observed and their typical properties.

The varying sizes raise the question of whether the regions are connected on an evolutionary basis. Taking an OB cluster such as the Orion Trapezium Cluster with a size of ~ 0.16 pc, it is capable of fitting within a compact or even UCH II region (Kurtz 2005). For a HCH II region the scale begins to approach that of a single star. Indeed, observations of broad radio recombination lines in HCH II regions have given evidence for the fast rotation and outflows associated with star formation (Johnson et al. 1998), something absent in UCH II regions. An expansion

scheme can therefore unfold - the HCH II and UCH II regions confined deep within molecular clouds and representing the earliest stages of star formation. Once ionisation from the OB stars drives the expansion of the gas out beyond the molecular cloud, H II regions can then become visible in the optical as in the compact and classical cases. Giant H II (GH II) regions will host a collection of these smaller regions across their giant molecular cloud. They are found in external galaxies with widespread star formation, a prime example being the Tarantula Nebula in the LMC, the focus of Chapters 4 & 5.

### 1.2.3 Ionising stars

Larger H II regions are home to larger quantities of ionising stars and therefore more ionising photons. Recalling that  $Q_0$  changes with SpT, the amount of ionised gas is tightly correlated with the stellar population and star formation of the region. The H $\alpha$  luminosity of a nebula is often used to measure this ionisation and ultimately its number of ionising O-type stars.

The total number of ionising photons,  $Q_0^{\text{Total}}$ , is commonly expressed in terms of the number of equivalent O7 V stars,  $N_{O7}$ :

$$Q_0^{\text{Total}} = N_{O7V} Q_0^{O7V}, \quad (1.9)$$

where  $Q_0^{O7V}$  is the Lyman continuum photon rate of a single O7 V star. A range of stars contribute to  $Q_0^{\text{Total}}$  and it will further vary with time. If  $Q_0(M_*, t)$  is the ionising photon rate of a star of initial mass  $M_*$  at time  $t$ ,

$$\eta_0(t) = \frac{\int_{M_{low}}^{M_{up}} \phi(M_*) Q_0(M_*, t) dM}{Q_0^{O7V} \int_{M_O}^{M_{up}} \phi(M_*) dM} \quad (1.10)$$

represents the IMF-averaged ionising photon rate normalised to the output of one equivalent O7 V star. The integral in the numerator has upper and lower mass limits equal to the IMF ( $\phi(M_*)$ ), while the lower limit in the denominator is that defined for O-type stars. The total number of O-type stars,  $N_O$ , is then:

$$N_O = \frac{Q_0^{\text{Total}}}{\eta_0(t) N_{O7V}}. \quad (1.11)$$

Normalising with respect to the ionising output of an O7 V star is a useful comparison since  $\eta_0(t)$  is typically  $\sim 1$  for a 1 Myr old region. This was shown by Schaerer & Vacca (1998) who used SPS to estimate the stellar contents of young starbursts. Figure 1.10 shows how  $\eta_0(t)$

falls with time as the O-type stars die out, with a further dependence on the metallicity of the region. They noted additional peaks at  $\sim 3$  Myr, for subsolar metallicities, as ionising outputs increased as stars reached the W-R phase. Determining the ionising contribution of W-R stars is one focal point of this study. The second peak in  $\eta_0(t)$  is related to the number of O-type stars falling to zero and hence the value of the denominator in Equation 1.10 approaches zero. At this stage, the definition of  $\eta_0(t)$  becomes meaningless and it will be the cooler B-type stars that will provide the ionising photons.

As the stellar population ages, these variations with time will equally be observed in the nebular gas. The changing ionising output will influence the  $H\alpha$  luminosity of the region. Meanwhile, the strength of the stellar winds is fluctuating too, forming new structures within the region and changing the density of the gas. These effects are even more significant when accounting for SNe.

#### 1.2.4 Star formation rates

From the observation of YSOs and indeed HCH II regions, H II regions are not only an environment for main-sequence stars but those that are undergoing formation as well. The models produced by Schaerer & Vacca (1998) in Figure 1.10 assumed a single instantaneous burst of star formation but in a GH II region, formation could easily be continuous: a cluster of stars triggering further formation in neighbouring gas clouds.

Given their short life spans, massive stars are a clear indication of recent star formation but the nebula once again holds clues that can be particularly beneficial when the stars themselves cannot be observed. The star formation rate (SFR) can be traced at a range of wavelengths from emission coming from the gas or even the heated dust. The different methods hold their advantages and disadvantages. For example, the  $H\alpha$  flux specifically requires the presence of ionising stars and will change on timescales comparable to the life spans of those stars, hence offering a near instantaneous measure of the SFR. Conversely, the  $1500 \text{ \AA}$  UV flux would directly trace the photospheric emission from young massive stars in the region. The UV emitting population has a comparatively longer life span ( $\sim 10^8$  Myr) such that deriving the SFR needs to assume that star formation has remained reasonably constant over this timescale. Section 5.6 compares several of these SFR tracers in order understand their discrepancies.

### 1.3 Relations to extragalactic studies

Many of the topics previously discussed extend on to the study of external galaxies. The analysis of massive stars is restricted at extragalactic distances: as observing techniques reach

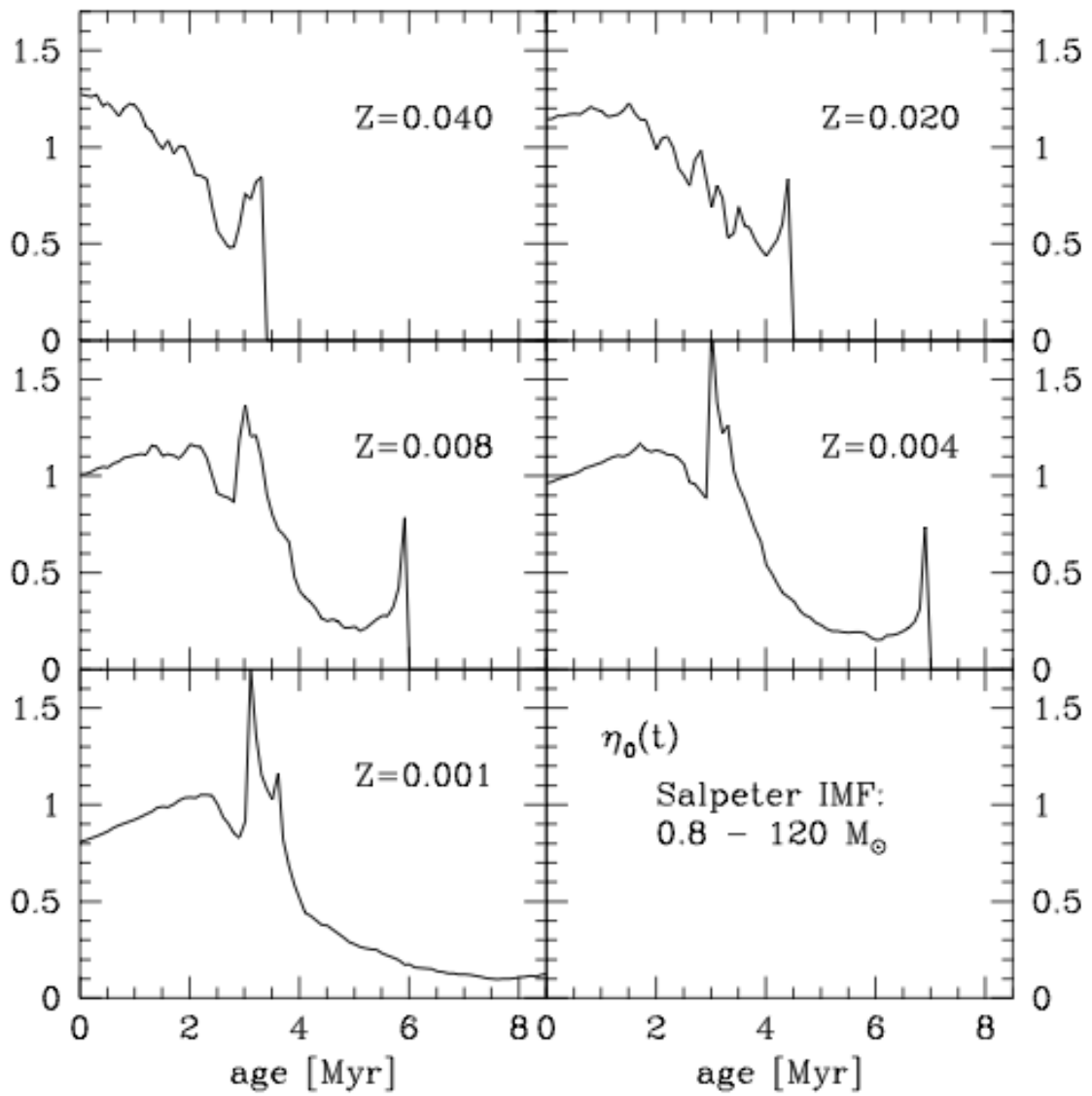


Figure 1.10: The evolution of  $\eta_0(t)$  as given by Equation 1.10 for starbursts at different metallicities and assuming a Salpeter IMF. Taken from Schaerer & Vacca (1998).

their limits, individual stars can no longer be spatially resolved and key spectral lines become merged. However, their signatures can still be observed as discussed in Section 1.2 and the stars dominate the luminosity of their host galaxies. Prominent spectroscopic features of stars can be used to estimate galactic ages, while H II regions can help to reveal abundance gradients and areas of star formation.

These provide a basis for the SPS modelling of extragalactic starforming regions (e.g. Vacca et al. 1995; Leitherer et al. 1999; Eldridge & Stanway 2009). In many extragalactic cases, these synthetic models are the only available method for estimating the nature of the stellar population, but how reliable are they? The same question of reliability equally applies to the different SFR tracers which are essentially derived from the population synthesis models. Discrepancies are found between certain techniques (Lee et al. 2009; Chomiuk & Povich 2011), but do these arise due to inaccuracies in the models or are some tracers more appropriate in certain circumstances?

Clearly the models feature several variables, not only those affecting the stars like mass-loss and rotation, but those intrinsic to the region such as the metallicity, the IMF and SFR. It is the study of nearby massive stars and the relation with their H II regions, which provides a test bed for these models. The properties of GH II regions in particular can then be used to probe the scales observed in external galaxies.

This analysis further aids our understanding of galactic evolution. The ever changing massive star population not only dictates the metallicity of a galaxy but may be the ionising source for its diffuse ionised gas (DIG). The DIG refers to a thick (~few kpc) layer of low density ( $n_e = 0.03 - 0.08 \text{ cm}^{-3}$ ) ionised H observed throughout the disks of spiral galaxies with SFRs, much like the Milky Way (Haffner et al. 2009). If all the ionising photons emitted by an OB star are not absorbed by its H II region, some can propagate further into the galactic medium, ionising and heating it to produce the DIG. A fraction of escaping photons would further influence any calibrations that relied on the ionised gas, so determining its value is crucial.

The effects of stellar winds and SNe can also extend throughout a galaxy. Where the wind of single stars can carve a small bubble into the surrounding ISM, a whole stellar population combines to form a galactic superwind. This is observed in starburst galaxies such as M82, where X-ray emission from the ejected gas reaches several kpc from the galactic disc (Stevens et al. 2003). The outflows drive material to the galaxy halo, but it remains unclear whether it can escape the galaxy altogether, or if it becomes re-accreted to fuel future starbursts.

On galactic scales, alternative sources of feedback must also be considered, in particular that of the active galactic nucleus (AGN). They are linked to shaping the luminosity function of a galaxy, regulating its star formation and the production of radio jets (Fabian 2012). AGN are powered by the gravitational energy of the supermassive black holes (SMBH) lying at

the centres of galaxies. A strong correlation has been found between the mass of the SMBH ( $\sim 10^7 M_{\odot}$  or higher) and the luminosity of the surrounding galaxy bulge (Ferrarese & Merritt 2000). Why this relation holds so well remains to be answered, but feedback from both the AGN and starbursts is potentially quenching the inflow of gas onto the accreting SMBH (Cen 2012).

## 1.4 The Focus of this Study

Many questions remain regarding our understanding of massive stars and their associated H II regions. This study aims to reveal the connections between these two components, with a particular focus on the ionising photon budget. It seeks to answer the following questions: How are the properties of massive stars and H II regions correlated, and can one be used as a reliable indicator for the other? Do certain massive stars govern the structures of H II regions more than others, if so what contributions do they make? How do these relations vary with the mass and age of a H II region?

The work is structured as follows: Chapter 2 investigates H II regions within the Milky Way. The stars and nebulae are separately analysed in an attempt to draw connections between the two. Estimates are made of the ionising photon budget of each region to determine whether the stellar photons are trapped or are able to escape the nebula. Chapter 3 focusses on the W-R star population within the GH II region 30 Doradus in the LMC. Armed with new spectroscopic data, analyses are made to improve our understanding of their binary fraction and companions. Atmospheric modelling is also carried out to establish their physical properties and reveal possible evolutionary relationships. Chapter 4 continues the study of 30 Doradus by compiling a census of the hot luminous star population. SpTs are assigned from a combination of new observations and literature. The spectroscopic completeness of the census is further calculated to determine whether the stellar population of 30 Doradus can be reliably used as a test bed for unresolved star forming regions. The spatial and number distributions of different SpTs are also derived for the region. Chapter 5 uses the census and estimates the mass, age and feedback of the stellar population, as well as the SFR. Their consistency with current population synthesis models and calibrations is explored. The ionising photon budget is estimated again for 30 Doradus as a probe for extragalactic GH II regions. Finally Chapter 6 summarises the findings of this study and discusses the potential for future work.



# Chapter 2

## A Study of H II Regions with Single Ionising Stars in the Outer Galaxy

### 2.1 Introduction

H II regions are predominantly located along the spiral arms of disk galaxies where they coincide with rich numbers of OB stars. The two are strongly linked as a star can govern the structure and dynamics of a region through its copious amounts of high energy photons and strong stellar winds. Strong nebular emission lines can equally reflect the ionising nature of the star, while also giving diagnostics on the gaseous environment. Both the stellar atmosphere and nebula can be modelled by separate codes but the consistency of the two requires further investigation.

H II regions can be surveyed at extragalactic distances thanks to strong H recombination lines. Establishing connections to a star is less straightforward as they start to be unresolved. Even at closer distances, a cluster of stars may be associated with the nebula and identifying the primary exciting star can be difficult. Sharpless (1953, 1959) surveyed different Galactic H II regions, many with multiple stars. Stellar positions and photometry were typically used to eliminate background/foreground stars and identify the bluer exciting stars (Chopin et al. 1973; Crampton et al. 1978; Russeil et al. 2007). This still left uncertainty in highly reddened nebulae where a SpT would be needed to decipher whether such a star was indeed capable of ionising the region.

A selection of Galactic H II regions, determined to contain a partially embedded O-type star, were chosen for this study. Along with strong H lines, the nebulae emit a number of forbidden lines from elements including O, N and S. Their intensity ratios offered diagnostics for the temperature, density and chemical abundance of the nebula. Separate spectroscopy

of the embedded star allowed a variety of stellar parameters to be determined along with a distance to the system.

This independent study of the star and its host H II region provides a test bed for stellar and nebular models alike (e.g. Giveon et al. 2002). Stellar models give estimates on a star's temperature and ionising radiation which in turn give expected properties for the surrounding gas. The opposite can be achieved with photoionisation models of the gas which can estimate the parameters of stellar body responsible. Self consistent models from the two methods are thus greatly sought after, as too is the relation between the ionising radiation of the star and that indicated by observations of the nebula. For a nebula that is optically thick to ionising photons, the two would be equal but discrepancies can arise due to dust absorption or photon leakage. Furthermore, this sample of H II regions is located in the outer Milky Way which would help reveal any effects of sub-solar metallicity when comparing to earlier studies that have focussed on the solar neighbourhood (Peeters et al. 2002; Giveon et al. 2002) or inner disc (Furness et al. 2010).

## 2.2 Observations

A total of 13 H II regions in the outer Milky Way, listed in Table 2.1, were targeted for observation. Robust surveys of the Galactic H II regions (e.g. Lumsden et al. 2013) were obtained after these observations, but they still showed only a limited number to lie beyond the solar circle. As such, no quantitative criteria was used in the selection of the target sample. They were largely selected from the Sharpless (1959) catalogue, ensuring their location within the outer Galaxy. The sample sought to cover a range of SpTs as indicated by Hunter & Massey (1990), as well as overlap with Infrared Space Observatory/Short Wavelength Spectrometer (ISO/SWS) surveys of regions studied by Peeters et al. (2002) and Giveon et al. (2002), to allow for future comparison.

Data were obtained with the 4.2 m William Herschel Telescope at the Roque de Los Muchachos Observatory in La Palma, Spain. The observing run covered two nights from 19-20th July 2010. Intermediate and low-resolution spectroscopy was carried out on the first and second nights, respectively, using the Intermediate dispersion Spectrograph and Imaging System (ISIS). A long slit was positioned to obtain spectra of both the main ionising star and nebula. Additional imaging of each region was made with the auxiliary-port camera (ACAM). Details of the observations are now discussed.

Table 2.1: Target H II regions.

H II Region	RA (2000) [h m s]	Dec (2000) [° ' '']	V [mag]	Reference
Sh2 99	20 00 54	+33 29 40	13.32	Crampton et al. (1978)
Sh2 100	20 01 48	+33 31 45	12.82	Crampton et al. (1978)
Sh2 101	19 59 49	+35 18 42	8.99	Blanco et al. (1968)
Sh2 112	20 33 50	+45 39 47	9.05	Lahulla (1985)
Sh2 128	21 48 57	+28 37 51	15.14	Mampaso et al. (1984)
Sh2 148	22 56 17	+58 31 17	12.72	Lahulla (1985)
Sh2 149	22 56 26	+58 32 12	12.44	Lahulla (1985)
Sh2 152	22 58 40	+58 47 04	11.93	Russeil et al. (2007)
Sh2 156	23 05 09	+60 14 47	11.23	Russeil et al. (2007)
Sh2 158	23 13 33	+61 30 16	11.76	Russeil et al. (2007)
Sh2 162	23 20 43	+61 11 41	8.67	Hiltner & Johnson (1956)
Sh2 170	00 01 34	+64 37 27	10.06	Lahulla (1985)
Sh2 206	04 03 20	+51 19 00	11.26	Mayer & Macák (1973)

**Notes.**  $V$  is the apparent  $V$ -band magnitude of the main ionising star within each H II region, taken from the references listed.

## 2.3 Spectroscopy

ISIS was used to perform long slit ( $\approx 4' \times 1''$ ) spectroscopy on each target. The slit was centred on the key ionising star and positioned according to the parallactic angle. The long slit provided spectra of both the stars and the surrounding nebula. The dichroic setup of ISIS allowed simultaneous observation with its blue and red arms. The covered wavelengths and corresponding resolution were decided by the selected grating. Intermediate resolution spectra of the star were desired for stellar analysis. These would encompass the key He I and He II diagnostic lines, along with  $H\alpha$ , all required for studying O-type stars. This favoured the R1200 and H2400 gratings (Table 2.2). A lower resolution was required for the nebular emission, lines allowing a wider spectral coverage. This favoured the R158R and R600B gratings. As the grating could not be manually changed over the course of the night, intermediate resolution observations were obtained during the first night and low resolution during the second. Table 2.3 lists the log of observations obtained through each grating of the respective H II regions.

To ensure accurate reduction of the science frames, a series of bias frames were obtained at the beginning and end of each night. Blue and red flat-field frames from a quartz lamp were also taken. Wavelength calibration was achieved using additional arc frames from a CuNe+CuAr lamp, and observations of standard stars were inserted at various times during the observing run.

Table 2.2: Spectral coverage of the ISIS gratings.

Grating	Central $\lambda$ [Å]	Spectral Range [Å]	$\Delta\lambda$ Å
R1200R	6499	5972 – 7027	0.62
H2400	4660	4439 – 4881	0.32
R158R	7257	3492 – 11022	3.2
R600B	4299	3387 – 5212	3.7

Table 2.3: Observing log for ISIS data.

H II Region	Date	Grating	Exposure Time	Grating	Exposure Time
Sh2 99	2010-07-19	H2400	3 × 1500 s	R1200	3 × 1500 s
	2010-07-20	R600B	2 × 1000 s	R158R	4 × 500 s
Sh2 100	2010-07-19	H2400	3 × 900 s	R1200	3 × 900 s
	2010-07-20	R600B	1 × 60, 1 × 180 s 1 × 240, 1 × 300 s	R158R	1 × 20, 2 × 30 s 1 × 60 s
Sh2 101	2010-07-19	H2400	1 × 120 s	R1200	1 × 120 s
	2010-07-20	R600B	3 × 600 s	R158R	6 × 300 s
Sh2 112	2010-07-19	H2400	2 × 90 s	R1200	2 × 90 s
	2010-07-20	R600B	1 × 40, 2 × 200 s	R158R	2 × 20, 10 × 40 s
Sh2 128	2010-07-19	H2400	1 × 1800 s	R1200	1 × 450, 3 × 600 s
	2010-07-20	R600B	3 × 600 s	R158R	6 × 300 s
Sh2 148	2010-07-19	H2400	3 × 1000 s	R1200	3 × 1000 s
	2010-07-20	R600B	1 × 285, 6 × 300 s	R158R	1 × 285, 6 × 300 s
Sh2 149	2010-07-19	H2400	3 × 1000 s	R1200	3 × 1000 s
	2010-07-20	R600B	1 × 285, 6 × 300 s	R158R	1 × 285, 6 × 300 s
Sh2 152	2010-07-19	H2400	3 × 600 s	R1200	3 × 600 s
	2010-07-20	R600B	1 × 300, 2 × 600 s	R158R	2 × 150, 3 × 300 s
Sh2 156	2010-07-19	H2400	6 × 600 s	R1200	3 × 450, 3 × 600 s
	2010-07-20	R600B	1 × 90, 3 × 500 s	R158R	1 × 90, 3 × 500 s
Sh2 158	2010-07-19	H2400	3 × 600 s	R1200	3 × 600 s
	2010-07-20	R600B	1 × 300, 1 × 600 s	R158R	6 × 150 s
Sh2 162	2010-07-19	H2400	3 × 60 s	R1200	3 × 60 s
	2010-07-20	R600B	1 × 20, 1 × 30 s 2 × 100 s	R158R	13 × 10, 2 × 20 s
Sh2 170	2010-07-19	H2400	3 × 180 s	R1200	3 × 180 s
	2010-07-20	R600B	1 × 100, 3 × 300 s	R158R	2 × 50, 3 × 100 s
Sh2 206	2010-07-19	H2400	3 × 400 s	R1200	3 × 400 s
	2010-07-20	R600B	1 × 100, 1 × 300 s 1 × 480 s	R158R	2 × 50, 4 × 120 s 2 × 120 s

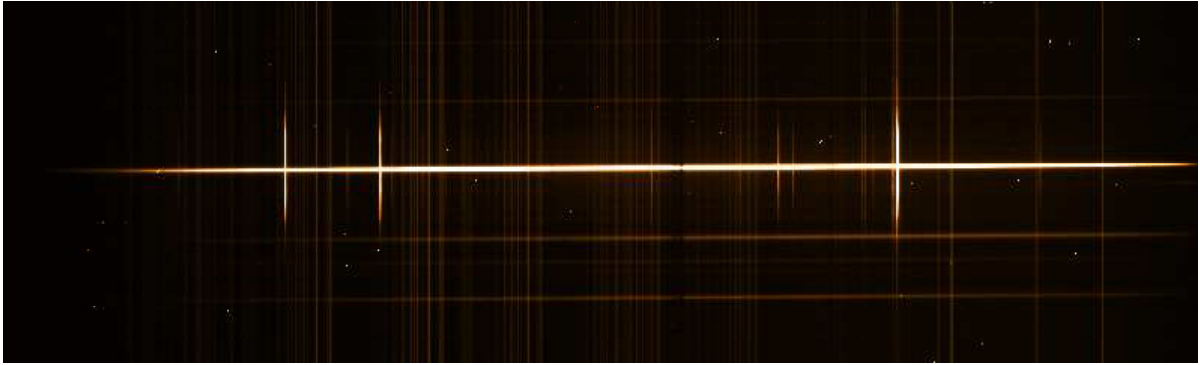


Figure 2.1: A 2-D spectrum of Sh2 100 in the R158R grating. Spatial axis: left-right = 4". Dispersion axis: top-bottom = 1".

### 2.3.1 Data reduction

Prior to any analysis, all frames would undergo a process of a bias subtraction and flat field normalisation. The output signal of all frames is increased by an additional base signal, the bias level. It is added to prevent negative readings and needs to be removed appropriately. The bias level was determined from a zero second exposure, meaning that counts recorded by the CCD in this case would only arise from the bias. Due to pixel-to-pixel variations the bias level will not be completely constant across the CCD so a mean bias frame was created using the `zerocombine` package within the IRAF software to combine all the bias frames taken on the individual nights. This mean bias frame was then subtracted from all other remaining science and calibration frames for their reduction.

Sensitivity varies across the CCD, meaning that separate pixels record different counts even when exposed to the same light source. This problem was tackled with a flat-field frame which, in the case of the spectroscopic observations, was an exposure to a quartz lamp that would resemble an even light source. As this sensitivity can vary with wavelength, a separate flat-field frame needed to be created for each grating. A mean flat-field frame was first created for each grating. To normalise the wavelength variation, the `response` package within IRAF was used to obtain a fit to any large scale variations along the direction of the dispersion axis. This produced a normalised flat-field image which was the ratio of the flat-field to the fit. Each science frame was then divided by this normalised flat-field (according to its corresponding grating) to correct for the CCD variations mentioned above.

### Spectral extraction

The spectra are originally obtained in a 2-D format as shown in Figure 2.1, where the spatial axis runs from left to right and the dispersion axis runs from top to bottom. They needed to be

converted to a 1-D format, conveying the number of counts to each pixel, to allow subsequent wavelength and flux calibration. The first step began using the `apa11` package. Within its interactive mode, a cut is made through the 2-D spectra at a given point on the dispersion axis, as shown in Figure 2.2. The number of counts is plotted for each pixel, the primary ionising star peaking at the centre with a surrounding flux from the nebula. In some cases, peaks from additional stars that fell under the slit would be present. For the intermediate resolution data, the ionising star was extracted individually to allow the accurate analysis of the stellar lines with minimal nebular contamination. A further extraction combining the star and nebula in the aperture was also made for both the high and low-resolution data. This would be used for studying nebular properties.

The size of the extraction aperture was manually selected for each target. The aperture for the star would include the peak but not always extend to the edge of the wings, such as cases where there was excess nebular emission. For the combined star+nebula aperture, boundaries were selected where the nebular flux appeared to show a notable fall. This proved difficult for some targets where the nebular flux showed fluctuations to the sides of the slit, suggesting the effects of an additional ionising star. For later analysis it was important that aperture sizes were kept consistent between different gratings. i.e. the blue (0.2"/pixel) and red (0.22"/pixel) spatial scales varied but the aperture sizes did not.

With each aperture, a corresponding sky aperture needed to be defined which would be subtracted to remove the underlying flux of the sky. Positioned far from the star, care was taken to ensure the sky aperture contained no, or as little nebular flux, as possible. However, the spectrum will not fall exactly perpendicular to the spatial axis. This is primarily a result of atmospheric refraction and optical imprecisions. Only after tracing the spatial profile as a function of the dispersion axis was the data finally extracted from the apertures and the background sky subtracted.

### Wavelength calibration

At the beginning and end of the night, a set of arc frames were created through each grating from exposures to a CuNe+CuAr lamp. Bearing in mind the varying line along the spatial axis, each science frame required a corresponding arc to be extracted. The science apertures had already been saved by `apa11` and so could easily be applied to the arc frames.

The wavelength calibration process was carried out using the `arc` package within FIGARO and began by matching a range of spectral lines in an arc frame with those listed in the arc-lamp maps provided for ISIS<sup>1</sup>. `arc` could then automatically identify further lines in order to

---

<sup>1</sup>[http://www.ing.iac.es/astronomy/instruments/isis/calibration\\_info.html](http://www.ing.iac.es/astronomy/instruments/isis/calibration_info.html)

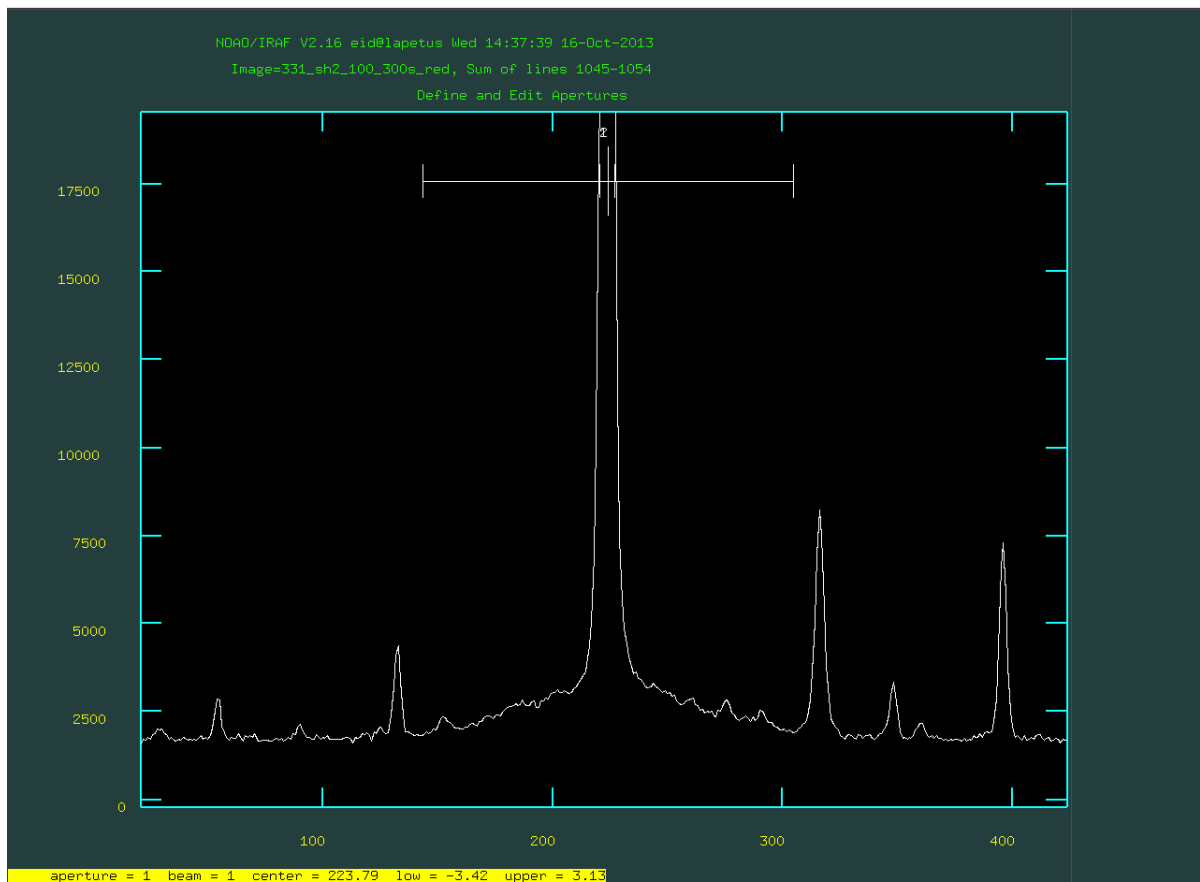


Figure 2.2: Defining extraction apertures using the `apall` package within IRAF. The larger boundaries at the top mark the nebular aperture and smaller boundaries mark the stellar aperture.

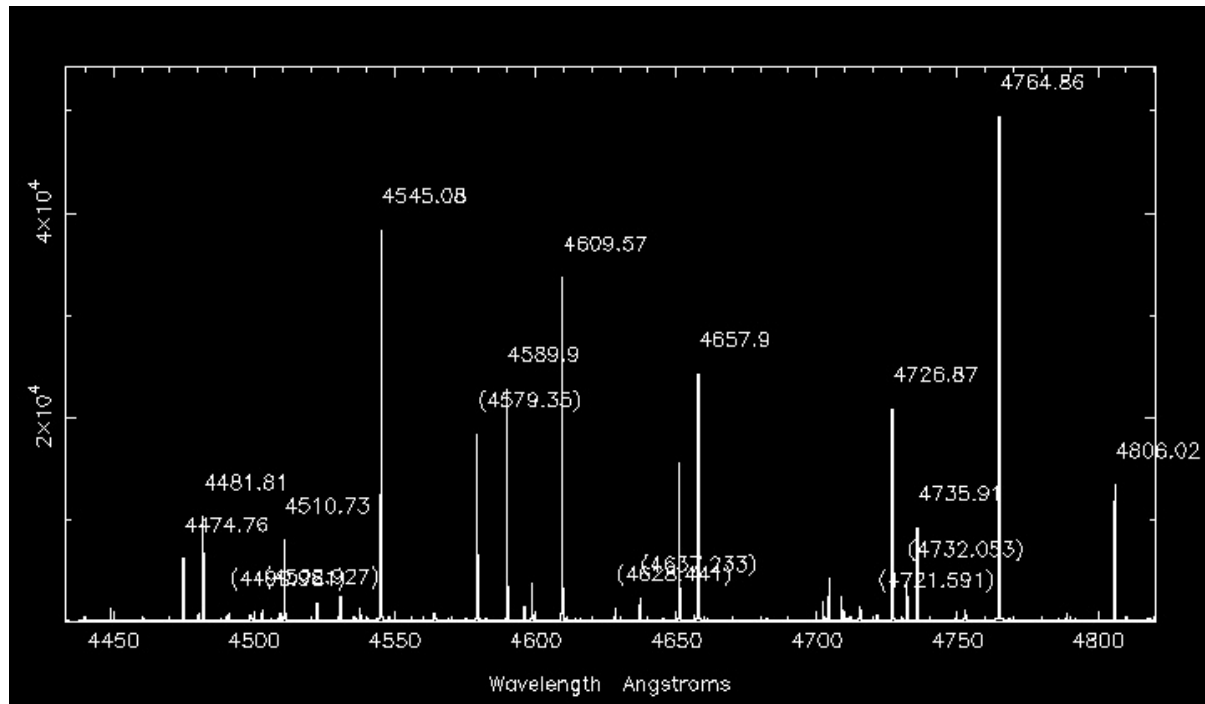


Figure 2.3: Wavelength calibration of an arc frame using the `arc` package within FIGARO. Lines were matched individually to those in the arc-lamp maps except for those in parentheses which have been automatically identified by `arc`.

make a fit to the arc spectrum and set a wavelength scale to it (see Figure 2.3). Each science frame was then wavelength calibrated according to the scale of its corresponding arc frame.

### Flux calibration

In order to convert the recorded CCD counts into an absolute flux, spectra of well studied “standard stars” were acquired each night (listed in Table 2.4). The observed spectra of the standard stars were first corrected for atmospheric extinction. This was based on data within the FIGARO database describing how the extinction of the atmosphere varies with wavelength. The data was set to coincide with the wavelength coverage of the gratings used, but the points only provide a spiketrum of the extinction. Interpolation was therefore carried out over the spiketrum to generate a spectrum of atmospheric extinction. The standard star spectra then needed to be scaled to their correct flux density. The SEDs and flux levels of the standard stars are well known and provided by Turnshek et al. (1990). These data were used to produce a spectrum for which to calibrate the observed standard star spectra. In a similar process to creating the atmospheric extinction spectrum, a spiketrum was formed from the “true” standard star data and interpolated.

Table 2.4: The standard stars.

Standard Star	RA (2000)	Dec (2000)	SpT	Ref.
G191-B2B	05 05 30.61	+52 49 51.96	DA0	Bohlin et al. (1990)
BD +28° 4211	21 51 11.02	+28 51 50.36	sdO	Gianninas et al. (2011)
BD +33° 2642	15 51 59.89	+32 56 54.33	B2 IV	Bohlin et al. (1990)

**Notes.** Standard star fluxes are based on data from Turnshek et al. (1990).

The science frames were similarly corrected for atmospheric extinction. They were then matched to the continuum of the standard star, ideally one which had been observed at a similar air mass. In theory, science spectra of the same target should have displayed a consistent continuum level but some targets did show small variations in their flux levels, between different epochs. Such fluctuations could be explained in the case of a variable or binary star but the chosen targets make this unlikely. Similarly, passing clouds could have prevented light from entering the detector and affected the flux levels. However, the most probable cause is a change in the seeing conditions over the course of observing. Unfortunately, the robotic Differential Image Motion Monitor (roboDIMM) at WHT had no available data for the observing nights. An estimate of the seeing conditions was therefore obtained with the `imexmine` package within IRAF, by measuring the FWHM of the science frames. It indicated an average seeing of  $\approx 0.9''$ , but varying between  $\sim 0.7 - 1.6''$  over the observing period. To ensure a reliable flux calibration, the science frames chosen for analysis were those with the most similar seeing conditions to the standard stars they had been calibrated by, typically consistent to within  $0.1''$ . These selected science frames were taken to have a reliable continuum level and it would act as the template for that target. For example, if additional science frames for a target were needed, e.g. to improve the signal-to-noise-ratio, but were observed at different seeing conditions, they were scaled to the template continuum level.

### 2.3.2 Stellar spectroscopy

The intermediate resolution spectroscopy would be the principal data for analysing the primary ionising star in each H II region. This would, of course, be carried out on the spectra which had been extracted solely over the star and allowed renewed classification and atmospheric modelling of the stars. While other ionising stars were evident both from the 2-D spectra and imaging, they have been set aside in this study, although are taken into account when considering the total ionising output of the regions.

### Spectral classification

Spectral classifications of the ionising stars were primarily based on the intermediate resolution blue spectra. The extra wavelength coverage of the low-resolution spectra provided information on additional lines, although it served as a secondary indicator. Final SpTs are listed in Table 2.5. Note that the priority was to identify a subtype and luminosity class so as to provide information on the  $T_{\text{eff}}$  and  $L_*$ , while finer details were listed if apparent. Classification was primarily based on the criteria laid out by Conti & Alschuler (1971) and Conti & Frost (1977), combined with the revisions from Mathys (1988). This approach made particular use of the  $W(\text{He I } \lambda 4471)/W(\text{He II } \lambda 4541)$  ratio to define the subtype. The appearance of He II  $\lambda 4686$  and N III  $\lambda 4634 - 4641$  lines would then establish the luminosity class. An exception to this were stars later than O8, where the He II  $\lambda 4686$  line is notably weaker due to its temperature sensitivity. For these later SpTs, He II  $\lambda 4686$  is combined with the He I  $\lambda 4388$  line to obtain the luminosity class according to the criteria in Mathys (1988). Figure 2.4 compares the spectra of an early, mid and late O-type star included in the sample to the standard template SpT found in the spectroscopic atlas by Walborn & Fitzpatrick (1990).

A typical main-sequence O-type star was classified for nearly all targets, as would be expected for a young H II region. However, one peculiar case was the star BD +60° 2522 in Sh2 162. This star was actually highlighted by Conti & Leep (1974) for its double-peaked He II  $\lambda 4686$  line. Additional broad absorption lines believed to arise from rapid rotation led them to classify it as an Oef star, making comparisons to classical Be stars. These same features were observed in the ISIS spectra, although an O6 subtype was favoured. The standard luminosity criteria could not be applied in this case so the giant class, assigned by Conti & Alschuler (1971) was adopted for this study. Walborn (1972) classified these objects (including star BD +60° 2522 being one of the prototype objects) as Ofnp stars, where the “n” related to rotation. However, in this work, the Oef terminology will be used. Figure 2.5 compares BD +60° 2522 to  $\zeta$  Puppis, another Ofnp star in the Walborn & Fitzpatrick (1990) atlas.

The spectra suggested no obvious sign of companions, with past studies drawing similar conclusions. While binarity may not be completely ruled out without multi-epoch observations, the potential impact of binaries on the ionising output of the star is considered in Section 2.5.

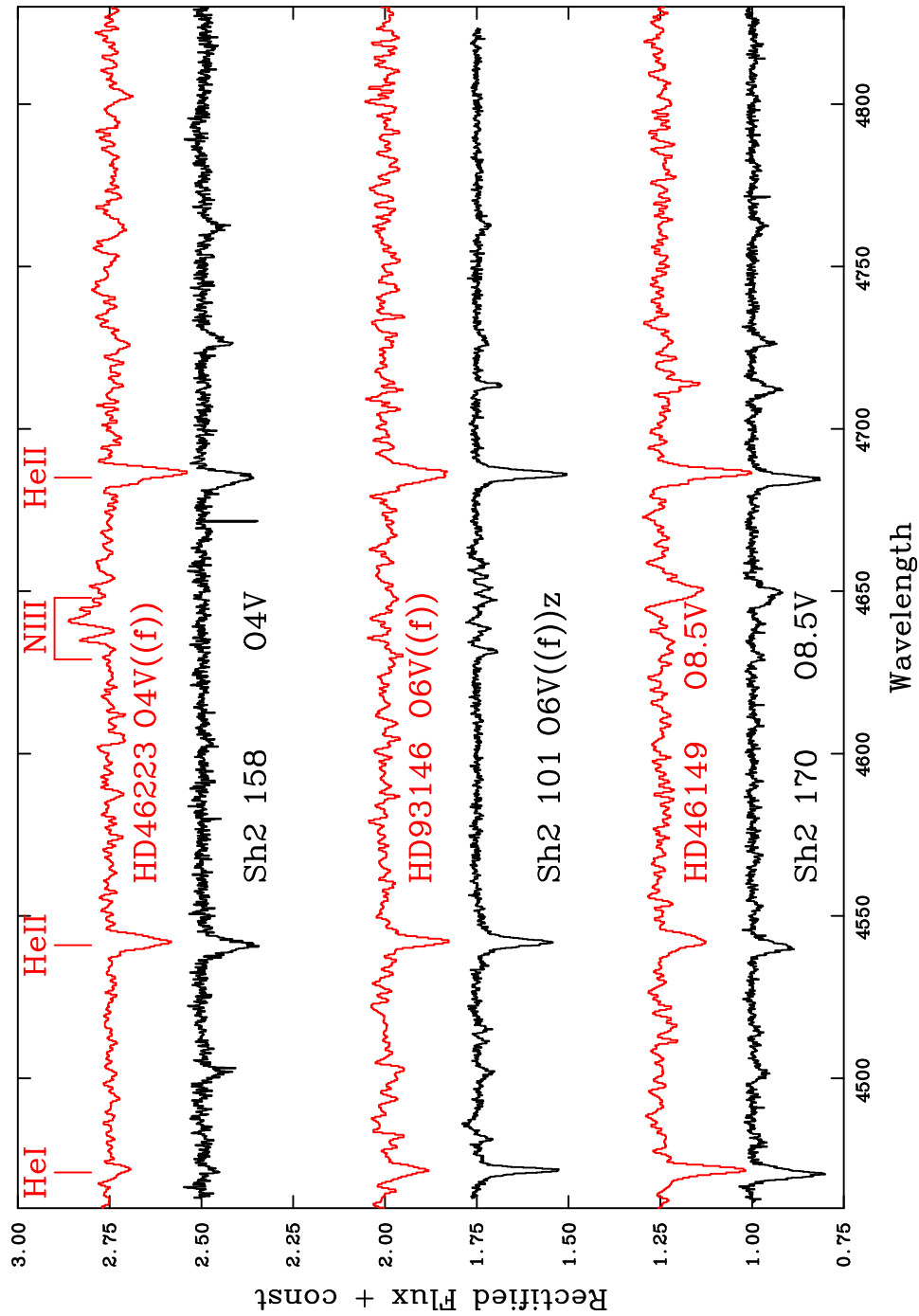


Figure 2.4: Spectra of three of the ionising stars through the H2400 grating alongside their equivalent spectral templates according to the Walborn & Fitzpatrick (1990) atlas. Note that the ionising star in Sh 2 158 was not classified to have the additional ((f)) feature. The “z” classification for Sh 2 101 refers to the strong He II  $\lambda 4686$  absorption which is > than both He I  $\lambda 4471$  and He II  $\lambda 4542$ .

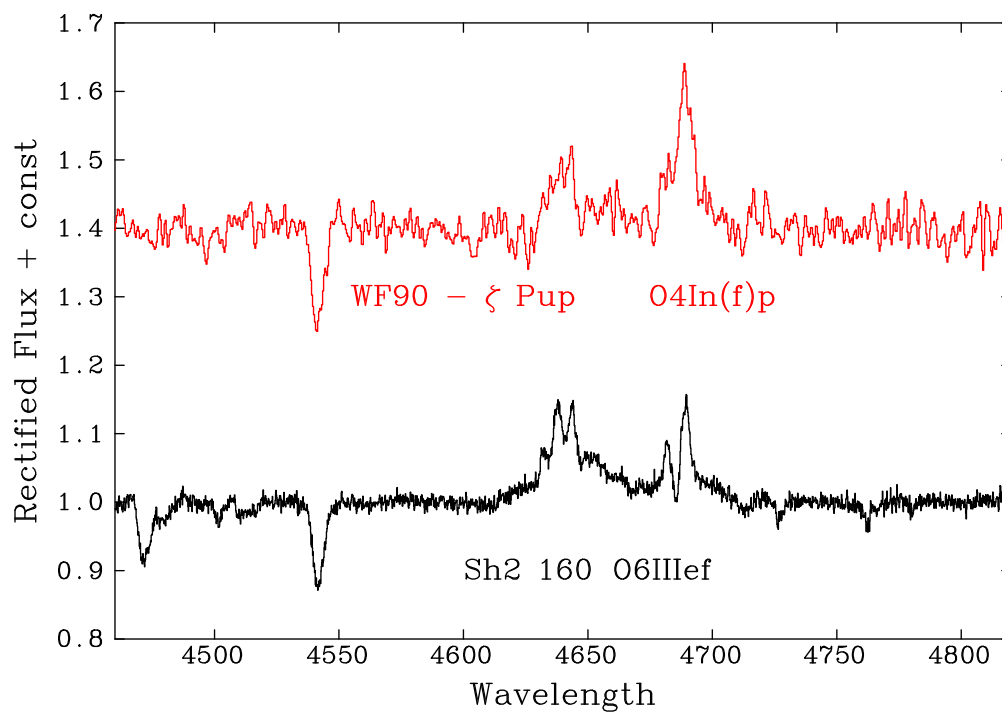


Figure 2.5: Spectra of BD +60° 2522, the primary ionising star in Sh2 160 compared to  $\zeta$  Puppis from the Walborn & Fitzpatrick (1990)[WF90] atlas.

Table 2.5: Properties of the ionising stars.

H II Region	Ionising star	Lit. SpT	SpT	B [mag]	V [mag]	$E(B - V)$ [mag]	$A_V$ [mag]	$M_V$ [mag]	Dist. [kpc]	$R_G$ [kpc]	$T_{\text{eff}}$ [kK]	$\log q_0$ [ph cm <sup>-2</sup> s <sup>-1</sup> ]
Sh2 99		O5: (1)	O6 V	14.1	13.2	1.2	3.7	-4.9	7.8	9.4	38.9	24.2 <sup>+0.1</sup> <sub>-0.1</sub>
Sh2 100		O5 V (1)	O4 V	13.9	13.0	1.3	3.9	-5.5	8.1	9.5	42.9	24.5 <sup>+0.1</sup> <sub>-0.1</sub>
Sh2 101	HDE 227018	O6 V (7, 2)	O6.5 V((f))	9.7	9.3	0.7	2.1	-4.8	2.5	8.1	37.9	24.1 <sup>+0.1</sup> <sub>-0.1</sub>
Sh2 112	BD +45° 3216	O8 V (2)	O8 V	9.5	9.2	0.6	1.8	-4.3	2.2	8.5	34.9	23.8 <sup>+0.1</sup> <sub>-0.1</sub>
Sh2 128		O7 V (3)	O7.5 V	16.7	15.5	1.5	4.7	-4.5	11.3	15.0	35.9	23.9 <sup>+0.1</sup> <sub>-0.1</sub>
Sh2 148		O8 V (1)	O8.5 V	13.1	12.7	0.8	2.3	-4.2	8.1	13.4	33.9	23.7 <sup>+0.1</sup> <sub>-0.2</sub>
Sh2 149		B0 V (1)	B0.5 III	13.8	13.1	0.9	2.9	-3.8	6.3	12.1	26.5	22.0 <sup>+0.3</sup> <sub>-0.3</sub>
Sh2 152		O9 V (1)	O8 V	13.2	12.4	1.1	3.3	-4.3	5.0	11.1	34.9	23.8 <sup>+0.1</sup> <sub>-0.1</sub>
Sh2 156		O7 V, O6.5 V: (2,4)	O7.5 V-III	13.6	12.6	1.3	3.9	-4.3	5.0	10.8	35.9	23.9 <sup>+0.1</sup> <sub>-0.1</sub>
Sh2 158	CGO 654	O3 V (6)	O4 V	13.2	12.1	1.4	4.3	-5.5	4.7	11.1	42.9	24.7 <sup>+0.1</sup> <sub>-0.1</sub>
Sh2 162	BD +60° 2522	O6.5 IIIef (5)	O6 IIIef	9.2	8.8	0.8	2.3	-5.7	2.7	9.8	38.2	24.2 <sup>+0.1</sup> <sub>-0.1</sub>
Sh2 170	BD +63° 2093	O9 V (7, 6)	O8.5 V	10.9	10.4	0.8	2.5	-4.2	2.6	10.0	32.3	23.7 <sup>+0.1</sup> <sub>-0.2</sub>
Sh2 206	BD +50° 886	O5: V (1, 7)	O3-4 V((f))	12.4	11.4	1.3	4.0	-5.5	3.8	12.0	43.4	24.5 <sup>+0.1</sup> <sub>-0.1</sub>

**Notes.**  $M_V$ ,  $T_{\text{eff}}$  and  $\log q_0$  are based on the calibrations from Martins et al. (2005) for O-type stars and Trundle et al. (2007) and Smith et al. (2002) for B-type stars. Literature SpTs are taken from: (1) - Crampton et al. (1978), (2) - Georgelin (1975), (3) - Chini & Wink (1984), (4) - Hunter & Massey (1990), (5) - Conti & Leep (1974), (6) - Russeil et al. (2007), (7) - Crampton & Fisher (1974).

### Stellar magnitudes and extinction

Apparent magnitudes were determined from low-resolution spectrophotometry of each star. Unfortunately, an error was noted with the wavelength range of the low resolution spectra. Coverage of the blue and red spectra should have overlapped but during the wavelength calibration process they had been unintentionally cut short. To overcome this, interpolations were made between the gap to represent the missing flux continuum level and the two spectra were merged (as seen in Figure 2.6). The merged spectrum could then be convolved with the standard Johnson  $B$  and  $V$  broad-band filters. The resulting convolutions were then divided by a HST/STIS spectrum (i.e. free from atmospheric extinction) of the star Vega, convolved through the same bandpasses. As Vega, by definition, has apparent magnitudes of  $B = 0.03$  and  $V = 0.03$ , the ionising star could be converted to the standard magnitude system as listed in Table 2.5.

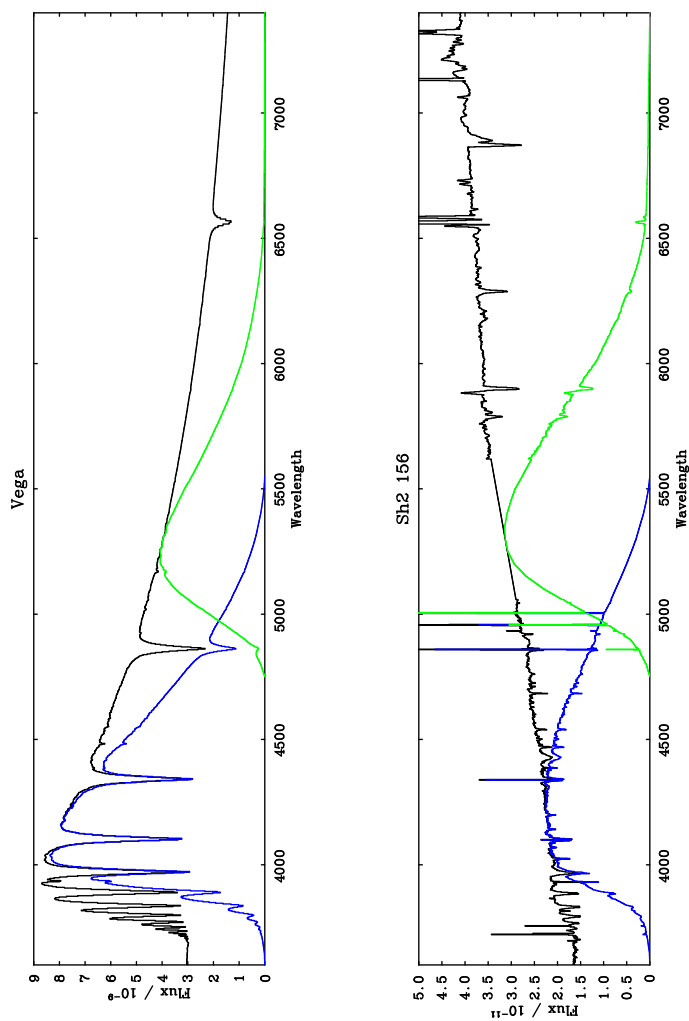


Figure 2.6: Spectra of Vega (top) and the ionising star of Sh2 156 (bottom) convolved with the Johnson  $B$  (blue line) and  $V$  (green line) broad-band filters.

With a SpT at hand, an intrinsic colour of each star,  $(B - V)_0$ , was adopted from Conti et al. (2008). All the stars were OB stars with  $(B - V)_0$  falling between a narrow range of  $-0.30$  to  $-0.32$  mag. This allowed the colour excess,  $E(B - V) = (B - V) - (B - V)_0$ , to be derived. Assuming a typical Galactic reddening value of  $R_V = 3.1$ , the extinction,  $A_V$  was subsequently calculated.

### Distances and Galactic positions

In the absence of independent distance estimates, spectroscopic parallax was used. This required an estimate of the star's absolute magnitude,  $M_V$  which was based on the observational stellar calibrations of Martins et al. (2005) using the star's SpT. The equatorial coordinates of each target were then converted into Galactic coordinates. Figure 2.7 plots their distances according to Galactic longitude (latitude showed little variation as the regions were focussed within  $\pm 3^\circ$  of the Galactic disk). The Galactic centre was taken to be at a distance of 8.5 kpc from the Sun (Caplan et al. 2000). The subsequent Galactocentric distance ( $R_G$ ) was calculated for each region (see Table 2.5). All were found to lie in the outer galaxy; at greater distances from the Galactic centre than the Sun with the exception of Sh2 101 ( $R_G = 8.1$  kpc). This should be reflected in properties such as their metallicity and even temperature as less stellar processing has occurred in the outer Galaxy (Deharveng et al. 2000). Distances remain very uncertain, however, and is largely due to the assumptions made to obtain  $M_V$ .

Many of the regions had previously been studied by Caplan et al. (2000) and Deharveng et al. (2000). They went on to produce calibrations for the temperatures and abundances of Galactic H II regions with respect to their galactocentric radii ( $R_G$ ). However, Caplan et al. (2000) and Deharveng et al. (2000) had used older Vacca et al. (1996) calibrations to obtain the  $M_V$  for their distances. While there will have been subtle changes in the SpTs and extinctions used, their distances tended to be systematically smaller (see Figure 2.8). In turn this would have provided a smaller  $R_G$  for each region.

Quireza et al. (2006) had also derived  $T_e$  and O abundance gradients found to be consistent with Deharveng et al. (2000). However, Quireza et al. (2006) had based their work on kinematic distances, an approach which relies on knowledge of the Galactic rotation curve, and where distances can be affected by non-circular motions. Large inconsistencies can arise between spectrophotometric and kinematic distances (Caplan et al. 2000) but future trigonometric observations (e.g. GAIA) will be more reliable to help reveal finer fluctuations in the Galactic gradients.

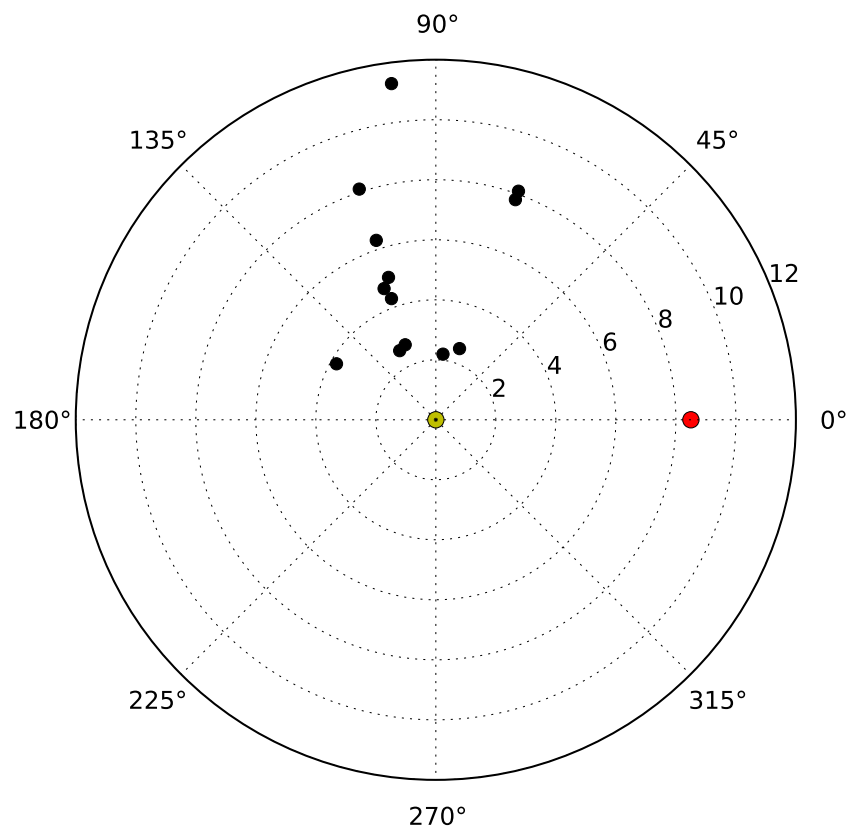


Figure 2.7: Galactic distribution of the H II regions (black circles). The Sun is located at the centre of the plot with a yellow circle and the Galactic centre is marked with a red circle. The dotted circles mark heliocentric distances in intervals of 2 kpc.

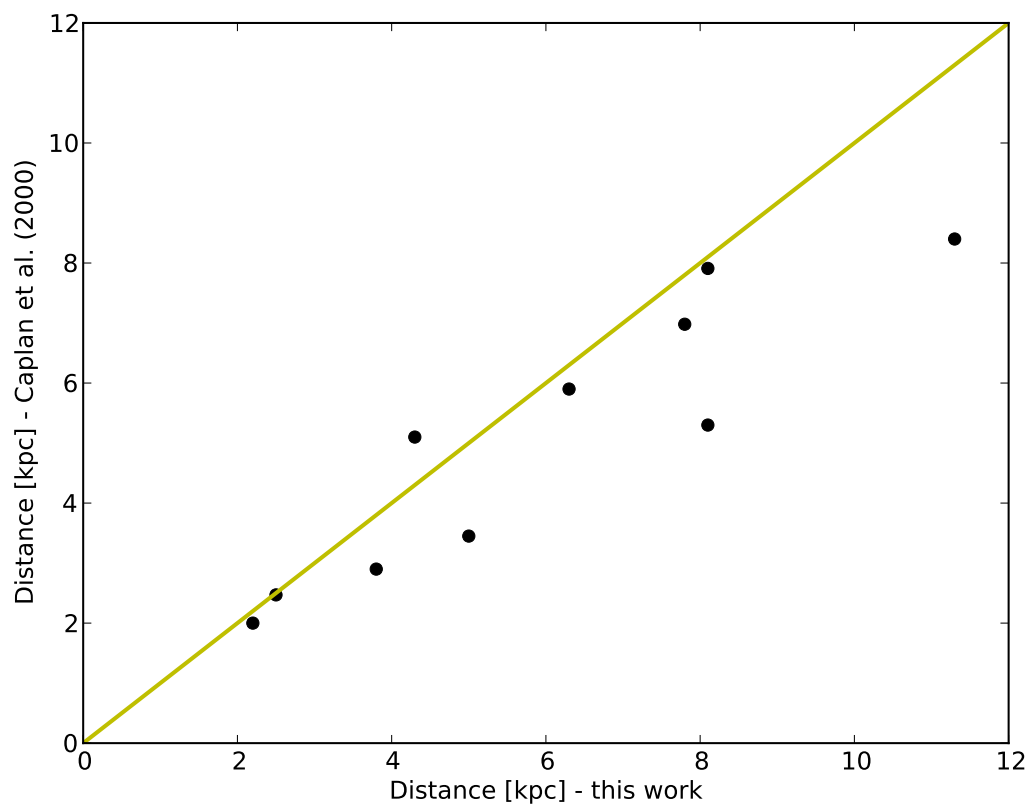


Figure 2.8: Comparison of the distances obtained by Caplan et al. (2000) and those derived for the sample of H II regions. The solid yellow line marks the 1:1 relation.

### Ionising photon rate

The ionising output of the star was also calculated from the renewed SpTs. For O-type stars, this again used calibrations of Martins et al. (2005) to estimate the effective temperature ( $T_{\text{eff}}$ ) and Lyman continuum ionising flux ( $q_0$ , the number of photons emitted/cm<sup>2</sup>/s) of each star. In the case of the B-type star,  $T_{\text{eff}}$  and  $q_0$  were adopted from Trundle et al. (2007) and Smith et al. (2002) respectively. Martins et al. (2005) offered the bolometric correction ( $BC_V$ ) calibration:

$$BC = 27.58 - 6.80 \times \log T_{\text{eff}}, \quad (2.1)$$

which allowed the stellar luminosity ( $L_*$ ) to be calculated:

$$\log(L_*/L_{\odot}) = -0.4 \times (M_V + BC_V - M_{\text{Bol}\odot}), \quad (2.2)$$

where  $M_{\text{Bol}\odot}$  is the bolometric magnitude of the Sun. Subsequently the stellar radius is derived from by Equation 1.1. The ionising photon rate of the star ( $Q_0^*$ ) is then:

$$Q_0^* = 4\pi R_*^2 \times q_0. \quad (2.3)$$

Simón-Díaz & Stasińska (2008) made a comparison of the ionising SEDs predicted by different stellar atmosphere codes (TLUSTY, CMFGEN, WM-BASIC and FASTWIND). Via their “evolutionary approach”, they assigned a stellar model of the same parameters ( $T_{\text{eff}}$ ,  $\log g$  and  $L$ ) to each stellar code. They found differences in  $\log Q_0$  of up to  $\sim 0.5$  dex. However, discrepancies were normally lower ( $< 0.08$  dex) at larger  $T_{\text{eff}}$ , and there was always a good agreement between WM-BASIC and FASTWIND models, and CMFGEN and TLUSTY models. Simón-Díaz & Stasińska (2008) found that the codes were most consistent ( $< 0.1$  dex) when using a so-called “observational” approach, whereby the H and He stellar lines had been used to estimate the stellar parameters in each model. With high-resolution spectra of the ionising stars at hand, this observational approach would also be the superior method for follow-up work since stellar parameters would not rely on calibrations.

In section 2.5, the ionising photon rates of the stars are compared to those of the H II gas for which they are responsible. This will determine the fate of the photons in each nebulae.

### 2.3.3 Nebular spectroscopy

A separate analysis was carried out on the nebular emission lines, based primarily on the low resolution spectroscopy and incorporating the combined star+nebular extracted spectra. A majority of the emission lines observed in gaseous nebula are forbidden lines such that they

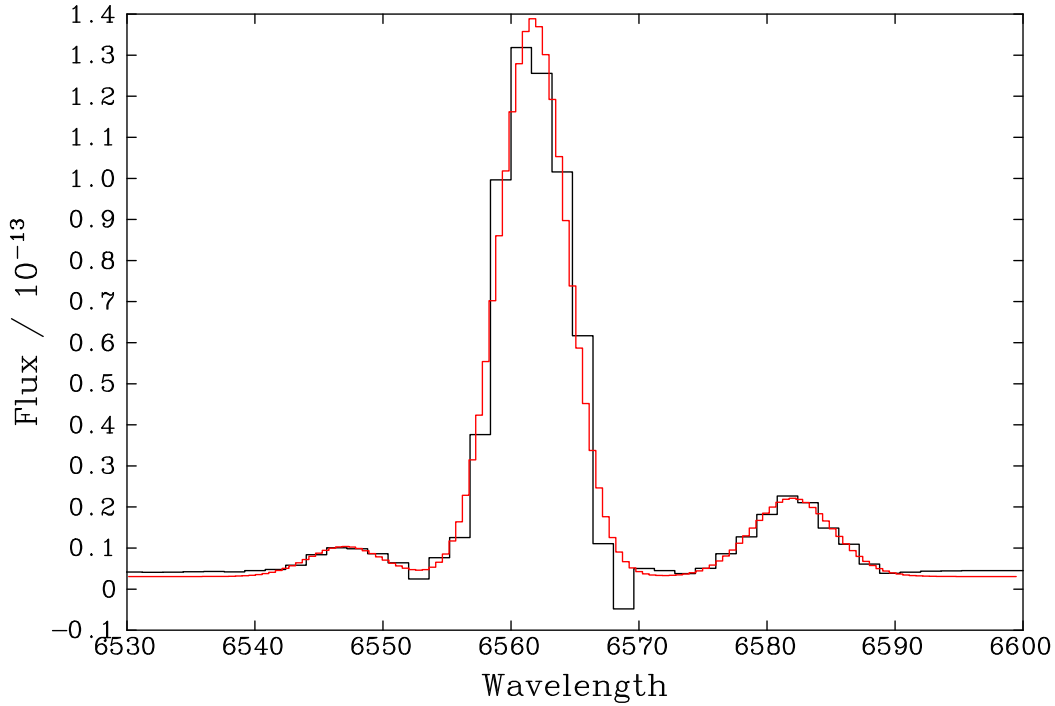


Figure 2.9: Gaussian fitting of the  $H\alpha$  line along with the adjacent  $[N II] \lambda 6548$  &  $\lambda 6583$  lines of Sh2 128.

are slower magnetic dipole or electric quadrupole transitions. As a result, their probabilities are much lower ( $\times 10^{-8}$ ) compared to electric dipole transitions such as those responsible for the  $H I$  recombination lines (Dyson & Williams 1997). Nevertheless, in the nebula these forbidden lines are typically collisionally excited by thermal electrons. This means ions in lower abundance such as  $O^+$  will still appear prominent in the spectrum as they have lower excitation potentials compared to  $H$  and  $He$ . The fluxes of key nebular lines were measured in each  $H II$  region using the ELF fitting package within DIPS0 (Howarth et al. 2004). Figure 2.9 demonstrates this technique where multiple profiles have been combined to simultaneously fit the  $H\alpha$  line and  $[N II] \lambda 6548$  &  $\lambda 6583$  lines. All of the measured line fluxes are listed in Table 2.6. Nebular properties can subsequently be determined by measuring the ratios of these different emission lines. A few of these techniques have been applied here.

### Extinction

Interstellar dust will absorb and scatter light from both the star and nebula. The emergent light is reduced according to:

$$F_{\lambda} = I_{\lambda} \exp(-\tau_{\lambda}), \quad (2.4)$$

where  $I_\lambda$  is the intensity observed if there were no extinction,  $\tau_\lambda$  is the optical depth at wavelength  $\lambda$  and  $F_\lambda$  is the actual intensity observed. The stellar flux in the  $B$  and  $V$ -bands has already been used to measure the amount of extinction and the nebular lines offer a similar alternative. When studying nebulae, the extinction function as a function of wavelength,  $f(\lambda)$ , is often normalised with respect to  $H\beta$  so that:

$$\frac{F_\lambda}{F_{H\beta}} = \frac{I_\lambda}{I_{H\beta}} 10^{-0.434(\tau_\lambda - \tau_{H\beta})} \quad (2.5)$$

$$= \frac{I_\lambda}{I_{H\beta}} 10^{-c(H\beta)[f(\lambda) - f(H\beta)]}, \quad (2.6)$$

where  $c(H\beta)$  can be used to measure the extent of extinction and  $f(\lambda) - f(H\beta)$  is the extinction relative to  $H\beta$ . With  $f(H\beta) = 0$ , the relative extinction will be positive for a bluer line and negative for a redder line.  $c(H\beta)$  can then be related to the colour excess via  $E(B - V) \approx 0.77c(H\beta)$  (Osterbrock & Ferland 2006).

Values of  $f(\lambda)$  were measured by Kingsburgh & Barlow (1994) for a variety of different emission lines observed in their planetary nebulae and have been adopted for this work. When normalising to  $H\beta$ , it is common to compare to the  $H\alpha$  line and use the ‘Balmer decrement’ to determine the extinction although essentially any two lines could be used. From atomic physics  $I_{H\alpha}/I_{H\beta} = 2.86$  (Hummer & Storey 1987) allowing  $c(H\beta)$  to be calculated (see Table 2.8). If  $c(H\beta)$  is known, the intensity of any desired spectral line relative to  $H\beta$  can then be found via:

$$I_\lambda = F_\lambda \times 10^{f_\lambda c(H\beta)}. \quad (2.7)$$

Weakness in  $H\beta$ , prevented the reddening from being determined in some regions. For those cases where  $E(B - V)$  could be derived, it showed a broad agreement with that found from the spectrophotometry, generally within  $\pm 0.25$  mag (Figure 2.10). For consistency, the stellar derived  $E(B - V)$  values were used to de-redden the line fluxes as they were available for all regions and also showed good consistency with the values found by Deharveng et al. (2000). Table 2.6 lists the line fluxes and de-redden intensities with respect to  $H\beta = 100$ .

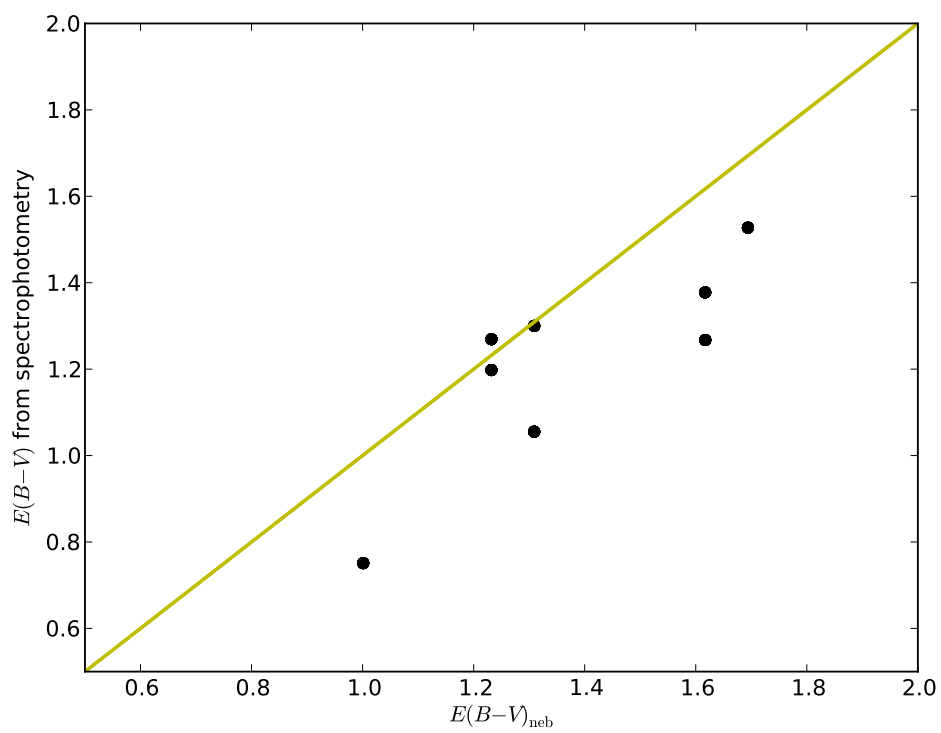


Figure 2.10: A comparison of the  $E(B - V)$  values from spectrophotometry against those obtained from the decrement of the Balmer lines (when possible). The solid yellow line marks the 1:1 relation.

Table 2.6: The observed nebular line fluxes ( $F_\lambda$ ) and de-reddened intensities ( $I_\lambda$ ) for each H II region, given relative to H $\beta$ . The true values of  $F_\lambda$  and  $I_\lambda$  for the H $\beta$  line are given in the final row in units of  $\text{erg s}^{-1} \text{cm}^{-2} \text{\AA}^{-1}$ .

	Sh2 99	Sh2 100	Sh2 101	Sh2 112	Sh2 128	Sh2 148	Sh2 149
$F_{\text{O II } \lambda 3727}$	54	32	-	-	49	804	140
error	1	7	-	-	34	402	55
$I_{\text{O II } \lambda 3727}$	137	83	-	-	159	1430	281
$F_{\text{O III } \lambda 4363}$	-	3.6	-	-	0.5	-	-
error	-	3.3	-	-	0.4	-	-
$I_{\text{O III } \lambda 4363}$	-	6.5	-	-	0.9	-	-
$F_{\text{H}\beta}$	100	100	-	-	100	100	100
error	43	2	-	-	40	197	4
$I_{\text{H}\beta}$	100	100	-	-	100	100	100
$F_{\text{O III } \lambda 4959}$	48	188	-	-	107	-	6
error	1	3	-	-	1	-	3
$I_{\text{O III } \lambda 4959}$	44	172	-	-	96	-	5
$F_{\text{O III } \lambda 5007}$	159	624	-	-	288	-	18
error	4	15	-	-	2	-	1
$I_{\text{O III } \lambda 5007}$	140	546	-	-	246	-	16
$F_{\text{N II } \lambda 5755}$	-	1.1	-	-	-	-	-
error	-	0.5	-	-	-	-	-
$I_{\text{N II } \lambda 5755}$	-	0.4	-	-	-	-	-
$F_{\text{N II } \lambda 6548}$	47	44	-	-	87	319	104
error	16	26	-	-	43	65	14
$I_{\text{N II } \lambda 6548}$	15	13	-	-	20	156	43

Table 2.6 – continued from previous page

$F_{\text{H}\alpha}$	849	1299	-	-	1496	2764	743
error	19	26	-	-	26	72	14
$I_{\text{H}\alpha}$	269	385	-	-	346	1349	302
$F_{\text{N II}, \lambda 6583}$	150	133	-	-	251	1107	333
error	20	29	-	-	49	75	14
$I_{\text{N II}, \lambda 6583}$	47	39	-	-	57	537	134
$F_{\text{S II}, \lambda 6716}$	70	31	-	-	59	714	74
error	14	1	-	-	3	29	3
$I_{\text{S II}, \lambda 6716}$	21	9	-	-	12	332	28
$F_{\text{S II}, \lambda 6731}$	45	29	-	-	56	513	66
error	5	1	-	-	3	30	3
$I_{\text{S II}, \lambda 6731}$	13	8	-	-	12	237	25
$c(\text{H}\beta)$	1.6	2.1	-	-	1.9	1.0	1.2
$F_{\text{H}\beta}$	1.12e-13	4.65e-13	-	-	6.04e-14	5.46e-15	2.07e-13
$I_{\text{H}\beta}$	6.22e-12	3.25e-11	-	-	1.01e-11	6.71e-14	4.81e-12

$F_{\lambda}$  measured using ELF package from within DIPSO software.

Errors are formal errors returned by ELF.

Lines too weak to be reliably measured are marked with ‘-’.

Line intensities are de-reddened according to  $c(\text{H}\beta)$  values derived from spectrophotometry.

Table 2.7: The observed nebular line fluxes ( $F_\lambda$ ) and de-reddened intensities ( $I_\lambda$ ) for each H II region, given relative to H $\beta$ . The true values of  $F_\lambda$  and  $I_\lambda$  for the H $\beta$  line are given in the final row in units of  $\text{erg s}^{-1} \text{cm}^{-2} \text{\AA}^{-1}$ .

	Sh2 152	Sh2 156	Sh2 158	Sh2 162	Sh2 170	Sh2 206
$F_{\text{O II } \lambda 3727}$	181	58	15	-	-	-
error	124	43	1	-	-	-
$I_{\text{O II } \lambda 3727}$	405	152	46	-	-	-
$F_{\text{O III } \lambda 4363}$	0.5	0.3	1.3	-	-	-
error	0.4	0.1	0.7	-	-	-
$I_{\text{O III } \lambda 4363}$	0.8	0.5	2.3	-	-	-
$F_{\text{H}\beta}$	100	100	100	100	-	100
error	1	29	33	79	-	46
$I_{\text{H}\beta}$	100	100	100	100	-	100
$F_{\text{O III } \lambda 4959}$	32	45	94	31	-	103
error	1	1	3	2	-	2
$I_{\text{O III } \lambda 4959}$	30	41	85	29	-	94
$F_{\text{O III } \lambda 5007}$	93	152	359	98	-	355
error	1	1	58	4	-	2
$I_{\text{O III } \lambda 5007}$	84	133	310	91	-	310
$F_{\text{N II } \lambda 5755}$	-	0.8	-	-	-	-
error	-	0.2	-	-	-	-
$I_{\text{N II } \lambda 5755}$	-	0.4	-	-	-	-
$F_{\text{N II } \lambda 6548}$	100	50	35	78	-	17
error	22	9	18	17	-	3
$I_{\text{N II } \lambda 6548}$	37	15	9	38	-	4

Table 2.7 – continued from previous page

$F_{\text{H}\alpha}$	1000	464	1316	175	-	968
error	22	9	22	24	-	18
$I_{\text{H}\alpha}$	366	138	351	85	-	279
$F_{\text{N II}, \lambda 6583}$	311	155	128	91	-	83
error	24	9	23	32	-	21
$I_{\text{N II}, \lambda 6583}$	113	46	34	44	-	24
$F_{\text{S II}, \lambda 6716}$	61	17	31	16	-	29
error	2	1	1	3	-	5
$I_{\text{S II}, \lambda 6716}$	21	5	7	7	-	8
$F_{\text{S II}, \lambda 6731}$	60	21	28	17	-	24
error	2	1	1	1	-	2
$I_{\text{S II}, \lambda 6731}$	20	6	7	8	-	6
$c(\text{H}\beta)$	1.4	1.7	1.8	1.0	-	1.7
$F_{\text{H}\beta}$	4.44e-13	1.68e-12	2.79e-13	1.25e-12	-	4.68e-13
$I_{\text{H}\beta}$	1.49e-11	1.17e-10	2.81e-11	1.53e-11	-	3.61e-11

$F_{\lambda}$  measured using ELF package from within DIPSO software.

Errors are formal errors returned by ELF.

Lines too weak to be reliably measured are marked with ‘-’.

Line intensities are de-reddened according to  $c(\text{H}\beta)$  values derived from spectrophotometry.

Table 2.8: Properties of the H II regions derived from the nebular spectral lines.

H II Region	$c(\text{H}\beta)$	$c(\text{H}\beta)^{\text{err}}$	$E(B - V)_{\text{neb}}$	$T_{\text{O III}}$ [ $10^3$ K]	$T_{\text{O III}}^{\text{err}}$ [ $10^3$ K]	$T_{\text{N II}}$ [ $10^3$ K]	$T_{\text{N II}}^{\text{err}}$ [ $10^3$ K]	Flux ratio $[I_{\lambda 6716}/I_{\lambda 6731}]$	$n_e$ [ $\text{cm}^{-3}$ ]	$12 + \log(\text{O}/\text{H})$ [N2 method]	$12 + \log(\text{O}/\text{H})$ [O3N2 method]
Sh2 99	1.6	0.6	1.2	-	-	-	-	1.55	-	8.47	8.44
Sh2 100	2.1	0.0	1.6	12.46	1.45	9.81	0.69	1.07	440	8.33	8.18
Sh2 101	-	-	-	-	-	-	-	-	-	-	-
Sh2 112	-	-	-	-	-	-	-	-	-	-	-
Sh2 128	2.2	0.5	1.7	8.56	1.64	-	-	1.06	420	8.45	8.36
Sh2 148	1.3	0.1	1.0	-	-	-	-	1.12	350*	8.70:	8.88:
Sh2 149	-	-	-	-	-	-	-	1.34	90*	-	-
Sh2 152	1.7	0.0	1.3	11.01	2.60	-	-	1.02	550	8.61	8.59
Sh2 156	1.6	0.4	1.2	8.83	0.34	7.90	0.40	0.84	1030	8.63 <sup>†</sup>	8.54 <sup>†</sup>
Sh2 158	2.1	0.4	1.6	10.86	1.00	-	-	1.12	370	8.32	8.25
Sh2 162	-	-	-	-	-	-	-	0.95	700*	8.74:	8.65:
Sh2 170	-	-	-	-	-	-	-	-	-	-	-
Sh2 206	1.7	0.6	1.3	-	-	-	-	1.21	230*	8.29:	8.23:

**Notes.**\* Assumed  $T_e = 10^4$  K for derivation of  $n_e$ .<sup>†</sup>  $12 + \log(\text{O}/\text{H}) = 8.49$  derived from weak line method.

Properties which could not be calculated due to unavailable or unreliable line fluxes are listed with “-”.

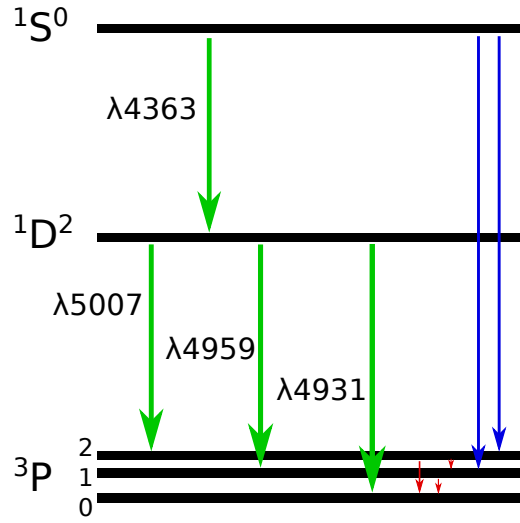


Figure 2.11: Energy level diagram for [O III]. The green arrows mark transitions in the optical. Blue and red arrows mark additional transitions in the ultraviolet and infrared, respectively.

### Nebular temperature

H II regions are consistently measured at temperatures of  $5 \times 10^3 - 10^4$  K (Osterbrock & Ferland 2006). While the Balmer recombination lines will radiate away some of the kinetic energy held by the electrons, it is the collisional excitation of low level ions that provides the primary cooling process in nebulae. [O III] is one such case, where three main forbidden lines are formed in the optical by collisional excitation (Figure 2.11).

As the rate of excitation to the  $^1S$  and  $^1D$  levels depends strongly on temperature so too will the relative strengths of the lines emitted from those levels. Equation 2.8 is taken from Osterbrock & Ferland (2006) giving the ratio of the line strengths:

$$[\text{O III}] \frac{j_{\lambda 4959} + j_{\lambda 5007}}{j_{\lambda 4363}} = \frac{7.90 \exp(3.29 \times 10^4 / T_e)}{1 + 4.5 \times 10^{-4} n_e / T_e^{1/2}} \quad (2.8)$$

where  $j_\lambda$  are the relative emission coefficients of each line,  $n_e$  is the electron density and  $T_e$  is the electron temperature. Hence, higher temperatures are more capable of exciting to the  $^1S$  level and producing the  $\lambda 4363$  line. As the  $\lambda 5007$  and  $\lambda 4959$  lines both originate from the  $^1D$  level, their strengths are decided by their transition probabilities (the  $\lambda 4931$  line can be ignored because it is only permitted by electric-quadrupole and so has a much smaller transition probability).

The emission coefficients can be equivalently replaced with the line intensities since the nebula is optically thin to this radiation. Therefore, by assuming a low density environment

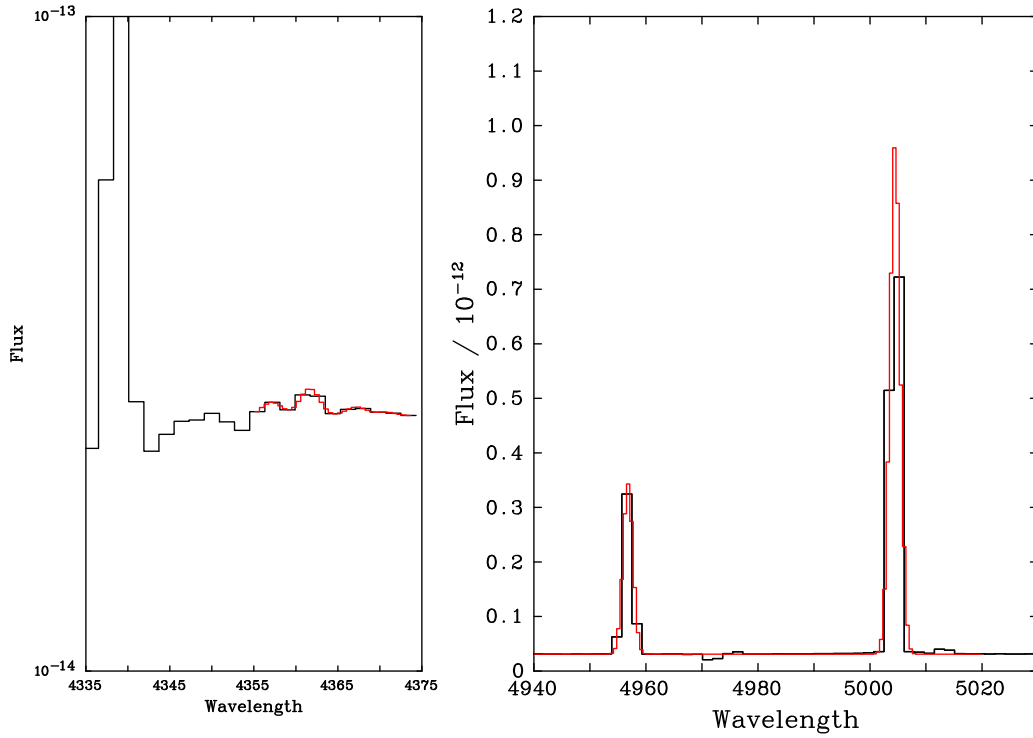


Figure 2.12: Gaussian fitting of the [O III] lines. Observed spectra are plotted in black and fits are in red.

where  $n_e \rightarrow 0$ ,  $T_e$  was directly determined (Table 2.8). All these line intensities needed to be corrected for interstellar extinction, although as the lines are relatively close, effects should be minimal. More critical to the ratio is obtaining a reliable  $\lambda 4363$  line. While the  $\lambda 5007$  and  $\lambda 4959$  lines are often strong,  $\lambda 4363$  is considerably weaker (see Figure 2.12). Its measurement requires on a good S/N ratio and can also suffer due to the neighbouring Hg I  $\lambda 4358$  line. In several cases, the  $\lambda 4363$  line was too weak to measure.

A similar estimate for  $T_e$  makes use of the [N II] forbidden lines. On this occasion, the ratio becomes:

$$[\text{N II}] \frac{j_{\lambda 6548} + j_{\lambda 6583}}{j_{\lambda 5755}} = \frac{8.23 \exp(2.50 \times 10^4 / T_e)}{1 + 4.4 \times 10^{-3} n_e / T_e^{1/2}}, \quad (2.9)$$

and it is the  $\lambda 5755$  line which is weakest and most difficult to measure. [N II] tends to be stronger in outer parts of a nebula where the ionisation is lower, and [O II] lines begin to dominate, rather than [O III]. The uncertainty of weak emission lines restricted the derivation of  $T_e$  for a number of regions, but when possible, the [O III] method delivered characteristic parameters.

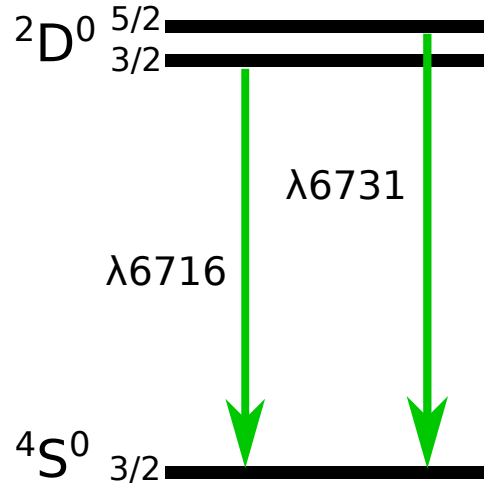


Figure 2.13: Energy level diagram for [S II].

### Nebular density

The ratio of line strengths can equally be used to determine the electron density,  $n_e$ , of the nebula. The [S II]  $\lambda 6716/\lambda 6731$  ratio is typically used, both lines originating from similar energy levels and thus having similar excitation energies (Figure 2.13). What determines the excitation rate to each level is thus a ratio of their collision strengths. As for de-excitation, the two levels could have different radiative transition probabilities or different collisional de-excitation rates, but the population of each level is dependent on the density. In turn, the line strengths will show this dependence on density.

In a low density limit,  $n_e \rightarrow 0$ , the levels are radiatively excited. The excitation rates to levels  ${}^2D_{5/2}$  and  ${}^2D_{3/2}$  will be proportional to their statistical weights and so too will the ratio of the line strengths:  $j_{\lambda 6716}/j_{\lambda 6731} = 3/2$ . Whereas in a high density limit,  $n_e \rightarrow \infty$ , excitation and de-excitation rates are dominated by collisions. In this case, the populations of levels  ${}^2D_{5/2}$  and  ${}^2D_{3/2}$  will again be a ratio of their statistical weights but the ratio of the line strengths will be:

$$\frac{j_{\lambda 6716}}{j_{\lambda 6731}} = \frac{n({}^2D_{3/2}) A_{\lambda 6716}}{n({}^2D_{5/2}) A_{\lambda 6731}} = \frac{3 \cdot 2.6 \times 10^{-4}}{2 \cdot 8.8 \times 10^{-4}} = 0.44, \quad (2.10)$$

where  $A_\lambda$  is the radiative transition probability of that line. The actual value of  $n_e$  for the region will lie between these two density limits. With a measured line ratio, the Lick Observatory five level atomic calculator, FIVEL (De Robertis et al. 1987), allows  $n_e$  to be determined for a given  $T_e$ . Where possible, the most reliable  $T_e$  determined was entered in each case to give the

resulting nebular densities in Table 2.8. As the intensity ratio is only very slightly dependent on temperature,  $T_e = 10^4$  K was adopted in the remaining cases.

Nearly all the densities derived were in the range  $n_e = 10^2 - 10^3$  cm<sup>-3</sup>; comparable to classical H II regions. Cases where a density failed to be measured represented regions with weak nebular lines which would have arisen due the nebula being too diffuse to absorb the ionising photons in the first place. Sh2 99 gave an unfeasible density, if only because  $I_{\lambda 6716}/I_{\lambda 6731} > 1.5$ , permitted by the ratio of the statistical weights. Accounting for uncertainties, the ratio would fall below the limit and still imply a density as low as 370 cm<sup>-3</sup>. These densities are later compared to imaging of the regions where higher densities would be associated with younger compact nebulae. Over time, gas will be driven out by hot luminous stars such that older nebulae have lower densities.

### Nebular abundance

Line intensities will also reflect the abundances of different ions in the nebula. The O abundance is commonly derived, since strong lines for both O II and O III are present in the optical.<sup>2</sup> These can be compared to the H $\beta$  line, so that the overall O abundance with respect to H can be calculated via:

$$\frac{I_{O\text{III}\lambda 5007}}{I_{H\beta}} = \frac{N(O\text{III})}{N(H)} \times \frac{j_{O\text{III}\lambda 5007}}{j_{H\beta}}; \quad (2.11)$$

$$\frac{I_{O\text{II}\lambda 3727}}{I_{H\beta}} = \frac{N(O\text{II})}{N(H)} \times \frac{j_{O\text{II}\lambda 3727}}{j_{H\beta}}; \quad (2.12)$$

$$\frac{N(O)}{N(H)} = \frac{N(O\text{II})}{N(H)} + \frac{N(O\text{III})}{N(H)}. \quad (2.13)$$

These O lines are collisionally excited so that their emission coefficients, and therefore intensities, are heavily dependent on  $T_e$ . Following the uncertainties on the derived  $T_e$ , only Sh 156 offered a reliable abundance ( $12 + \log(O/H) = 8.49$ ) via this approach. The uncertainty in the other cases arises due to the weakness of the O III  $\lambda 4363$  line.

Alternative methods rely on stronger lines as abundance indicators. One such case, referred to as the  $N2$  method by Pettini & Pagel (2004), uses the  $N2$  ratio:  $[N\text{II}]\lambda 6583/H\alpha$ . They took  $\sim 140$  extragalactic H II regions where  $O/H$  and  $N2$  was well defined and derived the following relation:

$$12 + \log(O/H) = 8.90 + 0.57 \times N2. \quad (2.14)$$

<sup>2</sup>Higher states can occur but only need to be considered in more extreme ionising environments such as planetary nebulae.

The  $N2$  method has the benefit of the lines being placed closely together. An abundance was calculated for all H II regions where nebular lines were observed and listed in Table 2.8. Following the scatter of the  $N2$  calibration, the abundances are estimated to be accurate to within a factor of  $\sim 2.5$ .

Pettini & Pagel (2004) offered another abundance indicator, their  $O3N2$  method, which made use of the  $O3N2$  ratio:  $([O\ III] \lambda 5007/H\beta)/([N\ II] \lambda 6583/H\alpha)$ . The relation

$$12 + \log(O/H) = 8.73 - 0.32 \times O3N2 \quad (2.15)$$

was used to derive an additional O abundance, listed in Table 2.8 for comparison. Pettini & Pagel (2004) noted a large scatter when  $O3N2 > 2$  but a tighter correlation at lower values when metallicity was higher. As the entire sample showed  $O3N2 < 1.7$ , abundances should be accurate to within a factor of  $\sim 2$ .

Taking the abundance of the Sun to be  $12 + \log(O/H) = 8.69$  (Asplund et al. 2009), nearly all the regions were found to be subsolar. Following their locations in the outer Galaxy, this would be expected as the Milky Way displays a metallicity gradient with greater metal abundances at the centre of the Galaxy falling to lower abundances towards the periphery (Afflerbach et al. 1997; Deharveng et al. 2000)

## 2.4 Imaging

Supplementary imaging was obtained of each target using ACAM and was acquired on the second night of observing. The circular aperture gave a field of view of 8.3' in diameter and a 0.25"/pixel scale. This provided a spatial orientation for each region and positions for any additional ionising stars. Furthermore, ACAM filters both "on" (H6553 - centred at 6553Å) and "off" (H6645 - centred at 6645Å) the  $H\alpha$  line were used to separately highlight the nebulae and stars. This would allow a separate  $H\alpha$  luminosity to be derived, this time sourcing from the whole nebula rather than that confined to the spectroscopic slit. Table 2.9 lists the log of observations obtained through each filter for the respective H II regions.

As with the spectroscopic data, a large number of bias frames were created at the beginning of the the night. Flat-field frames for both filters were captured at the beginning and end of night although on this occasion using a twilight exposure. No arc frames were necessary but standard stars could have been used for flux calibration of the  $H\alpha$  images. No standards stars were observed in the end so calibration was carried out via an alternative method (see Section 2.4.2).

Table 2.9: Observing log for ACAM data.

H II Region	Date	Filter	Exposure Time
Sh2 99	2010-07-20	H6553	1 × 30 s
		H6645	1 × 30, 1 × 60 s
Sh2 100	2010-07-20	H6553	1 × 10 s
		H6645	1 × 10, 1 × 40 s
Sh2 101	2010-07-20	H6553	1 × 3 s
		H6594 <sup>†</sup>	1 × 3, 1 × 6 s
Sh2 112	2010-07-20	H6553	1 × 10 s
		H6645	1 × 20 s
Sh2 128	2010-07-20	H6553	1 × 30 s
		H6645	1 × 60 s
Sh2 148	2010-07-20	H6553	2 × 10 s
		H6645	10 × 10, 1 × 60 s
Sh2 149	2010-07-20	H6553	2 × 10 s
		H6645	10 × 10, 1 × 60 s
Sh2 152	2010-07-20	H6553	1 × 40 s
		H6645	1 × 60 s
Sh2 156	2010-07-20	H6553	1 × 20 s
		H6645	1 × 30 s
Sh2 158	2010-07-20	H6553	1 × 10 s
		H6645	2 × 30 s
Sh2 162	2010-07-20	H6553	1 × 3 s
		H6645	1 × 5 s
Sh2 170	2010-07-20	H6553	1 × 20 s
		H6645	1 × 30 s
Sh2 206	2010-07-20	H6553	1 × 20 s
		H6645	1 × 40 s

**Notes.** <sup>†</sup>H6594 was originally tested as the “off-H $\alpha$ ” filter but H6645 was later favoured in order to minimise traces of the nebula.

### 2.4.1 Data reduction

As with the spectroscopic data, an equivalent mean bias count was determined and then subtracted from all other science frames. A mean flat-field was created for each filter as before but in this case the only normalisation that was made was to divide the flat field by its average value. The science frames were then divided by this normalised flat-field. An example of a reduced H6653 image is given in Figure 2.14, where the corresponding ISIS slit position has been overlaid for reference. Equivalent figures for the other targets can be found in the Appendix A.

### 2.4.2 Image analysis

Figure 2.14 clearly shows that the slit covers only a fraction of the nebula and so the nebular  $H\alpha$  flux obtained from spectroscopy will only represent a small fraction of that coming from the region. It is the global  $H\alpha$  flux of the nebula which relates to the ionising radiation of the star. This value can be determined from the H6653 image but first the contributions of any stars must be removed. The corresponding H6645 images represent the continuum flux from the stars and by subtracting these from the H6553 images, only the  $H\alpha$  emission from the nebula remained.

Before a subtraction could be made, the H6553 and H6645 images needed to be aligned as they had not been acquired simultaneously. This was carried out using the `imalign` package within IRAF, aligning the centroids of a few bright stars common to both frames. Furthermore, the exposure times varied between the two filters. Aperture photometry was thus carried out within `Gaia` on another selection of stars of varying brightness to determine the average count ratio between the two filters. This gave the factor needed to scale the H6645 images before subtraction. Figure 2.15 compares the H6553, H6645 and net ( $H6553 - H6645$ ) images for Sh2 158.

Although no standard stars had been observed with ACAM, flux calibration of the images was still possible because flux calibrated spectra in the  $H\alpha$  band had already been achieved. The approach is analogous to that taken to obtain the fluxes through the Johnson  $B-$  and  $V-$  bandpasses. On this occasion, the flux calibrated spectrum of the star needed to be convolved through the bandpass of the H6553 filter. Aperture photometry was performed on the H6553 images, to provide the flux of the ionising stars in image counts. The ratio between the stellar flux convolved through the H6553 bandpass and the image counts was calculated. This ratio should be consistent for all stars as there was no change in the detecting instruments. A mean ratio was therefore derived, and this was used to convert image counts of the nebulae

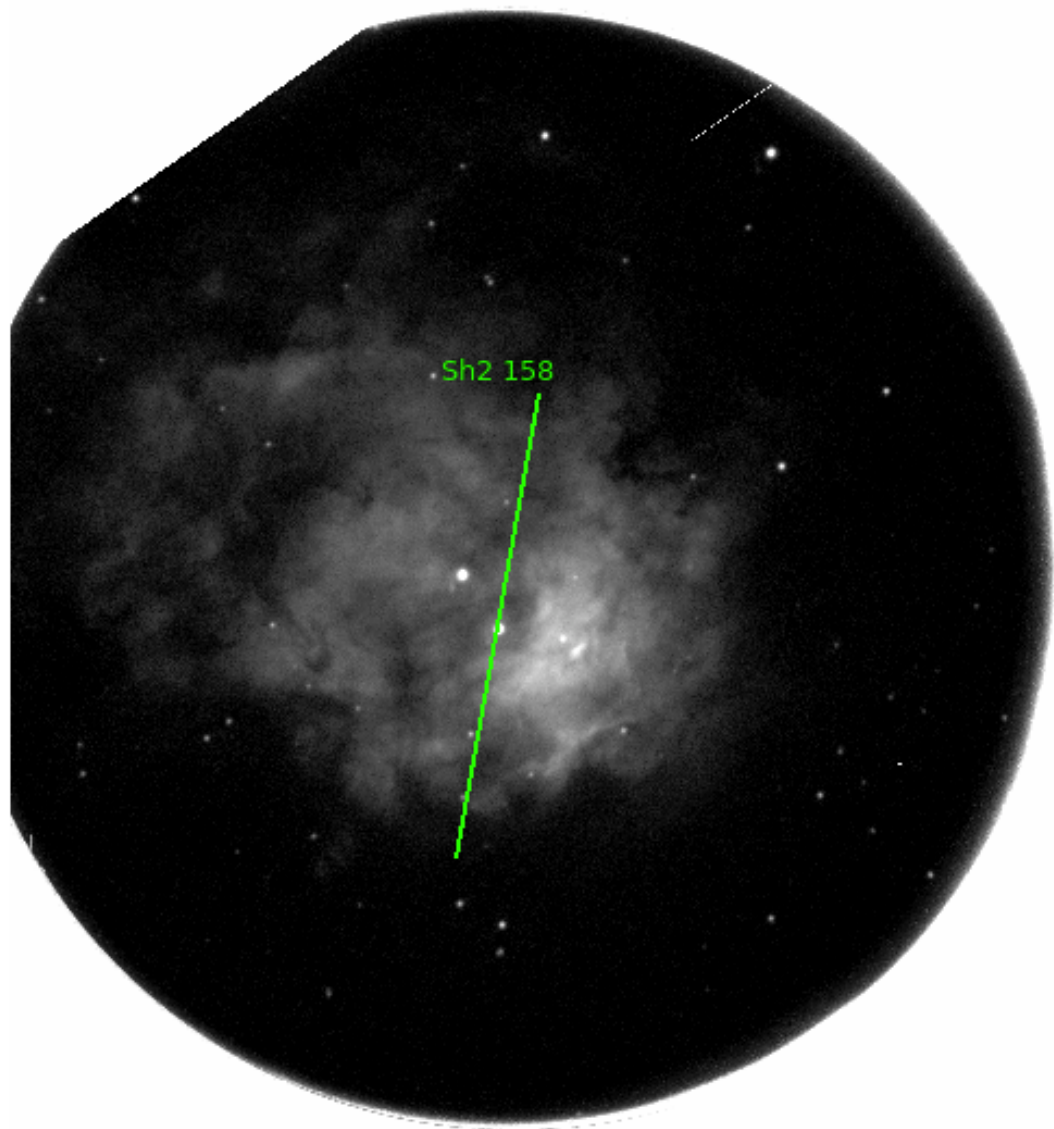
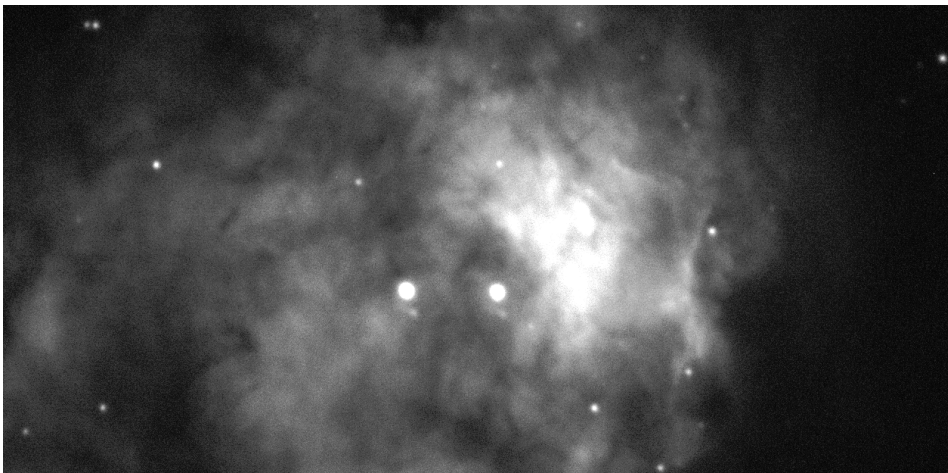
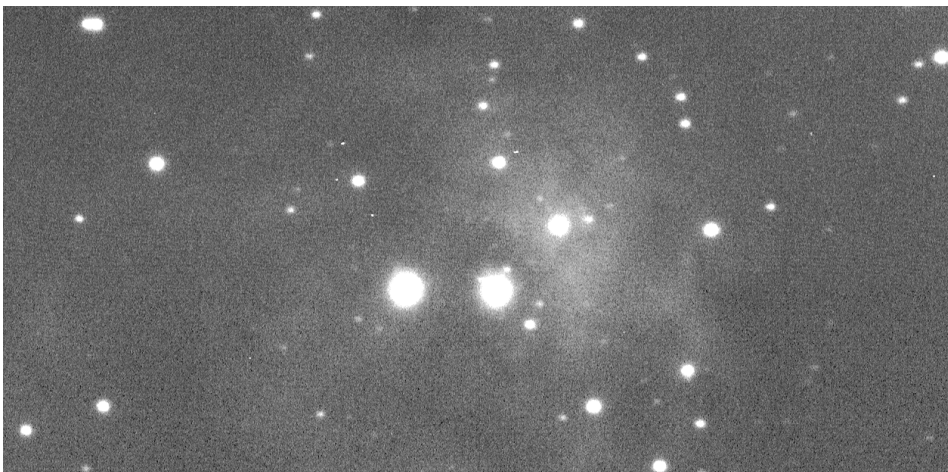


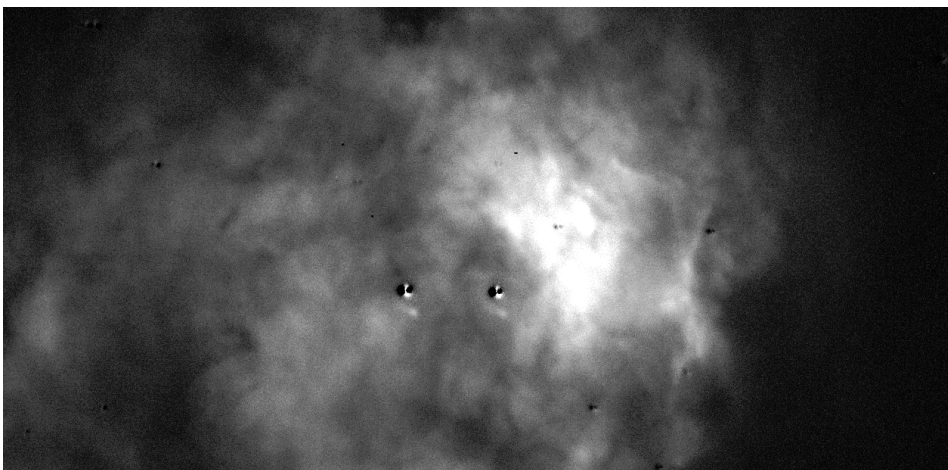
Figure 2.14: H6553 image of Sh2 158 overlaid with the ISIS slit. The aperture has a diameter of 8' and slit is 4'  $\times$  1". North is up and east is to the left.



(a)



(b)



(c)

Figure 2.15: Obtaining a nebular  $H\alpha$  image of Sh2 158, free of stellar contributions. Figure (a) is the H6553 image, (b) is the H6445 image, (c) is the net image (a)-(b).

into nebular fluxes. However, this was still not the true  $H\alpha$  flux, as the H6553 filter had a  $FWHM \approx 60 \text{ \AA}$  which also included the contaminating  $[\text{N II}] \lambda 6548$  &  $\lambda 6583$  lines. Once again the spectra could be used to rectify this by measuring the  $[\text{N II}]/H\alpha$  ratio (recall Figure 2.9). This revealed what fraction of the H6553 flux that actually sourced from  $H\alpha$  emission, and values could be scaled accordingly.

The eventual  $H\alpha$  fluxes of the nebulae were collected through different sized circular apertures. They were not always centred on the ionising star but positioned to extend over the local bright nebula regions. Plots of the selected apertures are given in Appendix A. These measured fluxes were then corrected for extinction to give the  $H\alpha$  intensity,  $I_{H\alpha}$ . The  $H\alpha$  extinction,  $A_{H\alpha}$ , was calculated using the Galactic extinction law of Howarth (1983), where  $E(B - V)$  from the stars was adopted and  $R_V = 3.1$  was assumed as before. Having estimated a distance to each target in Section 2.3.2, the luminosity,  $L_{H\alpha}$ , was then determined. The parameters are summarised in Table 2.10.

Table 2.10: Properties of the H II regions derived from the ACAM imaging.

H II Region	Aperture Diam. <sup>1</sup> [']	Nebula Diam. <sup>2</sup> [pc]	Observed Nebular flux <sup>3</sup> [erg s <sup>-1</sup> cm <sup>-2</sup> Å <sup>-1</sup> ]	Flux ratio <sup>4</sup> [Aperture/Slit]	Flux ratio <sup>†</sup> [N II/H $\alpha$ ]	A <sub>H<math>\alpha</math></sub> [mag]	I <sub>H<math>\alpha</math></sub> [erg s <sup>-1</sup> cm <sup>-2</sup> Å <sup>-1</sup> ]	L <sub>H<math>\alpha</math></sub> [erg s <sup>-1</sup> ]	log Q <sub>0</sub> <sup>neb</sup> [ph s <sup>-1</sup> ]
Sh2 99	2.2 (5)	5.0	6.8e-11	52	0.28	2.7	5.8e-10	4.2e+36	48.5
Sh2 100	1.1 (4)	2.7	1.3e-10	69	0.17	2.8	1.4e-09	1.1e+37	48.9
Sh2 101	5.0 (20)	3.6	4.2e-10	17	0.10*	1.5	1.5e-09	1.1e+36	47.9
Sh2 112	5.3 (15)	3.4	4.0e-10	12	0.10*	1.3	1.2e-09	6.8e+35	47.7
Sh2 128	1.4 (1)	4.5	2.0e-11	74	0.22	3.4	3.5e-10	5.4e+36	48.6
Sh2 148	1.7 (2)	4.0	8.3e-11	58	0.57	1.7	1.7e-10	1.3e+36	48.0
Sh2 149	1.0 (1)	1.9	5.6e-12	4	0.66	2.1	1.3e-11	6.2e+34	46.7
Sh2 152	1.6 (2)	2.4	1.5e-10	53	0.48	2.3	6.7e-10	2.0e+36	48.2
Sh2 156	1.4 (2)	1.7	2.3e-10	76	0.53	2.8	1.4e-09	3.2e+36	48.4
Sh2 158	5.7 (10)	7.8	8.9e-10	167	0.16	3.1	1.3e-08	3.3e+37	49.4
Sh2 162	6.2 (40)	4.9	1.0e-09	18	0.10*	1.7	4.4e-09	3.8e+36	48.4
Sh2 170	6.4 (20)	4.9	1.3e-10	9	0.10*	1.8	6.3e-10	5.1e+35	47.6
Sh2 206	4.4 (50)	4.9	5.1e-10	59	0.10*	2.9	6.6e-09	1.1e+37	48.9

**Notes.** <sup>1</sup> The diameter of the aperture used to measure the flux from the H6553-H6645 net image. The number in brackets is the diameter of the region as listed by Sharpless (1959).

<sup>2</sup> The projected diameter of the region assuming it is positioned at the distance given in Table 2.5.

<sup>3</sup> The flux measured from the H6553-H6645 net image through the aperture given in column 2. This value has been converted from counts to (erg s<sup>-1</sup> cm<sup>-2</sup>), as listed, using the average conversion ratio, (see text).

<sup>4</sup> The ratio of fluxes measured between the aperture (column 4) and the slit.

<sup>†</sup> Derived solely from the nebular spectrum except for exceptions (\*) where a flux ratio of 0.10 is assumed.

## 2.5 Relating the Ionising Stars and the Nebulae

Assuming a nebula optically thick to Lyman continuum photons, every photon will be absorbed to produce an ionisation. With the nebula in equilibrium, each ionisation is balanced by a recapture. The relation from Kennicutt (1998) can therefore be used to convert  $L_{\text{H}\alpha}$  into the rate of Lyman continuum ionising photons absorbed by the nebula ( $Q_0^{\text{neb}}$ ):

$$Q_0^{\text{neb}} = 7.31 \times 10^{11} L_{\text{H}\alpha}. \quad (2.16)$$

As these photons predominantly come from the stars, a direct comparison can then be made with the ionising photon rate of the star,  $Q_0^*$ , as shown in Figure 2.16, to see if there is a balance.  $Q_0^*$  is most dependent on  $T_{\text{eff}}$  of the star, which in this case has been decided by the SpT of the star. Classifications are likely to be within  $\pm 0.5$  of their correct subtype. Further the fact that any one SpT will cover a range of parameters rather than a single value, the accuracy of  $Q_0^*$  is estimated to be  $\pm 0.1 - 0.2$  dex. The uncertainty of  $Q_0^{\text{neb}}$  is affected by a number of parameters, namely the quality of the H6553–H6645 image subtraction process and the adopted extinction for the region.  $Q_0^{\text{neb}}$  is expected to be accurate to  $\pm 0.3 - 0.4$  dex.

For almost all regions, the star appeared to provide a surplus of photons compared to those absorbed by the nebula. Discrepancies were notably high, reaching up to  $\sim 0.9$  dex in cases such as Sh2 101, Sh2 112, Sh2 162 and Sh2 170. It is also noted that these were the nebulae to display particularly weak lines and hence their nebular parameters were essentially unconstrained. For other regions the offset between  $Q_0^*$  and  $Q_0^{\text{neb}}$  typically fell within uncertainties but could still suggest that stellar photons were being unaccounted for. Only Sh2 128 returned a similar photon rate from the nebula.

To help understand these different scenarios, the ionising star is considered first. Uncertainties over the SpT of the star have already been mentioned but so far it has been assumed that only a single star has ionised each region. The ACAM images clearly showed multiple stars to be present in the field of some regions. Ionisation fronts can often be seen around additional contributors but only photometry and spectroscopy of these stars would confirm their role in ionising the complex. These extra sources of ionising photons would increase  $Q_0^*$ , as too would a binary companion. With massive star binary fractions estimated to be at least 45% in clusters and OB associations (Sana et al. 2009), this might allow for several further ionising stars. The spatial resolution of the ACAM imaging could not reveal companions although none of the stellar spectra showed evidence of a double lined binary either. This indicated that any potential companion would have to be faint with a SpT notably later than that of the primary star. Given that the  $\log Q_0^*$  would typically fall by  $\sim 0.3 - 4$  dex per subtype (Martins et al.

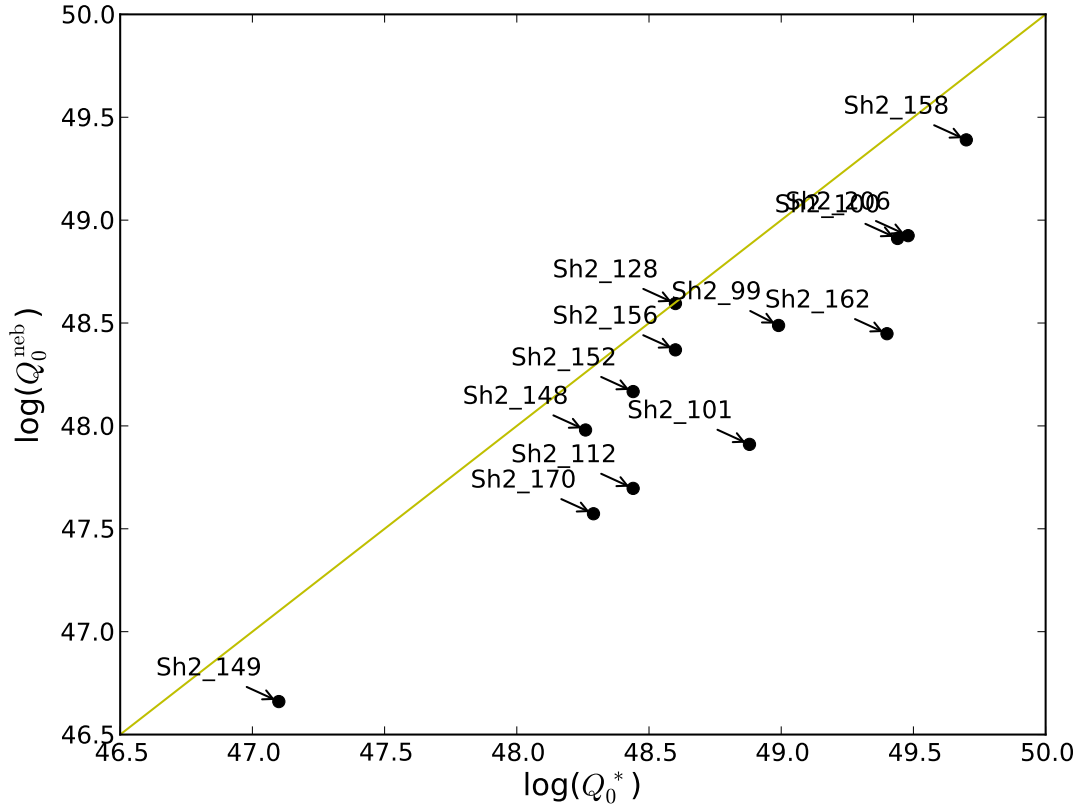


Figure 2.16: A comparison between the ionising photon capture rate of the nebula ( $Q_0^{\text{neb}}$ ) based on its  $H\alpha$  flux against the photon output rate of the ionising star ( $Q_0^*$ ) based on its SpT. The yellow line indicates a 1:1 relation.

2005), the contribution of such a companion is likely to be minimal.

Considering the nebula,  $Q_0^{\text{neb}}$  was selected by the circular aperture extending over the brightest regions on the H6553 image but not always being centred on the ionising star. Fainter sections were sometimes located beyond this aperture. The regional diameters for each H II region recorded by Sharpless (1959) were nearly always bigger than the apertures used and sometimes bigger than the field of view of ACAM. However, assuming the brightest nebular regions were measured, the contribution of these outer regions to  $Q_0^{\text{neb}}$  should still be limited.

Extinction can also change across a region, particularly one with a high dust content. Not only would this affect the derived  $I_{H\alpha}$  value but a fraction of the photons will be absorbed by the dust hence preventing gaseous regions from being ionised. With the heated dust re-emitting at longer wavelengths, such regions can be identified in the far-infrared (FIR) by all sky surveys performed by the Infrared Astronomical Satellite (IRAS). All regions where the discrepancy between  $Q_0^*$  and  $Q_0^{\text{neb}}$  was  $\leq 0.5$  dex are listed in the IRAS Faint Source Catalog (FSC) or were

found to bright in the FIR by Chan & Fich (1995) in their superior Full REsolution Survey CO-adder (FRESCO) IRAS images. A possible alternative, is that photons may have avoided absorption by the gas and dust and escaped the region altogether. With no tracer for these photons,  $Q_0^*$  would therefore appear to be in excess.

## 2.6 Comments on Individual Regions

This section gives a summary of the individual H II regions, considering the stars, the derived nebular properties and the ionising photon budget.

**Sh2 99** - ACAM imaging showed ionising gas to be focussed to the south and west of the targeted ionising star. The nebula spectrum for Sh2 99 was bright overall but  $T_e$  could not be measured due to the weakness of the [O III]  $\lambda 4363$  and [N II]  $\lambda 5755$  lines. The  $I_{\lambda 6716}/I_{\lambda 6731}$  ratio meant a realistic density could not be calculated, however, within the uncertainties,  $n_e$  could still be estimated at  $370 \text{ cm}^{-3}$ , not dissimilar to the other slightly dispersed nebulae in the sample. Despite the classification of a cooler O6 V star, its ionising photons remained above that of the nebula by  $\sim 0.5$  dex suggesting some photons had been unaccounted for. Several other bright stars are located in the field with the potential of being associated with the nebula. However, the region's FIR flux combined with its open structure to the north, are a likely cause of the discrepancy, as photons are absorbed by dust and escape the nebula, respectively.

**Sh2 100** - A bright nebula component is focussed within  $1'$  of the targeted ionising star with additional stars at its border and much thinner traces of gas located to the south-west. Plausible values for  $T_e$  and abundances were obtained within uncertainties, albeit being slightly higher and lower than expected, respectively. The stellar spectra favoured an earlier SpT of O4 V compared to previous classifications due to the weakness of the He I lines. This hotter ionising star left  $Q_0^*$  in excess of  $Q_0^{\text{neb}}$  by  $\sim 0.5$  dex. As the H II region showing the highest FIR luminosity in the Chan & Fich (1995) study, a young Sh2 100 with substantial remnant natal dust is the most probable explanation for the discrepancy.

**Sh2 101** - The region is very diffuse such that nebular lines were too weak to observe despite the long exposure times. This prevented most nebular properties from being derived but the ionising output of the star could still be compared. A O7 V SpT was favoured following the measured He I to He II ratio in the stellar spectrum.  $Q_0^*$  greatly exceeded  $Q_0^{\text{neb}}$  by  $\sim 0.9$  dex. Sharpless (1959) originally recorded the nebula to have a diameter of  $20'$ , notably larger than the  $5'$  aperture used in this work. Combined with its faintness, it suggests the nebula to be particularly old and dispersed whereby a large proportion of the photons are now escaping the region.

**Sh2 112** - The ACAM imaging showed large fluctuations with brighter regions to the south but darker regions to the north-east, suggesting varying dust obscuration. The slit covered a relatively fainter area and as with Sh2 101, the nebula spectrum of Sh2 112 was too weak to offer diagnostics. However, the changing extinction could help explain why  $Q_0^* > Q_0^{\text{neb}}$  by  $\sim 0.7$  dex. A uniform value for  $A_{\text{H}\alpha}$  was applied when it would clearly vary across the region and provide potentially higher values for  $I_{\text{H}\alpha}$  and thus  $Q_0^{\text{neb}}$ .

**Sh2 128** - This region is particularly compact within a 1.5' diameter with a slightly brighter feature to the north of the ionising star which is covered by the slit. It showed the highest levels of extinction in the sample and in turn the largest distance (13.7 kpc). However, the distance is suspect as it would place Sh2 128 at the very outskirts of the Galaxy. It is likely that the extinction has been overestimated to give the larger distance. This is supported by the fact that Sh2 128 is a listed IRAS object (IRAS 21306+5540), indicating the presence of heated dust around the star. The uniform extinction law adopted for all regions would therefore not accurately represent the reddening. As a result, the value of  $L_{\text{H}\alpha}$  would also be overestimated and explain why Sh2 128 was the exceptional case where  $Q_0^* \approx Q_0^{\text{neb}}$ .

**Sh2 148 + 149** - Sh2 148 is the brighter and larger of the two regions. They are separated by less than 3' and were observed simultaneously with a single ISIS slit and ACAM aperture. During the spectral extraction process, the ionising stars were easy to separate but the boundaries of the nebulae were blended and difficult to identify. While fluxes could be measured for a number lines, they often gave unpractical line ratios suggesting contamination from the other nebula. Nevertheless, their estimated densities did correspond to imaging; Sh2 148 showing a compact region while Sh2 149 was very diffuse. In terms of ionising photons,  $Q_0^*$  exceeded  $Q_0^{\text{neb}}$  by  $\sim 0.3$  dex in Sh2 148. The limiting resolution of IRAS meant that Chan & Fich (1995) could only determine a combined FIR luminosity for Sh2 147, 148 & 149. However, with Sh2 148 being the brightest and most compact of the three, a majority of the dust will likely be concentrated around it. Results indicated  $Q_0^* > Q_0^{\text{neb}}$  by  $\sim 0.4$  dex in Sh2 149. As it contained the only B-type ionising star, the separate calibrations used to estimate  $T_{\text{eff}}$  and  $q_0$  could explain this difference although it has likely followed the same relationship as the other open regions by leaking photons.

**Sh2 152** - The nebula is relatively small and isolated from other bright stars. The slit passed through a portion of the brighter gas to the south-east providing typical nebular properties. It showed  $Q_0^* > Q_0^{\text{neb}}$  but consistent within uncertainties. As another bright FIR source, dust could again absorb a fraction of the ionising photons.

**Sh2 156** - A very compact nebula reflected by the high density derived for the region. Sh2 156 is another IRAS object (IRAS 23030+5958), revealing the remains of a natal dust shell and helping to explain the inconsistency between the  $E(B - V)$  derived from the star and

nebula through varying extinction. Properties were otherwise comparable to Sh2 152 with the two lying at similar Galactic position. With no obvious candidates to serve as additional ionising sources, the small offset in  $Q_0^*$  and  $Q_0^{\text{neb}}$  could also be easily balanced after accounting for the dust.

**Sh2 158** - The bright extended nebula covered much of the ACAM field with the observed ionising star located in a fainter nebula region. A bright star to the north-east is believed to be a K-type star and insignificant to the ionisation but another star near the centre of the brighter nebula in the south-west could still make a contribution (Deharveng et al. 1979). Sh2 158 appeared to show sufficient ionisation from a single star though as  $Q_0^* > Q_0^{\text{neb}}$  by  $\sim 0.3$  dex. Again, as IRAS object IRAS 23030+5958, the presence of dust would justify the offset.

**Sh2 162** - The region is also known as the ‘‘Bubble Nebula’’ due to its round wispy appearance. The slit only sliced through part of this emission and did not include the brighter regions to the east of the ionising star. The spectrum still allowed nebular lines to be extracted but they were unfortunately too weak to be reliable. This drawback potentially arose during to the sky subtraction stage where a clean sky continuum was not selected to be subtracted from the nebula spectrum. Rather, some nebula features may have been selected in the sky frame and changed the true line fluxes. As a result the derived abundances which are supersolar are also likely to be unreliable. Regarding the ionising balance,  $Q_0^* > Q_0^{\text{neb}}$  by  $\sim 0.9$  dex. With the calibration from Martins et al. (2005) based on classical O-type stars, there is added uncertainty over  $Q_0^*$  given the unusual Oef SpT of the ionising star. Furthermore, the diffuse nature of the nebula allows for photon leakage.

**Sh2 170** - Another particularly weak nebula but containing several other stars in the field. In a similar case to Sh2 101, reliable line fluxes failed to be measured to provide nebular parameters.  $Q_0^*$  in Sh2 170 was also found to be considerably higher than  $Q_0^{\text{neb}}$  by a similarly large  $\sim 0.7$  dex, most probably a result of photon leakage out of the nebula.

**Sh2 206** - ACAM imaging revealed ionised gas concentrated to the south-west of the ionising star. It is relatively isolated but a somewhat uneven ionising boundary might suggest further contributors to the south-west. The slit cut through bright patches of the nebula but confusingly several key nebula lines remained hidden. A similar sky subtraction error, as mentioned for Sh2 162, is thought to explain the abnormality here as well as the unusually low abundance derived for Sh2 206. Traces of dust are seen once again with Sh2 206 being IRAS object IRAS 03595+5110 and explains the  $Q_0^* > Q_0^{\text{neb}}$  discrepancy of  $\sim 0.5$  dex.

## 2.7 Discussion

Both the stellar and nebular properties derived in this work can be obtained via more computational methods. The various codes developed to model stellar atmospheres were discussed in Chapter 1 and are able to provide more accurate results than the calibrations used here. Zastrow et al. (2013) investigated a similar sample of H II regions with single ionising stars, this time in the LMC. They modelled the ionising stars using grids from a series of the popular atmospheric codes. As in this work,  $L_{\text{H}\alpha}$  of the nebula was observed to make a comparison between  $Q_0^{\text{neb}}$  and  $Q_0^*$ . They found an overall agreement between the two values particularly from the TLUSTY and WM-basic codes while results from Smith et al. (2002) and CoStar (Schaerer & de Koter 1997) were slightly less consistent. It is thought that these variations arise from the hardness of the SED produced by the different models (Simón-Díaz & Stasińska 2008). Even without calibrations, uncertainties on  $T_{\text{eff}}$  as well as  $\log(g)$ , appear to be most influential on the accuracy of  $Q_0^*$  (Zastrow et al. 2013).

With regards to replicating the H II region, photoionisation simulations such as CLOUDY (Ferland et al. 2013) are available which model the gas to a microscopic level. By including the atomic and molecular processes, the ionisation, level populations and thermal state of the region can be produced and its spectrum can also be recreated. A range of temperatures and densities can be explored, meaning the codes are not restricted to gaseous nebulae but can extend to regions like a stellar corona or accretion disks. Photoionisation simulations are given a set of input nebular parameters along with an ionising source, in this case a star. The resulting nebular fluxes can therefore be used to reconstruct the ionising properties of the star. In the case of an UC H II region, this may be the only method of gaining information on a star obscured by dust.

Furness et al. (2010) studied a number of compact H II regions in the inner Milky Way. By observing them in the near and mid-IR, spectroscopy of both the nebula and ionising star could be obtained. The CMFGEN code was used to determine properties of the star, including its ionising flux distribution. Meanwhile, as in the optical, the nebula offers fine structure lines, in particular,  $[\text{Ne III}] 15.5 \mu\text{m}/[\text{Ne II}] 12.8 \mu\text{m}$  and  $[\text{S IV}] 10.5 \mu\text{m}/[\text{S III}] 18.7 \mu\text{m}$ . Furness et al. (2010) recreated these line ratios with CLOUDY but found poor agreement with observations with discrepancies of  $1.5 \pm 0.5$  dex. Whether this disagreement is due to the stellar atmosphere code not fully accounting for line blanketing or the photoionisation model being incomplete is unclear. They therefore derived new  $T_{\text{eff}}$  calibrations for the ionising O-type stars, based on the  $[\text{Ne III}]/[\text{Ne II}]$  and  $[\text{S IV}]/[\text{Ne II}]$  ratios. Its usage remains limited to compact and UC H II regions containing early-mid O-type stars that are capable of providing sufficient flux at the necessary ionising potentials.

This work has focussed on targets in the outer Milky Way, in contrast to the super-solar metallicities of the Furness et al. (2010) sample. Would the predicted and observed line ratios show similar disagreements in these poorer metal environments? By carrying out equivalent photoionisation modelling of the H II regions in this study this can be tested with the potential of explaining how the discrepancies arise. If necessary, a new  $T_{\text{eff}}$  calibration could also be obtained, this time relying on more readily available fine structure lines in the optical.

## 2.8 Summary

The 4.2 m William Herschel Telescope in La Palma, Spain was used to observe 13 H II regions, with sizes varying from 1 – 50', located in the outer Milky Way. Each region was believed to have a primary ionising star which was targeted with a 4' × 1" spectroscopic slit. This provided spectra of both the star and the surrounding nebula upon which analyses were made. To supply additional information on the ionisation and structure of the nebula, 8.3' diameter field of view images were captured of each region, through filters on and off the H $\alpha$  band.

All of the ionising stars were classified as OB stars. The new spectroscopy offered small changes to literature SpTs; no more than 1 subtype. Their *B* and *V*-band magnitudes were derived via spectrophotometry. These were combined with a series of stellar calibrations to determine the interstellar extinction, the distance to the star and its ionising output. Imaging typically found the stars to be close to, but detached from, the very brightest areas of the nebula. Deharveng (1974) noted similar positions in their Galactic H II region sample with the star often being located in a fainter nebula hole. However, from this imaging alone it was difficult to confirm whether the star was surrounded by dust, or if the gas density was genuinely lower in this area as a result of stellar feedback. The overall brightness of the nebulae showed large variations, and this was reflected in their spectra, as some spectral lines were too weak to be observed. This prevented nebular properties from being derived in some regions, but for the remainder, flux ratios were used as diagnostics for the nebular temperature, density and O abundance.

Stellar contributions obtained from the H $\alpha$ -off band were subtracted to create an H $\alpha$  image solely of the nebula. After calculating the H $\alpha$  luminosity of the region, the number of ionising photons was estimated and subsequently compared to that derived for the ionising star. The star provided a greater output in nearly all regions and they could be divided into two groups. The first showed offsets of  $\lesssim 0.5$  dex and were typically brighter and denser regions. They also indicated a presence of dust from their high FIR fluxes, suggesting them to be younger regions still to remove their natal shells. The discrepancy is thought to arise due to a fraction

of the stellar photons heating the dust as opposed to ionising the gas. The second group had offsets  $> 0.5$  dex and were much more open and diffuse regions. In many cases, their nebular lines were too weak to analyse, and they also lacked emission in the FIR. They represent older nebulae in which gas has dispersed and dust has been sublimated by the star. It is expected that large fractions of the photons are therefore escaping the region through cavities and avoid ionising the nebula. One region appeared to show a nebular photon rate comparable to the star, but when considering the uncertainties introduced by its high extinction, it too, was likely to follow a similar trend to the rest of the sample.

The offset is potentially greater in some cases, as other ionising stars in the field add to the stellar ionising output. Their ionising effects are thought to be limited compared to the primary star that was targeted, although their impact on heating the dust could be much larger. Indeed, for the regions that overlapped those covered by Lahulla (1985); Russeil et al. (2007), the SpTs of other stars in the association were often B-type or later. By determining their contributions to the dust heating, estimates could be made on the actual fractions of photons which end up ionising the gas, heating the dust and escaping the region. This approach is applied to the GH II region 30 Doradus in Chapter 5.

## Chapter 3

# Studying the Emission Line Stars of 30 Doradus with the VLT-FLAMES Tarantula Survey

*VFTS observing information and classification of emission line stars is published in Evans et al. (2011) and Crowther & Walborn (2011). Photometric properties of W-R stars and template W-R and Off/WN models (Section 3.7) are published in Doran et al. (2013). Determination of narrow band photometry (Section 3.7.1) and atmospheric modelling of the W-R stars (Section 3.7.4) was carried out by P. A. Crowther.*

### 3.1 Introduction

The VLT FLAMES Tarantula Survey (hereafter VFTS, Evans et al. 2011) is a European Southern Observatory (ESO) Large Programme that obtained multi-epoch spectroscopy of over 1000 stars in the Tarantula Nebula (30 Doradus, NGC 2070) in the Large Magellanic Cloud (LMC). With a rich source of massive stars spanning a large age range, 30 Doradus (hereafter 30 Dor) also benefits from close proximity and relatively low extinction (an overview of 30 Dor can be found in Chapter 4). The VFTS allows us to carry out a self-contained study of a single extensive star forming region. Targets spanned a diameter just in excess of 20 arcmin as shown in Figure 3.1, and were selected so as to include older regions such as Hodge 301 in the north west and NGC 2060 to the south west, along with the younger centre. After the removal of some foreground and late cool stars, more than 800 massive stars were identified using the primary MEDUSA observing mode including:  $\sim 350$  O-type stars;  $\sim 450$  B-type stars and 19 emission line stars.

The first half of the chapter (Sections 3.2-3.6) focusses on the emission line stars observed by the VFTS. Contemporary classifications are drawn from the new VFTS spectroscopy. The multi-epoch observations allow spectral variations to be monitored, in particular, by measuring the shifts in velocity arising from binary motions. More generally, all of the VFTS spectra are redshifted because of the recessional velocity of the LMC. It is important to understand which lines should be used to measure this shift and how this might change depending on the SpT being observed. The binary systems are further investigated, with literature orbital parameters being compared to those obtained from the VFTS spectra. Finally, the section highlights a few special spectroscopic cases observed in the VFTS emission line stars.

The second half of the chapter (Section 3.7) extends the work to all the emission line stars within 30 Dor, in particular, seeking to improve our understanding of their individual properties. This is greatly sought after, especially their scarcity and variability amongst different subtypes and binaries. In this study, atmospheric modelling is used to obtain reliable properties for a select few stars. They then serve as template stars, upon which the parameters of all 30 Dor emission line stars are based upon, not just those covered by the VFTS. The accuracy of this approach is second to modelling on an individual basis but has the advantage of being easily extended to a large sample of stars within 30 Dor. As such, the integrated properties of emission line stars can be later investigated and compared to the rest of the stellar population.

## 3.2 The VLT-FLAMES Tarantula Survey

The earlier VLT-FLAMES Survey of Massive Stars (Evans et al. 2005) had employed the Fibre Large Array Multi-Element Spectrograph (FLAMES) instrument at the VLT to obtain high resolution spectroscopy of massive stars in the Galaxy and the Magellanic Clouds. Developments were made in the understanding of rotational velocities and rotational mixing (Hunter et al. 2008; Brott et al. 2011), as well as the metallicity dependence of various stellar properties and wind parameters (Mokiem et al. 2007b; Trundle et al. 2007). The VFTS extended this work by focussing observations on 30 Dor. This section provides the observational details of the survey and its contribution to the study of W-R and other emission lines stars.

The primary dataset was acquired using the MEDUSA mode of the GIRAFFE spectrograph, whereby a total of 132 MEDUSA fibres were positioned for science and sky observations, each with a diameter of 1.2 arcsec. Three standard settings (LR02, LR03 and HR15N) were used per setup to provide medium-high resolution spectroscopy of the 3960 – 5070 Å wavelength range along with the H $\alpha$  line, both key to massive star diagnostics. The central R136 cluster was further supplemented by the ARGUS mode on the GIRAFFE spectrograph.

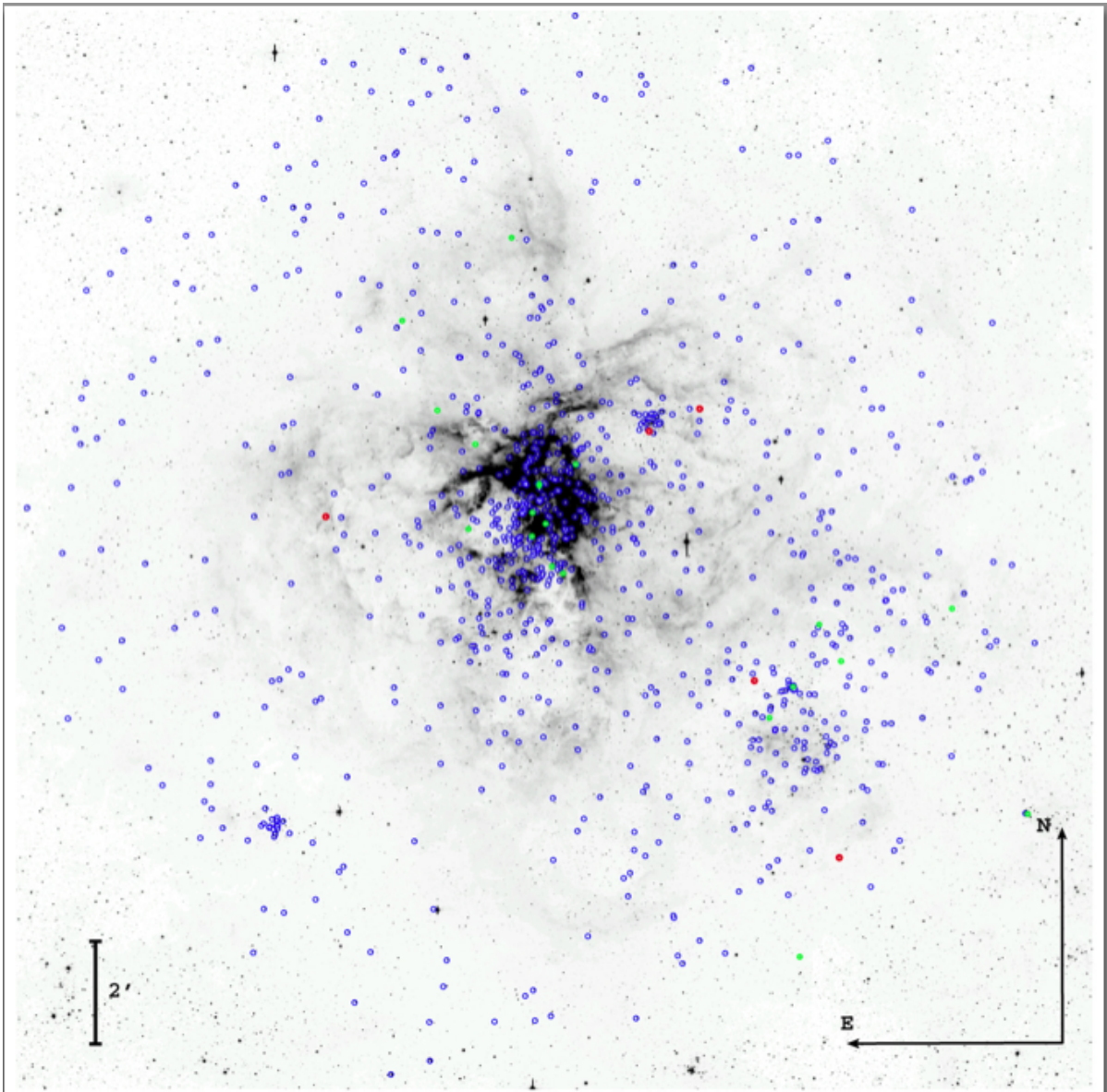


Figure 3.1: The FLAMES-MEDUSA targets (blue circles) overlaid on a V-band WFI image. Emission line stars are highlighted with green circles and luminous red supergiants with red circles. Taken from Evans et al. (2011).

Table 3.1: A summary of the VFTS setups including the exposure time per observing block (o.b.), measured spectral resolution ( $\Delta\lambda$ ) and resolving power  $R$  of each FLAMES mode and setting. Taken from Evans et al. (2011).

Mode	Setting	Exp.time/o.b. [s]	$\lambda$ -Coverage [Å]	$\Delta\lambda$ [Å]	$R$
MEDUSA	LR02	$2 \times 1815$	3960 – 4564	0.61	7000
MEDUSA	LR03	$2 \times 1815$	4499 – 5071	0.56	8500
MEDUSA	HR15N	$2 \times 2265$	6642 – 6817	0.41	16000
ARGUS	LR02	$2 \times 1815$	3960 – 4750	0.40	10500
UVES	520	$2 \times 1815$	4175 – 6200	0.10	53000

**Notes.** The UVES data do not include the 5155 to 5240 Å region because of the gap between the two detectors.

Five separate pointings were made with its integral field unit (IFU) containing 300 fibres and covering  $12 \times 7$  arcsec. Finally, the red arm of the Ultraviolet and Visual Echelle Spectrograph (UVES) was used to supply higher resolution observations for a small sample of stars in the inner region. A summary of the VFTS setups can be found in Table 3.1.

One feature of the VFTS was its multi-epoch observations. For the MEDUSA mode, seeing was restricted to  $< 1.2$  arcsec and a pair of exposures were taken in each observing block. These observing blocks spanned a whole year, giving an unprecedented opportunity to detect intermediate-long period binaries. The epochs of the observations are listed in Appendix B.

The data were primarily reduced using the ESO Common Pipeline Library (CPL) FLAMES routines (v2.8.7). These carried out initial bias subtraction, fibre location and extractions, divisions by a normalised flat-field and wavelength calibration. Further reduction steps were then taken to achieve: the transfer of data to the heliocentric frame; subtraction of the separate sky fibres; the removal of cosmic rays. An error spectrum was also produced, displaying the statistical error at each wavelength that had arisen from the different stages of reduction. Different extents of nebular emission along with changing seeing conditions left the spectra with varying amounts of nebular contamination but this was not universally subtracted. This contamination generally did not compromise the analysis of O-type stars, although B-type stars could suffer more, particularly if their He I lines were affected. Additional contamination could also have occurred from the dispersion of light from neighbouring fibres. This would typically arise at times of worse seeing and arise from bright emission line stars, but also luminous supergiants, as demonstrated in Section 3.5.1.

Dataset were reduced and made publicly available as part of the VFTS. Full details on all

Table 3.2: Classifications of the emission-line stars included in VFTS. Selected past classifications are listed. Corresponding aliases in the Breysacher et al. (1999) and Breysacher (1981) catalogues are also listed under BAT99 and Brey, respectively.

Identification					
VFTS	BAT99	Brey	Literature SpT	Ref.	VFTS SpT
002	85	67	WC 4+(OB)	a	WC 4+(O6-6.5 III)
019	86	69	WN 3o(+O9)	b	WN 3(h)
079	88	70a	WN 4b/WCE	b	
108	89	71	WN 7h	c	
136	90	74	WC 4	a	
147	91	73	WN 6.5h	e	WN 6(h)
180	93	74a	O3 If*/WN6	f	O3 If*
402	95	80	WN 7h	c	WN 7h+OB
427	96	81	WN 8(h)	c	
457	97	–	O3 If*/WN 7-A	g	O3.5 If*/WN 7
507	101/102	87	WC 4(+WN 6+O)	a	
509	103	87	WN 6	d	WN 5(h)+O(+early O)
542	113	–	O3 If*/WN 6-A	g	O2 If*/WN 5+late O/early B
617	117	88	WN 5ha	b	
682	118 <sub>a</sub>	–	–	–	WN 5h
695	119	90	WN 6(h)	c	WN 6h+?
731	121	90a	WC 4	a	
758	122	92	WN 5(h)	b	WN 5h

**Notes.** References (a) - Bartzakos et al. (2001), (b) - Foellmi et al. (2003), (c) - Crowther & Smith (1997), (d) - Moffat et al. (1987), (e) - Walborn et al. (1999), (f) - Testor & Schild (1990), (g) - Walborn & Blades (1997)

the observation reductions and handling (including the ARGUS and UVES modes, not used here) can be found in Evans et al. (2011).

### 3.3 Classification of Emission Line Stars

An initial inspection was made of all the MEDUSA spectra, which identified 18 sources (at least 19 emission line stars as VFTS 507 is composed of BAT99 101 and 102) showing prominent emission lines (see Table 3.2). All spectra in the sample were normalised and then classified. Normalisation can be difficult in WN stars, and even more so in WC stars, when no recognisable continuum can be traced between the broad emission lines. In such cases, the continuum would be estimated with a low order polynomial, or defined manually when favoured. Classifications were made as follows.

Table 3.3: Extract from Table 4a of Smith et al. (1996) used to determine the ionisation sequence of WN stars. Additional line ratios are also used including: He II  $\lambda 5411$ /He I  $\lambda 5875$ ; C IV  $\lambda 5808$ /He II  $\lambda 5411$  and C IV  $\lambda 5808$ /He I  $\lambda 5875$ , but were unavailable in the MEDUSA data.

Ionisation Subtype	<u>N v <math>\lambda 4604</math></u>			<u>N iv <math>\lambda 4057</math></u>	
	N III $\lambda 4640$			N v-III $\lambda 4604 - 40$	
	Peak/Continuum			Peak/Continuum	
	bndry	median	bndry	bndry	median
WN 2		<b>No N v</b>		<b>No N iv</b>	
WN 3		No N III			< 0.1
WN 4		> 2			0.6
WN 5	<b>0.5</b>	<b>1</b>	<b>2</b>	<b>1.25</b>	<b>2.5</b>
WN 6	<b>0.2</b>	<b>0.3</b>	<b>0.5</b>		0.8
WN 7	0.1	0.15	0.25		0.6
WN 8	0.05	0.1?	0.25		0.2
WN 9		0			< 0.1?

**Notes.** Values in bold define the ionisation class. The peak of the N v, III  $\lambda 4603 - 41$  blend is taken, regardless of which component dominates. A revised version of the boundaries for the WN 5-WN 9 subtypes is offered by Crowther & Walborn (2011). While their scheme was used to classify the Of/WN stars, the values in this table from Smith et al. (1996) determined the subtypes of the standard WN stars.

### 3.3.1 WN stars

An initial WN classification system was laid out by Smith (1968) under which the dominant ionisation state of N was used to determine the ionisation class of the star. However, this one dimensional system had drawbacks, as WN spectra displayed both broad and narrow emission lines, while H/He abundances were seen to affect the Pickering series with every other He II line being blended with a H line. Furthermore, the strength of the N lines could be affected by additional factors, other than the ionisation, such as the optical depth of the wind and selective excitation processes (Gray & Corbally 2009). A new three dimensional system was therefore introduced by Smith et al. (1996), as shown in Table 3.3, and was applied to the VFTS sample (see Figures 3.2 & 3.3). The degree of ionisation is determined from various He, N and C lines by measuring their peak fluxes in units of the local continuum. Unfortunately, the wavelength coverage of the MEDUSA data meant that the primary He II  $\lambda 5411$ /He I  $\lambda 5875$  diagnostic could not be measured, and so classification relied on the N v  $\lambda 4604$ /N III  $\lambda 4640$  and N iv  $\lambda 4057$ /N v-III  $\lambda 4604 - 40$  ratios.

Classifications were refined by determining the presence of H in the stellar wind. The Pickering series is typically blended with adjacent H lines (e.g. He II  $\lambda 4338$  and  $\lambda 4859$  blending with H $\gamma$  and H $\beta$ , respectively). Smith et al. (1996) again used the peak fluxes of lines with respect to the continuum and determined the following criteria for H content:

$$\begin{aligned} &= 0 \quad \rightarrow \text{o} \\ \text{He II } \lambda 4340 / \sqrt{(\text{He II } \lambda 4300 \times \text{He II } \lambda 4541)} - 1 &< 0.5 \quad \rightarrow \text{(h)} \\ &> 0.5 \quad \rightarrow \text{h} \end{aligned} \tag{3.1}$$

Rectification of the spectra led to some uncertainties in these ratios. For consistency, all fluxes were initially measured from the LR02 spectra, although the broad He II  $\lambda 4541$  line would lie close to the upper boundary of the spectra and at times not be completely covered. While this line could also be accessed from the LR03 spectra, blends with the adjacent emission line made the continuum more difficult to fit. Therefore, to assist with this (and all the classifying stages) additional spectral comparisons were also made to the predefined subtypes listed in Table 4e of Smith et al. (1996).

Smith et al. (1996) also included a criterion for line width whereby a broad-line WN star would have  $\text{FWHM He II } \lambda 4686 > 30 \text{ \AA}$  and be appended “b”. Only one star was found to meet this criterion, the rest being narrow-lined WN stars. Finally, absorption lines are present in the spectra of some WR stars. They can be caused by a companion star, and such cases are discussed in Section 3.4.2. In other cases, the absorption is intrinsic to the star. This may arise from the WR wind, hence showing a blue-shifted absorption, “a”, or be of unknown origin, “+abs”.

Previously published spectral types of all the VFTS emission line stars are listed in Table 3.2 along with any revisions following classification of the VFTS MEDUSA spectra.

### 3.3.2 WC stars

Smith (1968) also provided a classification scheme for WC stars, incorporating the C III  $\lambda 5690$ , C IV  $\lambda 5808$  and O V  $\lambda 5590$  lines. Progress in WC observations, as well as the quality of detectors, brought a revision by Smith et al. (1990), who used the C IV  $\lambda 5808$ /C III  $\lambda 5696$  and C III  $\lambda 5696$ /O IV  $\lambda 5590$  ratios. Meanwhile, Crowther et al. (1998) favoured the C IV  $\lambda 5808$ /C III  $\lambda 5696$  ratio as the primary classifying criterion as it was not dependent on C/O abundances. However, once again these key classifying lines were not included within the MEDUSA wavelength coverage (Figure 3.4). Smith et al. (1990) do provide typical FWHM values for the C III

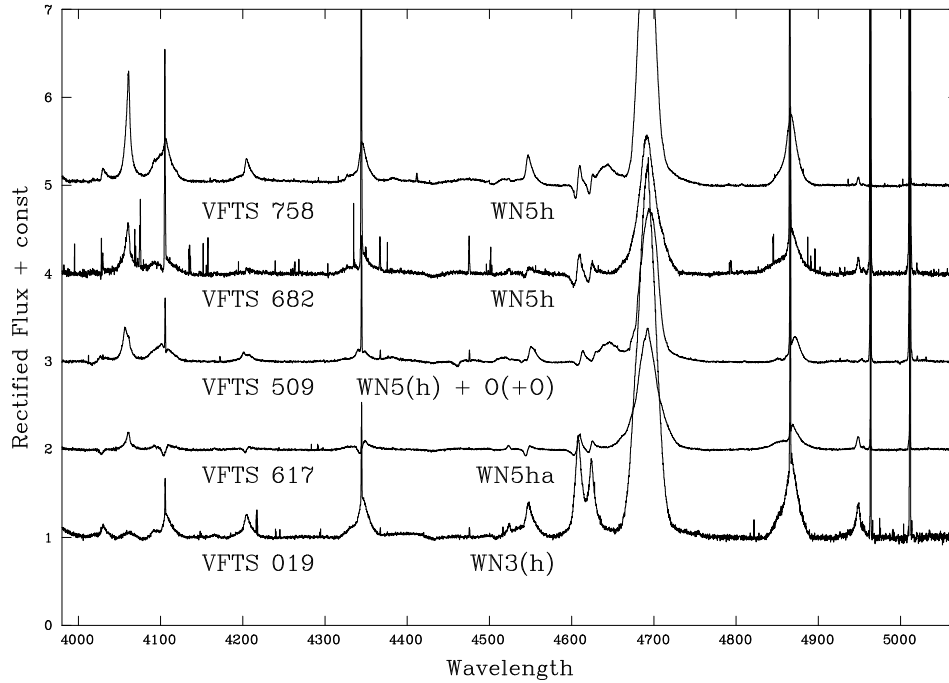


Figure 3.2: A spectral montage of the WN 3-WN 5 stars in the VFTS. Spectra from the LR02 and LR03 datasets obtained at the most consistent epochs were merged to produce the spectra shown.

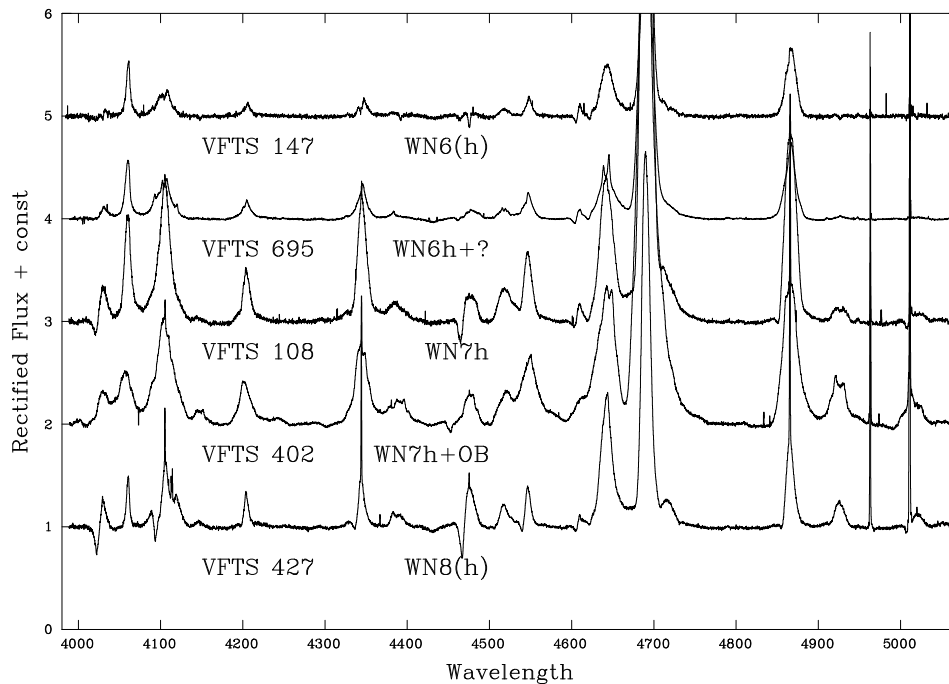


Figure 3.3: A spectral montage of the WN 6-WN 8 stars in the VFTS. Spectra from the LR02 and LR03 datasets obtained at the most consistent epochs were merged to produce the spectra shown.

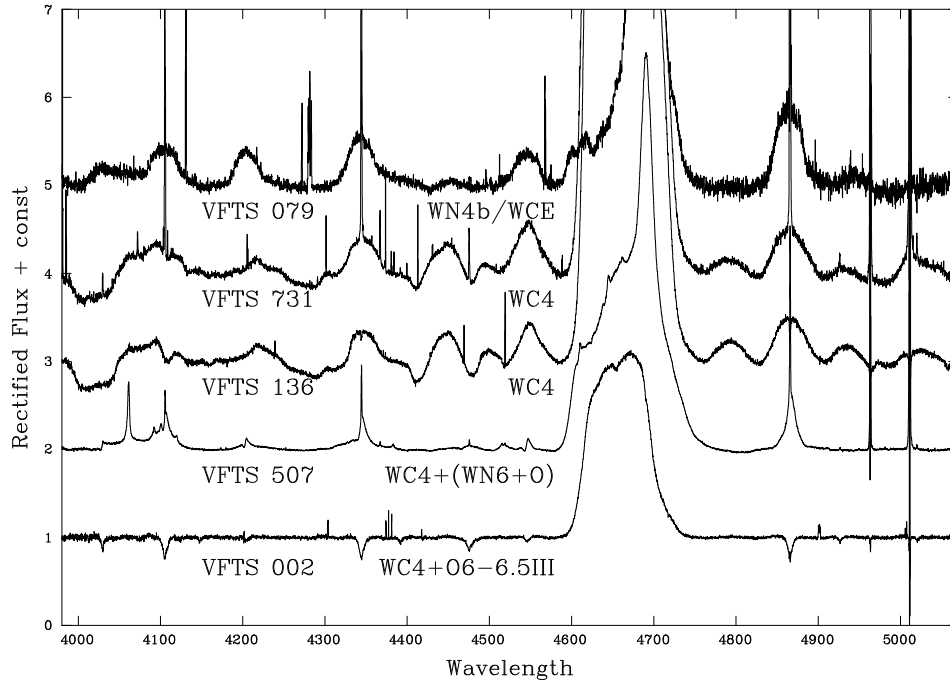


Figure 3.4: A spectral montage of the WC and WN/C stars in the VFTS. Spectra from the LR02 and LR03 datasets obtained at the most consistent epochs were merged to produce the spectra shown.

iv  $\lambda 4650$  line, offering some insight to the WC subtypes. Nevertheless, in nearly all cases, new conclusive classifications could not be made of the WC stars, and their spectral types were adopted from previous works.

Finally, some of these carbon emission lines are occasionally found in WN stars. However, the C III  $\lambda 5808$  to C III-IV  $\lambda 4650$  ratio is typically larger than in WC stars, favouring against a WN and WC star composite (Gray & Corbally 2009). These WN/C stars are thought to be intermediates between the two phases, with the WN/WCE class of VFTS 079 indicating high excitation.

### 3.3.3 Of/WN stars

Along with the W-R stars, the VFTS had observed stars previously classified as Of/WN stars (Figure 3.6). This classification was first introduced for the LMC star Sk  $-67^\circ 22$  but became widespread following the discovery of numerous further examples, particularly in 30 Dor (Walborn 1982). Of/WN stars display spectral features common to Of and O supergiants as well as late WN stars. Their intermediate characteristics naturally placed these “hot slash”

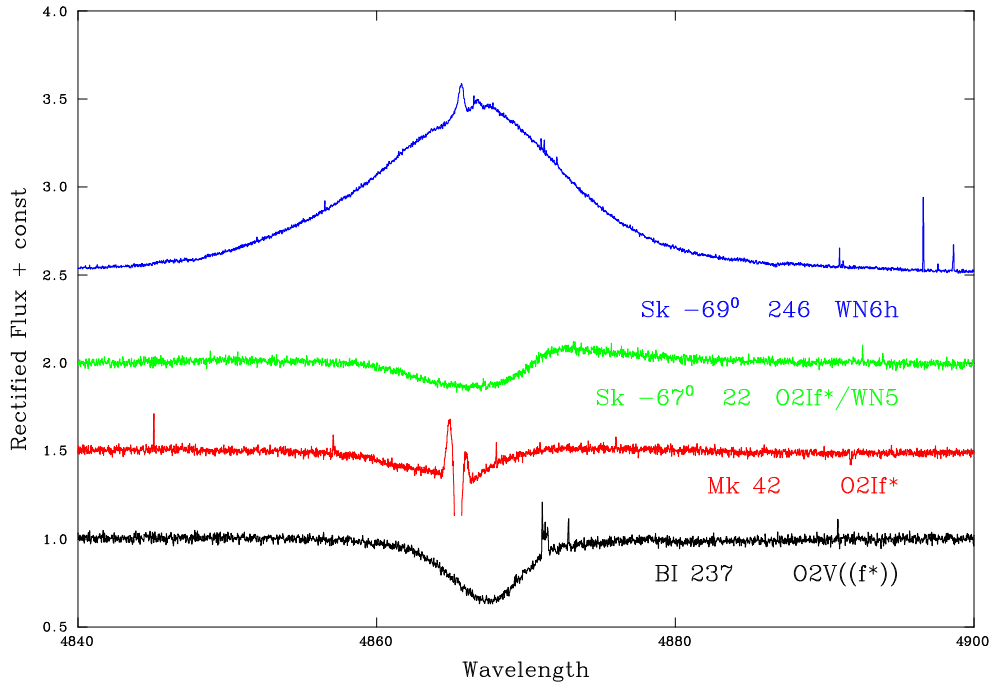


Figure 3.5: The changing morphology of the  $H\beta$  line between an O2 V( $f^*$ ), O2 If\*, Of/WN and WN star.

stars as the evolutionary phase between Of and WN stars. Crowther & Walborn (2011) took  $H\beta$  to be in absorption for all O-type stars, to have a P Cygni profile for Of/WN stars and be in stronger emission for WN stars. An example of this progression is presented in Figure 3.5 using non-VFTS stars as there is less nebular contamination in the  $H\beta$  line. Relations in the N emission lines (Walborn et al. 2002b) and a revised version of Smith et al. (1996) were subsequently used to determine the ionising subtypes of the stars. This approach was applied in the classification of all the Of and Of/WN stars in Table 3.2.

### 3.4 Spectral Variation

The VFTS data benefit from multi-epoch observations, allowing an investigation into the spectral variations of the W-R stars. In some cases, these changes could be intrinsic to the star and arise due to fluctuations in their strong stellar winds. Others could arise from binary systems with the VFTS giving the potential to classify companion stars and gain information on the orbital velocity and period. Knowledge of the companion was particularly important for later analysis, as it would contribute to both spectroscopic and photometric measurements. Finally,

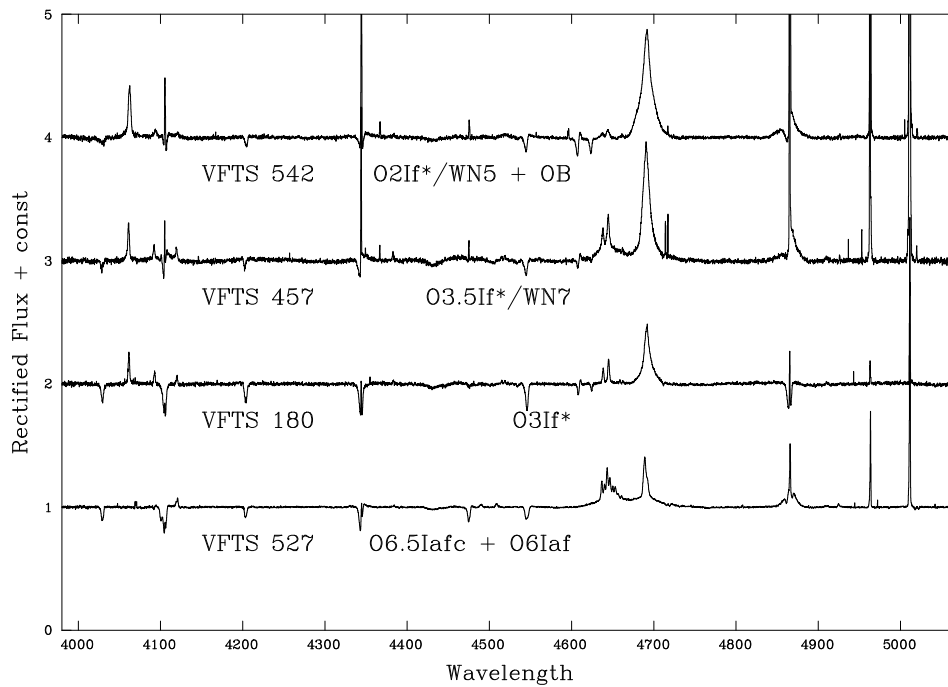


Figure 3.6: A spectral montage of the Of and Of/WN stars in the VFTS. Spectra from the LR02 and LR03 datasets with the closest epochs were merged to produce the spectra shown.

further spectral variations could be brought about by changes in the seeing conditions and issues with contamination. For each star, a median sky spectrum was obtained from  $\geq 12$  sky fibres in the field. These were inspected alongside the stellar spectrum to establish whether there were any correlations with the variations.

### 3.4.1 Radial velocities

The radial velocity ( $RV$ ) of an object is its velocity towards or away from the observer. By observing any spectral line and determining its observed wavelength,  $\lambda_{\text{obs}}$ ,  $RV$  can be calculated by the following equation:

$$\frac{\lambda_{\text{obs}} - \lambda_0}{\lambda_0} = \frac{RV}{c}, \quad (3.2)$$

where  $c$  is the speed of light,  $\lambda_0$  is the rest wavelength of the line (taken from the National Institute of Standard and Technology, NIST) and  $RV$  is the radial velocity of the observed target. All the VFTS spectra are redshifted, as the stars are located in the receding LMC. During the reduction of the data the orbital motions of the Earth around the Sun had been accounted for, making the velocities heliocentric. The mean radial velocity of the single VFTS O-type stars was found to be  $270.73 \text{ km s}^{-1}$ , with dispersion  $1\sigma = 10.50 \text{ km s}^{-1}$  (Bressert et al. 2012). Assuming all of the VFTS stars were positioned at similar distances, they would be expected to have the same  $RV$  distribution unless their movement was affected by another factor such as the gravitational pull of a companion star or if the star had been driven by a kick, i.e. a runaway star.

The ELF package within the spectrum analysis program DIPS0 was used to fit a Gaussian profile to various lines in the VFTS spectra. The profile centre returned was taken to be  $\lambda_{\text{obs}}$ . In O-dwarfs, their photospheric lines are narrow and well-defined, allowing an accurate measurement of  $RV$  (recall Figure 3.5). This proved more complicated in W-R stars as their broad emission lines can often be asymmetric and the profile centre harder to fit. Furthermore, their dense winds obscure the photosphere, and the observed emission lines instead form at various heights in the extended outflow. A different  $RV$  can therefore be measured from different spectral lines.

Table 3.4: The sample of LMC O2 stars chosen to be compared to the VFTS emission line stars to investigate discrepancies in *RV*.

Star	RA [h m s]	Dec [ $^{\circ}$ ' '']	SpT	$m_V$ [mag]
BI 237	05 36 14.6	-67 39 19	O2 V((f*))	13.89
BI 253	05 37 34.5	-69 01 10	O2 V((f*))	13.76
LH 10-3061	04 56 42.5	-66 25 18	O2 III(f*)	13.68
HD 269810	05 35 13.9	-67 33 28	ON2 III(f*)	12.28
Melnick 42	05 38 42.2	-69 05 54	O2 If*	12.84
Sk -67 $^{\circ}$ 22	04 57 27.4	-67 39 03	O2 If*/WN 5	13.44

**Notes.** Spectral types from Walborn et al. (2002b), Massey et al. (2005) and Crowther & Walborn (2011). Photometry from Massey (2002), Walborn et al. (2002b) and (Hunter et al. 1995).

Table 3.5: Spectra of the LMC O2 stars listed in Table 3.4.

Star	Instrument/Filter	Programme ID.	Ref.
BI 237	ESO/VLT(UT2)+UVES HST-STIS/G140L	74.D-0109 9412/Massey	Welty & Crowther (2010) Massey et al. (2004)
BI 253	ESO/VLT(UT2)+UVES HST-STIS/G140L	74.D-0109 9412/Massey	Welty & Crowther (2010) Massey et al. (2004)
LH 10-3061	ESO/VLT(UT2)+UVES	74.D-0109	Welty & Crowther (2010)
HD 269810	ESO/VLT(UT2)+UVES	70.D-0164	Welty & Crowther (2010)
Melnick 42	HST-FOS/G130H ESO/VLT(UT2)+UVES HST-HRS/G140L	4110/Kudritzki 70.D-0164 3030/Ebbets	Walborn et al. (1995) Welty & Crowther (2010) Heap et al. (1991)
Sk -67° 22	ESO/VLT(UT2)+UVES HST-STIS/G140L	74.D-0109 9412/Massey	Welty & Crowther (2010) Massey et al. (2005)

**Notes.** Only the optical spectra from Welty & Crowther (2010) were used to generate the atmospheric models the discussed. The UV spectra were used only for comparison. See Section 5.2.1 for further details on the modelling.

So when will a reliable  $RV$  be obtained? To investigate this, additional high resolution spectra were taken from observations published in Welty & Crowther (2010), for a sample of early O-type stars with progressively stronger winds listed in Table 3.4. They were separate from the VFTS data set and had been observed with the VLT-UVES. The spectra had a resolving power of  $R \approx 34,000$  and spanned  $3300 - 10250 \text{ \AA}$  in all cases except for Mk 42 and HDE 269810 which covered  $3300 - 6650 \text{ \AA}$ . A montage of the spectra is given in Figure 3.7. The CMFGEN code was used to generate atmospheric models of all of these stars as well as the WN 5h star VFTS 682 (details of the modelling can be found in Section 5.2.1).

The resulting synthetic spectra were plotted alongside the observed spectra but would require a velocity correction in order to coincide with observations as the models were based in the rest frame of the star. This velocity correction would be the  $RV$  of the star. A selection of spectral lines were individually inspected and different velocity corrections were applied. The synthetic and observed spectra were inspected by eye and the corrections showing the best fits were recorded. In general, this gave an uncertainty on  $RV$  of about  $\pm 10 \text{ km s}^{-1}$ . This was comparable to the formal uncertainties returned when measuring  $RV$  using the conventional Gaussian fitting - typically a few  $\text{km s}^{-1}$ , but sometimes higher for Balmer lines with nebular contamination. Note that this work only inspects the behaviour of a few spectral lines in a small sample of stars. The ‘by eye’ method limits the accuracy when measuring the relative shift between the synthetic and observed spectra. A more reliable fit could be achieved using a cross-correlation technique and would therefore be favoured for a more in depth study.

The  $RV$  values obtained from the two methods are listed in Table 3.6 and plotted in Figure 3.8. They show good agreement for O-dwarfs and giants, and even hold well for the stronger supergiant wind<sup>1</sup>. The  $RV$  obtained from both the models and observed spectra remained consistent for different spectral lines. This indicates that any spectroscopic line could be used to measure a reliable  $RV$  of a typical O2 V-I star. However, this relationship broke down for stars with stronger winds. A progressively larger scatter is seen in the  $RV$  of the Of/WN and WN star. Even in the case of the model derived  $RV$ , values were inconsistent for different lines, implying that a reliable  $RV$  may be difficult to obtain, particularly for WN stars. However, while synthetic lines can be dependent on the wind velocity law chosen for the star, Bestenlehner et al. (2011) found  $N \text{ v } \lambda 4944$  to be quite stable regardless of the wind structure they chose to model VFTS 682. In this work, the modelled  $N \text{ v } \lambda 4944$  line also showed good agreement with observations suggesting that there is at least one  $RV$  diagnostic line available. Nevertheless, caution is still needed as the atomic physics of certain transitions can be simplified by atmospheric codes. This too, can deliver a different velocity profile to that of the *true* spectrum.

<sup>1</sup>The two stars (Sk  $-67^\circ 22$  and BI 237) that show a notably higher  $RV$  compared to the mean value of  $270 \text{ km s}^{-1}$  are known to be runaway stars (Gvaramadze et al. 2010)

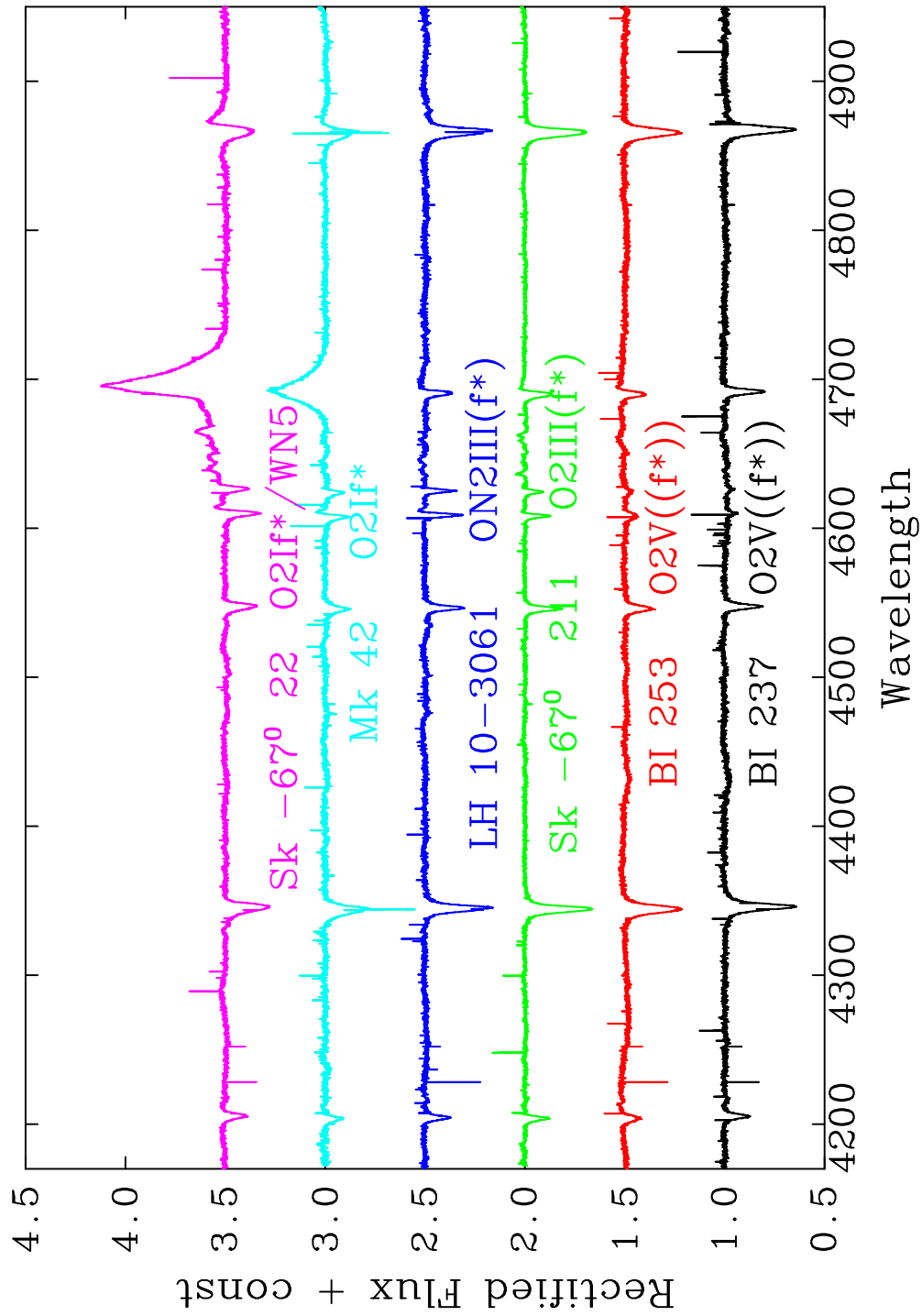


Figure 3.7: A spectral montage of the stars listed in Table 3.4 observed with VLT-UVES.

Table 3.6: A comparison between the observed and synthetic  $RV$  for different spectral lines. The observed  $RV$  was measured with a Gaussian fit to the line. The synthetic  $RV$  represents the velocity shift required to overlay the synthetic CMFGEN spectrum on top of the observed spectrum.

Star	Spectral Type	Line	Synthetic $RV$ [ km s <sup>-1</sup> ]	Observed $RV$ [ km s <sup>-1</sup> ]
BI 237	O2 V((f*))	N IV $\lambda$ 4057	385	385
		He II $\lambda$ 4686	375	374
		He II $\lambda$ 4542	385	384
		He II $\lambda$ 4200	385	390
BI 253	O2 V((f*))	N IV $\lambda$ 4057	265	276
		He II $\lambda$ 4686	285	288
		He II $\lambda$ 4200	290	275
HDE 269810	O2 III(f*)	N IV $\lambda$ 4057	280	278
		He II $\lambda$ 4686	295	300
		He II $\lambda$ 4200	290	275
LH 10-3061	ON2 III(f*)	N IV $\lambda$ 4057	315	316
		He II $\lambda$ 4542	325	318
Melnick 42	O2 If*	N IV $\lambda$ 4057	265	253
		He II $\lambda$ 4200	275	273
		He II $\lambda$ 4542	285	262
		H $\gamma$	285	255
Sk -67° 22	O2 If*/WN 5	N IV $\lambda$ 4057	445	432
		He II $\lambda$ 4200	435	394
		H $\gamma$	455	373
VFTS 682	WN 5h	N IV $\lambda$ 4057	205	167
		He II $\lambda$ 4686	195	410
		H $\alpha$	250	318
		N V $\lambda$ 4944	260	279

**Notes.** All stars had their radial velocities measured from UVES spectra (Table 3.4) except for VFTS 682 which used the VFTS MEDUSA spectra (Table 3.1).

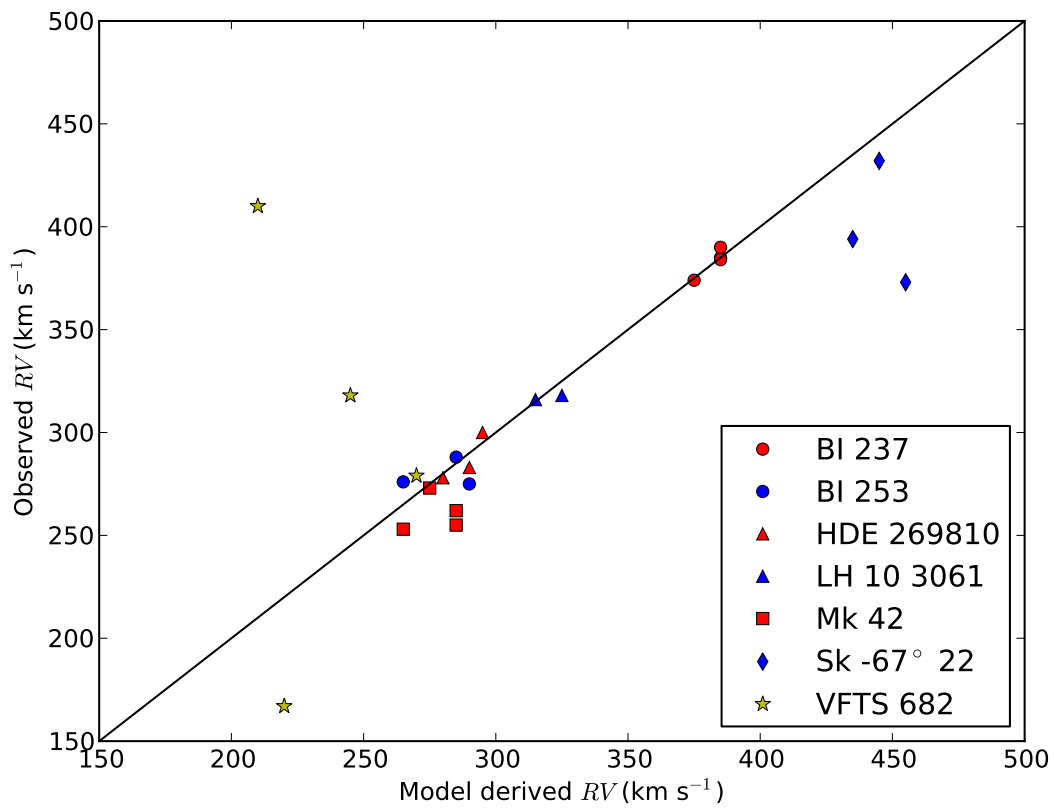


Figure 3.8: A plot of observed against synthetic radial velocities. Each point represents the  $RV$  measured for a different spectral line, see Table 3.6.

### 3.4.2 Binaries

While there are issues in determining an accurate value for  $RV$ , relative *changes* in  $RV$  from one epoch to another can still be easily recognised to identify binary systems. This was achieved by transferring the spectra into velocity space (as is shown in Figures 3.10, 3.11, 3.14, 3.16 & 3.18). In each case, the average  $270 \text{ km s}^{-1}$  velocity correction (Bressert et al. 2012) is made to the spectrum. A velocity of  $0 \text{ km s}^{-1}$  then corresponds to  $\lambda_0$  and is marked with a solid vertical black line. The spectra of the stars are overlaid on this with each colour representing a separate epoch.<sup>2</sup> A spectral line centred at a negative velocity is thus blue-shifted and one with a positive velocity has been red-shifted.

The variability in  $RV$  was determined by fitting a Gaussian component to an emission line, using the ELF package within DIPSO. A consistent emission line needed to be fitted for each epoch. In each case, a single Gaussian component was used to achieve a fit, Figure 3.9 showing examples of the fits made. The  $RV$  from these fits are listed in Table 3.7 with the formal uncertainties returned by ELF. The spectral line chosen for analysis would ideally be symmetrical to allow an accurate fit, and this was readily available in the spectra of the single emission stars. However, the binaries were found to show skewed profiles at some epochs, making the fitting of a single component less accurate and giving likely uncertainties on  $RV$  of  $\sim \pm 30 \text{ km s}^{-1}$ , exceeding those in Table 3.7.

All W-R stars with a binary history are discussed further in this section and compared to previous literature. Schnurr et al. (2008b), Foellmi et al. (2003) and Bartzakos et al. (2001) all made studies into the binary nature of W-R stars in the LMC. Their work covered all of the stars in Table 3.2 (excluding VFTS 682). In some cases, their orbital parameters had been derived so a consistency check could be made with the VFTS observations.

The W-R binaries show some significant line profile variabilities as seen in Figures 3.11, 3.14, 3.16 & 3.18. Nevertheless, it is important to note that some spectral changes can be intrinsic to a star, arising from local overdensities (clumps) in the W-R wind, with no requirement of a binary system (Lépine & Moffat 1999). St-Louis et al. (2009) studied a series of apparently single W-R stars which displayed periodic line profile variations. Galactic W-R stars with notable periodic variations include WR 6 and WR 134 found to show repeated spectroscopic observations over periods of  $P = 3.766$  (St-Louis et al. 1995) and  $P = 2.25$  days (Morel et al. 1999), respectively. Pulsations were ruled out as a possible cause due to the short time scales variations would occur on. However, it was believed that the variability could be brought about by inhomogeneities in the wind structure being combined with the surface rota-

<sup>2</sup>Note that not every epoch listed in Appendix B has been plotted in Figures 3.10, 3.11, 3.14, 3.16 & 3.18 as some of the epochs are separated by no more than an hour, and show no spectral differences.

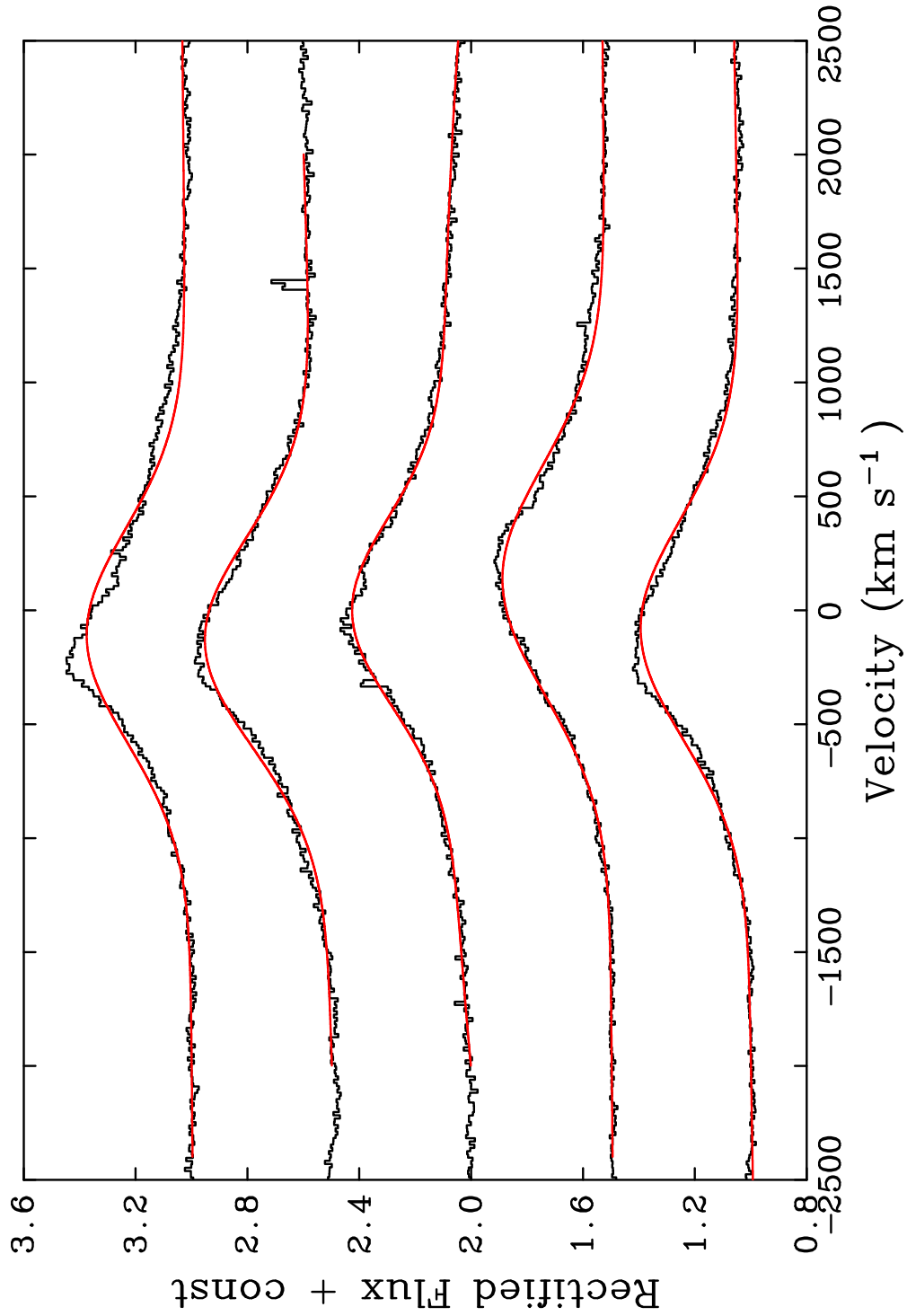


Figure 3.9: Gaussian fits to the He II 4200 line in VFTS 402. Each spectra represents a different epoch. Observed spectra are plotted in black and gaussian fits in red.

tion of the W-R star. Structures, termed as corotating interaction regions (CIRs), are thought to be created at the base of the wind and propagate outwards. These perturbations would spiral out as they are carried along by rotation to produce the profiles observed. As such, they offer a potential method for determining the rotation velocities of W-R stars, although this velocity would correspond to the radius at which the CIR had originated, rather than the surface rotation velocity.

Table 3.7: Radial velocities of the VFTS Of/WN and WN stars as measured from the N IV  $\lambda 4057$  line, unless stated otherwise. Radial velocities of the WC stars were not measured in this study.

Star	MJD	$RV$ [ km s <sup>-1</sup> ]
VFTS 019 (from He II $\lambda 4200$ )	54817.223	400 $\pm$ 15
	54817.267	391 $\pm$ 10
	54822.058	368 $\pm$ 11
	54860.105	377 $\pm$ 28
	54890.041	393 $\pm$ 16
	55112.361	391 $\pm$ 13
VFTS 108 (from He II $\lambda 4200$ )	54824.242	156 $\pm$ 2
	54824.285	157 $\pm$ 2
	54822.156	170 $\pm$ 2
	54858.171	167 $\pm$ 2
	54879.052	171 $\pm$ 2
	55111.336	160 $\pm$ 2
VFTS 147	54824.242	212 $\pm$ 3
	54824.285	212 $\pm$ 2
	54822.156	220 $\pm$ 3
	54858.171	211 $\pm$ 4
	54879.052	208 $\pm$ 3
	55111.336	218 $\pm$ 3
VFTS 180	54804.105	279 $\pm$ 2
	54804.148	283 $\pm$ 1
	54804.191	274 $\pm$ 2
	54836.239	279 $\pm$ 1
	54836.287	282 $\pm$ 2
	54867.109	284 $\pm$ 1
	55114.320	283 $\pm$ 3
	55108.318	281 $\pm$ 1
VFTS 402 (from He II $\lambda 4200$ )	54774.286	-88 $\pm$ 6
	54809.098	115 $\pm$ 4
	54809.141	132 $\pm$ 4
	54837.182	-8 $\pm$ 4

**Table 3.7 – continued from previous page**

	54867.159	$-142 \pm 5$
	55112.264	$-112 \pm 7$
	55459.292	$34 \pm 4$
VFTS 427	54824.242	$190 \pm 2$
	54824.285	$186 \pm 2$
	54822.156	$183 \pm 2$
	54858.171	$193 \pm 2$
	54879.052	$190 \pm 2$
	55111.336	$198 \pm 1$
VFTS 457	54822.254	$247 \pm 2$
	54822.298	$246 \pm 2$
	54822.341	$246 \pm 1$
	54824.333	$245 \pm 2$
	54858.220	$247 \pm 2$
	54889.052	$250 \pm 2$
	55114.272	$244 \pm 3$
VFTS 509	54817.223	$-258 \pm 3$
	54817.267	$-269 \pm 3$
	54822.058	$-282 \pm 3$
	54860.105	$31 \pm 5$
	54890.041	$164 \pm 3$
	55112.361	$-307 \pm 5$
VFTS 542	54817.223	$65 \pm 2$
	54817.267	$65 \pm 2$
	54822.058	$55 \pm 3$
	54860.105	$0 \pm 3$
	54890.041	$-118 \pm 1$
	55112.361	$57 \pm 2$
VFTS 617	54794.187	$195 \pm 6$
	54794.231	$201 \pm 5$
	54794.328	$207 \pm 5$
	54798.303	$190 \pm 5$
	54836.146	$209 \pm 5$
	54836.191	$213 \pm 5$

Table 3.7 – continued from previous page

	54867.058	$219 \pm 5$
	55108.281	$212 \pm 6$
VFTS 695	54794.187	$-116 \pm 2$
	54794.231	$-114 \pm 2$
	54794.328	$-113 \pm 2$
	54798.303	$-113 \pm 2$
	54836.146	$-78 \pm 3$
	54836.191	$-79 \pm 3$
	54867.058	$-61 \pm 3$
	55108.281	$-115 \pm 2$
VFTS 758	54794.187	$205 \pm 3$
	54794.231	$202 \pm 3$
	54794.328	$199 \pm 3$
	54798.303	$196 \pm 3$
	54836.146	$196 \pm 3$
	54836.191	$197 \pm 3$
	54867.058	$195 \pm 2$
	55108.281	$191 \pm 3$

Table 3.8: Orbital parameters of WN binaries.

Star	Schnurr et al. (2008b)		This work	
	$P$ [days]	$K$ [km s <sup>-1</sup> ]	$K^*$ [km s <sup>-1</sup> ]	$\sigma^*$ [km s <sup>-1</sup> ]
VFTS 402	$2.111 \pm 0.0018$	$107 \pm 3$	109	18
VFTS 509	$2.7595 \pm 0.00027$	$156 \pm 10$	298	68
VFTS 542	$4.699 \pm 0.010$	$125 \pm 15$	90	17

**Notes.** \*Values returned after adopting  $P$  from Schnurr et al. (2008b) and performing least-squares fit - see text for more details. All parameters are based on a circular orbit.

VFTS 002/BAT99-85/Brey 67 - is discussed separately in Section 3.5.1.

VFTS 019/BAT99-86/Brey 69 - Foellmi et al. (2003) had classified this star as WN 3o+O9: but noted no  $RV$  changes over their epochs. VFTS spectra also showed no  $RV$  variations and no absorption either, even in the Balmer lines (see Figure 3.10). This supported a single star system suggesting and that the absorption observed by Foellmi et al. (2003), perhaps arose

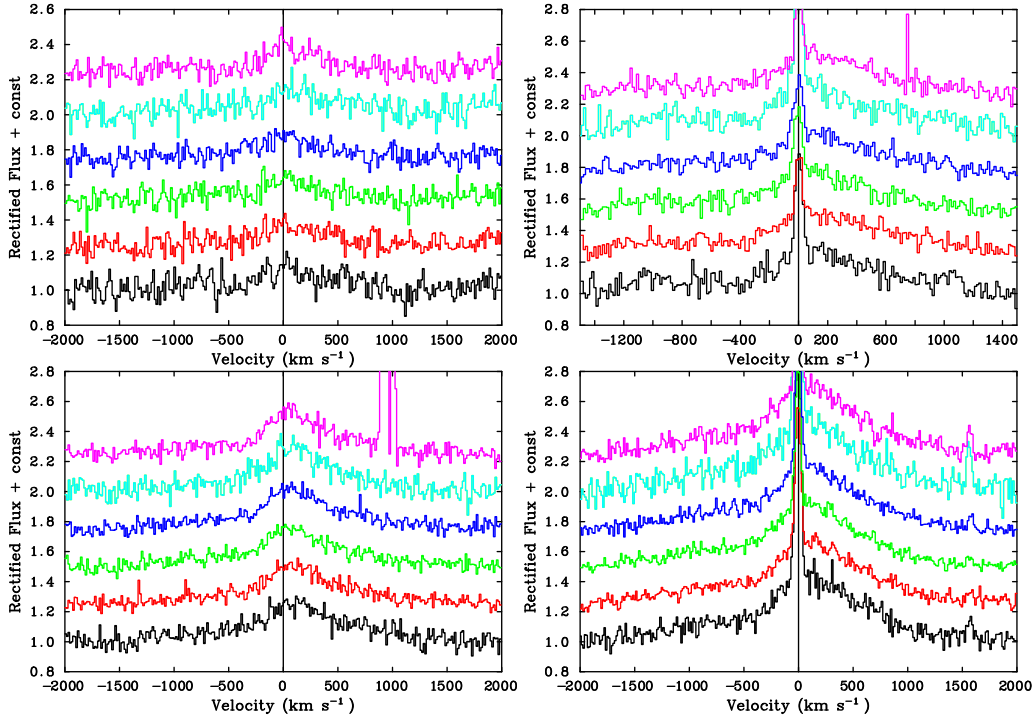


Figure 3.10: Spectral variations in VFTS 019 (WN 3(h)). Clockwise from top left, the spectral lines are: He II  $\lambda 4026$ , H $\delta$ , He II  $\lambda 4200$  and H $\gamma$ .

through bad sky subtraction.

VFTS 402/BAT99-95/Brey 80 - An OB companion was favoured following absorption at the red side of the Balmer lines along with reductions in the He II flux (Figure 3.11). The emission lines become stronger in the spectra as this dilution falls. A potential double peak in the N IV  $\lambda 4057$  line at one epoch might suggest the presence of an early O-type companion but is not consistent with other lines. Similarly, absorption noted in the He I  $\lambda 6678$  line is not found at other epochs so may relate to seeing issues.

Schnurr et al. (2008b) identified this star as a very close binary with a period of  $P = 2.111$  days. By adopting this period, the data was folded over a single phase and plotted in Figure 3.12. Assuming a circular orbit, a least squares fit of the sine function was then made to the points. The amplitude ( $K$ ) and standard deviation ( $\sigma$ ) of the resulting function is compared in Table 3.8 and is very consistent with the value derived by Schnurr et al. (2008b).

VFTS 507/BAT99-101+102/Brey 87 - Analysis of VFTS 507 is complicated as the data contains the spectra of two W-R stars. A similar blend was observed by Moffat et al. (1987) who first untangled the components. They identified three separate spectral features in the orig-

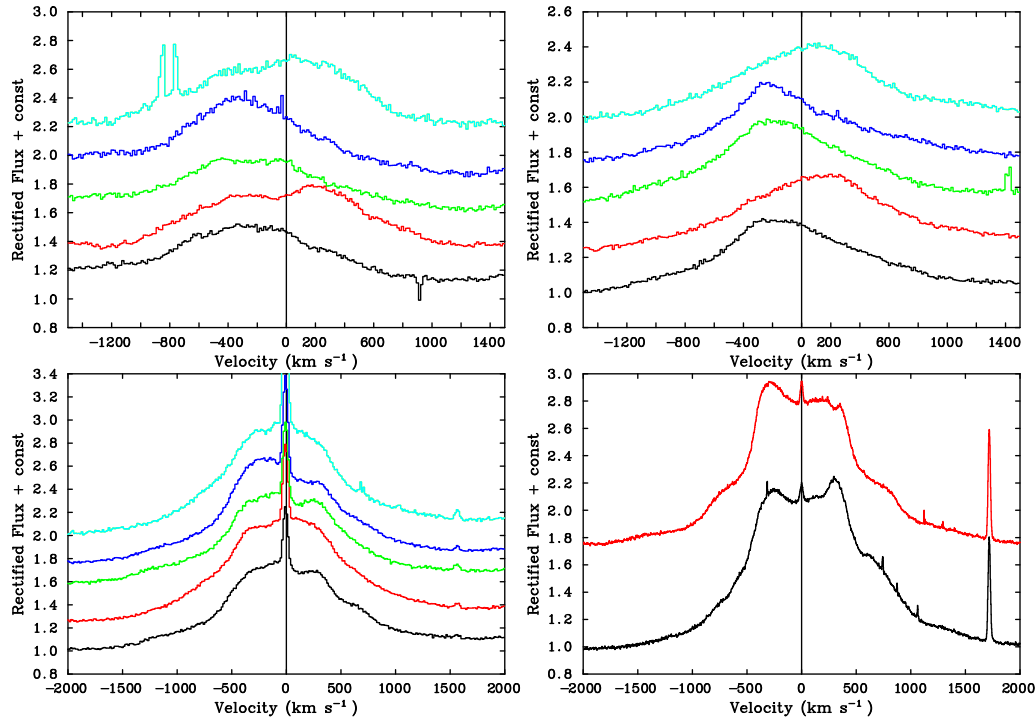


Figure 3.11: Spectral variations in VFTS 402 (WN 7h+OB). Clockwise from top left, the spectral lines are: N IV  $\lambda 4057$ , He II  $\lambda 4200$ , He I  $\lambda 6678$  and H $\gamma$ . Note that the He I  $\lambda 6678$  line was observed with the LR03 setting so was viewed at different epochs to the other lines.

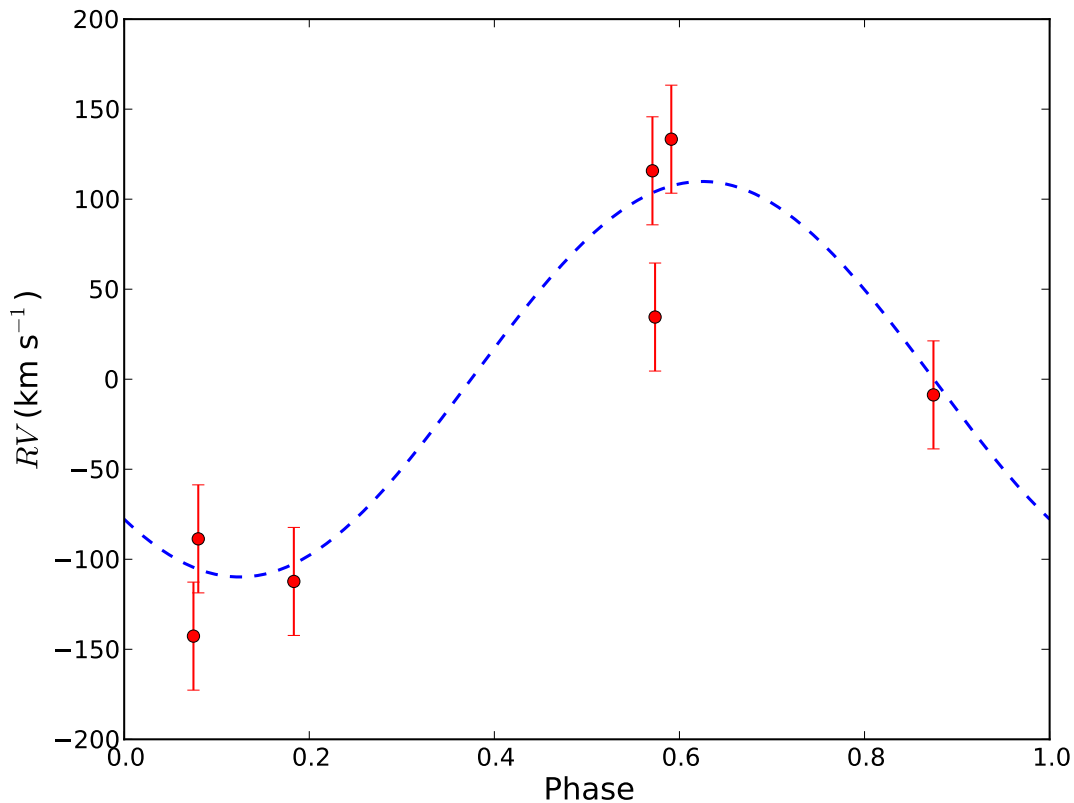


Figure 3.12: RV data for VFTS 402 folded with a period of 2.111 days (red circles) and fitted with a sine function (dashed blue line).

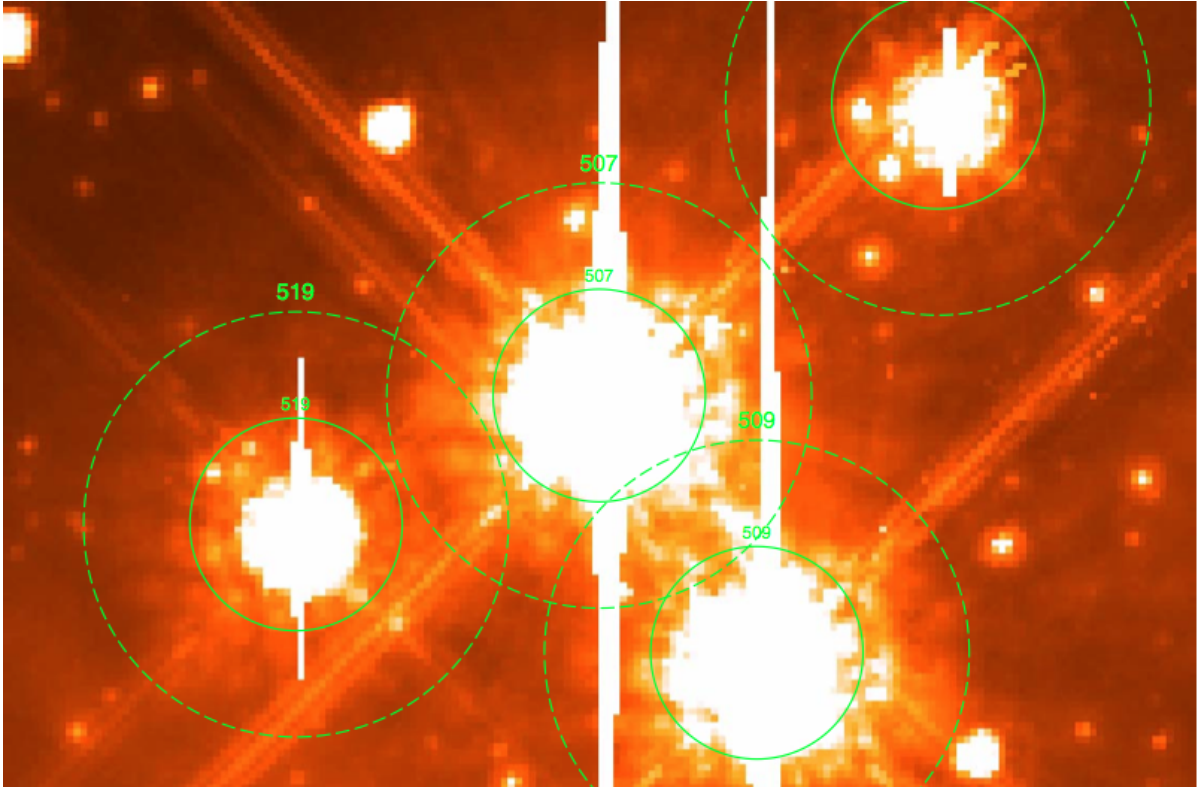


Figure 3.13: Postage stamp approximately  $6'' \times 4.5''$  showing crowding around VFTS 507 (S. E. de Mink - private communication). VFTS stars are labelled and surrounded by two circles: a solid line marks the aperture of the MEDUSA fibre ( $1.2''$ ) and a dashed line is twice this diameter. Overlaid on HST/WFC3 *I*-band image created by Sabbi et al. (2013). North is up and east is to the left.

inal R140 star. The first two were a WC (BAT99-101/R140a1) and WN (BAT99-102/R140a2) star, observed in VFTS 507 and another WN star (BAT99-103/R140b) which is observed in VFTS 509. R140a and R140b have since been separated with HST imaging as seen in Figure 3.13 but components R140a1 and R140a2, remain spatially unresolved.

Bartzakos et al. (2001) analysed R140a1, deeming there to be a WN+O visual component although did not rule out a long period binary. Meanwhile, Schnurr et al. (2008b) studied R140a2 and concluded it to be single. This was contrary to the work of Moffat et al. (1987) who found the star to be a binary with a 2.7595 day period. Coincidentally, this period was consistent with that found by Schnurr et al. (2008b) for R140b. Despite re-inspection of their's and Moffat et al's work, a confusion of stars was not apparent. Nevertheless, they do not rule out potential cross-contamination from the neighbouring R140b, whereby the same periodicity is observed in R140a2.

Returning to the VFTS data, no obvious *RV* changes were found. Some minor variations

in the strength of the Balmer lines might tentatively suggest absorption from a companion. It is hard to establish without deeper inspection, however, as this may have arisen through fluctuations in seeing or even inconsistent normalisation of the spectra .

VFTS 509/BAT99-103/Brey 87 - In the VFTS data, the binary nature is most pronounced in the He I absorption lines, which show a remarkably large  $RV$  shift between epochs (Figure 3.14). Similar absorption features are seen at consistent velocity shifts in the Balmer lines although are less apparent in the He II lines, suggesting a mid-late O-type companion. Such a massive companion is adhered to by similarly large  $RV$  shifts in the WN emission lines. However, further absorption is noted at each epoch in all of the lines discussed, only this time at the rest frame. This implies the presence of a further early O-type visual companion. As mentioned earlier, Schnurr et al. (2008b) had found BAT99-103 to be a 2.7595 day binary. Folding with this period and least squares fitting to the VFTS  $RV$  data gave Figure 3.15. On this occasion, the returned amplitude showed a large offset from that derived by Schnurr et al. (2008b). This has likely arisen from the large uncertainties in measuring  $RV$ , caused by the skewed line profiles at the different epochs.

VFTS 542/BAT99-113 - Figure 3.16 shows a notable  $RV$  shift that can be seen in all lines. It coincided with absorption in  $H\beta$  (also seen in  $H\gamma$ ) as well as in He II. However, minimal change to the He II lines suggested a late O or early B-type companion. Schnurr et al. (2008b) identified this star as a binary with an orbital period of 4.699 days. Using this value to fold the measured  $RV$  values as before, the least squares fit is shown in Figure 3.17. The amplitude agreed with the value derived by Schnurr et al. (2008b) within  $2\sigma$  to support their period.

VFTS 695/BAT99-119/Brey 90 - A binary nature was apparent from the  $RV$  variations of the VFTS data but details of the companion remained unclear. Figure 3.18 shows similar absorption features in the He I and He II lines. While this favours an O-type star, an absorption feature in the He I  $\lambda 4541$  line is also observed at a unique epoch. Except for minor fluctuations in  $H\delta$ , there is no coinciding absorption found in the Balmer lines. This would imply a H-deprived companion but with plenty of He, i.e. a He star, although such a scenario would be uncommon. The star had originally been claimed as a WN6(h)+O binary by Schnurr et al. (2009b) with respective masses potentially reaching  $300 M_{\odot}$  and  $125 M_{\odot}$ , depending on the inclination angle. However, subsequent observations with the Gemini Multi-Object Spectrograph (GMOS) portray a very different  $\sim 120 + 120 M_{\odot}$  binary system (O. Schnurr - private communication). Probing of the orbital parameters obtained in the Schnurr et al. (2009b) paper is therefore not carried out.

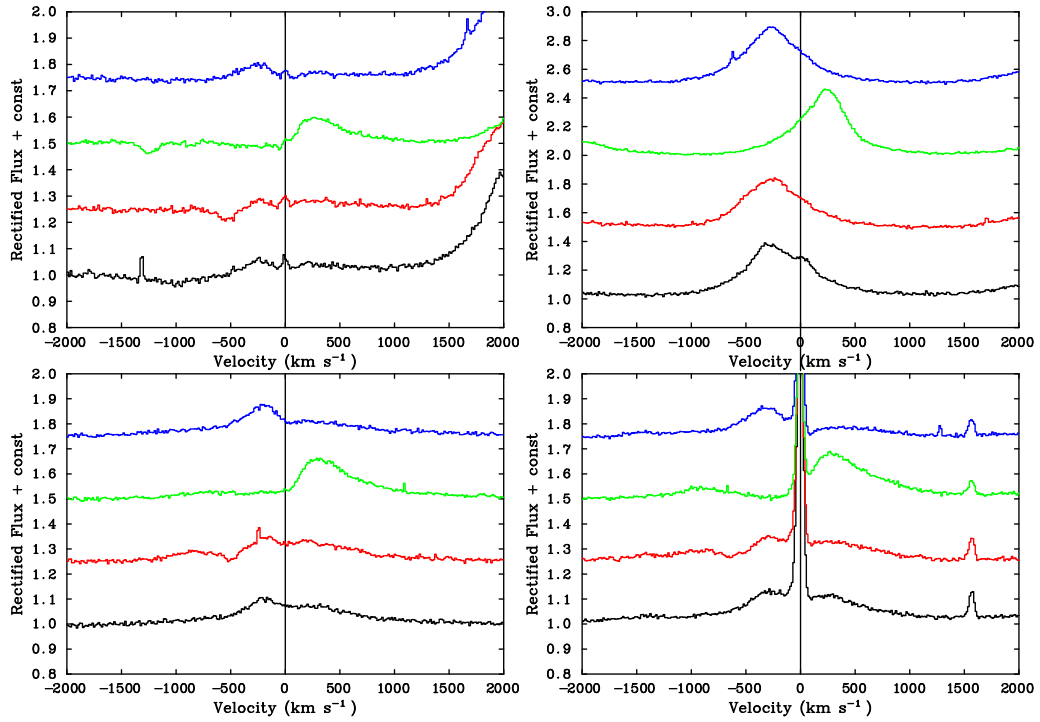


Figure 3.14: Spectral variations in VFTS 509 (WN 5(h)+O+(early O)). Clockwise from top left, the spectral lines are: He II  $\lambda 4026$ , N IV  $\lambda 4057$ , H $\gamma$  and He II  $\lambda 4200$ .

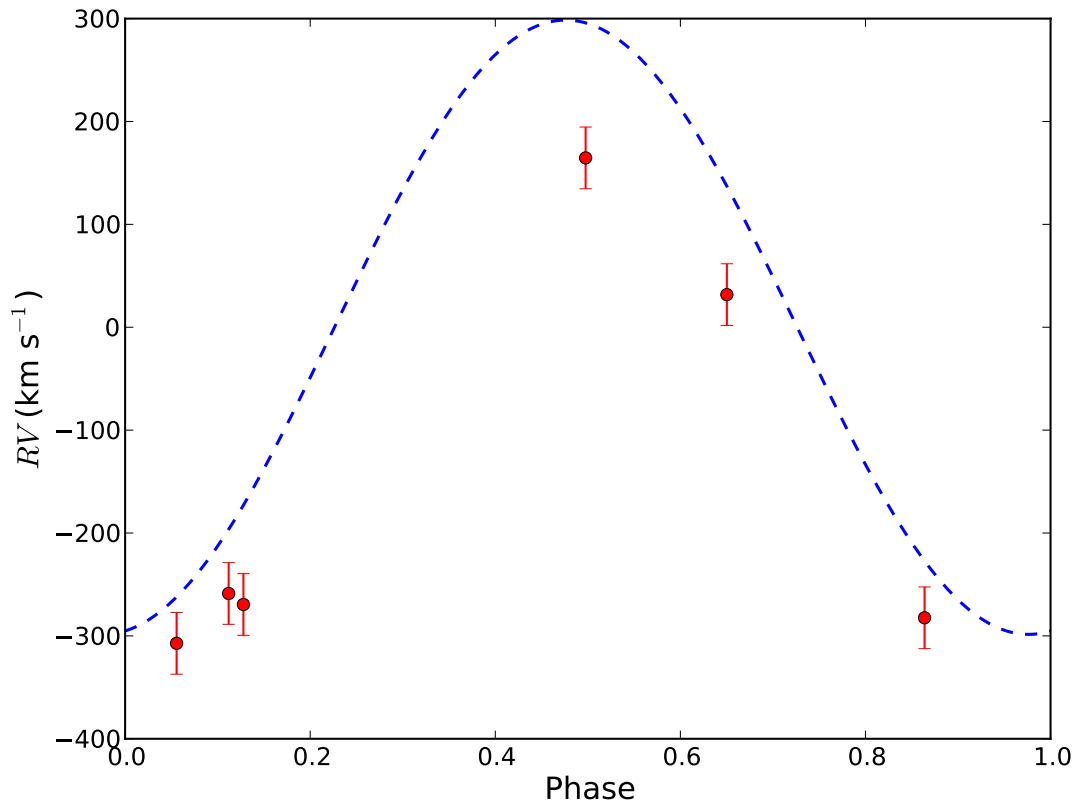


Figure 3.15:  $RV$  data for VFTS 509 folded with a period of 2.7595 days (red circles) and fitted with a sine function (dashed blue line).

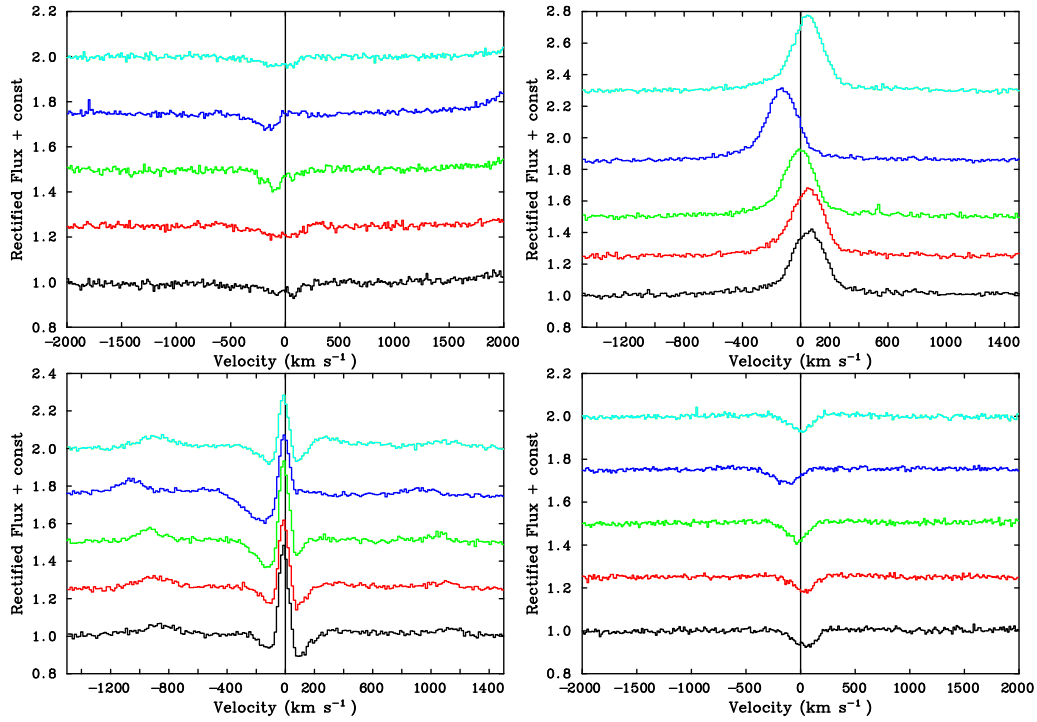


Figure 3.16: Spectral variations in VFTS 542 (O2 If\*/WN 5+late O/early B). Clockwise from top left, the spectral lines are: He II  $\lambda 4026$ , N IV  $\lambda 4057$ , He II  $\lambda 4200$  and H  $\delta$ .

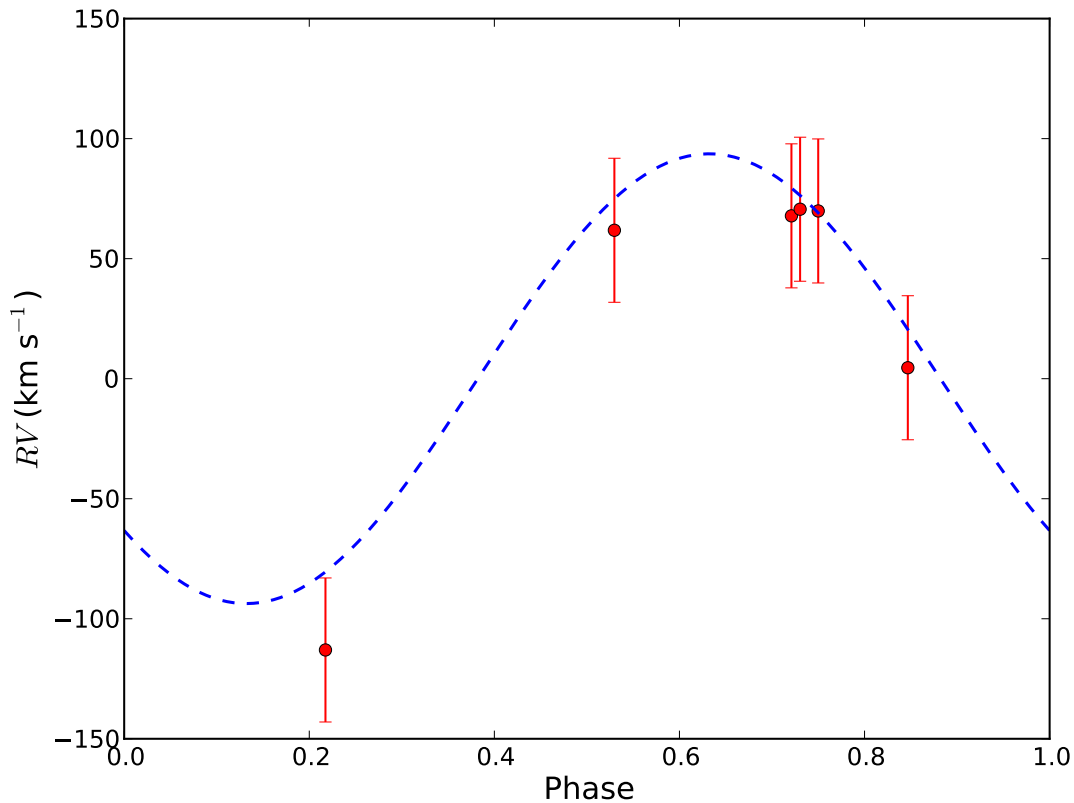


Figure 3.17: RV data for VFTS 542 folded with a period of 4.699 days (red circles) and fitted with a sine function (dashed blue line).

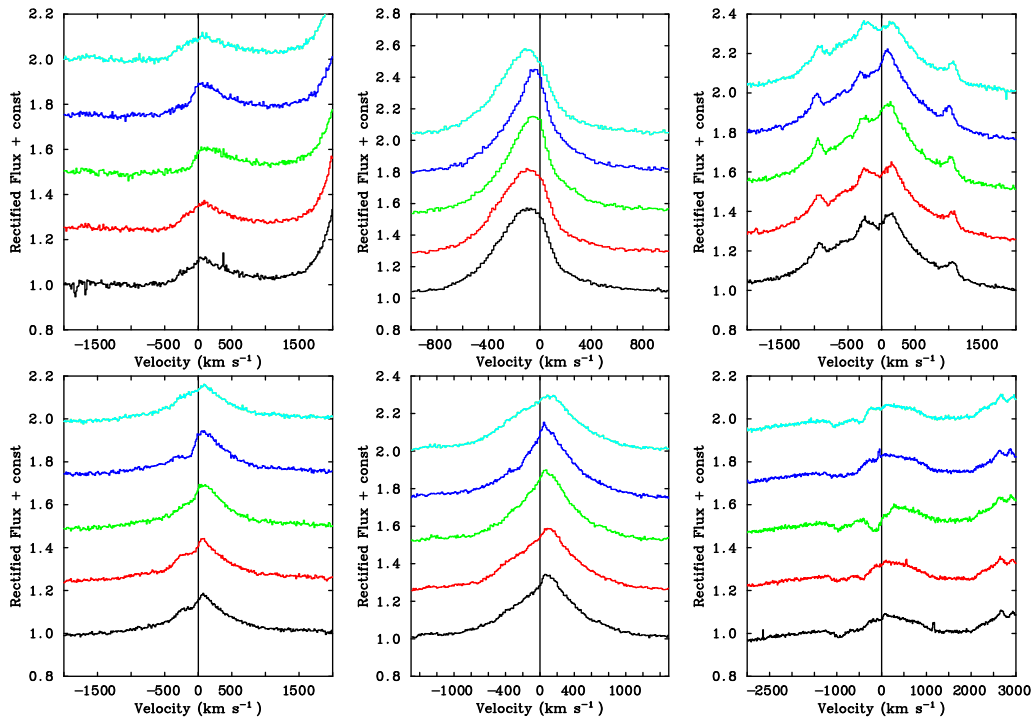


Figure 3.18: Spectral variations in VFTS 695 (WN 6h+?). Clockwise from top left, the spectral lines are: He II  $\lambda 4026$ , N IV  $\lambda 4057$ , H $\delta$ , He I  $\lambda 4471$ , H $\gamma$  and He II  $\lambda 4200$

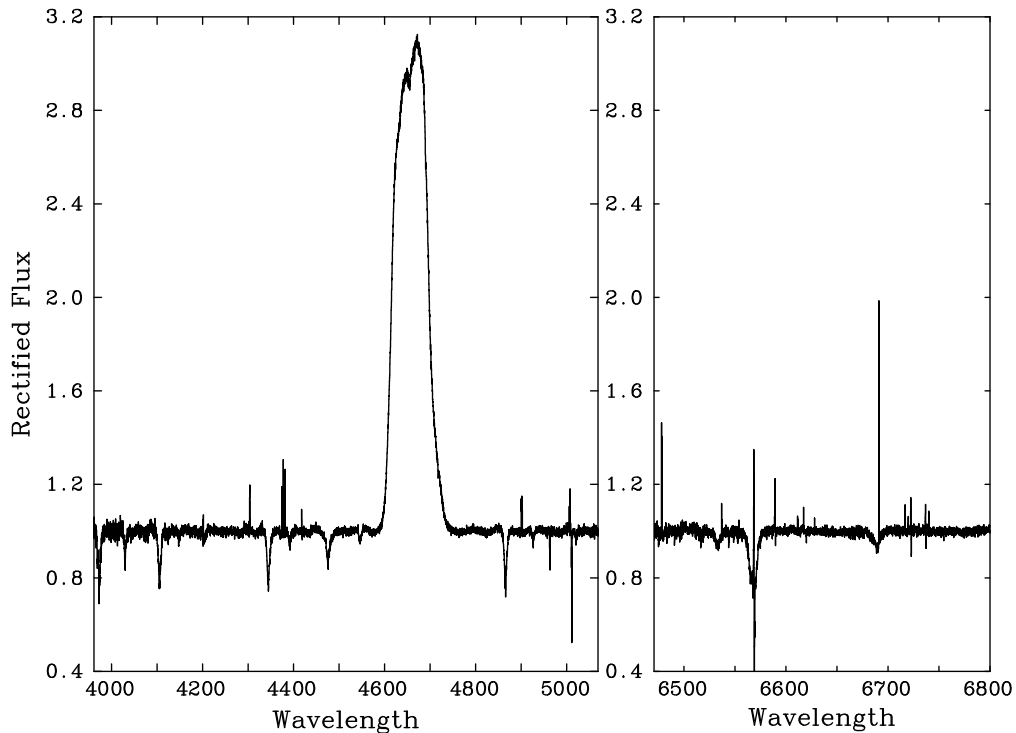


Figure 3.19: A spectrum of VFTS 002. The MEDUSA LR02 and LR03 spectra at the most consistent epoch have been merged and the HR15N spectrum attached separately.

## 3.5 Special Cases

### 3.5.1 Spectral variations in VFTS 002

Figure 3.19 shows the spectrum of VFTS 002. From the LR02 and HR15N spectral ranges, He and Balmer absorption lines indicated the presence of an O-type star. It was only from the broad C III  $\lambda 4650$  line that the WC component became evident. Classification of the companion favoured a O6-6.5 III star. This was based on the ratio  $\text{He II } \lambda 4541 / \text{He I } \lambda 4471 > 1$ , which would have had a value of unity at subtype O7. This was also supported as  $\log[W(\text{He I } \lambda 4471) / W(\text{He II } \lambda 4541)] \approx -0.2$ , (Mathys 1988). The luminosity class was determined from  $\log[W(\text{He I } \lambda 4143) / W(\text{Si IV } \lambda 4116)] \approx +0.27$ , which favoured a giant star by the criteria in Conti & Alschuler (1971).

Bartzakos et al. (2001) had previously studied VFTS 002 and determined it to be a visual binary but were unable to rule out a long period or eccentric orbit. Meanwhile, from the VFTS spectra, both components appeared to have time variations in their spectral lines (Figure

3.20a). Figure 3.20b shows a dramatic change in  $W(\text{C III } \lambda 4650)$  with values varying by up to a factor of two. This could be linked to an eclipsing binary scenario whereby when the O-type star eclipses the WC star (but not its extensive wind, responsible for the emission line) and the continuum level of the system falls and so  $W(\text{C III } \lambda 4650)$  rises. However, things are complicated as these variations take place on an extremely short timescale, the LR03 spectra spanning less than seven hours and the greatest change occurs within 48 minutes.

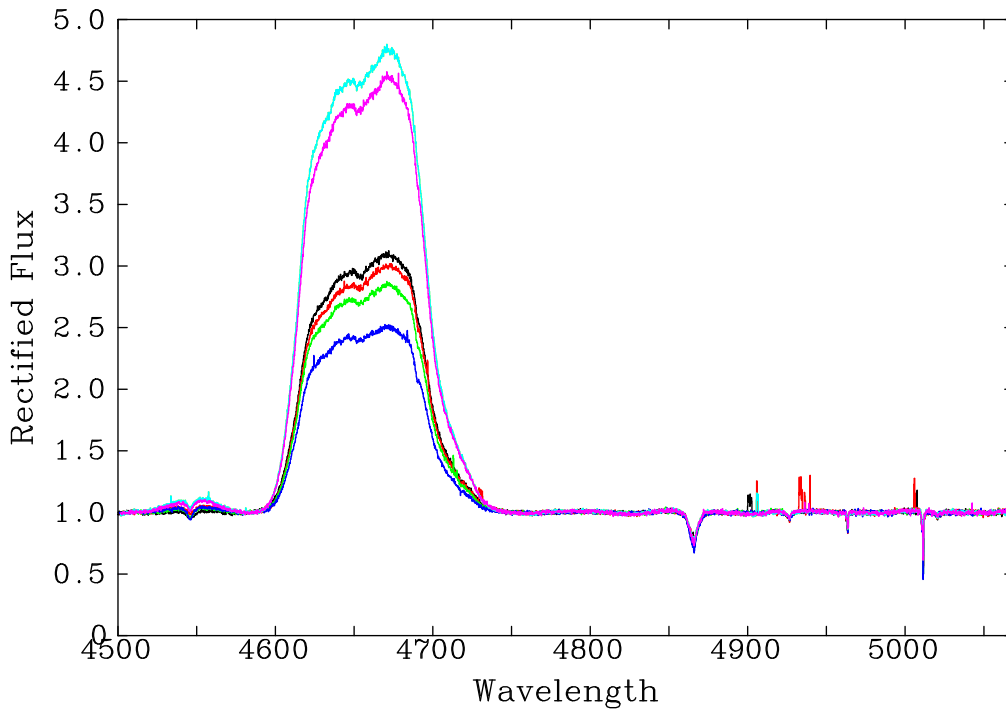
The accompanying  $\text{H}\beta$  line in the LR03 spectra showed a relatively constant  $RV$  during the changes in  $W(\text{C III } \lambda 4650)$ . While the LR02 and LR03 spectra were obtained at different epochs, they were often subsequent to one another allowing the common  $\text{He II } \lambda 4541$  line to be compared in both data sets. All the measured radial velocities were similar within uncertainties and consistent with the mean radial velocity. This did not favour an orbiting binary scenario and so required an alternative, non-intrinsic explanation to produce such large changes in  $W(\text{C III } \lambda 4650)$  on a short time scale.

An initial inspection of the sky spectra showed them to be unchanging and indicate that the observed effects were not brought about during the sky subtraction. However, the seeing conditions during the course of the observations, recorded by the Differential Image Motion Monitor (DIMM), did fluctuate and in worse conditions would have led to contamination from both the companion as well as another bright neighbouring BN0.7 Ib star, VFTS 003<sup>3</sup>. Figure 3.22a is an image from the VLT-Focal Reducer and low dispersion Spectrograph (VLT/FORS) showing the small separation ( $\sim 3''$ ) between VFTS 002 and VFTS 003. Assuming the blend of sources at VFTS 002 comes from the two unresolved components (separated by  $< 1''$ ), each one could be identified by investigating how levels of contamination varied.

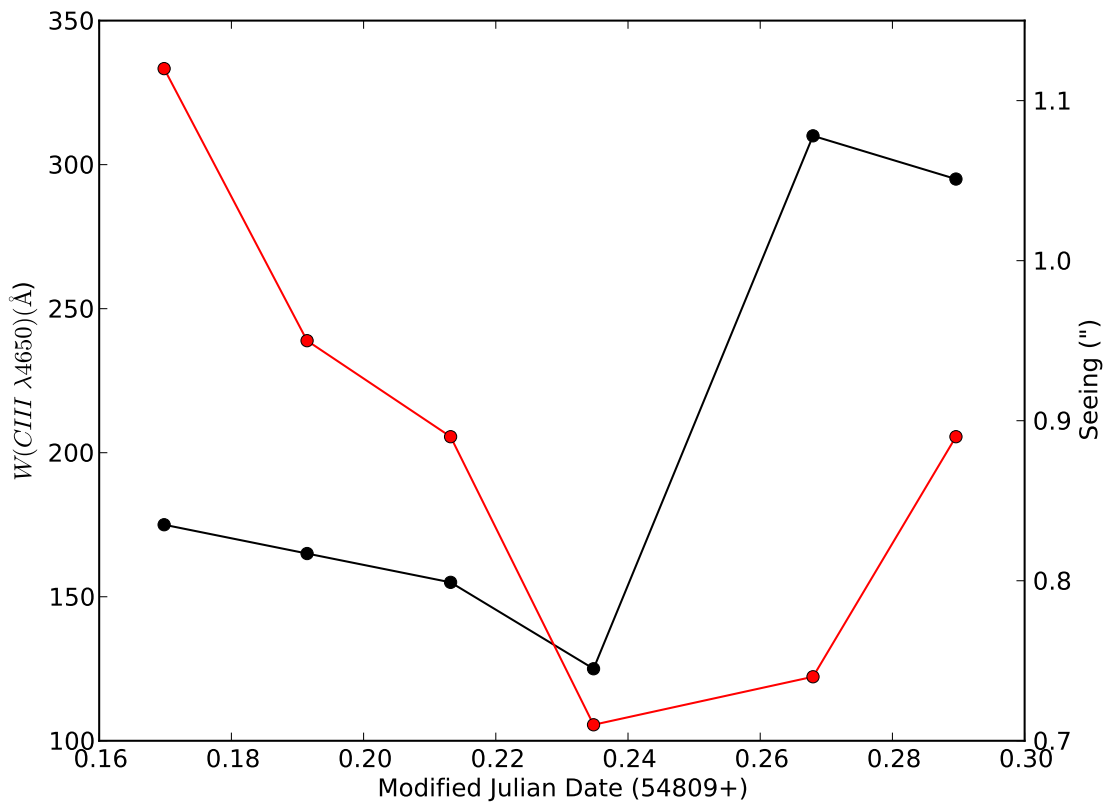
The MEDUSA fibres have a  $1.2''$  field of view on the sky so contamination from the companion O-star would be unavoidable. This is evident as  $W(\text{C III } \lambda 4650) \sim 300 \text{ \AA}$  when observed at maximum, yet intrinsically it would be expected to be  $W(\text{C III } \lambda 4650)_0 \sim 1200 \text{ \AA}$ , indicating a high level of dilution by the companion. During bad seeing, even the nearby VFTS 003 would have an effect as is produced in Figure 3.21b. An asymmetric profile can be seen in the  $\text{H}\alpha$  and  $\text{He II}$  lines, brought about by contamination from VFTS 003 as seeing declined.

The variation of  $W(\text{C III } \lambda 4650)$  and seeing with epoch is plotted in Figure 3.20b. By the dilution process,  $W(\text{C III } \lambda 4650)$  would be expected to rise as seeing improved, assuming the fibre was accurately centred on the WC star. The opposite would be expected if the O-star had been centred upon. Both of these dilution effects appear to be at work, however, they

<sup>3</sup>As multiple MEDUSA fibres were positioned on the sky at each epoch, the flux from bright sources had the potential of “spilling” into adjacent fibres even if they were spatially separated by a large distance; so called cross-contamination. This was not possible in the case of VFTS 002 and 003 as they were observed on different nights but the process needed to be considered for other targets.



(a)



(b)

Figure 3.20: Variations of  $W(\text{C III } \lambda 4650)$  in VFTS 002. Figure (a) shows the LR03 spectra with different epochs plotted in a separate colour. Figure (b) plots the changes in  $W(\text{C III } \lambda 4650)$  (black) and seeing conditions (red) with to time.

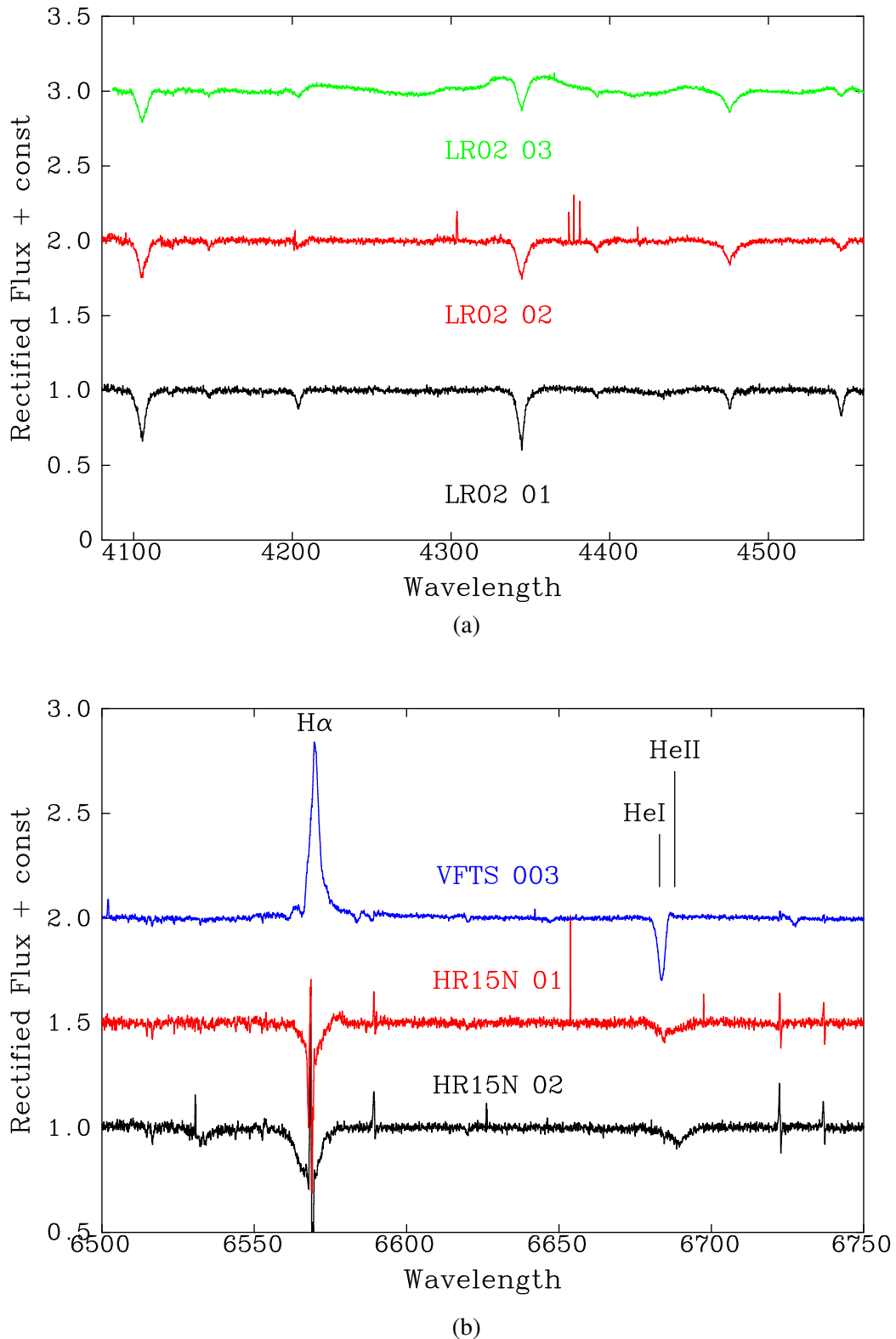


Figure 3.21: Contamination of VFTS 002. Figure (a) shows the LR02 spectra with different epochs plotted in separate colours. Figure (b) shows the HR15N spectra at two separate epochs (black & red). The spectrum of VFTS 003 is plotted above for comparison.

occur between different observing blocks. To understand this switch in relation, details of the telescope positioning must be introduced.

The observing logbook noted a  $\sim 50$  min interruption to observations due to clouds, following the LR03 02 o.b. This forced a reacquisition of the target when observing resumed for the LR03 03 o.b. While seeing had not changed drastically despite the cloud coverage, the telescope had centred on a new position,  $\sim 0.4''$  from the previous one, as shown in Figure 3.22b. This shift toward VFTS 002 would have reduced flux from VFTS 003 from entering the fibre and hence lowered contamination. A similar effect was seen under the LR02 setting (see Figure 3.21a). Prominent absorption lines from the O-star coincide when the telescope was positioned further south and slightly diluted (by VFTS 003) when shifted to the east. They are diluted further still when shifted north as the continuum of the WC star becomes evident. This also allows the two components to be identified, with the WC star being the fainter, more northerly, of the two.

These shifts in telescope positions would actually have affected *all* VFTS targets observed during the same MEDUSA observing block and so was something to bear in mind when examining other spectra. As a result, even non-WR stars could suffer from contamination from a neighbouring star

### 3.5.2 VFTS 147

VFTS 147 represents a similar case where observed spectra in a crowded region are affected by the seeing conditions. The W-R star was originally classified WN 4,5+OB and was catalogued as Brey 73 by Breysacher (1981), but not without evidence of a composite nature. Testor et al. (1988) later revealed 12 components to the system while Walborn et al. (1995) split the brightest sources further still (1A, 1B & 1C, see Figure 3.23a). These were later observed with HST/FOS with the W-R star, 1A, being classified as WN 6.5h, while 1B was a O7 V and 1C a O9.5-B1pe (Walborn et al. 1999).

The VFTS data delivered a similar classification of WN 6(h) for the W-R star but some variations in the  $W_\lambda$  were noted. Figure 3.23b shows the most extreme change observed at different epochs, where the spectrum plotted in red shows a fall in the  $W(\text{N IV } \lambda 4057)$  and  $W(\text{He II } \lambda 4200)$ , while the  $\text{H}\gamma$  and  $\text{H}\delta$  lines suffer from absorption. As this spectrum coincides with poorer seeing, the absorption is likely to come from the neighbouring O-stars which will also contribute to the overall continuum level.

On comparison to the spectrum observed by Walborn et al. (1999) plotted with a dotted line, could this contamination affect the final classification of the W-R star? Non-integer subtypes were not offered by the Smith et al. (1996) classification criteria but access to the He II

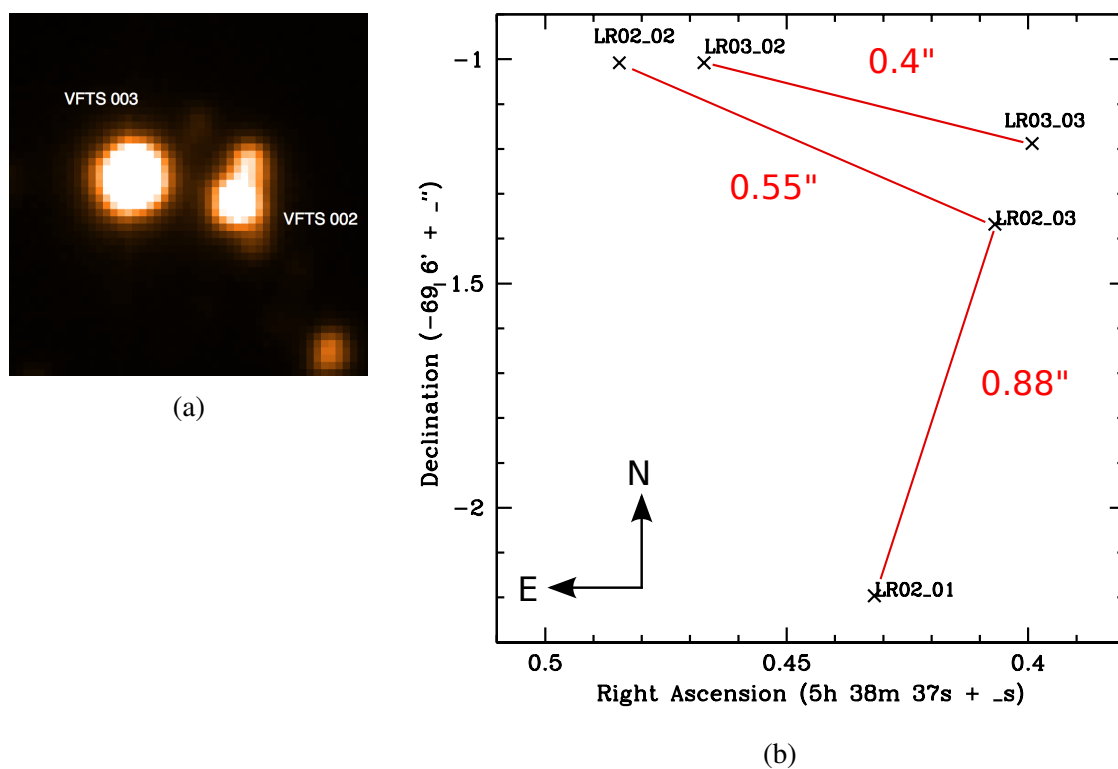


Figure 3.22: Figure (a) gives a  $10 \times 10''$  VLT/FORS V-band image of VFTS 002 and 003. Figure (b) shows the relative MEDUSA fibre pointings at different epochs. North is up and east is to the left in both figures.

$\lambda 5411$  and  $\text{He I } \lambda 5875$  lines may have favoured a later subtype. Even during good seeing conditions, the derived H content could have been affected by contamination from the nearby O-stars, recalling that the MEDUSA fibres cover a  $1.2''$  field of view.

### 3.5.3 VFTS 682

The VFTS also observed a previously unknown W-R star, VFTS 682. Due to its faint appearance ( $m_V = 16.08$  mag), the multiple-epoch spectra were co-added to produce the spectrum shown in Figure 3.2 and following the criteria discussed in Section 3.3, it was classified as a WN5h star. Separate to the stellar model used to produce the  $RV$  values in Section 3.4.1, Bestenlehner et al. (2011) produced a more comprehensive model of VFTS 682 with the CM-FGEN code. Favouring a reddening parameter of  $R_V = 4.7$ , they derived the luminosity of VFTS 682 as  $\log L/L_\odot = 6.5 \pm 0.2$ . In turn, this has led to mass estimates  $\sim 150 M_\odot$ , being both physically and spectroscopically comparable to the core star R136a3 (Bestenlehner et al. submitted).

With VFTS 682 located  $\sim 30$  pc north east of R136 and the VFTS data showing no obvious sign of binary nature, this poses the question as to whether the star formed “in situ” or was ejected from a previous star forming region i.e. R136. Simulations by Banerjee et al. (2012) would suggest the ejection of such a massive star from R136 is very plausible. While values of its  $RV$  may indicate a small offset from the mean 30 Dor velocity, only knowledge of the star’s tangential velocity will help reveal its origin.

## 3.6 The Significance of the VFTS on Emission Line Stars in 30 Doradus

Within the Breysacher et al. (1999) catalogue, 25 stars are listed to be located in the OB association LH 100 - corresponding to 30 Dor. The VFTS includes 12 stars from this list ( $\approx 50\%$ ), as well as revealing the previously unidentified WN5h star VFTS 682. A number of the remaining stars have undergone previous spectral modelling, including the four core R136 WN5 stars (Crowther et al. 2010). However, some of the most luminous WN stars such as BAT99-118/Brey 89 were omitted from the VFTS, and their inclusion would be important when considering the global impact of emission line stars. Chapter 5 makes a quantitative discussion on these contributions.

Unfortunately, as already seen in the classification process, the VFTS data was not ideally suited for W-R stars analysis. Primary diagnostic lines were observed for WN stars but WC

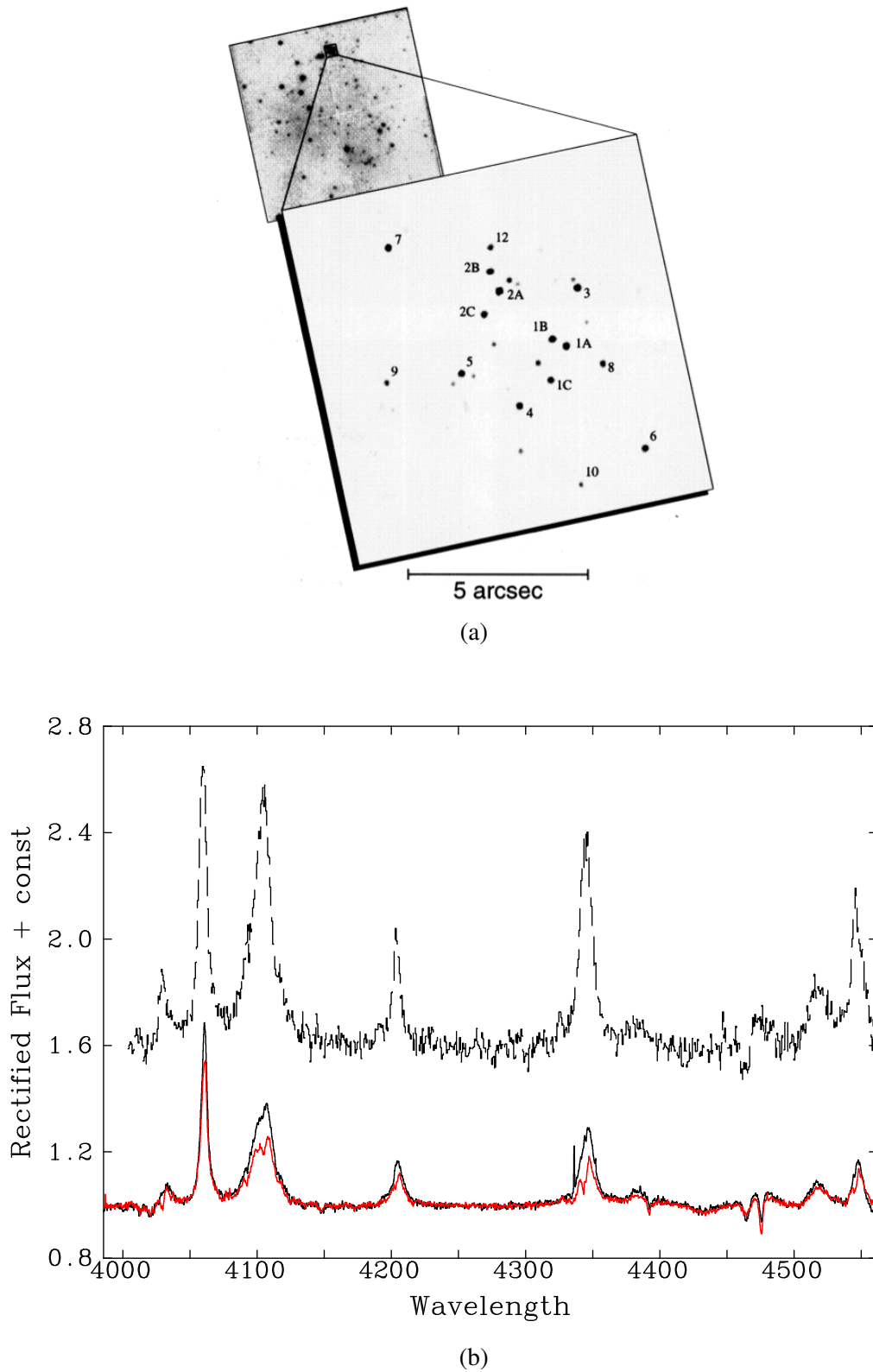


Figure 3.23: Figure (a) is a HST/WFC image of VFTS 147 and its surrounding cluster taken from Walborn et al. (1995). North is up and East is to the left. Figure (b) shows the LR02 spectra of VFTS 147 at two separate epochs (black & red solid lines). The HST/FORS spectra from Walborn et al. (1999) is plotted above with a dotted line for comparison.

stars lacked coverage of important lines in the yellow to far-red spectrum. Spectral analysis is still possible thanks to supplementary spectra from previous studies, completing the necessary wavelengths. The VFTS provided supplementary photometry in the Johnson *B*- and *V*-bands as well as the *JHK* bands. However, these broad band filters have been found to overestimate the continuum levels of W-R stars by up to 1 mag due to contamination from their wide emission lines (Crowther 2007). Smith (1968) therefore introduced equivalent *ubv* narrow band filters. A comparison of the wavelength coverage between the broad and narrow band filters, and the emission lines they include, is shown in Figure 3.24. Magnitudes from these narrow-band filters are favoured to give an accurate brightness of the W-R stars and can be obtained for the VFTS sample. The following section discusses how they are combined with spectra to form a basis for estimating physical properties.

## 3.7 Properties of Emission Line Stars

Having assessed line variation and binarity in the VFTS sample, this section turns to the stellar properties of the emission line stars and further extending the study to non-VFTS emission line stars in 30 Dor. By doing so they can be related to the nebular properties of 30 Dor in a similar method to the single star H II regions discussed in Chapter 2. Of course, this would also need to account for the numerous OB stars in the region which are addressed in a global census of 30 Dor in Chapter 4. Nevertheless, earlier studies have found W-R stars to make notable contributions to the stellar feedback of the region (Crowther & Dessart 1998) and determining accurate stellar properties is important for constraining this fraction. A total of 25 W-R and 6 Of/WN stars are identified within a 10 arcmin radius of the centre of R136<sup>4</sup>.

### 3.7.1 Photometry of W-R stars

As noted in Section 3.6 using Johnson broad-band filters with W-R stars can lead to a false reading of the stellar continuum and overestimate their magnitudes. A more reliable measurement is obtained through narrow-band filters (Smith 1968). For all W-R stars<sup>5</sup>, narrow-band *b* & *v* magnitudes were used to obtain their absolute magnitudes and are listed in Table 3.9.

For most stars these values were adopted from the photometric work of Crowther & Hadfield (2006), Schmutz & Vacca (1991), and Torres-Dodgen & Massey (1988). Others were

<sup>4</sup>Note that VFTS 002 lies just beyond this boundary and is not included in the subsequent modelling or the census of Chapter 4.

<sup>5</sup>Broad band magnitudes were still used for the Of/WN stars as contamination from their emission lines would be limited.

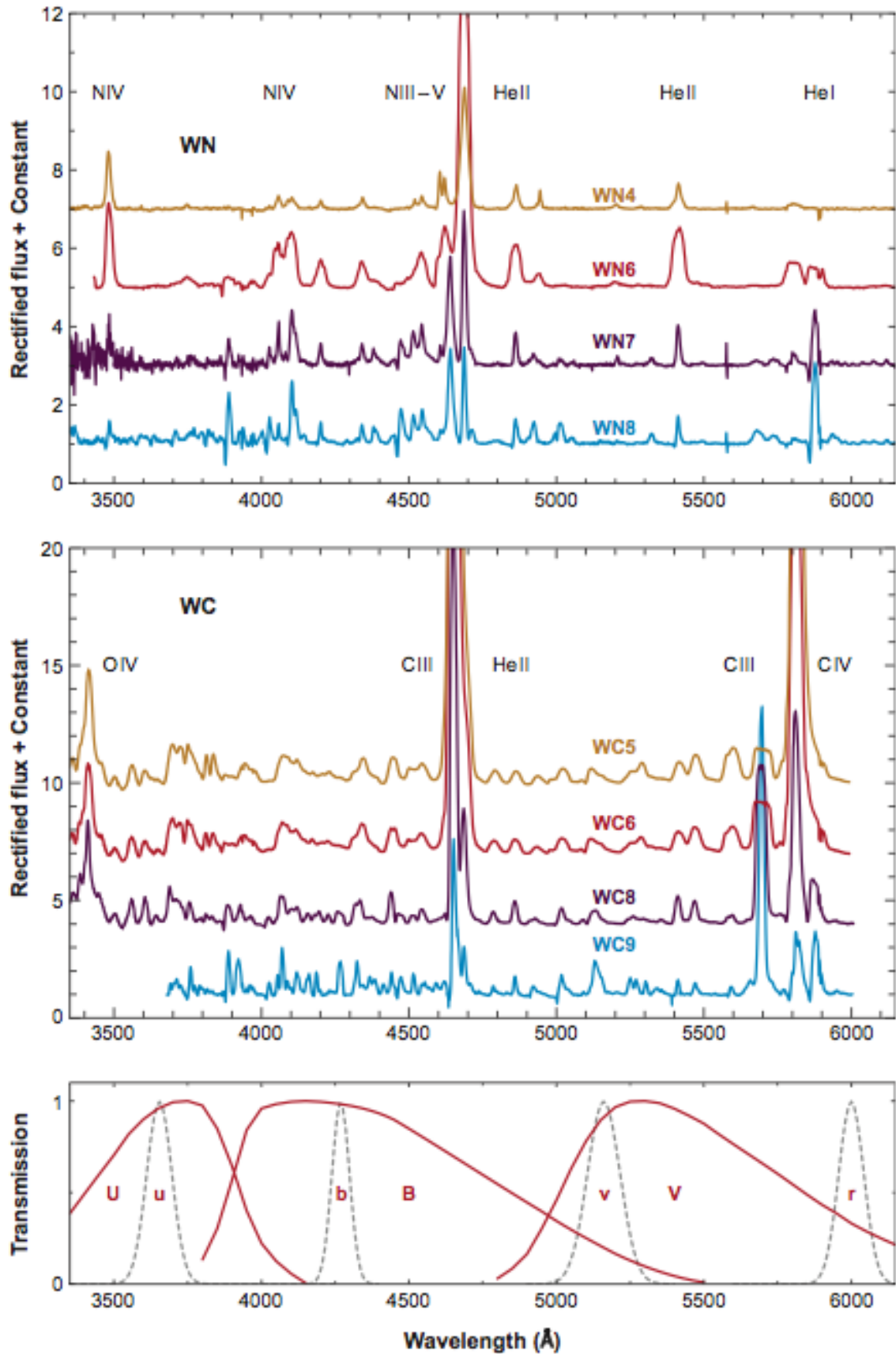


Figure 3.24: Wavelength coverage of the Johnson *UBV* broad-band filters and the Smith (1968) *ubv* and Massey (1984) *r* narrow-band filters. A spectral montage of WN and WC stars and their key emission lines is given for comparison. Taken from Crowther (2007).

obtained from spectrophotometry carried out through the narrow-band filters on the spectra obtained by Crowther & Smith (1997) and the HST/FOS observations of Walborn et al. (1999) de Koter et al. (1997) and Massey & Hunter (1998).

In a few exceptions, photometric assumptions were made about the star (magnitudes in *italic* in Table 3.9). In some cases, the magnitude offsets ( $\Delta m_b = m_b - m_B$  and  $\Delta m_v = m_v - m_V$ ) found by Breysacher (1986) were adopted and applied to contemporary broad-band photometry to achieve estimates of the narrow-band magnitudes. This approach was applied to the combined R140a (BAT99-101+102) system as neither broad or narrow-band photometry could separate the contributions of the two stars. These magnitude offsets would also be expected to be similar for stars which had a close spectroscopic resemblance. The same is the case for  $b - v$  unless the reddening of the stars was different. A  $b - v$  colour could therefore be estimated by comparing the respective  $B - V$  colour of the stars. For example, BAT99-116 had broad-band photometry  $m_V = 13.09$  mag and  $B - V = 0.25$  mag from De Marchi et al. (2011). It is spectroscopically very similar to BAT99-112 which has  $B - V = 0.16$  mag,  $b - v = 0.05$  mag and  $b - B = 0.10$  mag. The narrow-band colour of BAT99-116 is therefore estimated at  $b - v = 0.14$  mag while the magnitude offset suggests  $b = 13.24$  mag and hence  $v = 13.10$  mag.

Intrinsic colours of all WN stars used the  $(b - v)_0 - W_\lambda(4686)$  relation from Crowther & Hadfield (2006):

$$(b - v)_0 = -0.32 + 0.000476 W_\lambda(4686) - 4.2 \times 10^{-7} W_\lambda^2(4686) \text{ [mag]}, \quad (3.3)$$

where  $W_\lambda(4686)$  is the equivalent width of the He II  $\lambda 4686$  line in Å.  $W_\lambda(4686)$  was either measured from the available spectroscopy or adopted from the measurements made by Schnurr et al. (2008b), see references in Table 3.10. In the case of WC stars,  $(b - v)_0$  was adopted from Crowther & Hadfield (2006) if available, otherwise an average value of  $(b - v)_0 = -0.28$  was applied to single WC stars and  $(b - v)_0 = -0.32$  to WC binaries where an O-type star dominated the light.

Interstellar extinction was based on an assumed  $R_V = 4.2$  for stars within R136 or  $R_V = 3.5$  for stars beyond (see Section 4.3 for derivations). Their equivalent narrow-band  $R_v$  values were required to match the photometry of the W-R stars. These were derived using Equation 24 of Schmutz & Vacca (1991) to give  $R_v = 5.4$  and  $R_v = 4.6$  for the respective regions. The corresponding extinctions ( $A_v$ ) and absolute magnitudes for each system ( $M_v^{\text{sys}}$ ) are listed in Table 3.9.

### 3.7.2 W-R binaries

In cases of W-R stars known to be multiple,  $M_v^{\text{sys}}$  was also accounting for the light from a companion star with magnitude  $M_v^{\text{OB}}$ . It therefore needed to be scaled to the desired W-R magnitude ( $M_v^{\text{W-R}}$ ) before stellar properties were calculated. This was achieved by measuring the dilution of different emission lines in the spectra. In a binary, the  $W_\lambda$  of a line would fall as it is diluted by the additional continuum flux of the companion. This reduction in  $W_\lambda$  relates to the ratio of the continuum fluxes of the two stars, and in turn gives the difference in their apparent magnitudes.

This is demonstrated in Figure 3.25 which takes the spectrum of the W-R binary VFTS 002 classified earlier as WC 4+(O6-6.5 III). It is compared to VFTS 136, a WC 4 star believed to be single and a template O6 star spectrum. It is clear that a large fraction of the continuum light of VFTS 002 is due to the companion. By co-adding the fluxes of VFTS 136 and the O-type star and taking the contribution of the companion to be  $\approx 93\%$ , a spectrum of VFTS 002 can be approximately reproduced. An O:WC flux ratio of 15.2:1 would correspond to a difference in magnitude of  $\Delta M_v \sim 2.96$  mag following the relation:

$$\Delta M_v = M_v^{\text{W-R}} - M_v^{\text{OB}} = -2.5 \log(F_v^{\text{W-R}}/F_v^{\text{OB}}). \quad (3.4)$$

Thus, for VFTS 002 where  $M_v^{\text{sys}} = 11.71$  mag, the individual components are calculated to be  $M_v^{\text{W-R}} = 14.71$  mag and  $M_v^{\text{OB}} = 11.78$  mag.

For a single undiluted WN 6 star, the strength of the He II  $\lambda 4686$  line was taken to be  $W_\lambda(4686) \approx 75 \text{ \AA}$  (Crowther & Smith 1997). Similarly, for a single undiluted WC 4-5 star, the strength of the C IV  $\lambda 5808$  line was assumed to be  $W_\lambda(5808) \approx 1400 \text{ \AA}$  (Crowther & Hadfield 2006). However, C IV  $\lambda 5808$  was not accessible in the spectra of some WC stars in which case the level of dilution was measured using the C IV  $\lambda 4650$  line. Its undiluted equivalent width was taken to be  $W_\lambda(4650) \approx 1200 \text{ \AA}$ , based on the BAT99-90 spectra. In the case of a binary WN/C star (BAT99-92), comparisons were made to the other single WN/C star (BAT99-88) for which  $W_\lambda(4686) = 225 \text{ \AA}$  and  $W_\lambda(5808) = 1600 \text{ \AA}$ .

The necessary magnitude corrections ( $\Delta M_v$ ) for the W-R multiple systems, are given in Table 3.10. This method assumes that extinction is the same when comparing  $W_\lambda$  between different stars and it can be seen that  $W_\lambda(4686)$ ,  $W_\lambda(5808)$  and  $W_\lambda(4650)$  can fluctuate from the chosen undiluted values, even for stars believed to be single. While dilution from a companion cannot be ruled out, magnitude corrections are only applied to known binary systems.

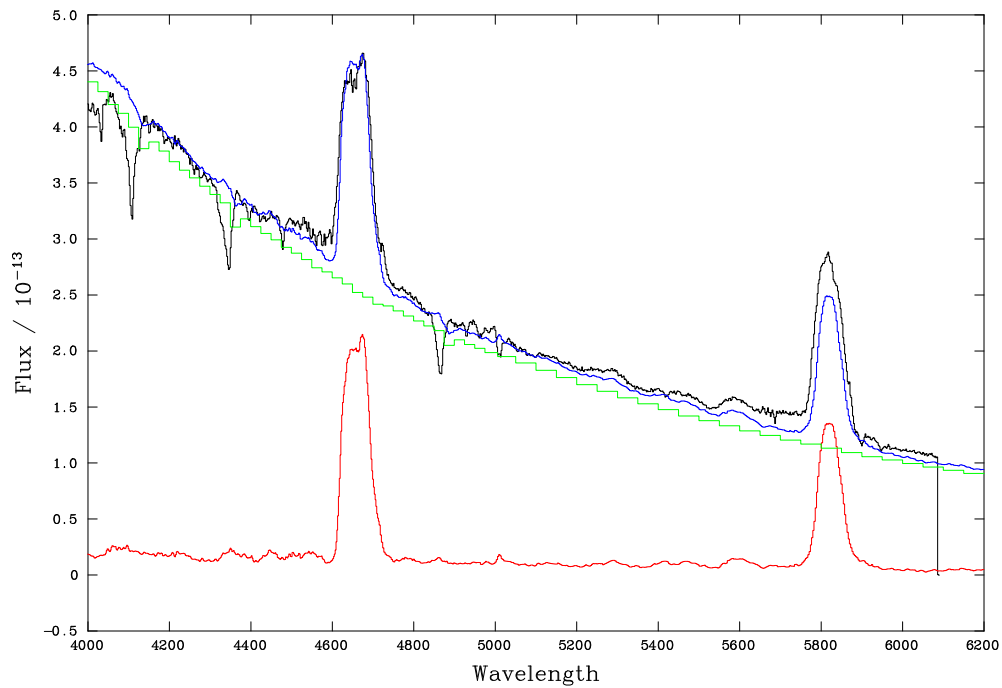


Figure 3.25: The dilution of the W-R spectrum in a binary system. The spectra of VFTS 002, a binary (WC 4+O6-6.5 III) star, is plotted in black, VFTS 136 a single WC 4 star is in red and a template companion O-type star spectrum is in green. The blue line is a combination of VFTS 136 and the O-type star spectra. Note that the stellar spectra in this plot are flux calibrated data from Crowther et al. (2002), not VFTS data.

Table 3.9: The photometric properties of all the W-R stars in 30 Dor. Values in *italic* indicate where magnitudes or colours have been assumed.

ID <sup>†</sup>	BAT99	Star	Spectral	Ref.	$m_v$	$b - v$	Ref.	$(b - v)_0$	$R_v$	$A_v$	$M_v^{\text{SYS}}$
#	VFTS	Alias	Type		[mag]	[mag]		[mag]		[mag]	[mag]
24	86	Br 69	WN 3(h)	(1)	16.68	0.11	(11)	-0.27	4.6	1.7	-3.6
92	88	Br 70a	WN 4b/WCE	(2)	17.75	0.46	(12)	-0.23	4.6	3.2	-3.9
117	89	Br 71	WN 7h	(3)	14.13	0.22	(3)	-0.28	4.6	2.3	-6.7
144	90	Br 74	WC 4	(4)	15.42	0.12	(12)	-0.16	4.6	1.3	-4.4
155	91	Br 73-1A	WN 6(h)	(1)	14.98	0.15	(13)	-0.30	4.6	2.1	-5.6
185	92	Br 72, R130	WCE/WN+B1 I	(5)	11.47	0.03	(11)	-0.31	4.6	1.6	-8.6
375	95	Br 80, R135	WN 7h+OB	(1)	13.04	0.09	(3,14)	-0.28	4.6	1.7	-7.2
402	96	Br 81	WN 8(h)	(3)	13.82	0.49	(3)	-0.30	4.6	3.6	-8.3
443	98	Br 79, Mk 49	WN 6(h)	(6)	13.37	0.10	(3)	-0.31	4.6	1.9	-7.0
493	100	Br 75, R134	WN 7h	(3)	12.40	0.14	(3)	-0.31	5.4	2.4	-8.5
543	101	Br 87, R140a1	WC 4(+WN 6+O)	(7)	<i>12.50</i>	<i>0.03</i>	(16,17)	-0.32	4.6	1.6	-7.6
544	102	Br 87, R140a2	WN 6+(O)	(8)	<i>12.50</i>	<i>0.03</i>	(16,17)	-0.31	4.6	1.6	-7.6
545	103	Br 87, R140b	WN 5(h)+O(+early O)	(1)	12.80	0.03	(16,17)	-0.30	4.6	1.5	-7.2
613	106	Br 82, R136a3	WN 5h	(6)	13.02	0.05	(15)	-0.29	5.4	1.8	-7.3
630	108	Br 82, R136a1	WN 5h	(6)	12.23	0.03	(15)	-0.30	5.4	1.8	-8.1
633	109	Br 82, R136a2	WN 5h	(6)	12.77	0.06	(15)	-0.30	5.4	2.0	-7.7
706	112	Br 82, R136c	WN 5h	(6)	13.39	0.20	(9,17)	-0.30	5.4	2.7	-7.8
762	115	Br 83, Mk33Sb	WC 5	(9)	15.23	0.12	(9)	-0.28	5.4	2.2	-5.4
770	116	Br 84, Mk34	WN 5h	(6)	<i>13.10</i>	<i>0.14</i>	(9,17)	-0.33	5.4	2.6	-7.9
862	117	Br 88, R146	WN 5ha	(2)	12.95	-0.16	(12)	-0.30	4.6	0.6	-6.2
916	118	Br 89	WN 6h*	(10)	11.20	-0.17	(11)	-0.29	4.6	0.6	-7.8
928	118a		WN 5h	(1)	<i>16.30</i>	<i>0.60</i>	(1,16)	-0.30	4.6	4.1	-6.3 <sup>‡</sup>
938	119	Br 90, R145	WN 6h+?	(1)	12.06	0.03	(11)	-0.30	4.6	1.5	-7.9
973	121	Br 90a	WC 4	(4)	17.21	0.31	(12)	-0.28	4.6	2.8	-4.1
1001	122	Br 92, R147	WN 5h	(1)	12.75	0.03	(12)	-0.29	4.6	1.5	-7.2

**Notes.** <sup>†</sup> Relates to the ID number assigned to the star in the 30 Dor census compiled in Chapter 4. <sup>\*</sup> Revealed as a WN 5-6+WN 6-7 binary system by Sana et al. (2013b). <sup>‡</sup>  $M_v^{\text{SYS}}$  was estimated using broad-band photometry and  $v - v \approx 0.2$  mag relation from Breysacher (1986). However, high reddening allows for a large uncertainty and the star is thought to be more comparable to BAT99-106 (F. Najarro private communication). References: (1) - This work, (2) - Foellmi et al. (2003), (3) - Crowther & Smith (1997), (4) - Smith et al. (1990), (5) - Conti & Massey (1989) (6) - Crowther & Dessart (1998), (7) - Bartzakos et al. (2001), (8) - Moffat et al. (1987), (9) - Massey & Hunter (1998), (10) - Smith et al. (1996), (11) - Schmutz & Vacca (1991), (12) - Crowther & Hadfield (2006), (13) - Walborn et al. (1999), (14) - Torres-Dodgen & Massey (1988), (15) - de Koter et al. (1997), (16) - Breysacher (1986), (17) - De Marchi et al. (2011), (18) - Schnurr et al. (2008b).

Table 3.10: Values for the  $W_\lambda$  of the He II  $\lambda 4686$  line in WN stars or the C IV  $\lambda 5808$  line in WN/C and WC stars. The spectra used for these measurements are referenced. Magnitude corrections were applied to W-R binaries, where  $\Delta M_v = M_v^{W-R} - M_v^{OB}$ . See text for more details.

ID <sup>†</sup>	BAT99	VFTS	Star	Spectral	Ref.	$W_\lambda(4686)$	$W_\lambda(5808)$	Ref.	$M_v^{SYS}$	$\Delta M_v$	$M_v^{W-R}$
#			Alias	Type		[Å]	[Å]		[mag]	[mag]	[mag]
24	86	019	Br 69	WN 3(h)	(1)	110	-	(1)	-3.6	-	-
92	88	079	Br 70a	WN 4b/WCE	(2)	225	1660	(1,12)	-3.9	-	-
117	89	108	Br 71	WN 7h	(3)	96	-	(1)	-6.7	-	-
144	90	136	Br 74	WC 4	(4)	-	1451	(12)	-4.4	-	-
155	91	147	Br 73-1A	WN 6(h)	(1)	39	-	(1)	-5.6	-	-
185	92		Br 72, R130	WCE/WN+B1 I	(5)	14	73	(14,18)	-8.6	+3.2*	-5.4
375	95	402	Br 80, R135	WN 7h+OB	(1)	80	-	(1)	-7.2	-3.5	-7.2
402	96	427	Br 81	WN 8(h)	(3)	40	-	(1)	-8.3	-	-
443	98		Br 79, Mk 49	WN 6(h)	(6)	19	-	(18)	-7.0	-	-
493	100	1001	Br 75, R134	WN 7h	(3)	27	-	(18)	-8.5	-	-
543	101	507	Br 87, R140a1	WC 4(+WN 6+O)	(7)	-	170	(1)	-7.6	+2.0	-5.5
544	102	507	Br 87, R140a2	WN 6+(O)	(8)	53	-	(1)	-7.6	-1.0	-7.2
545	103	509	Br 87, R140b	WN 5(h)+O(+early O)	(1)	42	-	(1)	-7.2	-0.3	-6.6
613	106		Br 82, R136a3	WN 5h	(6)	55	-	(15)	-7.3	-	-
630	108		Br 82, R136a1	WN 5h	(6)	37	-	(15)	-8.1	-	-
633	109		Br 82, R136a2	WN 5h	(6)	41	-	(15)	-7.7	-	-
706	112	1025	Br 82, R136c	WN 5h	(6)	54	-	(15)	-7.8	-	-
762	115		Br 83, Mk33Sb	WC 5	(9)	-	1100	(9)	-5.4	-	-
770	116		Br 84, Mk34	WN 5h	(6)	30	-	(18)	-7.9	-	-
862	117	617	Br 88, R146	WN 5ha	(2)	37	-	(1)	-6.2	-	-
916	118		Br 89	WN 6h*	(10)	60	-	(18)	-7.8	-	-
928	118a	682		WN 5h	(1)	39	-	(1)	-6.3	-	-
938	119	695	Br 90, R145	WN 6h+?	(1)	39	-	(1)	-7.9	-0.1	-7.2
973	121	731	Br 90a	WC 4	(4)	-	1258	(12)	-4.1	-	-
1001	122	758	Br 92, R147	WN 5h	(1)	76	-	(1)	-7.2	-	-

<sup>†</sup> Relates to the ID number assigned to the star in the 30 Dor census compiled in Chapter 4. \* Revealed as a WN 5-6+WN 6-7 binary system by Sana et al. (2013b). \* Based on  $W_\lambda$  dilution of C IV  $\lambda 5808$  line. References: (1) - This work, (2) - Foellmi et al. (2003), (3) - Crowther & Smith (1997), (4) - Smith et al. (1990), (5) - Conti & Massey (1989) (6) - Crowther & Dessart (1998), (7) - Bartzakos et al. (2001), (8) - Moffat et al. (1987), (9) - Massey & Hunter (1998), (10) - Smith et al. (1996), (11) - Schmutz & Vacca (1991), (12) - Crowther & Hadfield (2006), (13) - Walborn et al. (1999), (14) - Torres-Dodgen & Massey (1988), (15) - de Koter et al. (1997), (16) - Breysacher (1986), (17) - De Marchi et al. (2011), (18) - Schurr et al. (2008b).

### 3.7.3 Templates stars

Ideally, homogeneous spectroscopic and photometric datasets would have been sought for deriving the properties of the emission line stars. While the VFTS MEDUSA mode had made observations of 19 of the emission line stars, as noted earlier, the spectra were not flux calibrated and lacked large sections in the yellow and red wavelengths, which hold important diagnostic lines for W-R star modelling. Fortunately, additional flux calibrated spectra were available for a selection of stars. Given the varied data quality, the stars were modelled via a template approach. This involved taking a single example of each W-R and Of/WN subtype and analysing it using the non-LTE atmospheric code CMFGEN (Hillier & Miller 1998). This model would then be used as a template for other stars of the same SpT. Stars holding the best spectral quality and coverage to strengthen the modelling were chosen as templates and are listed in Table 3.11.

### 3.7.4 Stellar modelling

CMFGEN solves the radiative transfer equation in the co-moving frame, subject to radiative and statistical equilibrium. Since CMFGEN does not solve the momentum equation, a density/velocity structure is required. For the supersonic part, an exponent of  $\beta = 1$  is adopted for the velocity law, while the subsonic velocity structure is defined using a plane-parallel TLUSTY model (Lanz & Hubeny 2003).

CMFGEN incorporates line blanketing through a super level approximation, in which atomic levels of similar energy are grouped into a single super level that is used to compute the atmospheric structure. The WN and Of/WN subtypes included the following model atoms H I, He I-II, C III-IV, N III-V, O III-VI, Si IV, P IV-V, S IV-VI and Fe IV-VII while the WC model atoms comprised He I-II, C II-IV, O II-VI, Ne II-VI, Si IV, P IV-V, S IV-VI, Ar III-VIII and Fe IV-VIII. Other than H, He, CNO, a half-solar abundance was adopted from Asplund et al. (2009).

Stellar temperatures,  $T_*$ , correspond to a Rosseland optical depth of 10, which is somewhat higher than effective temperatures,  $T_{2/3}$ , relating to an optical depth of two thirds. Wind clumping is incorporated using a radially dependent volume filling factor,  $f$ , with  $f_\infty = 0.1$  at  $v_\infty$ , resulting in a reduction in mass-loss rate by a factor of  $f^{-0.5} \sim 3$  with respect to a smooth wind.

As mentioned earlier, reddening assumed  $R_V = 4.2$  or  $R_V = 3.5$  for stars in and outside of R136, respectively. The only exception was the template star Sk  $-67^\circ 22$  (O2 If\*/WN5) which lies outside of 30 Dor and for which  $R_V = 3.1$  was adopted. The value of  $A_V$  in Table 3.9 follows from the relation  $A_V = R_V \times E(b - v)$ . Conversely, the atmospheric modelling of the

template stars utilises data from a range of wavelengths to constrain the amount of extinction. The value of  $A_v$ , (and subsequently  $M_v^{\text{sys}}$ ), returned by CMFGEN and listed in Table 3.12 is therefore favoured and will differ from those in Table 3.9.

For some of the W-R stars in the sample, similar CMFGEN tailored analyses had already been performed in previous studies. Crowther et al. (2010) had studied the bright WN stars within R136 (BAT99-106, 108, 109, 112) and so their properties were adopted in this work. R136a3 (BAT99-106) was also used as the template for other WN 5 stars in the census. BAT99-90 (Brey 74) had been analysed by Crowther et al. (2002) and served as the template for WC stars in the census. Note that all of these adopted models would also give different  $A_v$  and  $M_v^{\text{sys}}$  values than those in Table 3.9.

The inferred physical and wind properties for the template stars are listed in Table 3.12. Spectral fits of the models can be found in Appendix C. One example of each WR subtype was used in order to serve as calibrators for other stars in 30 Dor. While specific lines were used to provide properties, not all lines are reproduced by each model. The overall agreement is satisfactory, although there are differences in a few instances. For example, He II  $\lambda 5412$  in BAT99-89/Brey 71 is well reproduced by AAT observations, while He II  $\lambda 4686$  is less satisfactory, in part due to rectification issues in this region. Similarly, He II  $\lambda 5412$  is well matched for BAT99-88/Brey 70a, but He II  $\lambda 4686$  is too weak (AAT) or too strong (VFTS) and C IV  $\lambda 5808$  is notoriously difficult to reproduce in WN/C stars, being very susceptible to EUV blanketing. As a result, the AAT integrity is questionable given the inconsistencies between it and VFTS for He II  $\lambda 4686$ .

For non-template stars, properties such as stellar temperatures, bolometric corrections and the  $L_{\text{EUV}}/L_{\text{Bol}}$  ratio were adopted from their relevant template. If possible, individual  $v_\infty$  values were obtained from literature (e.g. Crowther & Smith 1997), or otherwise also taken from the template star. While  $Q_0$  may vary between stars,  $q_0$  is assumed to be relatively constant and was adopted for consistent SpTs. Individual luminosities would be derived from  $M_v^{\text{sys}}$ , or binary corrected  $M_v^{\text{WR}}$  values in Table 3.10. In the case of mass-loss rates, stars were taken to have identical wind densities (i.e. identical transformed radii ( $R_t$ ) Schmutz et al. 1989) to the template stars.  $\dot{M}$  could therefore be scaled according to the relation:

$$R_t = R_* \left[ \frac{v_\infty}{2500 \text{ km s}^{-1}} / \frac{\sqrt{D}\dot{M}}{10^{-4} M_\odot \text{ yr}^{-1}} \right]^{2/3}, \quad (3.5)$$

where the  $\sqrt{D}$  factor accounts for the clumped winds, with  $D = 1/f$ . The properties of all the emission line stars based on templates stars are presented in Table 5.9 as part of a census to determine properties for all the hot luminous stars in 30 Dor.

Table 3.11: Spectroscopic data used in atmospheric modelling of the template stars.

Star	Alias	Spectral Type	Instrument	$\lambda$ -coverage [Å]	Reference
12	Sk -67° 22	O2 If*/WN 5	HST-STIS	1150-1740	Massey et al. (2005)
			VLT-FLAMES-UVES	3300-10250	Welty & Crowther (2010)
97	Mk 51	O3.5 If*/WN 7	VLT-FLAMES-MEDUSA	3960-5060 & 6640-6820	Evans et al. (2011)
86	Brey 69	WN 3(h)	VLT-FLAMES-MEDUSA	3960-5060 & 6640-6820	Evans et al. (2011)
106	R136a3	WN 5h	HST-GHRS	1150-1750	de Koter et al. (1997)
			HST-FOS	3200-6700	de Koter et al. (1997)
			VLT-SINFONI	19500-24500	Schnurr et al. (2009a)
118	Brey 89	WN 6h*	AAT-RGO	3670-6000	Crowther & Smith (1997)
			MSO	4740-6710	Crowther & Smith (1997)
			IUE-HIRES	1150-1950	Crowther & Smith (1997)
89	Brey 71	WN 7h	AAT-RGO	3670-6000	Crowther & Smith (1997)
			VLT-FLAMES-MEDUSA	3960-5060 & 6640-6820	Evans et al. (2011)
96	Brey 81	WN 8(h)	MSO	4010-5980	Crowther & Smith (1997)
			VLT-FLAMES-MEDUSA	3960-5060 & 6640-6820	Evans et al. (2011)
88	Brey 70a	WN 4b/WCE	VLT-FLAMES-MEDUSA	3960-5060 & 6640-6820	Evans et al. (2011)
			CTIO-RC	3600-6800	Foellmi et al. (2003)
90	Brey 74	WC 4	HST-FOS	1150-3300	Grafener et al. (1998)
			SSO-DBS	3240-6080 & 6410-11010	Crowther et al. (2002)

**Notes.**

\* Recently revealed as a WN 5-6+WN 6-7 binary system by Sana et al. (2013b) but for the WN 6 template model, properties were adopted in the case of a single star.

Table 3.12: Template W-R and Of/WN star models. Values in parentheses are given in broad-band and apply to Of/WN stars. Narrow-band is used for all other W-R stars. Abundance ratios are given in H:He:N for Of/WN and WN stars, He:C:N for WN/C stars and He:C:O for WC stars. See Appendix C for model fits.

Star	Spectral	$(A_V)/A_V$	$(M_V^{\text{SYS}})/M_V^{\text{SYS}}$	$T_*$	$T_{\text{eff}}$	$(BC_V)/BC_V$	$\log L$	$v_{\infty}$	$\dot{M}$	Abundance	$L_{\text{EUV}}$	$\log q_0$	$\log Q_0$	Ref.
BAT99	Type	[mag]	[mag]	[kK]	[kK]	[mag]	[ $L_{\odot}$ ]	[ $\text{km s}^{-1}$ ]	[ $M_{\odot} \text{ yr}^{-1}$ ]	(by mass)	[ $L_{\text{Bol}}$ ]	[ $\text{ph cm}^{-2} \text{ s}^{-1}$ ]	[ $\text{ph s}^{-1}$ ]	
12	O2If*/WN 5	(0.4)	(-5.4)	49.8	49.3	(-4.4)	5.83	2650	$3.7 \times 10^{-6}$	60:39:0.3	0.64	24.79	49.67	(1)
97	O3.5If*/WN 7	(2.2)	(-6.9)	41.0	40.8	(-3.7)	6.14	1500	$4.7 \times 10^{-6}$	60:39:0.5	0.49	24.40	49.83	(1)
86	WN 3(h)	1.98	-3.75	79.3	74.9	-5.2	5.43	1750	$3.2 \times 10^{-6}$	20:79:0.5	0.85	25.63	49.34	(1)
106	WN 5h	1.86	-7.29	53.0	53.0	-4.5	6.58	2200	$3.7 \times 10^{-5}$	40:59:0.4	0.69	24.90	50.47	(2)
118	WN 6h*	0.58	-7.83	45.0	39.4	-3.5	6.41	1450	$8.0 \times 10^{-5}$	20:79:0.5	0.54	24.62	50.26	(1)
89	WN 7h	1.53	-5.85	49.8	44.5	-3.6	5.75	1000	$1.9 \times 10^{-5}$	15:84:0.5	0.58	24.96	49.61	(1)
96	WN 8(h)	2.40	-7.03	42.5	36.9	-3.4	6.04	850	$4.0 \times 10^{-5}$	6:93:0.3	0.48	24.49	49.82	(1)
88	WN 4b/WCE	4.04	-4.74	80.0	72.1	-5.0	5.78	1750	$1.5 \times 10^{-5}$	99:0.5:0.1	0.82	25.66	49.67	(1)
90	WC 4	1.48	-4.52	85.0	72.0	-4.7	5.57	2600	$1.6 \times 10^{-5}$	45:43:1.1	0.72	25.76	49.31	(3)

**Notes.** \* Recently revealed as a WN 5-6+WN 6-7 binary system by Sana et al. (2013b) but for the WN 6 template model, properties were adopted in the case of a single star. References: (1) - This work, (2) - Crowther et al. (2010), (3) - Crowther et al. (2002).

### 3.7.5 Discussion

All of the WN stars in 30 Dor are revealed to be H-rich. A quick comparison of the template models with the properties given in Table 1.2 clearly shows how these stars stand apart from other Milky Way W-R stars. Temperatures may be similar but they are significantly more luminous and have much higher ionising outputs. Due to the relatively large number of WN stars in 30 Dor, Chapter 5 investigates whether their feedback is significant when compared to the rest of the massive star population. Their properties are characteristic of the ‘WNH’ class star discussed by Smith & Conti (2008), who separate them from core He burning W-R stars despite a similar spectral appearance. They concluded WNH stars to have a distinct evolutionary state, originating from the most massive O-type stars. Their H abundances and very high mass-loss rates suggest that core H burning is taking place in the star, if only in its latter stages. They would then follow on from the most massive O-supergiants, with Of/WN stars providing a potential intermediate phase.

Hainich et al. (2014) have since carried out spectral modelling of nearly all the WN stars in the LMC allowing a comparison with the template stars in Table 3.12. They too, fitted to a combination of UV and optical spectra which was often in common with that used in this study, with the exception of the VFTS data. However, they had used the PoWR atmospheric modelling code and generated a grid of models to determine the best fitting parameters of each star. The templates for the O2 If\*/WN 5, O3.5 If\*/WN 7, WN 5 and WN 7 stars showed relatively consistent properties. Hainich et al. (2014) favoured large temperature differences of  $-8$  kK and  $+30$  kK in the case of the WN 3 and WN 4b/WCE templates, respectively, but their other parameters remained comparable. Conflicting reddening parameters gave Hainich et al. (2014) a 0.36 dex higher luminosity for the WN 8 template.

Differences were also noted in the template WN 6 star (BAT99-118), although this has since been revealed to be a WN 5-6+WN 6-7 binary system by Sana et al. (2013b). A single star analysis was carried out in this work as well as by Hainich et al. (2014), but revised parameters for the system can be estimated by using bolometric corrections from the template WN 5+WN 7 stars. Sana et al. (2013b) found the mass ratio of the WN 7 secondary to WN 5 primary to be  $\sim 1.17$ , so for an adopted  $L_{\text{Bol}} \propto M^{1.5}$  for very massive stars (Yusof et al. 2013), the approximate ratio of their luminosities is  $1.17^{1.5} = 1.26$ . Based on the systemic absolute magnitude of R144 in Table 3.9, the inferred absolute magnitudes of the WN 5 primary and WN 7 secondary are  $-6.4$  and  $-7.4$  mag, respectively, from which bolometric luminosities of  $10^{6.2}$  and  $10^{6.3} L_{\odot}$  are obtained. Consequently, the systemic bolometric luminosity of R144 may be up to  $10^{6.6} L_{\odot}$ , i.e. 0.2 dex higher than that obtained in Table 3.12.

Initial comparisons between the ionising photon rate ( $Q_0$ ) and wind luminosity ( $L_{\text{SW}} =$

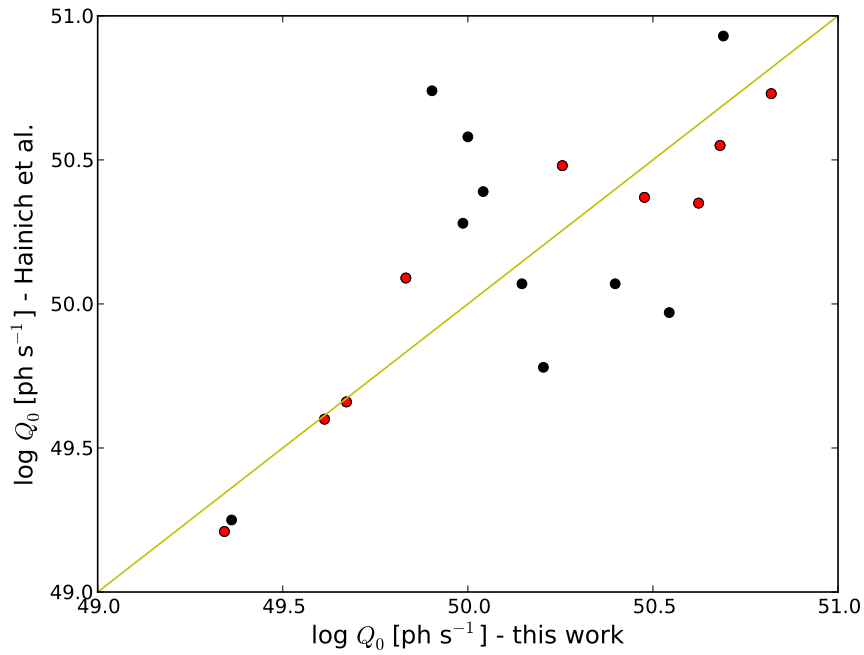
$\frac{1}{2}\dot{M}v_{\infty}^2$ ) of this work and the Hainich models are shown in Figure 3.26. As expected, the template models show a reasonably good consistency despite the discrepancies of some other properties mentioned. In the case of the ionising outputs, there was a broad scatter in results of up to 0.8 dex, but still a weak agreement that could potentially balance out for the integrated 30 Dor value. The wind luminosities were systematically weaker from Hainich models by  $\sim 0.3$  dex. While this might point towards a reduction in wind luminosity of the WN, the integrated value of 30 Dor may only see a minor change as the top ten contributing stars (see later Table 5.11) only feature individually modelled WN stars or WC stars.

Upcoming work by Bestenlehner et al. (submitted) will permit further comparisons of the luminous O, Of/WN and WN stars in the VFTS. Their grid approach works with a homogeneous set of optical and IR data and uses the CMFGEN code to model the atmospheres. Such individual approaches, even when fitting to a grid of models, would be favourable when estimating the properties of each star. With a template model, any inaccuracies would propagate through to all of the stars which had their properties based on them. Note, this would not be a concern for WN 3 and WN 8 stars as Table 3.9 shows only one star of these SpTs to be present in 30 Dor. Nevertheless, the limited modelling of WC stars in 30 Dor leaves the template approach as the suitable option for estimating the remaining population.

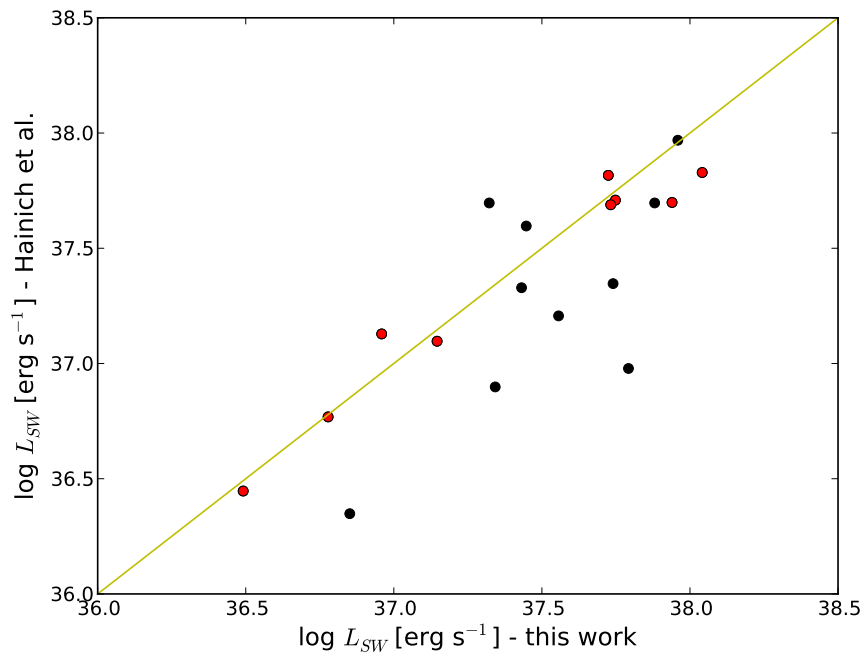
### 3.8 Summary

The VFTS has brought mid-high resolution multi-epoch spectroscopy to 19 W-R and Of/WN stars in the central  $\sim 20$  arcmin of 30 Doradus. Spanning the blue spectrum as well as the H $\alpha$  line, the data are well suited to the analysis of the 15 WN and Of/WN stars. They have been newly classified using the Smith et al. (1996) and Crowther & Walborn (2011) schemes, respectively. As a result, seven stars have seen adjustments to their previous spectral types - in most cases these have been new perspectives on the H content or arisen from the new criteria from Crowther & Walborn (2011). In addition, the VFTS revealed a new WN 5h star, VFTS 682. Previously obscured due to high levels of extinction, VFTS 682 appears relatively isolated and  $\sim 30$  pc from the centre of 30 Dor. Atmospheric modelling is now underway of all of these stars Bestenlehner et al. (submitted), with some Of/WN stars benefiting from spectra obtained under the superior UVES mode. Four WC stars were observed by the VFTS but unfortunately the spectral range of the data did not include their key diagnostic lines. Past spectral classifications were therefore unchanged and the VFTS will likely only be able to serve as subsidiary data in the atmospheric modelling of WC stars.

Thanks to its multi-epoch observations, the VFTS brings further information to the study



(a)



(b)

Figure 3.26: Comparison between WN star feedback properties in this work and Hainich et al. (2014). Template models stars in Table 3.12 and stars whose properties were adopted from other works i.e. core R136 stars from Crowther et al. (2010) are plotted in red circles. Stars based on template stars are plotted in black circles. The solid yellow line marks the 1:1 relation. Figure (a) compares the ionising luminosities and Figure (b) compares the wind luminosities of the stars.

of binarity in these stars. Spectral variations have been identified in both the single and binary systems, with classifications of the companion star where possible. The orbital parameters of previous studies have been tested against the new data although the work has been limited, in part due to the small number of epochs. Future work would require some care as measuring a reliable  $RV$  from the emission lines of these W-R stars proved difficult. While O-dwarfs produced reliable and consistent values between their spectral lines, discrepancies were found as stars moved off the main-sequence and became most severe for W-R stars. Atmospheric models avoid this uncertainty although certain assumptions which accompany the atomic physics used to create them suggest that some caution should still be taken.

Combined with the VFTS sample, the total number of Of/WN and W-R stars in 30 Dor reaches six and 25, respectively. Stellar properties have been derived for all of these stars by generating a model atmosphere of each SpT and scaling similar stars to this template. While secondary to an individual analysis, recent models indicate a reasonable consistency in results where the WN stars are H-rich and amongst the most luminous stars. These values can now be combined with the rest of the massive stars in 30 Dor to determine its integrated stellar properties.

# Chapter 4

## A Census of the Hot Luminous Stars in 30 Doradus

*Details on the compilation of the census are published in Doran et al. (2013), with a complete table of candidate hot luminous stars (Table 4.3) available at <http://cdsarc.u-strasbg.fr/viz-bin/qcat?J/A+A/558/A134>. Classifications of VFTS B-type stars that featured in the census were finalised by C. J. Evans (see Section 4.5).*

### 4.1 Introduction

Chapter 2 looked at analysing individual isolated stars and relating them with the surrounding nebulae. However, such massive stars are typically found in clusters where large numbers of stars will affect the gas and dust. Observing these nebular properties can still give clues to the global stellar parameters though. For example, the  $H\alpha$  recombination line can still be related to the ionising output of the stars and further calibrated to the SFR of the region. Meanwhile, the velocities of the gas clouds can give clues to the stellar winds and supernovae that drive them. Combining with knowledge of stellar evolution, it is even possible to model entire star forming regions through stellar population synthesis. The resulting models are capable of predicting the age of stellar populations, estimating feedback from both stars and supernovae and recreating the spectra of the region.

However, the reliability of such models can only be accurately tested with knowledge of the stellar populations they are attempting to reproduce. One therefore seeks a complete census of stellar population so that a quantitative study can be made; comparing the integrated properties of the stars to those observed for the entire region. Chapter 2 has already investigated the ionisation balance for single star Galactic H II regions and its connection to the age of the

star, but how are relations expected to change for larger populations or even GH II regions. Smith (2006) and Smith & Brooks (2007) carried out a census approach on the Carina Nebula and were able to estimate the ionising luminosity of its stars. They found the  $H\alpha$  luminosity provided just a third of the stellar output. This large discrepancy was thought to arise from a large non-uniform extinction that had not been accounted for. Meanwhile the integrated radio continuum flux accounted for only  $\sim 75\%$  of stellar output, suggesting that a significant fraction of the photons was escaping or was absorbed by dust. Lower luminosity H II regions in the LMC have also been studied by Oey & Kennicutt (1997). Initial comparisons to the  $H\alpha$  luminosity suggested 0-51% of ionising photons escape their regions. However, these H II regions were later revisited by Voges et al. (2008) with updated atmospheric models, indicating a reduced photon escape fraction, with radiation being bound to the regions in all but 20-30% of cases.

This technique is essential for constraining the calibrations that are relied on when studying distant extragalactic star forming regions. In these cases, stars are no longer resolved and only the global observations are available to make deductions. Understanding the photon escape fraction is equally important as these photons have the potential to go on and ionise the diffuse ionised medium (DIM). By quantifying the luminosity of the stellar winds, better connections can be made to the gas kinematics and their impacts on star formation. Comparison can also be made to the luminosity of subsequent supernovae to determine how the kinetic energy of a region varies with age.

Furthermore, a census provides information on the numbers of different stellar morphologies and their varying contribution to the feedback. We learn their spatial distribution and how this can vary over the lifetime of the region. The previous H II regions studied by Oey & Kennicutt (1997) and Smith (2006) were typically composed of a few dozen ionising stars (70 in the case of the Carina Nebula). In this work, a much larger scale census is compiled by choosing to study the Giant H II region, 30 Doradus. Being powered by hundreds of massive stars of various spectral types (SpTs), it acts as an ideal test bed, particularly for comparing to extragalactic regions, and is discussed in the next section.

### 4.1.1 The giant HII region of 30 Doradus

30 Doradus (NGC 2070, hereafter “30 Dor”) is located to the eastern side of the stellar bar passing through the Large Magellanic Cloud (LMC). With gas filaments seen to extend for hundreds of light years, it has also acquired the name of the Tarantula Nebula (see Figure 4.1). The gas is excited and shaped by the vast number of massive stars that have been identified in the region (Melnick 1985; Schild & Testor 1992; Walborn & Blades 1997; Evans et al. 2011),

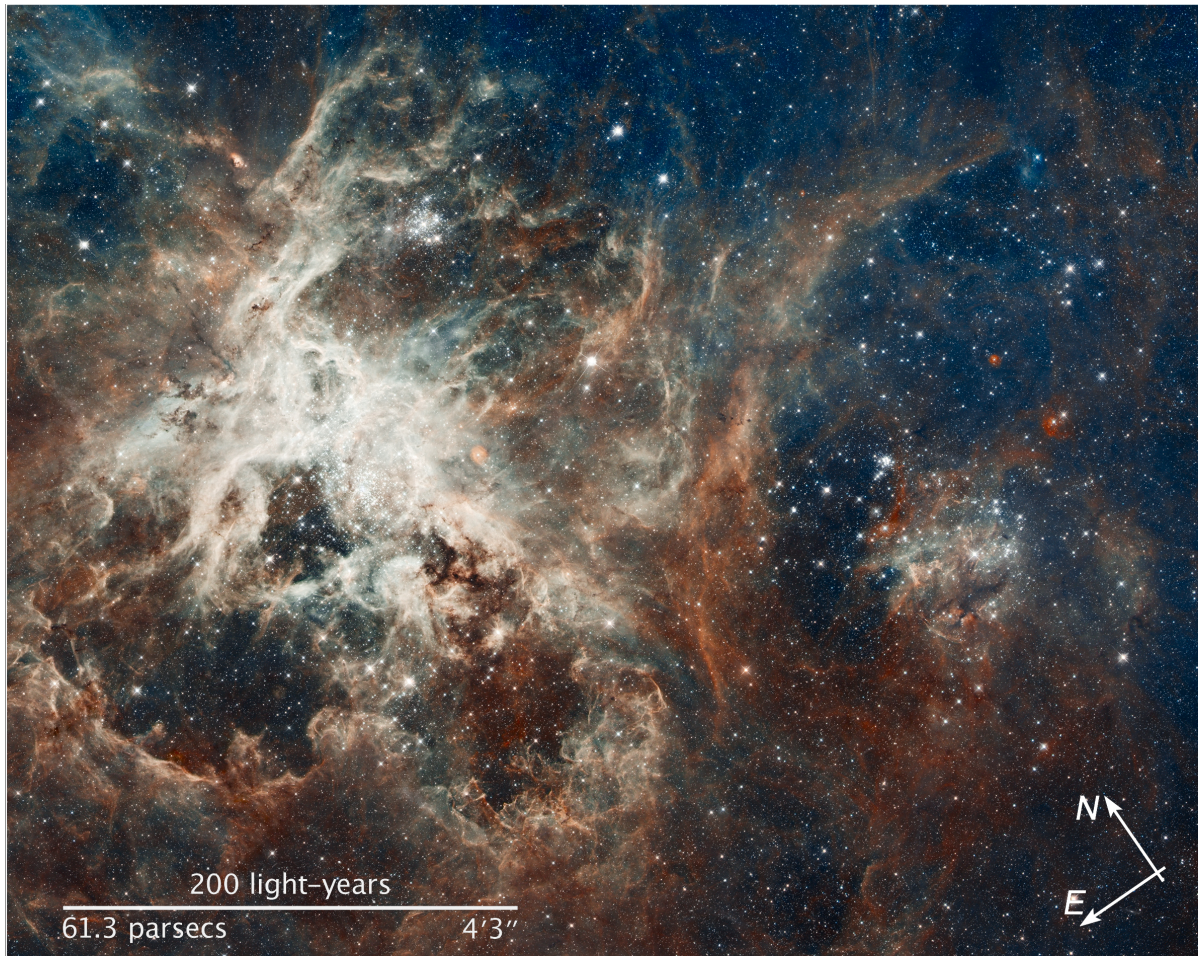


Figure 4.1: The Tarantula Nebula. A composite image obtained with the HST-ACS/WFC3 F775W filter and the ESO-WFI [O III]/8 and H $\alpha$ /7 filters. Courtesy of NASA, ESA and D. Lennon.

many of which are located within the central cluster known as R136 (Massey & Hunter 1998). They help to make 30 Dor the most massive and optically brightest H II region in the Local Group.

Defining boundaries for such a complex region is not straightforward. Nevertheless, whether considering the nebula as a whole, or the main group of stars which energises it (the 30 Dor cluster), all span a large angular region of sky. If, however, 30 Dor were to lie at a distance of 10 Mpc, equivalent to that of the Virgo Cluster, they would cover no more than a few arcseconds (see Table 4.1). For most of the extragalactic star forming regions we observe, this small amount of light is the only information available. With its close proximity, all the bright stars in 30 Dor can be resolved and may hold the key to understanding its distant counterparts.

For this reason, 30 Dor is often referred to as a Rosetta Stone and has been the subject

Table 4.1: Relative scale of 30 Dor and its associated regions  
- Taken from Walborn et al. (1999).

	Linear	Angular Diameter		
		52.5 kpc	1 Mpc	10 Mpc
LMC	5000 pc	5°	15′	1.5′
30 Doradus Region	1000 pc	1°	3′	20″
30 Doradus Nebula	200 pc	15′	50′	5″
30 Doradus Cluster	40 pc	3′	10″	1″
R136	2.5 pc	10″	0.5″	0.05″
R136a	0.25 pc	1″	0.05″	0.005″

**Notes.** The census of 30 Dor carried out in this work was able to extend to a diameter of 20′ and adopted a distance of 49.5 kpc.

of numerous surveys. This is due, in part, to its favourable location in the LMC; lying out of the plane of the Milky Way where interstellar extinction is kept to a minimum. To date, observations predominantly from the VFTS have revealed a rich supply of massive stars (at least 360 O-type stars) and more than 60 identified within R136. There is an abundance of W-R stars, with roughly a third of the LMC W-R stars being found in the 30 Dor nebula (Breysacher et al. 1999). Furthermore, stars have been shown to span multiple ages, from evidence of ongoing star formation (Brandner et al. 2001; Walborn et al. 2013) to older ( $\sim 20 - 25$  Myr) supergiants in the Hodge 301 cluster (Grebel & Chu 2000).

The R136 cluster shown located in the right-centre of Figure 4.2 is a perfect example of this stellar laboratory. Originally thought to be a single star exceeding  $1000 M_{\odot}$ , R136 is now known to be home to dozens of W-R and O-stars (Massey & Hunter 1998), some being the most massive stars known to date (Crowther et al. 2010). Studying these stars has not only aided our understanding of individual SpTs but massive star clusters as well. The IMF of R136 has been analysed by a number of authors, showing it to be relatively consistent to other clusters (Hunter et al. 1995; Selman et al. 1999; Sirianni et al. 2000). It has provided a basis for star formation simulations and allowed the stellar dynamics to be assessed (Hénault-Brunet et al. 2012).

#### 4.1.2 The VLT FLAMES Tarantula Survey

In view of the observational advantages offered by 30 Dor, the VLT Flames Tarantula Survey (VFTS, Evans et al. 2011) was recently completed, obtaining multi-epoch optical spectroscopy for more than 800 massive stars across the region (see Section 3.2 for details on the observations). The project aimed to address various outstanding questions in massive star physics and

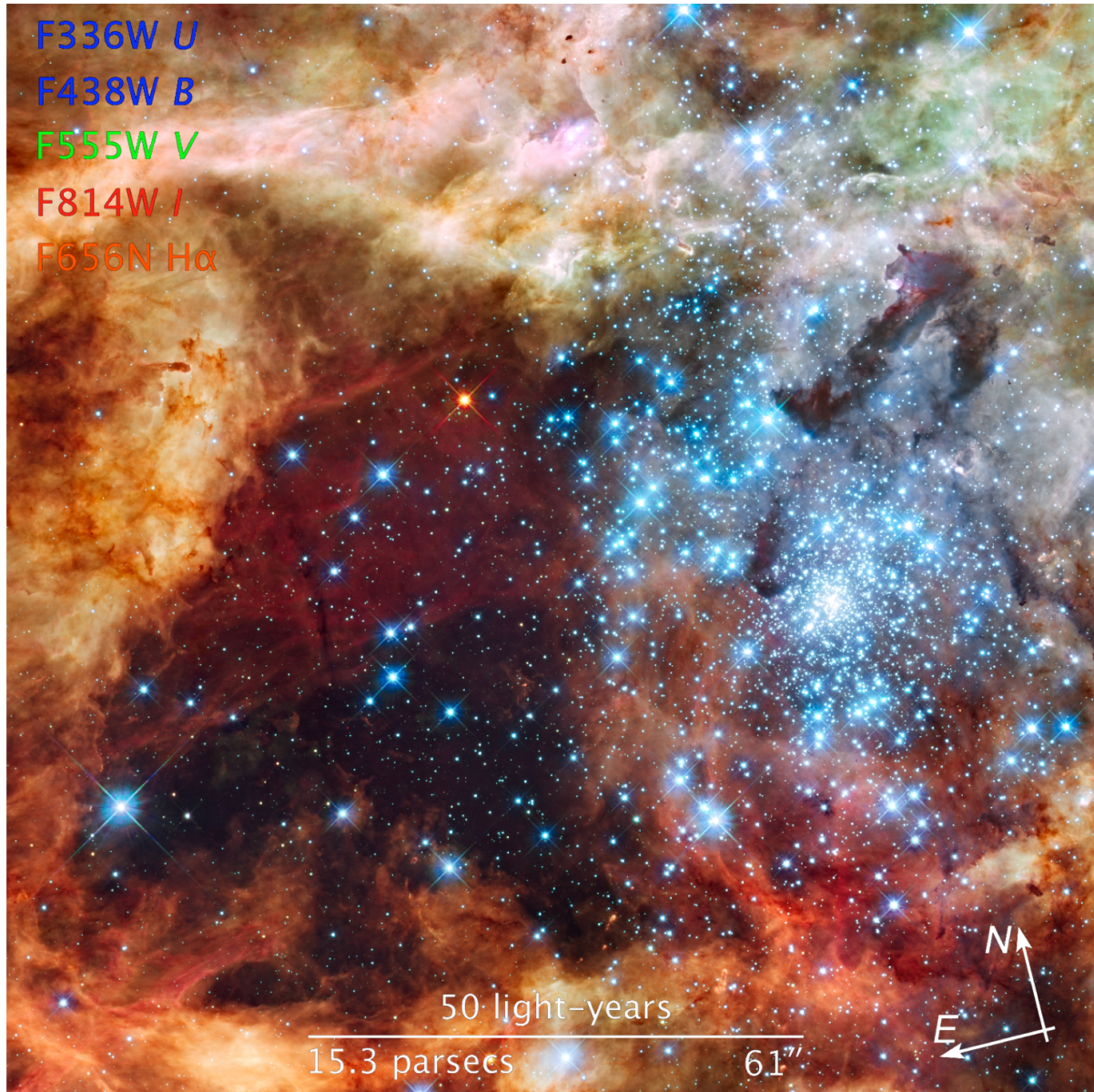


Figure 4.2: The 30 Doradus nebula and star cluster. A composite image obtained with the HST-WFC3/UVIS F336W (*U*), F438W (*B*), F555W (*V*), F814W (*I*), and F656N (H $\alpha$ ) filters. Courtesy of NASA, ESA, F. Paresce, R. O’Connell and the WFC3 Science Oversight Committee.

evolution. Several serendipitous findings have so far been made (Taylor et al. 2011; Bestenlehner et al. 2011; Dufton et al. 2011b; Dunstall et al. 2012), showing the diversity of the region. The comprehensive properties have also been studied. The multi-epoch observations allowed estimates of the multiplicity fraction (Sana et al. 2013a), and rotational velocity distributions have been made for both the O-type (Ramírez-Agudelo et al. 2013) and B-type stars (Dufton et al. 2013).

While 30 Dor has been a regular target for past observations, stellar spectroscopy was minimal and generally limited to the brightest central stars. Less than 20% of the massive stars had known SpTs but this was recently enhanced by the VFTS, improving the spectroscopic completeness to  $\sim 85\%$  as shown later in Section 4.6. This census takes advantage of the new spectroscopy and seeks to catalogue all the hot luminous stars in 30 Dor.

As discussed in Chapter 3, 30 Dor contains a number of W-R stars, several of which were observed as part of the VFTS. Oey & Kennicutt (1997) and Voges et al. (2008) omit W-R stars when studying their H II regions, in view of uncertainties in their ionising luminosity. However, earlier work by Crowther & Dessart (1998) compiled a list of the hot luminous stars in the inner 10 pc of 30 Dor and found the W-R stars to play a key role in the overall feedback. The census extends their study to a larger radius, employing updated stellar calibrations and models to determine whether the W-R star contribution still remains significant.

## 4.2 Photometry

The census itself was chosen to extend out to a radial distance of  $r_d = 10$  arcmin (150 pc) from the centre of R136 (specifically star R136a1,  $\alpha = 05^h38^m42^s.39$ ,  $\delta = -69^\circ06'02.91''$ ). The 10 arcmin radius was selected as it encompassed the regions of 30 Dor observed to have the highest surface brightness (Kennicutt et al. 1995). It was also consistent with the spatial extent of the VFTS, to ensure a substantial number of the stars had been observed. From here onwards, when discussing the census, the term “30 Dor” will refer to this  $r_d < 10$  arcmin region. The first step in compiling the census began with obtaining a photometric list of every star in the region, from which the potential hot luminous candidates could be selected.

### 4.2.1 Photometry for the 30 Dor Region

In common with the VFTS, the census had four primary photometric catalogues: Selman, WFI, Parker and CTIO, outlined below.

The ‘Selman’ photometry (Selman et al. 1999), with Brian Skiff’s reworked astrometry<sup>1</sup>,

<sup>1</sup><ftp://cdsarc.u-strasbg.fr/pub/cats/J/A+A/341/98/>

used observations from the Superb-Seeing Imager (SUSI) on the 3.5 m New Technology Telescope (NTT) at La Silla. Data covered the central 90 arcsec of 30 Dor in the *UBV* bands. The completeness limit was  $V = 19.2$  mag although sources reached fainter, with typical photometric errors spanning 0.005-0.05 mag.

The ‘WFI’ photometry was the main source of photometry used for the census, based on the same observations outlined in Section 2.1 of Evans et al. (2011). *B*- and *V*-band photometry was obtained with the Wide-Field Imager (WFI) at the 2.2 m Max-Planck-Gesellschaft (MPG)/ESO telescope at La Silla. Data covered  $14 < V < 19$  mag with photometric errors between 0.002-0.020 mag although once this was bootstrapped to the Selman et al. (1999) catalogue, the scatter showed standard deviations of  $< 0.1$  mag (see also Section 3.2 of Evans et al. 2011). WFI sampled the outer sources of 30 Dor, extending at least 12 arcmin from the centre although the R136 cluster was largely omitted due to saturation.

The ‘Parker’ photometry (Parker 1993), with Brian Skiff’s reworked astrometry, used observations from RCA #4 CCD on the 0.9 m telescope at Cerro Tololo Inter-American Observatory (CTIO). The catalogue offered *UBV*-band photometry for a majority of sources and just *BV*-band in other cases. Parker sources predominantly spanned the inner 2 arcmin with additional coverage of regions north and east of R136. Data reached  $B = V = 18$  mag and  $U = 17$  mag, with average photometric errors in the range of 0.01-0.1 mag. However, it is noted that subsequent Hubble Space Telescope/Wide Field Planetary Camera (HST/WFPC2) data showed an incompleteness in the Parker catalogue, revealing some sources to be unaccounted for, and others to be spurious (see Footnote 6 of Rubio et al. 1998).

The ‘CTIO’ photometry comes from Y4KCAM camera observations on the 1 m CTIO telescope, outlined in Section 3.5 of Evans et al. (2011). It was complete out to a radius of  $\approx 7.5$  arcmin and was required to supply photometry for the brighter sources, not covered by the WFI data. The CTIO data reached  $V < 17.25$  mag with photometric errors between  $\sim 0.02$ – $0.1$  mag. As mentioned in Evans et al. (2011), the CTIO photometry was not transformed to the exact same system as the WFI photometry but the two remain in reasonable agreement:  $\Delta V$  and  $\Delta B \leq 0.5$  mag.

The Selman, WFI and Parker catalogues all showed consistent astrometry with common sources lying  $< 0.5$  arcsec away from one another. Unfortunately astrometry of the CTIO sources was found to be inconsistent, giving varying displacements of up to 5 arcsec (see Figure 4.3). To correct for this, every star with CTIO photometry, that was eventually selected for the census, had its astrometry individually extracted from the imaging used to produce the WFI photometry.

The spatial coverage of these four photometric catalogues is shown in Figure 4.4. However, given the spatial limit of the CTIO data ( $r_d < 7.5$  arcmin), the brightest targets in the far

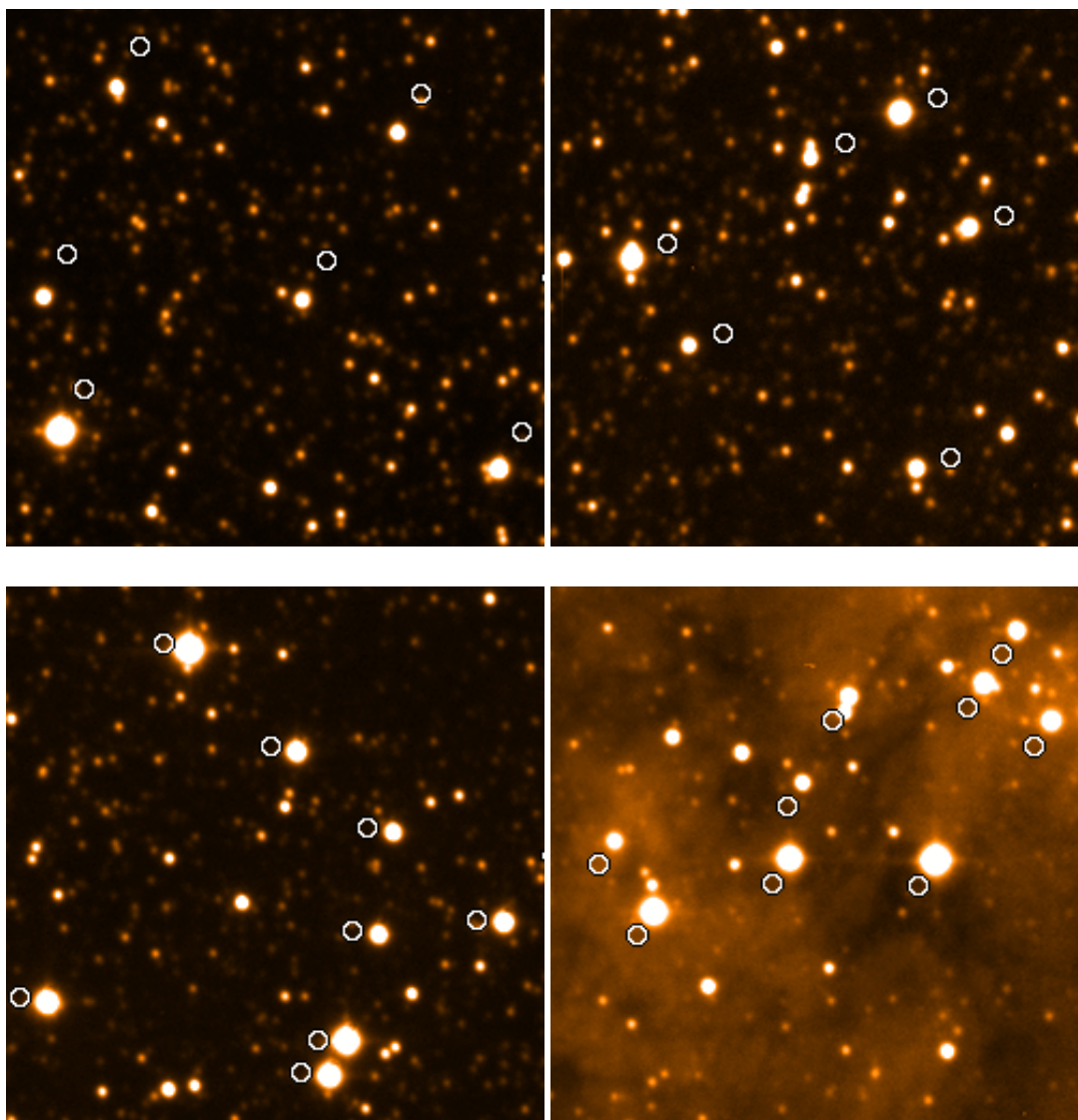


Figure 4.3: Offsets in the CTIO astrometry. The CTIO catalogue sources have been overlaid on a V-band WFI image. Each postcard shows a separate region of outer 30 Dor, clockwise from top left: north-east, north-west, south-west, south-east. Each postcard shows an area of  $1 \times 1$  arcmin.

western and southern regions of 30 Dor had not been covered. To ensure complete coverage, the few remaining brighter objects were taken from the Magellanic Clouds Photometric Survey of Zaritsky et al. (2004). Finally, due to the crowding in the dense cluster Brey 73, space-based photometry was favoured, obtained from the HST/Wide Field Planetary Camera (HST/WFPC) in the F336W, F439W, F569W bands (Walborn et al. 1999).

### 4.2.2 Photometry for the R136 Region

The central R136 cluster is particularly crowded and, similar to Brey 73, favoured photometry at a higher spatial resolution to the four primary catalogues. This was desired for all stars within  $r_d < 20$  arcsec (5 pc). This boundary was chosen as it was consistent with HST/FOS spectroscopy of Massey & Hunter (1998) that would later be used to complement the photometry. From here onwards, when discussing the census, the term “R136 region” will refer to this  $r_d < 20$  arcsec region.

#### Near-Infrared photometry

The initial approach for the R136 region followed on from the work of Crowther & Dessart (1998) who had listed and estimated the feedback of the brightest stars in the inner 10 pc. They had used optical photometry to determine the stellar parameters but near-IR (NIR) photometry was now available for all of these stars. This was originally favoured given that the extinction and the corresponding uncertainties on the photometry would be smaller in the NIR in comparison to the visible.

Campbell et al. (2010) had observed R136 with the VLT-Multiconjugate Adaptive Optics Demonstrator (VLT-MAD), obtaining three separate fields which all overlapped the central core. They obtained  $H$  and  $K$ -band photometry for the stars with the data estimated to have a 50% completeness of down to  $K \approx 19.45$  mag, depending on the field. Their study had excluded stars in the central 2.8 arcsec (0.7 pc) due to crowding/blending, however, for this initial work, the obtainable photometric accuracies of  $\lesssim 0.1$  mag would be sufficient. Multiple aperture photometry of the R136 region was therefore performed on the three original VLT-MAD  $K$ -band fields studied by Campbell et al. (2010) using the DAOPHOT package within IRAF. Campbell et al. (2010) used existing Two Micron All Sky Survey (2MASS) and VLT-High Acuity Wide-field  $K$ -band Imager (HAWK-I) photometry to determine a zero-point (ZP) calibration for each field. The apparent  $m_K$  magnitudes from Campbell et al. (2010) were compared to newly obtained photometry from DAOPHOT so that their own ZP could be calibrated. In regions of overlap, the field which showed the lowest spread in the ZP was used to calculate the new  $m_K$  magnitudes. Equivalent  $m_H$  magnitudes, were not obtained from new aperture

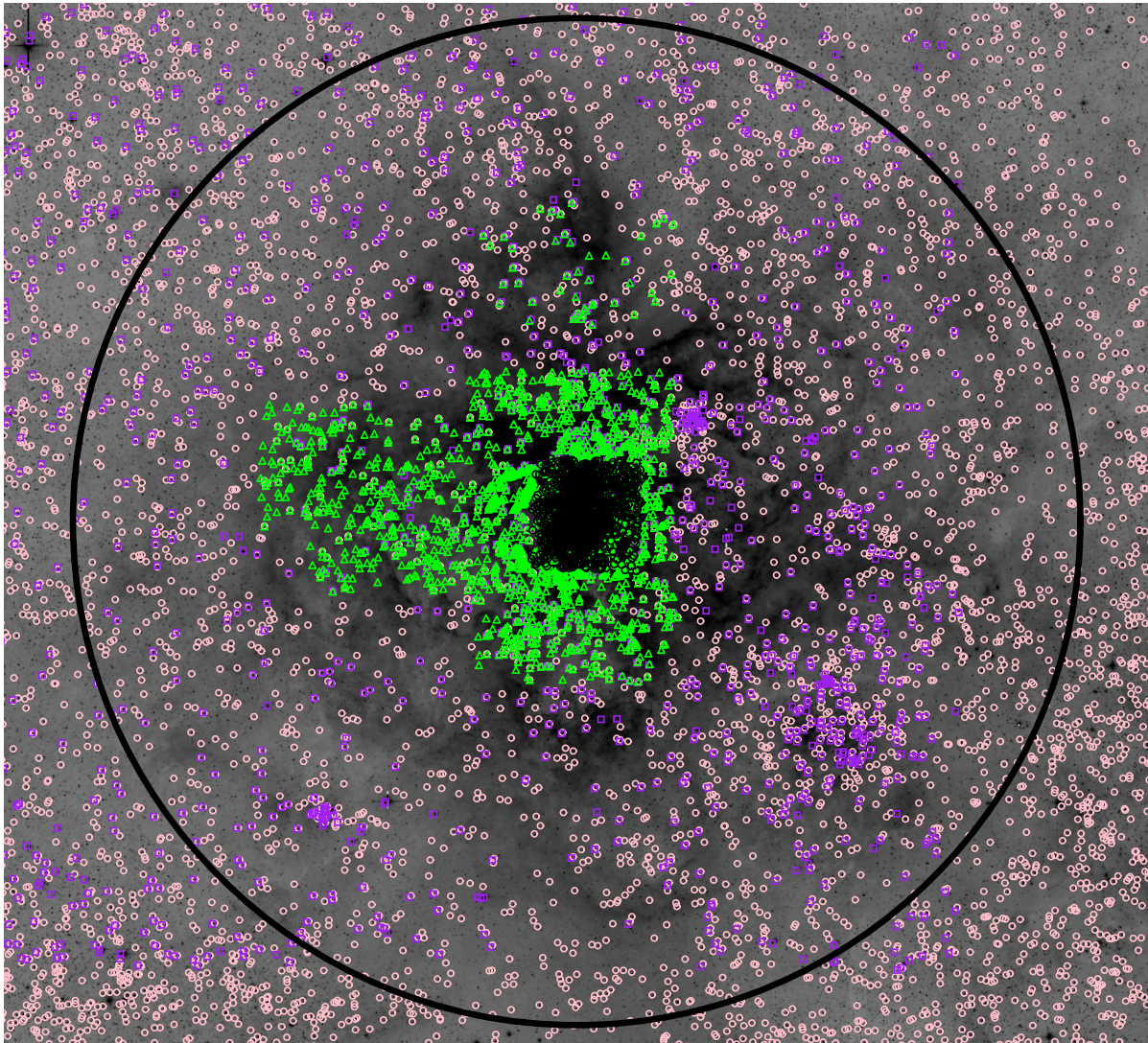


Figure 4.4: The spatial coverage of photometric sources from the four main catalogues used in the census, overlaid on a  $V$ -band WFI image. Selman (black circles), WFI (pink circles), Parker (green triangles) and CTIO (purple squares). The large black circle marks the  $r_d = 10$  arcmin region of the census. North is up and east is to the left.

photometry, but were adopted from Campbell et al. (2010) in the cases of the limited stars they had studied ( $> 2.8$  arcsec).

At the very core, DAOPHOT was unable to fit a PSF to some stars either due to their broad profiles or crowding. Where possible, IR photometry for the additional stars were adopted from Crowther et al. (2010), otherwise differential photometry was carried out from SINFONI data to estimate their magnitudes.

### Optical photometry

Optical imaging with the HST was carried out as part of the Wide Field Camera 3 (WFC3) Early Release Science Programme. De Marchi et al. (2011) provided photometry for R136 stars in the F336W, F438W, F555W and F814W bands. These data were favoured due to the superior resolution in the optical wavelengths, despite the larger extinction uncertainties. Furthermore, using optical photometry meant that the subsequent selection process of hot luminous candidate stars (see Section 4.4) was consistent for the entire 30 Dor region.

#### 4.2.3 Overlapping photometric sources

As some regions were covered by multiple catalogues, attempts were made to exclude any duplicates. Searches for sources within 0.5 arcsec of each other were made. Any that were found were subject to the same selection priority as in Evans et al. (2011). This was based on the quality of the photometry, where Selman was the primary dataset in central regions (excluding the R136 region). If the source lay beyond the Selman region, WFI was used. In the case of brighter sources, Parker was used, otherwise CTIO was used in outer regions of 30 Dor. The De Marchi et al. (2011) photometry was favoured for all sources in the R136 region. Table 4.2 gives a breakdown of the number of candidates, and spectroscopically confirmed, hot luminous stars that were eventually selected from each photometric catalogue.

#### 4.2.4 Photometry of W-R stars

To date, in excess of 600 W-R stars have been identified in the Milky Way (Crowther et al. 2014) although models of the Galaxy estimate several thousand more, located largely within dense star forming regions and hence obscured from the latest surveys (Rosslowe et al. in prep.; Shara et al. 2012, 2009). Surveys of the LMC benefit from low extinction and so are much more extensive. The Breysacher et al. (1999) catalogue of 134 stars is thought to be 90% complete (Shara et al. 2012) with only limited new discoveries adding to this tally (Howarth & Walborn 2012; Bestenlehner et al. 2011). It was therefore assumed that all W-R stars in

Table 4.2: The literature used to select the 1145 photometric candidates and classify the 500 spectroscopically confirmed hot luminous stars in the census. The number in brackets represents those located within the R136 region. Papers which form part of the VFTS series are identified with ‘(VFTS)’.

Source of Photometry	Candidates	Confirmed (in R136)
De Marchi et al. (2011)	212	70 (70)
Selman et al. (1999)	200	123 (2)
WFI (Evans et al. (2011))	518	196 (0)
Parker (1993)	71	42 (0)
CTIO (Evans et al. (2011))	126	57 (0)
Walborn et al. (1999)	15	10 (0)
Zaritsky et al. (2004)	3	1 (0)
Source of Spectral Type		Confirmed (in R136)
Schild & Testor (1992)		7 (0)
Parker (1993)		3 (0)
Walborn & Blades (1997)		8 (0)
Massey & Hunter (1998)		38 (38)
Crowther & Dessart (1998)		8 (8)
Bosch et al. (1999)		24 (0)
Walborn et al. (1999)		9 (0)
Breysacher et al. (1999)		3 (0)
Evans et al. (2011)	(VFTS)	16 (1)
Taylor et al. (2011)	(VFTS)	1 (0)
Dufton et al. (2011b)	(VFTS)	1 (0)
Crowther & Walborn (2011)		7 (6)
Hénault-Brunet et al. (2012)	(VFTS)	15 (14)
Walborn et al. (2014)	(VFTS)	295 (5)
McEvoy et al. (in prep.)	(VFTS)	35 (0)
This work	(VFTS)	30 (0)

the region had been previously identified through spectroscopy and, while their photometry was not used for their selection (see Section 4.4), it would still be needed to determine stellar parameters (as shown in Section 3.7).

### 4.3 Extinction in R136 and 30 Dor

For simplicity, a uniform extinction law was applied to the census, one to the R136 region and a separate one to the rest of 30 Dor. The level of extinction will inevitably fluctuate across the whole census but the application of a uniform law allows a straightforward modification of the census when stars lie in regions of higher or lower reddening. As this study took place, the

large coverage and high quality of the latest photometric surveys were being used to map the extinction across 30 Dor (e.g. Maíz-Apellániz 2004). The degree of this variation is discussed later in the section.

Extinction in the R136 region was initially determined in the  $K$ -band using the NIR photometry explained in Section 4.2.2. Each star had its  $H - K$  colour calculated and was assigned an intrinsic colour of  $(H - K)_0 = 0.1$  mag from the Martins & Plez (2006) O star calibrations. The colour excess  $E(H - K) = H - K - (H - K)_0$  was determined, followed by an extinction in the  $K$ -band via the relation  $A_K = 1.82 \times E(H - K)$  following the relation found by Indebetouw et al. (2005). To check the accuracy of  $A_K$ , an equivalent  $V$ -band extinction was calculated for a selection of 20 stars. A typical ratio of  $A_K/A_V \approx 0.12$  would have been expected but a higher average value of  $\sim 0.2$  was found instead. Assuming accurate intrinsic colours were adopted, the uncertainty lies in the observed colour of each star. It most likely arises from the large uncertainty on the  $H$ -band photometry, for which Campbell et al. (2010) quote  $\pm 0.15$  mag, as ZP calibrations could only be obtained from 2MASS imaging. This value is comparable to that found for the  $BV$  photometry. However, it is notably high relative to  $A_K \sim 0.31$  and in turn gives a large uncertainty on the extinction. As a result,  $A_K = 0.12 \times A_V$  was used to derive the  $K$ -band extinction of the 20 selected stars. The average value of  $A_K = 0.17$  mag,  $\sigma = 0.04$  mag was then applied to all stars to obtain an absolute magnitude  $M_K$ .

Extinction in the  $K$ -band is so small that a uniform  $A_K$  value can be used. However, this is not the case for  $A_V$ , which is needed to unreddden the optical photometry, given its larger variations from star to star. What is expected to remain relatively consistent is the average reddening value,  $R_V = A_V/E(B - V)$  (Cardelli et al. 1989), for the region. It is noted by Maíz Apellániz et al. (2014) that the free parameter in the extinction laws of Cardelli et al. (1989) should not strictly be called  $R_V$  but  $R_{5495}$  instead. The reason is that  $R_V \equiv A_V/E(B - V)$  is a function not only of the type of extinction but also of the input SED and the amount of extinction (see Figure 3 of Maíz Apellániz 2013). Nevertheless, for hot stars with low extinctions ( $A_V < 4$  mag), the approximation  $R_V = R_{5495}$  holds reasonably well and was used in this work.

To determine  $R_V$ , the  $M_K$  obtained from the VLT-MAD photometry was converted to an absolute magnitude in the  $V$ -band ( $M_V^{\text{VLT-MAD}}$ ) by using the  $(V - K)_0$  Martins & Plez (2006) calibrations. Another absolute magnitude in the  $V$ -band ( $M_V^{\text{WFC3}}$ ) was obtained directly from optical HST/WFC3 photometry of De Marchi et al. (2011).  $M_V^{\text{VLT-MAD}}$  was plotted against  $M_V^{\text{WFC3}}$  for varying values of  $R_V$  value. In theory, both values would be equal at a particular  $R_V$  value, with all points falling on the 1:1 relationship line. Despite some scattering, most likely where VLT-MAD photometry became less reliable in the core, a value of  $R_V = 4.2$  was favoured for the R136 region, as shown in Figure 4.6a.

For the rest of 30 Dor,  $R_V$  was derived using the same method on the single VFTS O-type stars. These stars had their  $K$ -band photometry supplied by the InfraRed Survey Facility (IRSF, see Table 6 of Evans et al. 2011). The extinction was expected to remain similar to the R136 region so that  $A_K = 0.17$  mag was used to determine their  $M_K$ . After applying the  $(V - K)_0$  Martins & Plez (2006) calibration, the corresponding absolute magnitudes in the  $V$ -band were termed  $M_V^{\text{IRSF}}$ . These were plotted in Figure 4.6b against absolute magnitudes derived from the original VFTS photometry ( $M_V^{\text{VFTS}}$ ), i.e. using Selman, WFI, Parker or CTIO photometry. A value of  $R_V = 3.5$  was favoured in this case.

In comparison, earlier work by Selman et al. (1999) found  $R_V$  to be consistent with a Galactic value of  $R_V = 3.1$ , at least within the central 10 arcsec of R136. However, more recent studies have indicated  $R_{5495} \approx 4.1$  but with a significant scatter (J. MaízApellániz, private communication). This value was obtained using the CHORIZO code (Maíz-Apellániz 2004) from stars within the central 2 arcsec of R136, but still showed good agreement with the uniform value of  $R_V = 4.2$  applied to the census.

Extending out to 30 Dor and a similar process was performed on the VFTS O-type stars using new WFC3  $UBVI$  photometry and supplementary  $JHK$  photometry from VFTS (Maíz Apellániz et al. 2014). In this case, an average value of  $R_{5495} \approx 4.7$  was derived, but again with a large variation amongst stars. This is notably larger than the census value of  $R_V = 3.5$ . When the extinctions of the stars are compared for equivalent  $A_V$  bands, Figure 4.5, some large differences ( $\Delta A_V > \pm 0.5$  mag) are evident. Such cases indicate the need for a non-uniform extinction law, either one which can assign an extinction to stars within a given region or better still, on an individual basis. While this is the eventual aim for the census, Figure 4.5 still shows a mean  $\Delta A_V < \pm 0.15$  mag. This is a relatively small offset with respect to the likely larger uncertainties that would arise in the stellar parameters, following the later use of spectroscopic calibrations (see Chapter 5).

## 4.4 Candidate Selection

Of the tens of thousands of photometric sources included in the  $r_d < 10$  arcmin spatial cut, only the hottest and most luminous stars were sought after for the census, to estimate the stellar feedback. The hottest stars will produce the bulk of the ionising photons, while the most luminous early type stars will have the strongest stellar winds, hence the largest wind luminosity. Therefore, from all the 30 Dor stars, one needs to account for all the W-R and O-type stars, along with the earliest B-type stars (given their contribution of ionising photons through large numbers and high  $T_{\text{eff}}$ ) and B-supergiants (given their strong winds). Various

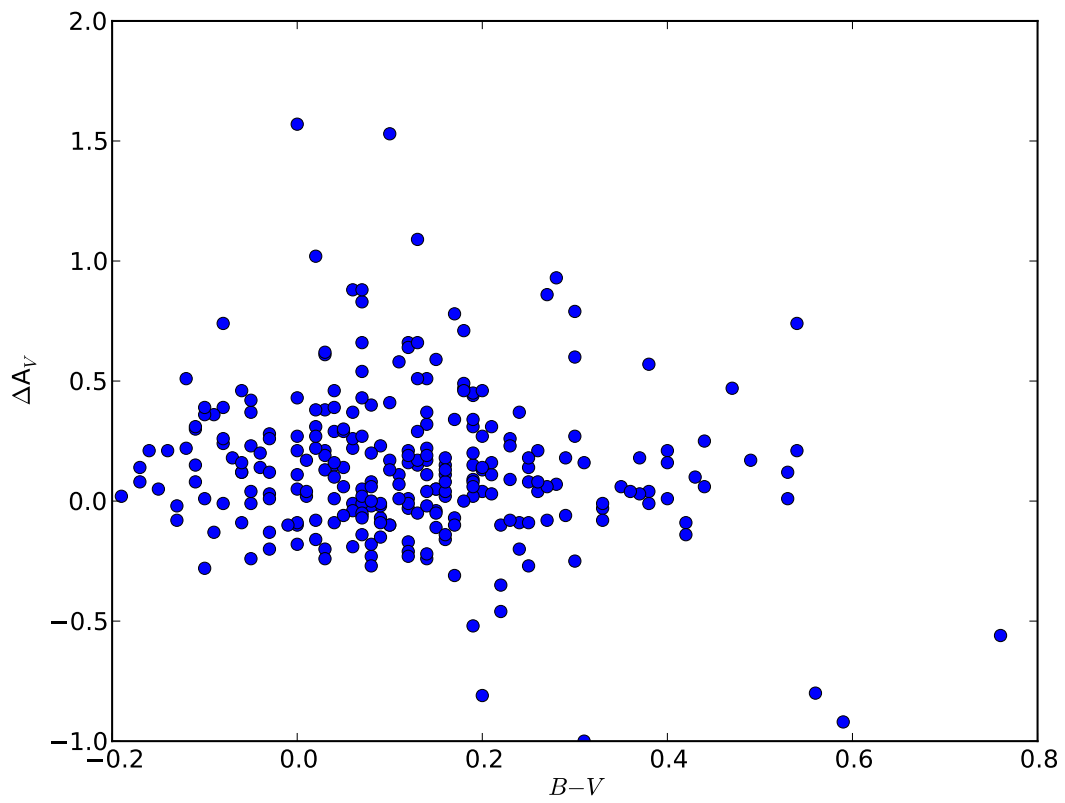
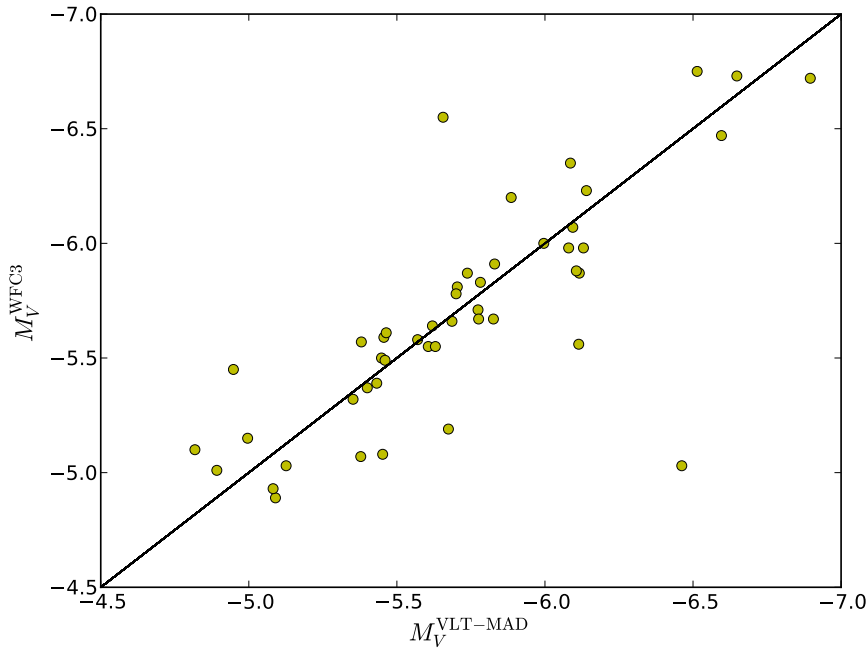
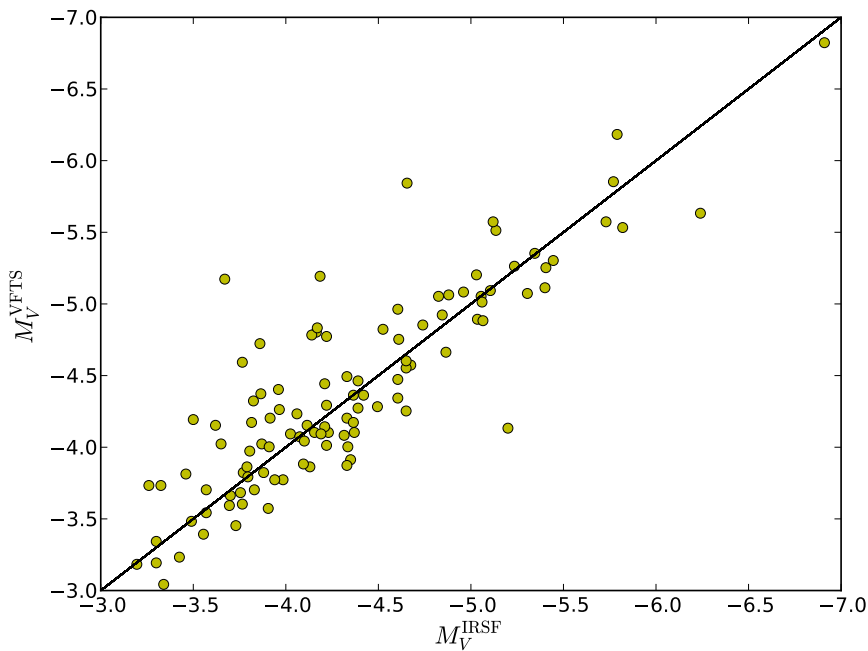


Figure 4.5: Comparison of extinction values from different extinction laws.  $\Delta A_V = A_V$  from (Maíz Apellániz et al. 2014) -  $A_V$  from the census.



(a)



(b)

Figure 4.6: Determination of  $R_V$  for 30 Dor. In the R136 region,  $R_V = 4.2$  (a): The  $M_V$  of single O-type stars derived from HST/WFC3 photometry is plotted against the expected  $M_V$  derived from VLT-MAD  $K$ -band photometry after applying the Martins & Plez (2006) calibration. Beyond the R136 region (the MEDUSA region),  $R_V = 3.5$  (b): The  $M_V$  derived from VFTS photometry is plotted against the expected  $M_V$  derived from IRSF  $K$ -band photometry after applying the Martins & Plez (2006) calibration. Solid lines indicate the 1:1 relations.

colour and magnitude cuts were applied to the photometric data to extract these stars without prior knowledge of their spectral classification.

In order to determine the boundaries of these cuts, an initial test was carried out upon the VFTS sample for which SpTs were already known. Figure 4.7 shows a colour-magnitude diagram of all the VFTS O and B-type stars. The left vertical line aims to eliminate all stars with unreliable photometry, given that a typical unreddened O-type star is expected to have a colour of  $B - V = -0.32$  mag (Fitzgerald 1970). Stars that lie to the left of this line would therefore be ‘too blue’. Similarly, the right vertical line eliminates late-type stars, too cool to contribute to the overall feedback. However, the W-R, O and early B-type stars that were desired, can still suffer from interstellar reddening which will shift them to the lower right hand side of the diagram. The boundary was therefore set to  $B - V = 0.8$  mag to account for as many potentially highly reddened hot stars as possible, whilst keeping the number of unwanted, cooler stars to a minimum.

In an attempt to identify the most luminous stars, a further magnitude cut was made with the diagonal reddening line. This line has a gradient which is equivalent to  $R_V = A_V/E(B - V)$ . The magnitude cut begins at  $m_V = 15$  mag and  $B - V = -0.32$  mag. This would be the position of the faintest stars that were sought if they suffered from no reddening at all, where an absolute magnitude of  $M_V \approx -3.5$  mag and distance modulus of 18.49 mag are adopted. A star suffering from interstellar reddening, however, is expected to be shifted along the diagonal line. A value of  $R_V = 3.5$  ensured the inclusion of all the most luminous stars. While Figure 4.7 shows that some VFTS O-type stars are omitted (those below the line), almost all were found to be O9 or later, and given their position on the diagram, would be subluminous and hence have negligible contributions to the feedback (this is derived quantitatively in Sections 5.4.1 and 5.4.2). With the limit of  $B - V = 0.8$  mag, this allows stars with extinctions up to  $A_V = 3.9$  mag to be accounted for.

A further method was also applied to select the hot luminous stars involving the ‘ $Q$ -parameter’ or reddening free index (Aparicio et al. 1998). The  $Q$ -parameter incorporates  $U$ -band photometry and takes advantage of the fact that different SpTs may have similar  $B - V$  colours but have different  $U - B$  colours. Aparicio et al. (1998) made the relationship  $Q = (U - B) - 0.72 \times (B - V)$  in the case of the Milky Way where  $R_V = 3.1$ . This was adjusted for 30 Dor using the reddening laws of Cardelli et al. (1989) so that the  $Q$ -parameter took the form of  $Q = (U - B) - 0.67 \times (B - V)$ . A limit of  $Q < -0.65$  was selected to filter out any mid-late B-type dwarfs and later SpT stars. This removed a further 26 stars from the candidate list and would ideally have been the best selection criterion to use. Unfortunately reliable  $U$ -band photometry was only available for a small subset of the sources. Furthermore, as some spurious detections had been noted in the Parker (1993) and CTIO catalogues, a further

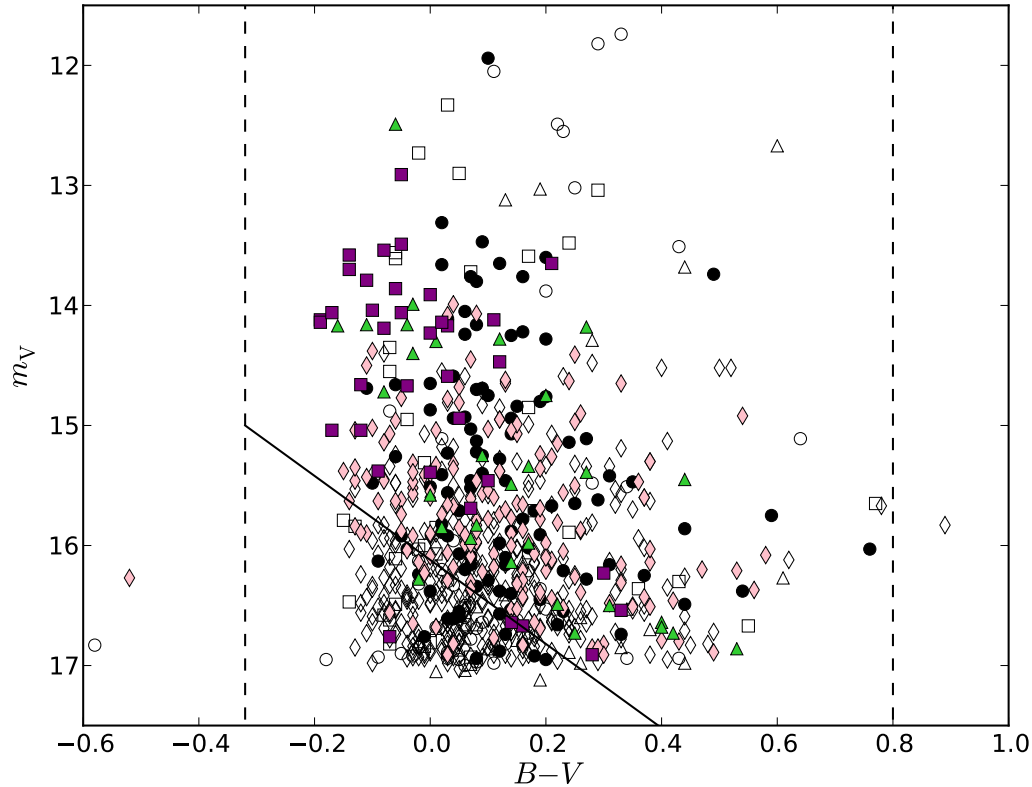


Figure 4.7: A colour magnitude diagram of all the VFTS O-type stars (filled) and B-type stars (open). Photometry is from: Selman (black circles), WFI (pink diamonds), Parker (green triangles), CTIO (purple squares). Solid and dashed lines mark the  $M_V$  and  $B - V$  colour cuts made on the sample, respectively.

visual inspection was made of all of their sources that survived the selection cuts, to ensure that they were, indeed, true stellar sources.

An exception was made when selecting W-R and Of/WN stars. Their notably high contribution to the stellar feedback meant all needed to be accounted for. Some W-R stars were rejected by the selection criteria mentioned due to the unusual colours that can be brought about by their broad emission lines. For this reason, all of the W-R and Of/WN stars given in Table 3.2 were manually entered into the final sample along with any further known W-R stars listed by Breysacher et al. (1999) in the selected region.

A total of 1145 candidate hot luminous stars were finally selected from the photometry via the criteria discussed. These are listed in Table 4.3 which gives an extract of the full census which is accessible at <http://cdsarc.u-strasbg.fr/viz-bin/qcat?J/A+A/558/A134>. The table assigns each candidate star a census identification number and provides its corresponding

astrometry and photometry with accompanying references. A list of well known, but non-exhaustive, aliases are also given. These were obtained through the same proximity method used to match SpTs (discussed in the following section) while individual matching was required in the crowded R136 region.

## 4.5 Spectroscopy

With a list of candidate stars selected, the aim was now to match as many of these as possible to spectral classifications. The best and most extensive spectroscopy of 30 Dor was offered by the VFTS. So far, all of the  $\sim 360$  VFTS O-type stars had been classified including any binary companions, where possible (Walborn et al. 2014). Classification of VFTS B-type supergiants was also complete and will become available in McEvoy et al. (in prep.).

Recalling that the census only sought stars with strong winds and hot ionising photons, in terms of the B-type stars, this concerned all the B-supergiants but only the earliest B-dwarfs and giants. While later B-type stars may be more numerous than their O-type equivalents, their ionising outputs are much smaller. For example, Smith et al. (2002) estimates a single O4 V to produce a thousands times more ionising photons than a B1 V. Therefore, only B-dwarfs and B-giants as late as (and inclusive of) B0.5 V and B1 III, respectively, were desired for the census. Stars later than these SpTs were estimated to have ionising outputs  $< 1000\times$  that of a single O4 V and were considered negligible. Analogous to the criteria used to select the initial census candidates, this process ensured the selection of the earliest B-type stars and prevented the census from being filled with late B-type stars with insignificant ionising contributions.

At the time of this work, classification of the VFTS B-type dwarfs and giants was still to be carried out. The spectra of a remaining 146 VFTS B-type star candidates were therefore inspected. Any spectra displaying a strong Mg II  $\lambda 4481$  line or particularly weak Si IV  $\lambda 4089, 4116$  lines, characteristic of later types, were disregarded. For the remainder, an initial classification was carried out via comparison to the Walborn & Fitzpatrick (1990) spectral atlas (as in Figure 4.8). For the 29 stars that were selected (Table 4.4), a final verification of their SpTs was made with further comparisons to standard Galactic B-type stars from Sota et al. (2011) and Sana et al. (in press.) which accounted for the reduced LMC metallicity that would affect the appearance of the metal and He absorption lines. Details on these VFTS B-type star classifications, as well as the later B-types will be available in Evans et al. (in press.).

Additional non-VFTS matches were made to classifications by Bosch et al. (1999), Walborn & Blades (1997), Parker (1993) and Schild & Testor (1992).

SpT matching was achieved by setting a proximity distance of  $< 1$  arcsec between the posi-

Table 4.3: The candidate hot luminous stars in the census as selected by the criteria explained in Section 4.4. Stars are listed in order of increasing right ascension. The first 20 candidate stars are given here, see online data for full census. References for the photometry are as follows: dM - De Marchi et al. (2011), S - Selman, W - WFI, P - Parker, C - CTIO, Z - Zaritsky et al. (2004) and Wal - Walborn et al. (1999). Common aliases are also included from the following catalogues: VFTS - Evans et al. (2011), HSH95 - Hunter et al. (1995), S99 - Selman et al. (1999), P93 - Parker (1993), ST92 - Schild & Testor (1992) and Sk - Sanduleak (1970) catalogues.

ID #	$\alpha$ (h m s)	$\delta$ ( $^{\circ}$ ' ")	$V$ (mag)	$B - V$ (mag)	Ref.	VFTS	HSH95	S99	P93	ST92	Sk
1	05 36 51.12	-69 05 12.20	16.63	0.67	W	-	-	-	-	-	-
2	05 36 53.82	-69 04 30.13	17.00	0.32	W	-	-	-	-	-	-
3	05 36 55.98	-69 07 36.70	17.36	0.61	W	-	-	-	-	-	-
4	05 36 56.85	-69 05 59.36	17.98	0.68	W	-	-	-	-	-	-
5	05 36 57.18	-69 08 47.40	15.85	0.04	W	-	-	-	-	-	-
6	05 36 57.22	-69 07 23.33	18.33	0.80	W	-	-	-	-	-	-
7	05 36 57.26	-69 05 00.01	15.11	0.69	W	-	-	-	-	-	-
8	05 36 57.62	-69 03 44.04	14.56	0.61	W	-	-	-	-	-	-
9	05 36 58.95	-69 08 21.66	15.33	0.01	W	-	-	-	-	-	-
10	05 37 03.59	-69 10 22.32	16.71	0.32	W	-	-	-	-	-	-
11	05 37 03.91	-69 10 03.60	13.01	0.20	Z	-	-	-	-	-	-
12	05 37 04.01	-69 08 23.83	14.36	0.80	W	-	-	-	-	-	-
13	05 37 04.26	-69 08 05.46	16.18	0.11	W	009	-	-	-	-	-
14	05 37 04.47	-69 04 00.08	15.56	0.20	W	-	-	-	-	-	-
15	05 37 05.63	-69 09 12.20	15.83	0.15	W	012	-	-	-	-	-
16	05 37 06.29	-69 04 41.20	16.36	0.13	W	013	-	-	-	-	-
17	05 37 08.72	-69 04 45.51	17.36	0.47	W	-	-	-	-	-	-
18	05 37 08.88	-69 07 20.39	13.55	0.04	Z	016	-	-	-	-	-
19	05 37 09.68	-69 02 21.39	15.88	-0.02	W	-	-	-	-	-	-
20	05 37 10.17	-69 05 24.10	17.29	0.37	W	-	-	-	-	-	-

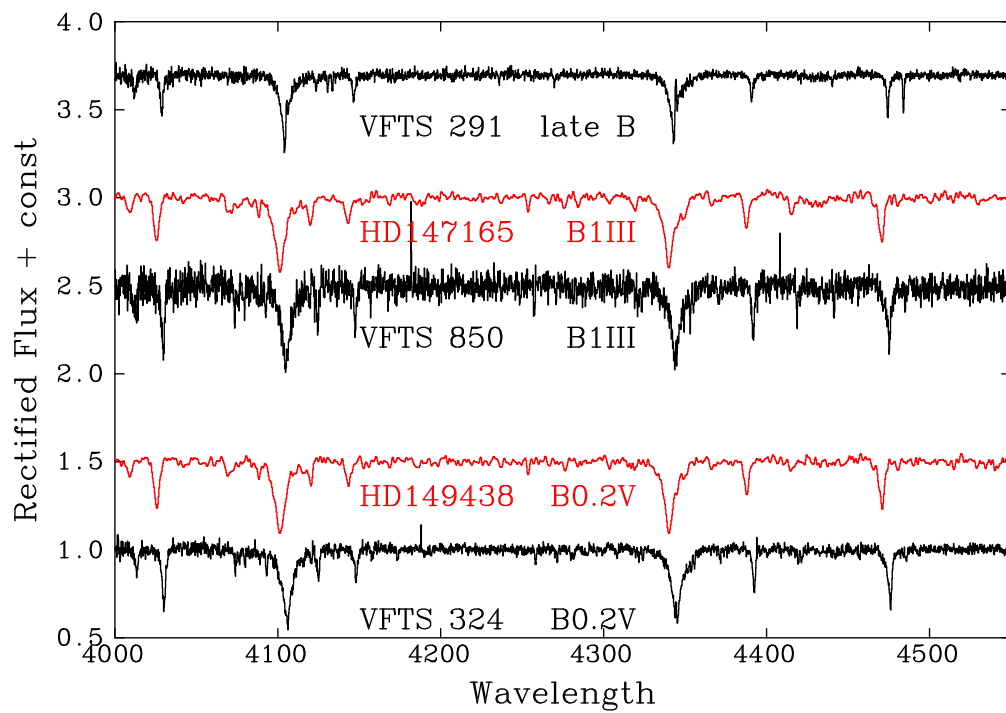


Figure 4.8: Comparison of VFTS B-type stars (black) with standard stars from the Walborn & Fitzpatrick (1990) atlas (red).

Table 4.4: The VFTS B-dwarfs and giants classified for the census. Columns are as in Table 4.3 but include the projected radial distance from star R136a1 ( $r_d$ ) and the SpTs of the B-type stars.

ID #	$\alpha$ (h m s)	$\delta$ ( $^{\circ}$ ' '')	$V$ (mag)	$B - V$ (mag)	Ref.	VFTS	$r_d$ (pc)	SpT
797	05 38 44.91	-69 05 33.10	15.11	0.02	S	575	8.18	B0.7 III
889	05 38 50.27	-69 06 04.36	14.95	0.14	S	646	10.55	B0.5 III(n)
904	05 38 51.77	-69 06 01.16	15.96	0.04	S	659	12.56	B0-0.5 V(n)
470	05 38 39.81	-69 07 10.66	16.72	0.32	W	478	17.29	B0.7 V-III
338	05 38 29.36	-69 05 59.13	16.15	0.05	C	359	17.46	B0.5 V
331	05 38 28.39	-69 06 40.67	15.98	0.08	W	351	20.97	B0.5 V
937	05 38 56.93	-69 06 38.92	16.17	0.05	P	692	21.43	B0.2 V
821	05 38 45.58	-69 07 34.86	15.83	0.15	P	589	23.38	B0.5 V
867	05 38 48.15	-69 07 41.29	16.10	0.14	W	623	25.77	B0.2 V
357	05 38 32.29	-69 07 31.81	16.10	0.20	W	383	26.01	B0.5: V
931	05 38 55.63	-69 07 23.52	14.99	0.17	W	686	26.82	B0.7 III
433	05 38 38.79	-69 04 12.33	15.31	-0.03	W	453	28.06	B0.5 V
369	05 38 33.29	-69 10 23.58	16.32	0.11	W	396	66.29	B0.5 V
1064	05 39 37.21	-69 04 04.31	15.53	0.17	W	817	79.15	B1 III-II
132	05 37 42.25	-69 07 14.12	15.96	0.06	W	121	82.36	B1 IV
256	05 38 08.87	-69 10 39.62	16.83	0.45	W	246	82.40	B1 III
99	05 37 36.82	-69 06 33.01	15.24	-0.06	W	088	88.02	B0-0.2 V-III(n)
1037	05 39 25.10	-69 01 30.55	16.15	0.09	W	788	88.95	B1 III
59	05 37 28.91	-69 06 52.65	15.28	0.09	W	053	99.05	B1 III
60	05 37 28.91	-69 07 06.45	14.55	-0.07	C	052	99.53	B0.2 III-II
308	05 38 21.85	-69 12 47.83	15.53	-0.13	W	324	104.87	B0.2 V
36	05 37 16.68	-69 08 50.12	16.02	0.37	W	024	121.92	B0.2 III-II
232	05 37 57.99	-69 13 09.40	15.84	0.27	W	214	121.97	B0 IV-III
31	05 37 15.08	-69 08 43.00	16.67	0.55	C	022	123.35	B0-0.5 V-III
1099	05 39 51.19	-69 11 53.53	16.15	0.18	W	850	126.95	B1 III
1133	05 40 17.26	-69 06 26.86	15.66	-0.06	W	881	127.03	B0.5 III
1135	05 40 18.04	-69 08 35.75	16.49	0.13	W	883	133.42	B0.5: V
696	05 38 42.78	-69 15 39.77	15.66	0.21	W	534	144.22	B0 IV-III
982	05 39 06.02	-69 15 41.28	16.50	0.35	W	740	147.98	B0.7 III

tion of the photometric candidates and the spectral catalogues. This method relies on accurate and consistent astrometry. The spectral classifications of Bosch et al. (1999) followed on from the photometric work of Selman et al. (1999), and so checks were made to ensure an authentic matching. The same was done for Walborn & Blades (1997) matches who provided a Parker (1993) alias to the stars they classified. For any stars that did become matched with more than one SpT (most likely due to a nearby star in the field of view), the original photometry and that of the spectral catalogue were compared, the SpT with the most consistent photometry being selected.

About 30 classified stars lacked a luminosity class. These were estimated (only for the purpose of calculating stellar parameters) by taking their derived  $M_V$  and comparing them to the average  $M_V$  of stars in the census of a known SpT (see Table 4.8).

Within R136, stars were individually matched to the SpTs of Massey & Hunter (1998), Crowther & Walborn (2011) and Crowther & Dessart (1998), along with a few VFTS star classifications from Hénault-Brunet et al. (2012). For the crowded Brey 73 cluster, the same SpTs obtained by Walborn et al. (1999) were applied.

A total of 31 W-R and Of/WN stars were manually entered into the census. If they were VFTS stars, spectral classifications were taken from Table 3.2, while non-VFTS stars took their classifications from various literature sources: Massey & Hunter (1998), Breysacher et al. (1999) or Crowther & Walborn (2011), and references therein.

Inevitably, duplications occurred, with some stars having been classified in multiple previous studies. As with the photometry, an order of priority was assigned to the literature when selecting a SpT. If available, a VFTS classification (e.g. Taylor et al. 2011, Dufton et al. 2011b, Hénault-Brunet et al. 2012, Walborn et al. (2014), McEvoy et al. in prep. or this work) was always favoured because of the often high data quality and homogeneity of the approach. Otherwise, classifications by Bosch et al. (1999) were adopted, followed by Walborn & Blades (1997) and Schild & Testor (1992) and in turn Parker (1993). Table 4.2 indicates the number of stars classified from each reference. Note that a larger number of stars were matched to spectra as indicated in Table 4.5. Table 4.2 only lists the spectroscopically confirmed hot luminous stars for which stellar parameters and feedback were later determined. Figure 4.9 gives the spatial distribution of the classified stars listed in Table 4.2. Figure 4.10 provides a closer look at the central crowded R136 region.

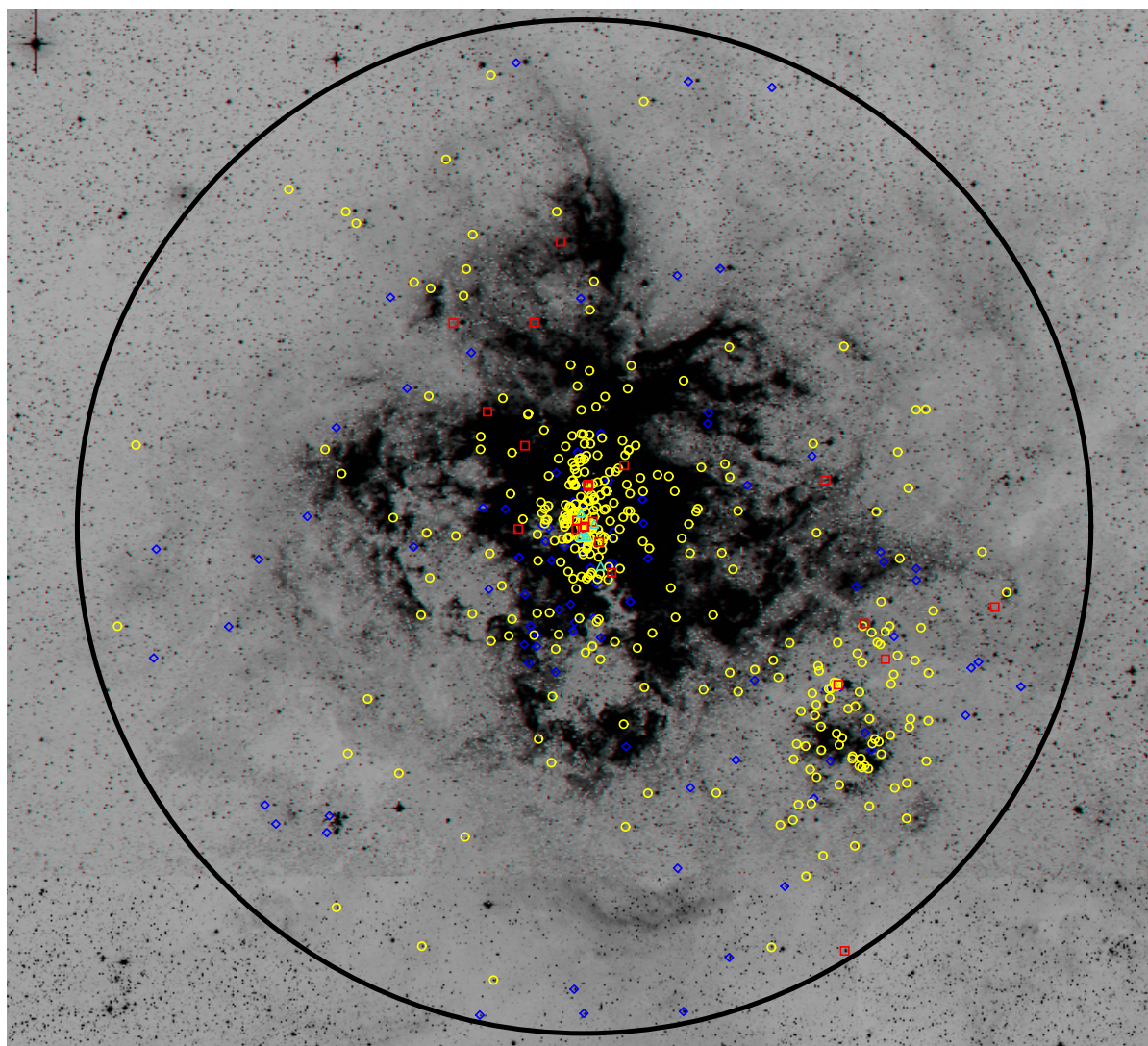


Figure 4.9: All the spectroscopically confirmed hot luminous stars within 30 Dor ( $r_d = 10$  arcmin indicated by the large white circle), overlaid on a V-band WFI image. W-R stars (red squares), Of/WN stars (cyan triangles), O-type stars (yellow circles) and B-type stars (blue diamonds). North is up and east is to the left.

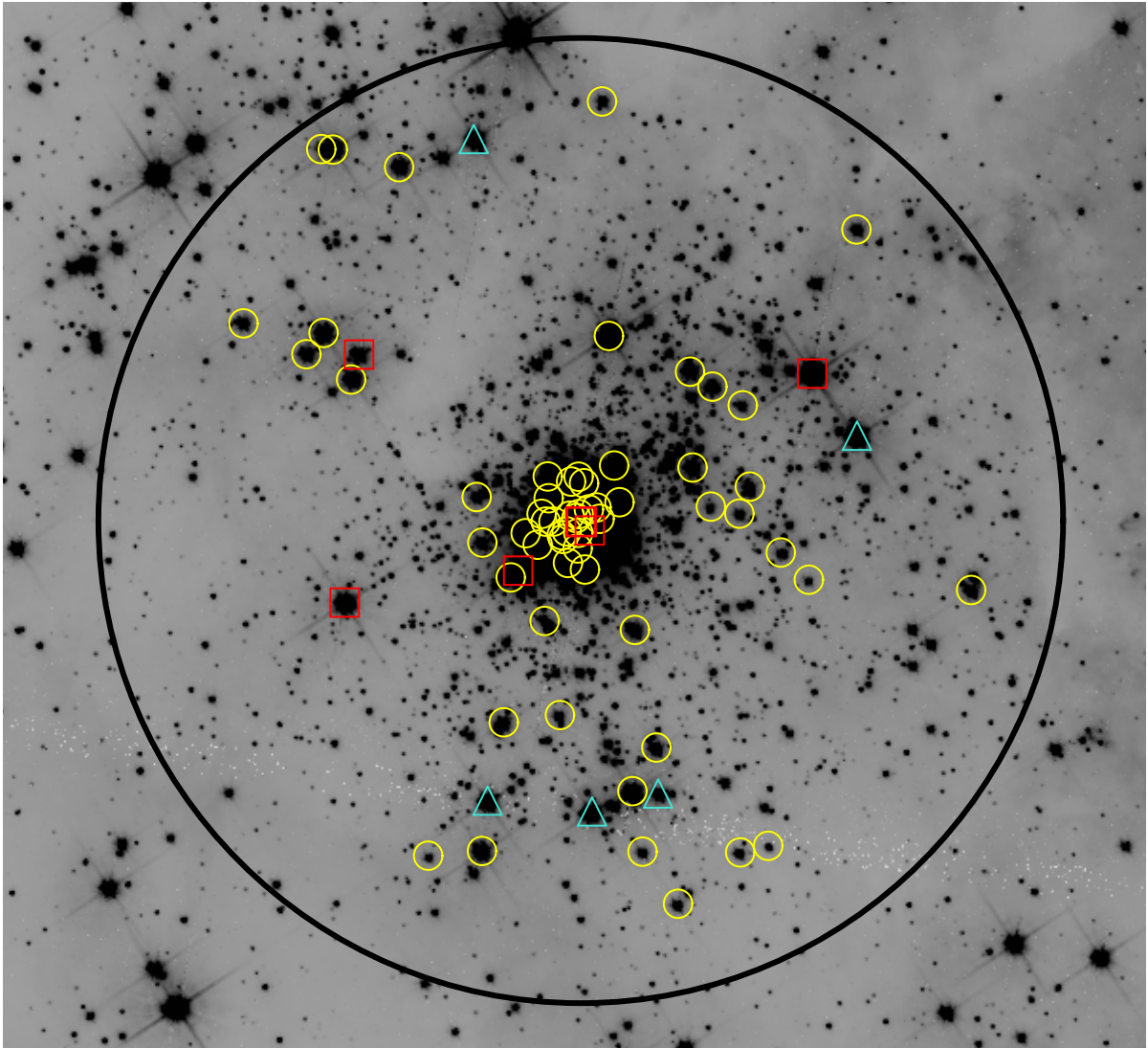


Figure 4.10: All the spectroscopically confirmed hot luminous stars within the R136 region ( $r_d = 20$  arcsec indicated by the large white circle), overlaid on a F555W HST/WFC3 image. W-R stars (red squares), Of/WN stars (cyan triangles), O-type stars (yellow circles). North is up and east is to the left.

Table 4.5: The spectral type distribution of all the stars meeting the photometric selection criteria in Section 4.4.

		Total
ALL STARS		1145
Stars without spectra		463
Stars with spectra	VFTS (% of Total)	non-VFTS
W-R	17 (68)	8 25
Of/WN	6 (100)	0 6
O-type	322 (84)	63 385
B-type	219 (92)	18 237
later than B-type	21 (72)	8 29
Total	585 (86)	97 682

## 4.6 Spectroscopic Completeness

This section aims to estimate the spectroscopic completeness of hot luminous stars in 30 Dor. In particular, the completeness of the VFTS data is determined, as several studies are being carried out upon it. It is therefore important to establish that the VFTS sample does indeed form a majority of the hot luminous stars in 30 Dor, and thus accurately represents their characteristics.

Figure 4.11 presents colour magnitude diagrams, similar to that in Figure 4.7, now including all stars photometrically selected in the census. About 60% of stars in the census have spectroscopy available, either from the VFTS or a previous study. The different morphologies of these stars are shown and also listed in Table 4.5.

Almost 40% of all the candidates lack spectroscopy. However, this fraction rises as one moves to increasingly redder and fainter stars. This is expected since fainter stars are more difficult to observe. As explained in Section 4.4, more contaminant (non-OB) stars will be found in the lower right hand side of Figure 4.11. Ideally, these contaminants would have been removed through the  $Q$ -parameter cut, but the limited availability of  $U$ -band photometry meant this was rarely possible. The key question is what fraction of the unclassified stars are in fact hot luminous stars, and how complete is the spectroscopic coverage of these types of stars, if they are taken into account? Figure 4.11 shows that the stars with spectroscopy are governed by the magnitude limit of the VFTS ( $m_V < 17$  mag). Therefore, an accurate spectroscopic completeness level can only really be estimated for stars brighter than this limit.

From this point onwards, a separate region is defined, the ‘MEDUSA region’ ( $0.33 < r_d < 10$  arcmin) along with the previously defined ‘R136 region’ ( $r_d < 20$  arcsec). Using a distance modulus of 18.49 mag these regions span projected radii of about  $5 < r_d < 150$  pc and  $r_d <$

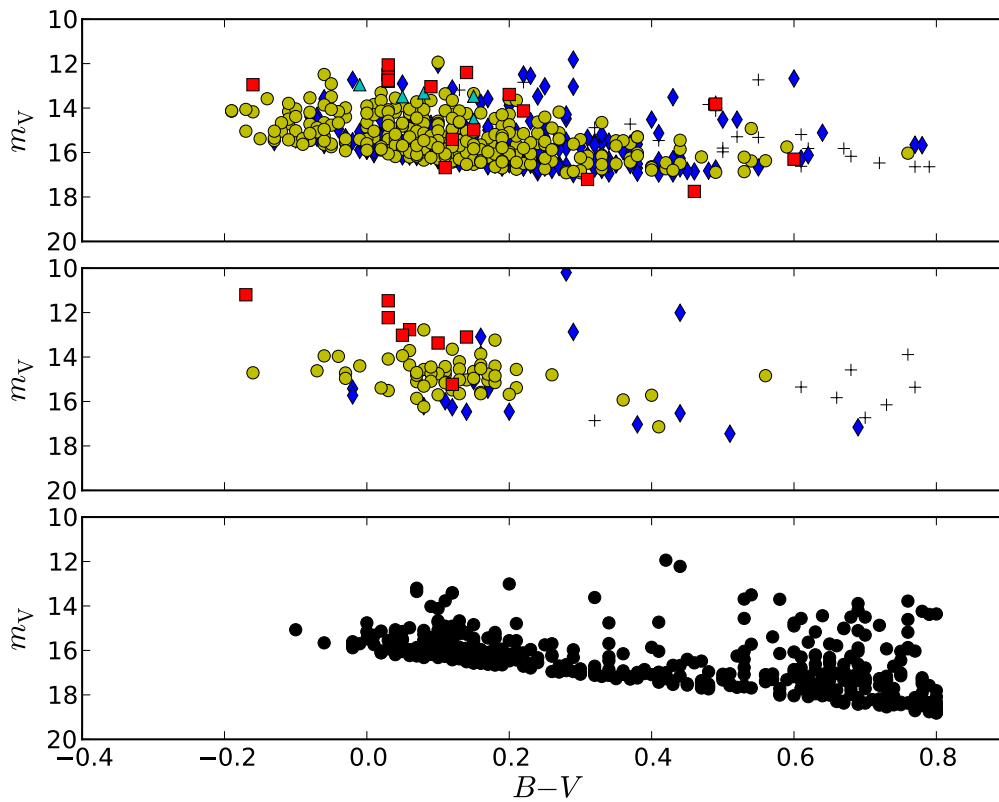


Figure 4.11: Colour magnitude diagrams of all the stars meeting the selection criteria. Stars with VFTS spectral classification (top), stars with non-VFTS spectral classification (middle) and stars with no spectral classification (bottom). Key for classified stars: W-R stars (red square), Of/WN stars (cyan triangle), O-type stars (yellow circle), B-type stars (blue diamond) and stars later than B-type (crosses).

5 pc, respectively. This allowed for a less biased measure of the spectroscopic completeness of the VFTS, since its FLAMES/MEDUSA observations largely avoided the R136 vicinity because of crowdedness.

#### 4.6.1 Spectroscopic completeness in the MEDUSA region

Figures 4.12a & 4.12b show histograms of the fraction of photometric candidates for which spectroscopy was available, in relation to magnitude and colour, respectively. Within the MEDUSA region, 80% of candidates have been spectroscopically observed, of which about three quarters were included in the VFTS. Of these, only a subset will be spectroscopically confirmed as hot luminous stars. These are the stars given in Table 4.6.

In an attempt to obtain an accurate completeness level for the region, Figure 4.13a gives the fraction of stars that are spectroscopically confirmed as hot luminous stars as a function of colour. Moving redward of the typical O-type star intrinsic colour  $(B - V)_o = -0.32$  mag, the fraction is seen to fall from unity as more contaminants populate each colour bin. At high values of  $B - V$ , these fractions become poorly constrained as a result of small number statistics. By accounting for the fraction of contaminants, a new completeness plot can be made as shown in Figure 4.13b which, unlike Figure 4.12b, has had the predicted contaminant stars removed. Applying this correction, the completeness of the hot luminous stars is estimated at 84%, of which 76% were included in the VFTS.

#### 4.6.2 Spectroscopic completeness in the R136 region

Figure 4.14a shows that only the brightest targets ( $\approx 35\%$ ) in the R136 region have archival spectroscopy, primarily obtained with HST/FOS by Massey & Hunter (1998), with the VFTS covering only a limited number of stars through its FLAMES-ARGUS observations (see Evans et al. 2011; Hénault-Brunet et al. 2012). A breakdown of their SpTs is listed in Table 4.7. This will be improved following new HST/STIS spectroscopy of the central parsec (GO 12465/13052 Crowther et al. 2014). The colours of these unclassified stars plotted in Figure 4.14b suggests that they are predominantly early type stars i.e. mid-late O-type stars having eluded spectroscopic confirmation, simply because they are faint. More importantly, completeness is still high at the brighter end, and includes the more luminous W-R, Of/WN and supergiant stars which will contribute most to the feedback of the region. Therefore, 35% of the hot luminous stars are estimated to have been spectroscopically observed so far.

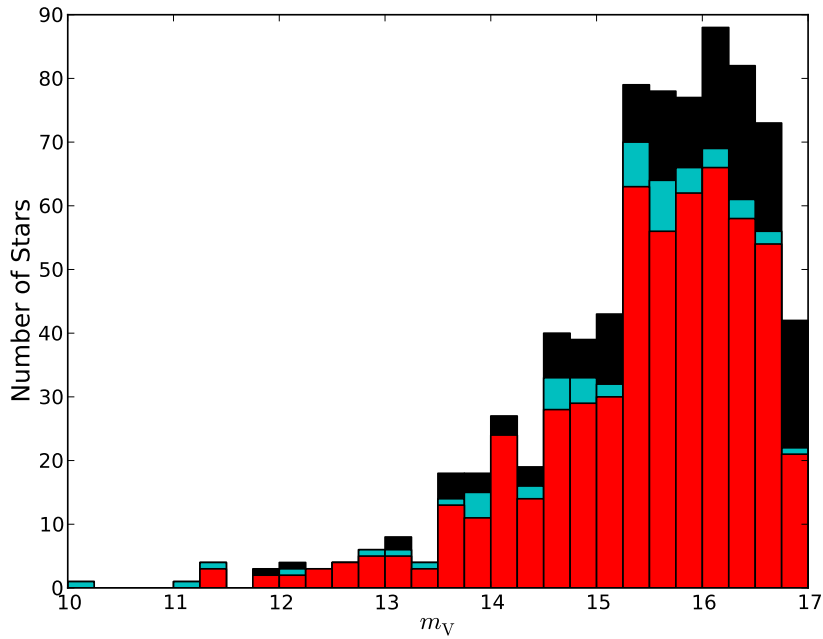
Table 4.6: The spectral type distribution of the spectroscopically confirmed hot luminous stars within the MEDUSA region ( $5 < r_d < 150$  pc)

W-R and Of/WN stars	WR 2-WR 5		WR 6-WR 9	Total
WN/WNC	7		8	15
WC	3		0	3
Of/WN	0		1	1
Total	10		9	19
O-type stars	O2-O3.5	O4-O6.5	O7-O9.7	Total
V	15	60	143	218
III	5	11	66	82
I	2	3	20	25
Total	22	74	229	325
B-type stars	B0-B0.7		B1 and later	Total
V	23		-	23
III	19		4	23
I	12		26	38
Total	54		30	84
GRAND TOTAL				428

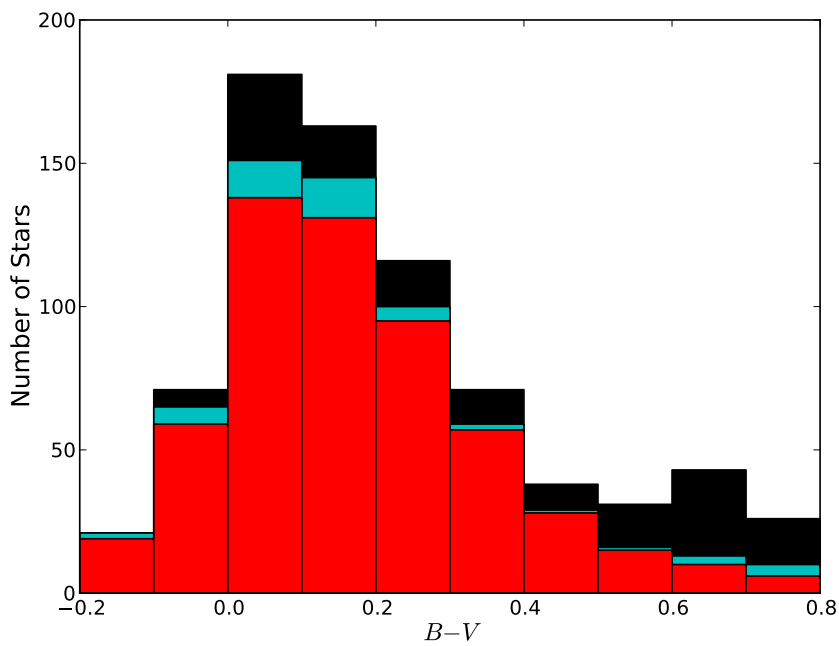
**Note.** The numbers given for B-type stars are not complete for 30 Dor. The reader is reminded that later B-type stars were omitted from the census, both during the selection criteria and afterwards due to their negligible contributions to the feedback. These included dwarfs later than B0.5 V and giants later than B1 III. All selected supergiants were included. The completeness of the W-R, Of/WN and O-type stars is discussed in Section 4.6.

Table 4.7: The spectral type distribution of the spectroscopically confirmed hot luminous stars within the R136 region ( $r_d < 5$  pc).

W-R and Of/WN stars	WR 2-WR 5		WR 6-WR 9	Total
WN/WNC	5		1	6
WC	1		0	1
Of/WN	3		2	5
Total	9		3	12
O-type stars	O2-O3.5	O4-O6.5	O7-O9.7	Total
V	19	11	11	41
III	9	0	2	11
I	4	4	0	8
Total	32	15	13	60
GRAND TOTAL				72

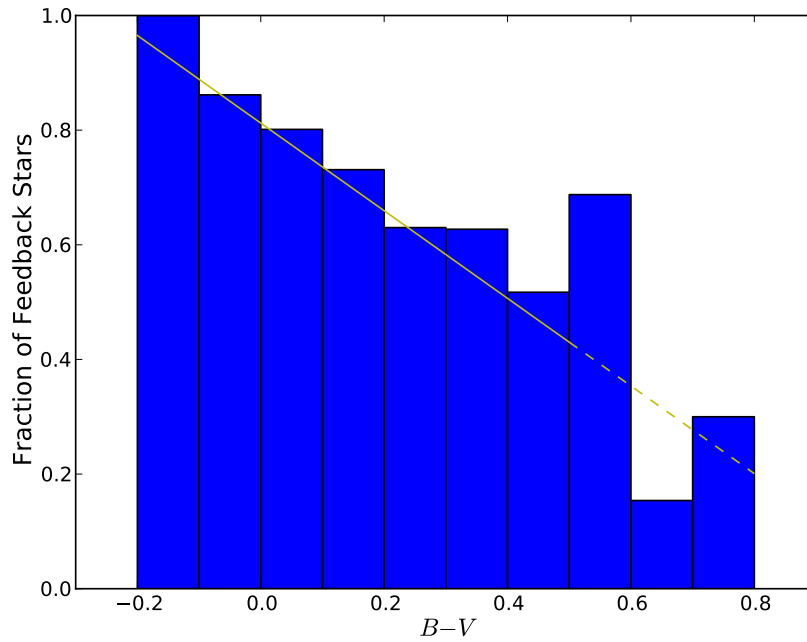


(a)

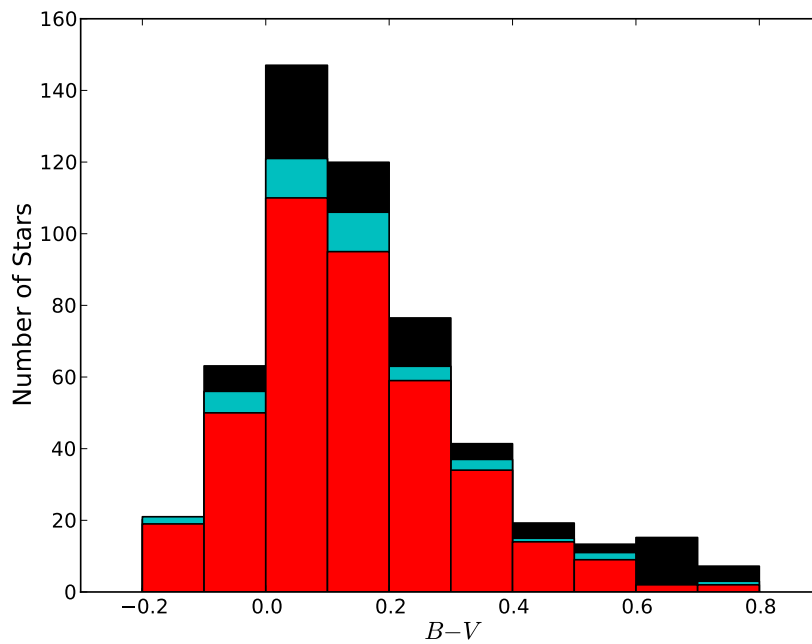


(b)

Figure 4.12: Spectroscopic completeness in the MEDUSA region. Figure (a) plots the spectroscopic completeness with respect to  $m_V$ , of all stars meeting the selection criteria and with  $m_V < 17$  mag. Figure (b) plots the same spectroscopic completeness with respect to  $B - V$ . Stars with VFTS spectroscopy (red), stars with non-VFTS spectroscopy (cyan) and stars with no spectroscopy (black).

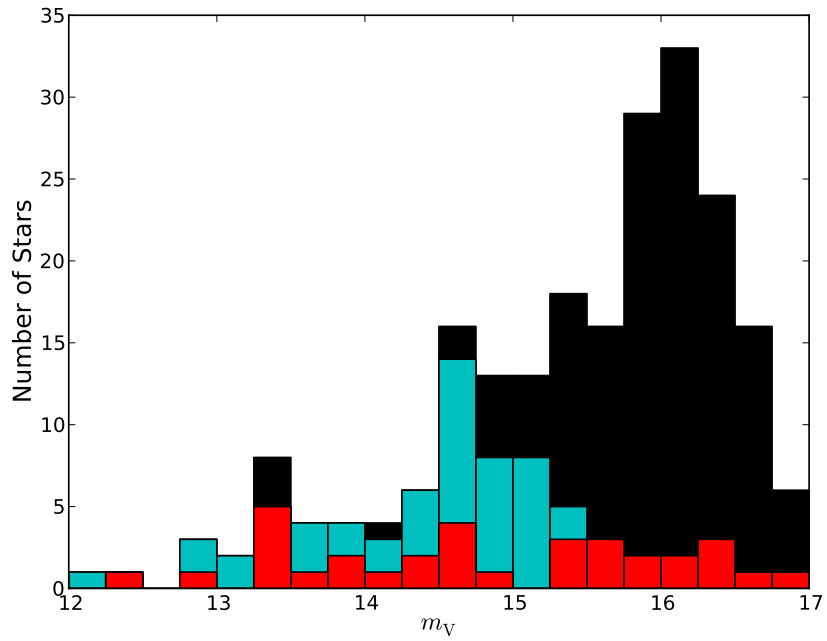


(a)

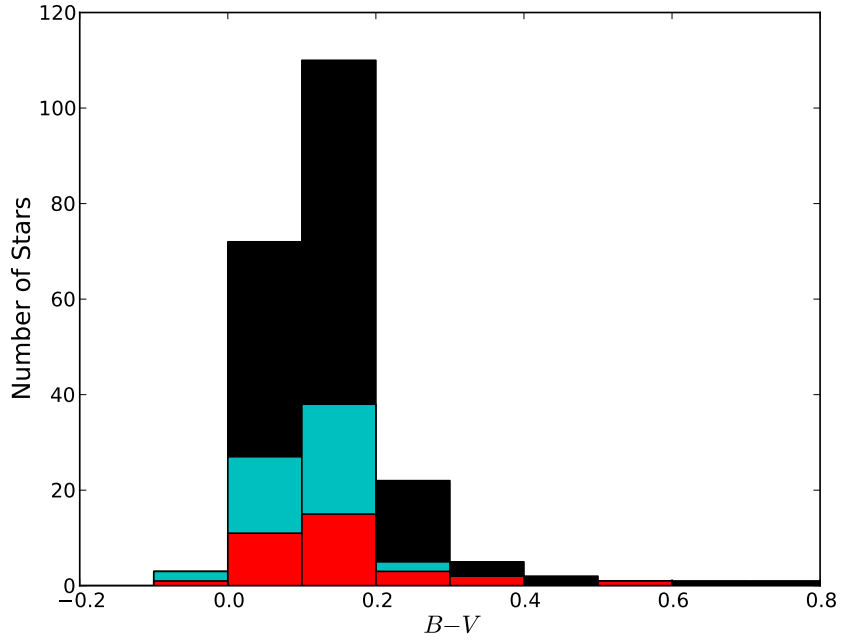


(b)

Figure 4.13: Spectroscopic completeness in the MEDUSA region accounting for contaminant stars. Figure (a) plots the fraction of stars meeting the selection criteria with both  $m_V < 17$  mag and spectra, and which were also spectroscopically confirmed to be hot luminous stars. A low order polynomial was fitted to the distribution (solid line) and extrapolated redward of  $B-V = 0.5$  mag (dashed line). Figure (b) plots the spectroscopic completeness of hot luminous stars with  $m_V < 17$  mag in the MEDUSA region, with respect to  $B-V$ . Colours are as in Figure 4.12.



(a)



(b)

Figure 4.14: Spectroscopic completeness in the R136 region. Figures (a) and (b) are the same as Figures 4.12a and 4.12b, respectively, only showing completeness in the R136 region. Colours are also identical.

### 4.6.3 Stars that are unaccounted for

While the census attempts to include all the hot luminous stars in 30 Dor, the following factors may have prevented certain candidates from entering the final sample.

1. *Crowding* - The four primary photometry catalogues (Selman, WFI, Parker, CTIO) provided sound coverage of 30 Dor. Potential concern arises in dense regions where candidates may have been lost as a result of less reliable photometry.
2. *High extinction* - An average extinction of  $A_V \approx 1.5$  mag is calculated for 30 Dor, with the selection criteria allowing for extinctions as high as  $A_V = 3.92$  mag. For some stars, the extinction will be higher than this limit. In particular, young embedded stars will have evaded selection through their surrounding gas and dust but could still contribute to the stellar feedback (see Section 5.4.3).
3. *Spectroscopic Completeness* - Section 4.6 showed a good spectroscopic completeness for the census, but the remaining stars lacking spectroscopy are still important and their contribution is considered in Section 4.6.4. Furthermore, the magnitude coverage of the spectroscopy was limited to  $m_V < 17$  mag. This means that a few faint and highly reddened hot luminous stars could also have avoided classification.
4. *Binary systems* - Stars found in binary systems will provide further candidates through their companions as well as changing the photometric properties of each component. Section 5.2.5 addresses the case of double-lined (SB2) binary systems where a knowledge of both stars can provide a combined feedback contribution but single-lined (SB1) binary systems and any further unknown multiple systems, remain uncertain.
5. *Unresolved stellar systems* - Spectroscopic binary detection is limited to shorter periods of a few days. While HST imaging is capable of revealing likely composite spectra, many large separation and/or line of sight systems will still appear single and are so far unidentified.

### 4.6.4 Correcting for unclassified stars

The spectroscopic census provides lower limits to the true stellar feedback of 30 Dor. Section 4.6.1 looked at removing the estimated number of contaminant stars in different colour bins. Even after applying this method to determine the true number of hot luminous stars, some still lacked spectroscopy. For the MEDUSA region, a total of 152 of the candidates ( $m_V < 17$  mag) lacked spectroscopy, of which it was estimated that only  $\approx 50\%$  would actually be

hot luminous stars. Meanwhile, in R136, 141 candidates ( $m_V < 17$  mag) lacked spectroscopy, but in this case all were taken to be hot luminous stars capable of contributing to the feedback. This is a reasonable assumption given that all other R136 stars in the census are classified as W-R, Of/WN or O-type stars. Furthermore, as noted earlier, the magnitudes and colours of these unclassified stars suggest them to be mid-late O-type stars.

Voges et al. (2008) estimated the SpT of unclassified stars in their LMC H II regions using a colour-SpT calibration. It was based on  $U$ - and  $B$ -band magnitudes as these lay closest to the peaks in the spectral distributions of the OB stars. However, this approach relied upon accurate photometry, and in the case of the  $U$ -band, this was only available for a select number of stars. An alternative method was to derive the  $M_V$  for each star. Photometry was already known and extinction laws had been used throughout the census. OB stars are found to have a typical intrinsic colour of  $(B - V)_o = -0.3$  mag, showing only a small ( $< 0.05$  mag) spread (Conti et al. 2008) so this value was adopted for the unclassified stars in the census.

Meanwhile, the classified stars in census had been used to produce Table 4.8. It lists the average  $M_V$  found for each SpT in the census. Some SpTs are grouped given the limited numbers. The dwarfs were found to be consistent with the earlier  $M_V$  calibration of Walborn (1973) while the giants and supergiants showed a broader agreement due to limited data. With the  $M_V$  of all the unclassified stars at hand, their SpTs were assigned by matching to the most equivalent value found in Table 4.8. Some crude assumptions had to be made when more than one luminosity class was suggested by a  $M_V$  but in R136, stars were largely taken to be dwarfs. All W-R and Of/WN stars were assumed to be already accounted for.

The  $M_V$  was therefore calculated for each star, assuming a common intrinsic colour of  $(B - V)_o = -0.3$  mag. Its SpT was then estimated based on this  $M_V$ , using the average  $M_V$  found for each SpT in the rest of the census. These averages are listed in Table 4.8. The dwarfs were found to be consistent with the earlier  $M_V$  calibration of Walborn (1973) while the giants and supergiants showed a broader agreement due to limited numbers. Some crude assumptions had to be made when more than one luminosity class was suggested by a  $M_V$  but in R136, stars were largely taken to be dwarfs. All W-R and Of/WN stars were assumed to be already accounted for.

This addition of photometrically classified stars offers an even better view on the stellar population, and so are combined with the original spectroscopically classified stars (Sp+Ph) in later analysis. Stars solely classified from spectroscopy (Sp) will still be the most reliable, however, so comparisons are made between the two samples throughout the following chapter.

Table 4.8: The average absolute magnitudes of O and B0 stars in the census.

SpT	Luminosity Class								
	V			III			I		
	$M_V$	$N$	$\sigma$	$M_V$	$N$	$\sigma$	$M_V$	$N$	$\sigma$
O2	-5.6	5	0.5	-5.9	14	0.3	-6.3	6	0.6
O3	-5.5	22	0.4						
O3.5	-5.0	8	0.5						
O4	-4.8	13	0.5	-5.7	5	0.5	-6.2	5	0.6
O5	-4.7	14	0.4	-5.6	4	0.4			
O5.5									
O6	-4.7	17	0.5	-5.5	7	0.2			
O6.5	-4.4	18	0.6						
O7	-4.7	18	0.5						
O7.5	-4.7	13	0.5	-4.9	11	0.4			
O8	-4.4	20	0.4						
O8.5	-4.4	18	0.5						
O9	-4.3	25	0.5	-4.9	8	0.5			
O9.5	-4.0	43	0.4	-4.6	14	0.5			
O9.7	-3.9	12	0.3	-4.0	22	0.4			
B0	-3.8	11	0.3	-					

**Notes.** The number of stars ( $N$ ) the average  $M_V$  is based on, and their spread ( $\sigma$ ), are both given. Note the number of stars used to determine these magnitudes varies from those in Table 4.5 as some stars were omitted due to spurious values.

Table 4.9: The brightest *Swift* UVOT sources not identified in the census

ID/RA, Dec #/(h m s), ( $^{\circ}$ ' ")	VFTS (#)	SpT	$r$ (")	$F_{2250}$ ( $\text{erg s}^{-1} \text{cm}^{-2} \text{\AA}$ )
BI253	72	O2 V	467	$1.8 \times 10^{-13}$
05:37:07.7, -69:05:06	-	-	509	$7.3 \times 10^{-14}$
R138	424	A0 Iab	33	$9.4 \times 10^{-14}$
Melnick 1	732	B2 I	165	$9.4 \times 10^{-14}$

### 4.6.5 Queries with candidate selection

Upon completion of this study, a mosaic UV image of the LMC was acquired by the UV/optical telescope (UVOT) aboard the *Swift* Gamma Ray Burst Explorer using the M2 filter at 2250 Å. The spatial resolution in the UV ( $\sim 2''$ ) approaches that of ground-based optical images. With hot luminous stars emitting in the UV, the *Swift* imaging of 30 Dor offers a direct view of the stars the census was seeking to identify. The candidate hot luminous stars in Table 4.3 were overlaid on the *Swift* data to show a generally good overlap with stars in the image, although this comparison was only possible beyond the R136 region where crowding was reduced. Some candidates had no underlying stars at their positions but this could be explained by large amounts of extinction, something the UV imaging would be more susceptible to. However, some bright UV stars were found not to be matched to a candidate, indicating that the selection criteria had failed to include at least some hot luminous stars.

Further inspection revealed that some of these “missing” stars were included in the original photometric catalogues but had been removed as a result of the  $Q$ -parameter cut. This would question the reliability of their  $U$ -band photometry, but the stars could be easily re-entered into the census. Other cases were more complicated suggesting hot luminous stars had been omitted due to a combination of astrometric differences and human error. Excluding the cluster core, Table 4.9 lists all sources within 10 arcmin of R136a1 with fluxes brighter than  $F_{2250} > 7 \times 10^{-14} \text{ erg s}^{-1} \text{cm}^{-2} \text{\AA}$ . Of these, BI 253 being an early O-type star would be the most critical omission. However, the omission of A-type stars is less of a concern and their appearance on the *Swift* imaging shows that they can also be bright in the UV. Following this finding, the estimates for completeness discussed in Section 4.6 are therefore open to more uncertainty. Nevertheless, the overall conclusions from the census discussed here and in Chapter 5 remain reliable.

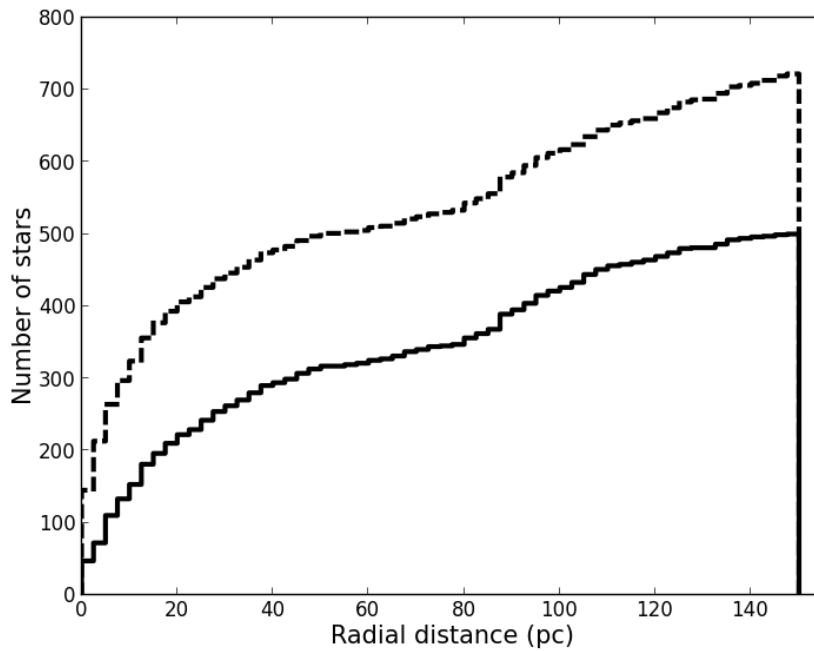
## 4.7 Spectral Types and Distribution

Even prior to determining the stellar properties, the census offers information on the different morphologies of stars in 30 Dor and their distribution across the region. Figure 4.9 already showed the spatial distribution of the hot luminous stars. Figures 4.15a & 4.15b now plot this information in a radial format. The stellar density is shown to be significantly higher in the central 20 pc, with close to half of the hot luminous stars residing here. They correspond to the young R136 cluster while the older outer regions are less populated as would be expected. A notable bump is also seen at a radial distance of 80 – 110 pc, which coincides with the cluster LH 99, located to the south-west of R136.

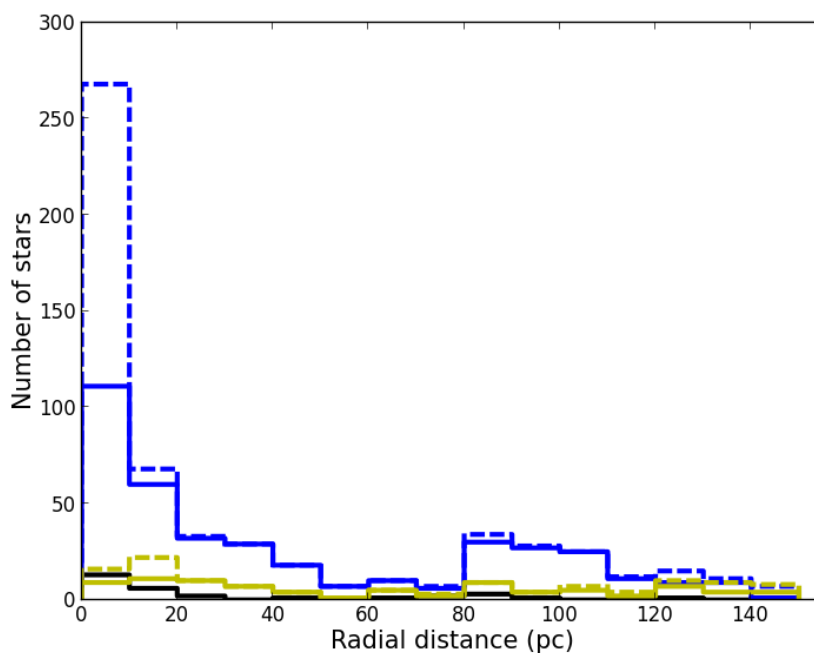
The stellar ages could be reflected by the O/B-type star ratio found at each distance. As a group of coeval stars evolve, this ratio will gradually decrease as the O-type stars die out. This may seem apparent at radii beyond 120 pc (Figure 4.15b) but it is noted that many late B-type stars were omitted from the census. Furthermore and at larger distances, each radial bin plotted will not necessarily represent a single coeval group of stars. A better representation is perhaps given by Figure 4.16a which shows the radial distribution of the different O-type star luminosities. No O-type stars were omitted from the census and the older, more evolved giants and supergiants are found to be more common in the outer periphery, relative to the younger dwarfs.

In addition, Figure 4.16b plots the distribution of W-R and Of/WN stars. Similar to the O-type stars, more than half of the WN stars are concentrated in the inner 20 pc, with many of the others being found at  $\sim 80$  pc. Essentially all of the WN stars in 30 Dor are H rich, implying they have not undergone significant evolution from the main sequence as other classical H poor WN or WC stars would have done. Indeed, in the case of more massive stars, the transition from main sequence to WN may be remarkably quick (recall Section 3.7.5). Interestingly, all but one of the Of/WN stars are located within the R136 region ( $< 5$  pc) and the remainder also lies close by ( $< 15$  pc). The WN and Of/WN stars would therefore also appear to mark out the younger regions of 30 Dor. The WC stars would then naturally represent the older regions but their brief phase leaves just four in the census, too few to analyse.

While using the stellar morphologies gives some clues to the age of the population, a more quantitative approach is required. Determining how the rotational velocities of stars are distributed across 30 Dor (Ramírez-Agudelo et al. 2013) will play a key role in understanding where and when star formation has taken place. A further assessment of the age of 30 Dor is made in Chapter 5, with the use of isochrones, once the individual stellar properties have been established.

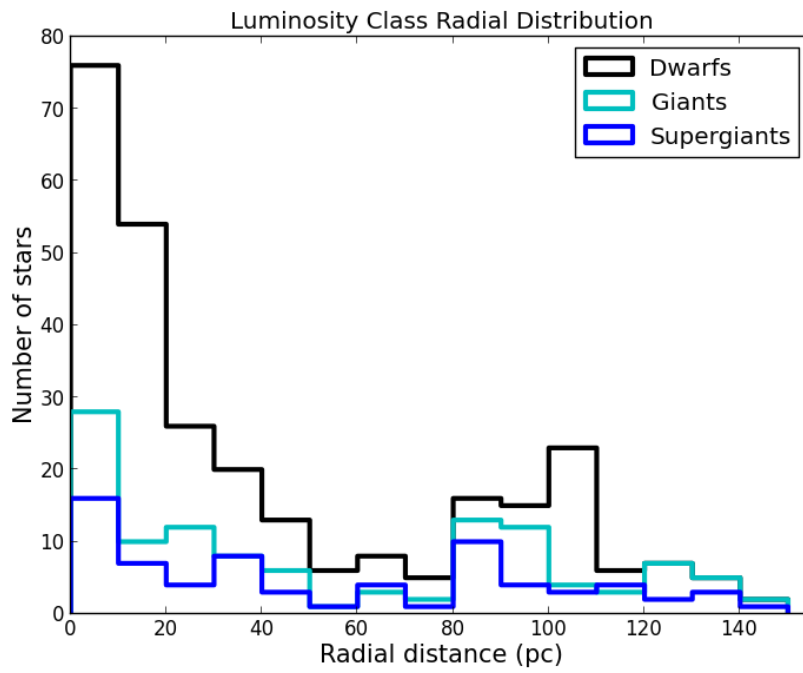


(a)

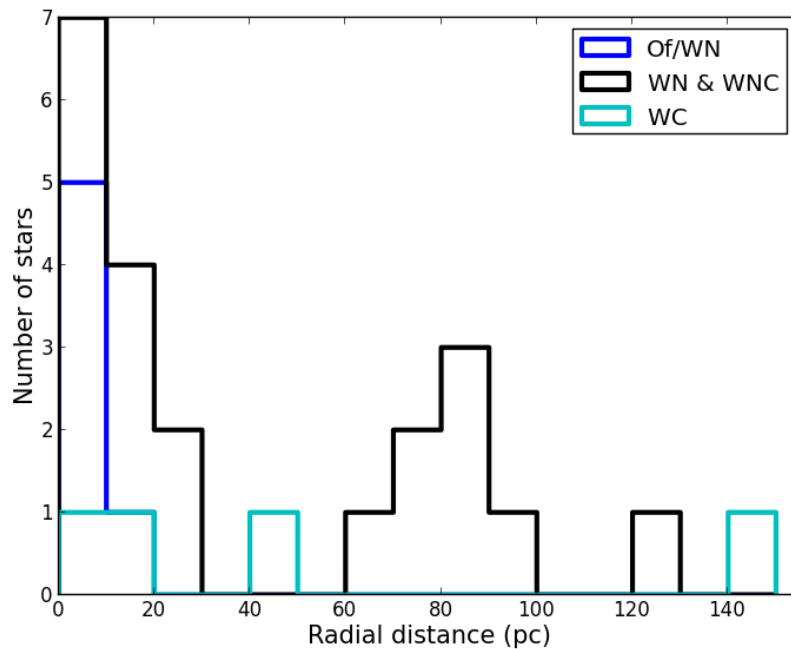


(b)

Figure 4.15: Radial distribution of all hot luminous stars in the census. Figure (a) plots the cumulative distribution of stars. Figure (b) gives a breakdown of the spectral morphologies: W-R or Of/WN stars (black), O-type stars (blue), B-type stars (yellow). A solid line represents stars that were spectroscopically classified (Sp), a dashed line represents stars that were spectroscopically and photometrically classified (Sp+Ph).



(a)



(b)

Figure 4.16: Radial distribution of O-type (a) and W-R and Of/WN (b) stars.

## 4.8 Summary

The global properties of 30 Dor can be obtained directly from its individually resolved stars or through observations of the entire region. For extragalactic star forming regions, only the latter is a possibility. As one of the most massive and closest star forming regions, 30 Dor therefore serves as the ideal template for more distant targets. Following spectroscopic observations from the recent VFTS, this has given rise to the compilation of the most extensive census of hot luminous stars in the region. The census extends out to a radial distance of 10 arcmin from the centre of 30 Dor, where stars have been selected by different criteria, based on their *UBV*-band photometry. These selected stars were then matched to as many spectral classifications as possible to confirm their hot luminous nature. Further SpTs were estimated using photometry, to account for any additional hot luminous stars which lacked spectroscopy. All the stars were chosen on the basis of the large radiative and mechanical feedback they provide to the region.

Overall, a total of 1145 candidate hot luminous stars were photometrically selected in the census of which 722 were believed to be relevant in the context of feedback. Spectroscopy was available to confirm 500 of these, including: 25 W-R stars, 6 Of/WN stars, 385 O-type stars and 84 B-type stars. The spectroscopic completeness of the census varies, as stellar crowding has limited the available data. Completeness typically reaches  $\sim 85\%$  down to  $m_V = 17$  mag, but falls to  $\sim 35\%$  in the central R136 cluster. In both cases, however, the census shows good spectral completeness of the brightest and bluest stars.

The census stars were predominantly located within the central regions of 30 Dor. Over half of the O-type and WN star samples were found in the inner 30 pc. They help reflect the younger populations in the region and will make the prime contribution to its feedback. The subsequent chapter parameterises each star to quantitatively derive this feedback and further allow extragalactic calibrations to be tested.

# Chapter 5

## The Mechanical and Radiative Stellar Feedback of 30 Doradus

*Details on determining the stellar feedback of 30 Dor are published in Doran et al. (2013) with a complete table of spectroscopically confirmed hot luminous stars (Table 5.9) available at <http://cdsarc.u-strasbg.fr/viz-bin/qcat?J/A+A/558/A134>. Analysis of the O2 stars (Section 5.2.1) is published in Doran & Crowther (2011) where atmospheric modelling was carried out by P. A. Crowther. Values for  $F(\text{H}\alpha)/F(\text{H}\beta)$  and  $A_{\text{H}\alpha}$  (Section 5.6.3) were also determined by P. A. Crowther.*

### 5.1 Introduction

In Chapter 4, a census of the hot luminous stars in 30 Doradus was compiled. Individual photometry was obtained and a SpT assigned to as many stars as possible. Individual parameters for the stars can now be determined and compared to global properties, allowing 30 Dor to be used as a laboratory for testing a range of codes and calibrations.

Prior to the census, details of the 30 Dor stellar population were primarily estimated through indirect methods: a technique that is usually relied on for extragalactic targets. Vacca et al. (1995) observed the UV continuum spectrum of 30 Dor with the IUE and compared it to spectral synthesis models to make estimates of the population of O-type stars, their age and upper mass limit. Their observations were approximately centred on R136 and spatially covered  $20'' \times 20''$ ,  $1' \times 1'$  and  $3' \times 3'$  regions. All of these overlap, with the census, with Vacca et al. (1995) estimating an age of  $\sim 3$  Myr and over 200 O-type stars to lie within the largest region. This estimate agrees well with the census, although W-R stars tend to be underpredicted. However, these numbers are particularly dependent on what star formation history is adopted

as well as the upper cutoff mass applied to the IMF. Inclusion of the most massive stars could be crucial to obtaining an accurate model of a star forming region. Furthermore, the models used by Vacca et al. (1995) are about 20 years old, such that more recent developments in the understanding of stellar atmospheres had not been incorporated.

In this chapter, the widely used population synthesis code *Starburst99* is used to recreate the radiative and mechanical feedback of the R136 cluster. With the census now providing the true stellar population numbers, the importance of massive stars is reassessed with the application of updated stellar calibrations. The feedback made by different SpTs, is also estimated for both the R136 region and 30 Dor as a whole. The significance of W-R stars to the integrated properties of young star clusters was demonstrated by Crowther & Dessart (1998). They estimated a contribution of 15% and 40% to the ionising outputs and wind luminosities, respectively, within the inner 10 pc of 30 Dor. However, their results were also based on dated calibrations and non-line blanketed W-R models. Renewed treatment of the W-R stars (several of which are amongst the most massive in the census) determines if this is still consistent.

There will be additional sources of feedback, in particular, from shocks and supernovae, but this study focusses on the stellar contributions. Indeed, photoionisation from stars is believed to be the dominant process in 30 Dor. Indebetouw et al. (2009) studied the IR emission lines to determine the physical conditions of the ionised gas. The ionic line strengths from their models favoured photoionisation, with higher excitation noted in the R136 cluster and along its surrounding bubble. They particularly noted regions with more intense and harder radiation, as they typically coincided with hot isolated stars. Their “Source A” located along the molecular ridge to the north of R136 and “Source E” located to the east of R136, both correspond with the positions of the W-R stars R140a+b and R145, respectively. This again reflects the importance of the W-R stars, with Indebetouw et al. (2009) suggesting that with increasing distance from R136, they could potentially influence over the large scale effects of the cluster. Interestingly, they highlight another region they denote “Source D” to the north-east of R136 which correlates with high excitation and relatively high extinction. At the time, no hot stars were matched to the region, but the VFTS has since revealed it to coincide with the newly discovered WN 5h star VFTS 682 (Section 3.5.3).

Pellegrini et al. (2010) performed a similar study on 30 Dor using optical emission lines. They too found line ratios consistent with photoionisation, and with R136 dominating the ionisation field. Nearly all the observed bright pillars and ionisation fronts led back to the central cluster. However, contrary to Indebetouw et al. (2009), they expected the ionising effects of isolated stars to be negligible compared to R136. Only the OB star association LH 99 (identified in Figure 4.15b), appeared to provide notable ionisation fronts of its own.

As discussed in Chapter 2, the ionising radiation from the stars not only excites the gas but

has the potential to escape the region altogether. Further comparisons are made with nebular observations to try and quantify what proportion of the stellar feedback might achieve this and not ionise the gas or heat the surrounding dust. As a result, more accurate estimates can be made of parameters such as stellar content, age and SFR, not just in 30 Dor but all star forming regions, as synthesis models are refined.

## 5.2 Stellar Properties

This work specifically sought to derive the radiative and mechanical stellar feedback. Firstly, the Lyman continuum ionising flux ( $q_0$ ) was determined. This is related to the total number of ionising photons emitted by the star per second ( $Q_0$ ) via  $Q_0 = 4\pi R^2 q_0$ , where  $R$  is the stellar radius at a Rosseland optical depth of two thirds ( $R_{2/3}$ ), or in the case of W-R stars, an optical depth of  $\sim 10 (R_*)$ . Similarly, if the effects of supernovae are omitted, the primary source of mechanical feedback is that produced by the stellar winds. The stellar wind luminosity ( $L_{SW}$ ) was calculated via  $L_{SW} = \frac{1}{2} \dot{M} v_\infty^2$ , where  $\dot{M}$  is the mass-loss rate of the star,  $v_\infty$  is the terminal velocity of the stellar wind and  $L_{SW}$  is given in units of  $\text{erg s}^{-1}$ . In addition, the modified wind momentum  $D_{\text{mom}} = \dot{M} v_\infty R^{0.5}$  was also calculated, with  $D_{\text{mom}}$  in cgs units.

Given their important role in feedback contribution, the properties of the W-R and Of/WN stars were based on atmospheric models and templates as already discussed in Section 3.7. A variety of calibrations were employed to supply parameters for the OB stars needed to determine their feedback. Details on these different methods are discussed below.

### 5.2.1 Modelling of early O-type stars

The stellar calibrations of Martins et al. (2005) are widely used to obtain individual parameters for a sample of stars. However, they come with their limitations. In particular, Martins et al. (2005) based their work on Galactic stars but many stellar properties are known to vary with metallicity, one of these being  $T_{\text{eff}}$ , as hotter stars were found by Mokiem et al. (2007a) in the lower metallicity environments of the LMC and SMC. Furthermore, the work of Martins et al. (2005) relied on modelling He I-II lines, but due to their progressive weakening in earlier O subtypes, accuracy could only be maintained up to an O3 subtype. Mokiem et al. (2007a) had studied a limited number of earlier subtypes by modelling their H and He lines and Weidner & Vink (2010) subsequently offered new calibrations for  $T_{\text{eff}}$  and  $\log L$  at a LMC metallicity, based on the work. However, the very weak He I line still left Mokiem et al. (2007a) with uncertainties on  $T_{\text{eff}}$  that were much larger ( $\sim 10\%$ ) compared to the rest of their sample ( $\sim 3\%$ ).

A total of 22 stars in the census were identified to have an O2-O3.5 subtype. They are classified differently to their later counterparts, relying on the different N lines rather than just the ratio of the He lines (Walborn et al. 2002b), and would be open to large uncertainties if treated with the Martins et al. (2005) or even Weidner & Vink (2010) calibration. These early subtypes are among the hottest stars in the the census and would therefore provide some of the highest ionising fluxes.

To obtain more reliable properties for O2 stars, individual analyses were carried out on six O2 stars (first introduced in Chapter 3, see Table 3.4). All of the stars are located in the LMC, Melnick 42 (Mk 42) lying within 30 Dor. A range of photometry, listed in Table 5.1, was adopted to help establish the SEDs of the stars. *UBV* bands taken from Massey (2002) and Walborn et al. (2002b) and *JHK* bands from the Two Micron All Sky (2MASS) Catalog. Mk 42 was an exception to this, due to its location in the crowded 30 Dor region, for which the higher spatial resolution HST/WFPC2 photometry (Hunter et al. 1995) and VLT/MAD photometry (Campbell et al. 2010) was adopted. As previously mentioned, all the stars had been observed with VLT-UVES, covering a wavelength range of 3300-10250 Å at a resolving power of  $\sim 40000$ , with the exception of Mk 42 and HDE 269810 which only spanned 3300-6650 Å.

As with the emission line stars of Chapter 3, the properties of this sample of O2 stars were derived using the CMFGEN atmospheric modelling code. In all cases,  $T_{\text{eff}}$  was calculated from the N IV  $\lambda 4058$  and N V  $\lambda \lambda 4604-4620$  lines. Since the N abundance of each star was unknown, this was simultaneously derived.  $H\alpha$  was used to derive the mass-loss rates. A clumped wind model was applied for the two supergiants, using a volume filling factor  $f = 0.1$ , and a smooth wind in all other cases. For O-supergiants there is some evidence that the  $H\alpha$  line is already clumped (Eversberg et al. 1998) since it shows structure. This suggests that the spectral analysis of the O2 stars may be weaker in cases where the  $H\alpha$  line formation is assumed to be independent of clumping. Consequently, all O2 star models should allow for clumping, but it is the supergiants that require the most concern regarding their cumulative wind feedback.

Stellar luminosities were estimated by adopting a LMC distance modulus of  $18.45 \pm 0.18$  mag (slightly different to the 18.49 mag applied to the census, as this modelling preceded the work). Fits to the photometric data sets were then made by applying varying amounts of extinction that accounted for foreground Galactic and LMC dust and assuming  $R_V = 3.1$  (see Figure 5.1). Furthermore, Mk 42 featured an additional term allowing for the extinction within 30 Dor. As noted earlier, the near-IR has the advantage that extinction in these bands will be small compared to the visible, as too will the uncertainties. The near-IR photometry therefore served as anchor points when fitting the model. The resulting extinction values and absolute magnitudes in the *K*-band are given in Table 5.2.

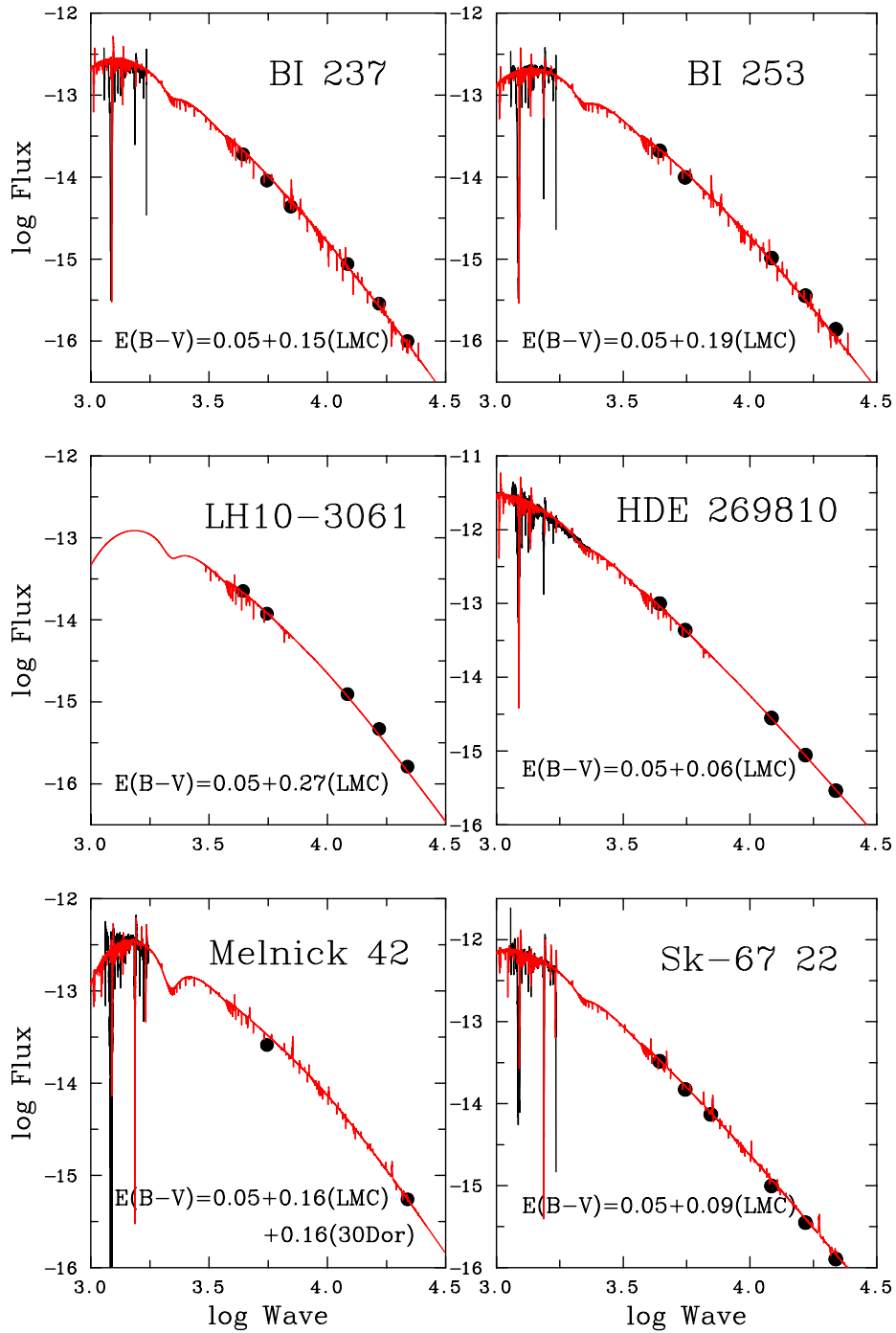


Figure 5.1: Spectral energy distributions returned from the CMFGEN models (red) reddened to the observed photometric data (black circles). The UV spectra (black) has also been overlaid for comparison, except in the case of LH 10-3061 where none was available.

Supplementary UV spectra were obtained from different instruments including HST/GHRS, FOS and STIS. However, the UV data did not serve as diagnostics but rather as a consistency check for the optical results. Spectral fits of the models can be found in Appendix D. The broad wings of the He II  $\lambda 4686$  line were overestimated in the supergiants but theoretical models showed good agreement with the supplementary UV spectra. However, for the giants and dwarfs, the C IV  $\lambda 1550$  line was predicted too strong and the O V  $\lambda 1371$  line was underestimated.

A  $T_{\text{eff}} \gtrsim 50$  kK was obtained in all cases, together with high luminosities,  $10^{5.8-6.6} L_{\odot}$ . The giants presented the highest  $T_{\text{eff}}$ , with the dwarfs and then supergiants being progressively cooler. Table 5.3 compares these N derived results with other works. In the case of Massey et al. (2005), only a lower temperature limit could be set owing to the weakness of the He I  $\lambda 4471$  line, but consistency was found with Mokiem et al. (2007a). A more extensive study of LMC O-type stars by Rivero González et al. (2012b) & Rivero González et al. (2012a) (hereafter RG12a and RG12b, respectively) succeeded this work. They re-analysed the stars from Mokiem et al. (2007a) to form a larger sample of over 30 stars, including 12 stars with an O2-O3.5 subtype. They too, generated atmospheric models that were focussed on fitting the N lines, this time using FASTWIND. Information on the giant and supergiant subtypes currently remains limited to the few stars covered in this study. However, a recent work by Bestenlehner et al. (submitted) based on the VFTS O, Of, Of/WN and WNh stars should provide new insights into this. Indeed, two of the stars, BI 253 (VFTS 072) as well as Mk 42 are included in the study. Their spectra are analysed via a grid of CMFGEN model atmospheres and the He I  $\lambda 4471$  line and N lines are used to constrain  $T_{\text{eff}}$ . The next section combines the work of RG12a/b with the O2 models in this work, to derive a set of calibrations for all the necessary stellar parameters.

Table 5.1: Photometry used in the modelling of the O2 stars.

Star	SpT	$U$ [mag]	$B$ [mag]	$V$ [mag]	$J$ [mag]	$H$ [mag]	$K$ [mag]
BI 237	O2 V((f*))	12.8	13.77	13.89	13.95	14.01	14.04
BI 253	O2 V((f*))	12.65	13.67	13.76	13.77	13.77	13.68
HDE 269810	O2 III(f*)		12.05	12.28	12.68	12.79	12.88
LH 10-3061	ON2 III(f*)		13.67	13.68	13.57	13.49	13.52
Mk 42	O2 If*			12.84			12.19
Sk -67° 22	O2 If*/WN 5	12.21	13.26	13.44	13.81	13.78	13.78

**Notes.**  $UBV$ -band photometry taken from Massey (2002) and Walborn et al. (2002b).  $JHK$ -band photometry is taken from the 2MASS Catalog. Mk 42 is an exception where  $V$  is taken from Hunter et al. (1995) and  $K$  from Campbell et al. (2010).

Table 5.2: CMFGEN model parameters of the O2 stars.

Star	SpT	$m_K$ [mag]	$A_K$ [mag]	$M_K$ [mag]	$T_{\text{eff}}$ [kK]	$\log L$ [ $L_{\odot}$ ]	$v_{\infty}$ [ $\text{km s}^{-1}$ ]	$\dot{M}$ [ $M_{\odot} \text{ yr}^{-1}$ ]	Wind model
BI 237	O2 V((f*))	14.04	0.08	-5.0	52	5.83	2400	$8 \times 10^{-7}$	smooth
BI 253	O2 V((f*))	13.68	0.09	-4.6	53	5.93	3180	$2 \times 10^{-6}$	smooth
HDE 269810	O2 III(f*)	12.88	0.04	-5.8	54	6.38	3700	$3.5 \times 10^{-6}$	smooth
LH 10-3061	ON2 III(f*)	12.52	0.12	-5.1	55	6.10	3150	$1.1 \times 10^{-6}$	smooth
Mk 42	O2 If*	12.19	0.12	-6.5	50	6.54	2900	$8.5 \times 10^{-6}$	clumped
Sk -67° 22	O2 If*/WN 5	13.78	0.05	-4.9	49	5.88	2650	$4 \times 10^{-6}$	clumped

**Notes.** Stars with a clumped wind model adopted a volume filling factor of  $f = 0.1$ .

Table 5.3: Comparison of  $T_{\text{eff}}$  derived for O2 star sample with other studies. Differences in analysis techniques and diagnostic lines are also given.

Star	Spectral Observations	Puls96		Mas05		Mok07		RG12a/b		B14	This work
		ESO/Caspec	Various	CTIO/RC Spec	FASTWIND	FASTWIND	FASTWIND	FASTWIND	FASTWIND	FASTWIND	FASTWIND
Atmospheric Code	Diagnostic	H/He	He I/He II	He I/He II	He I/He II	He I/He II	He I/He II	N III-V	N III-V	He I/N III-V	N IV/N V
SpT		$T_{\text{eff}}$ (kK)									
BI 237	O2 V((f*))	-	48	48	53.2	53.2	53.2	53.2	53.2	-	52.1
BI 253	O2 V((f*))	-	>48	>48	53.8	53.8	53.8	54.8	54.8	50.1	52.8
HDE 269810	O2 III(f*)	60	-	-	-	-	-	-	-	-	54.3
LH 10-3061	ON2 III(f*)	-	-	-	-	-	-	-	-	-	54.7
Mk 42	O2 II*	50.5	-	-	-	-	-	-	-	47.3	49.8
Sk -67° 22	O2 II*/WN 5	-	>42	>42	-	-	-	46.0	46.0	-	49.3

**Notes.** Puls96 - Puls et al. (1996), Mas05 - Massey et al. (2005), Mok07 - Mokiem et al. (2007a) and B14 - Bestenlehner et al. (submitted).

### Evolutionary sequence and stellar masses

The stars conveniently sample the O2 V, O2 III and O2 I SpTs as well as an Of/WN such that their properties can help establish an evolutionary sequence. For example, Mk 42 showed notable chemical enrichment with a depleted H abundance and a N abundance factor  $\sim 35$  larger than that derived for the LMC by Russell & Dopita (1990). These model abundances were compared to those predicted from contemporary evolutionary tracks to give further insight into their masses. Figure 5.2 plots the stars on an H-R diagram. Overlaid are LMC metallicity evolutionary tracks from the Geneva group (R. Hirschi, private communication). The tracks range from  $60 < M_{\text{init}} < 200 M_{\odot}$  for stars rotating with an initial to critical rotational velocity ratio of  $v_{\text{init}}/v_{\text{crit}} = 0.4$ .

The two dwarfs showed very little enhancement in N, and within the uncertainties matched the ZAMS predictions. Masses of  $\sim 75 M_{\odot}$  and  $\sim 85 M_{\odot}$  for BI 237 and BI 253, respectively, were in agreement with the typical mass ( $< 100 M_{\odot}$ ) of O2 dwarfs found by Walborn et al. (2002b). The giants both showed enhanced N, more in the case of LH 10-3061. While both lay close to the ZAMS, a more evolved status was favoured for LH 10-3061. This would likely place HDE 269810 as a young  $M_{\text{init}} \sim 150 M_{\odot}$  giant, no older than 1 Myr, while LH 10-3061 is a less massive and more evolved giant of  $M_{\text{init}} \sim 75 - 80 M_{\odot}$ . Mk 42 is  $\sim 5$  times more luminous than Sk  $-67^{\circ} 22$ . This supported a very high mass of  $M_{\text{init}} \sim 180 M_{\odot}$  for Mk 42, allowing it to achieve its greatly enriched N surface abundance through mixing at a relatively young age of  $\sim 1.5$  Myr. Meanwhile Sk  $-67^{\circ} 22$  represented a star of much lower mass,  $M_{\text{init}} \sim 60 M_{\odot}$ , at a later age of at least 2.5 Myr.

While the masses of these O2 stars are quite uncertain, a typical evolutionary sequence can still be followed for O2 stars with  $M < 100 M_{\odot}$  - starting from dwarfs such as BI 253, passing through a giant phase like LH 10-3061 and ending up as a supergiant in a similar mass regime to Sk  $-67^{\circ} 22$ . The high luminosities of stars with  $M \gg 100 M_{\odot}$  naturally produce strong winds at the outset, favouring an O2 giant ZAMS stage for very high mass stars (eg. HDE 269810), rapidly followed by a supergiant stage (eg. Mk 42). These are likely precursors to the massive WNh stars studied by Crowther et al. (2010) at the core of the R136.

### 5.2.2 O-type star calibrations

#### O-type star temperatures

Martins et al. (2005) provided a  $T_{\text{eff}}$ -SpT scale for Galactic O-type stars. Following recent findings (Massey et al. 2005; Mokiem et al. 2007a; RG12a; RG12b), a small upward adjustment to the scale was necessary before applying it to stars in 30 Dor, due to their metallicity

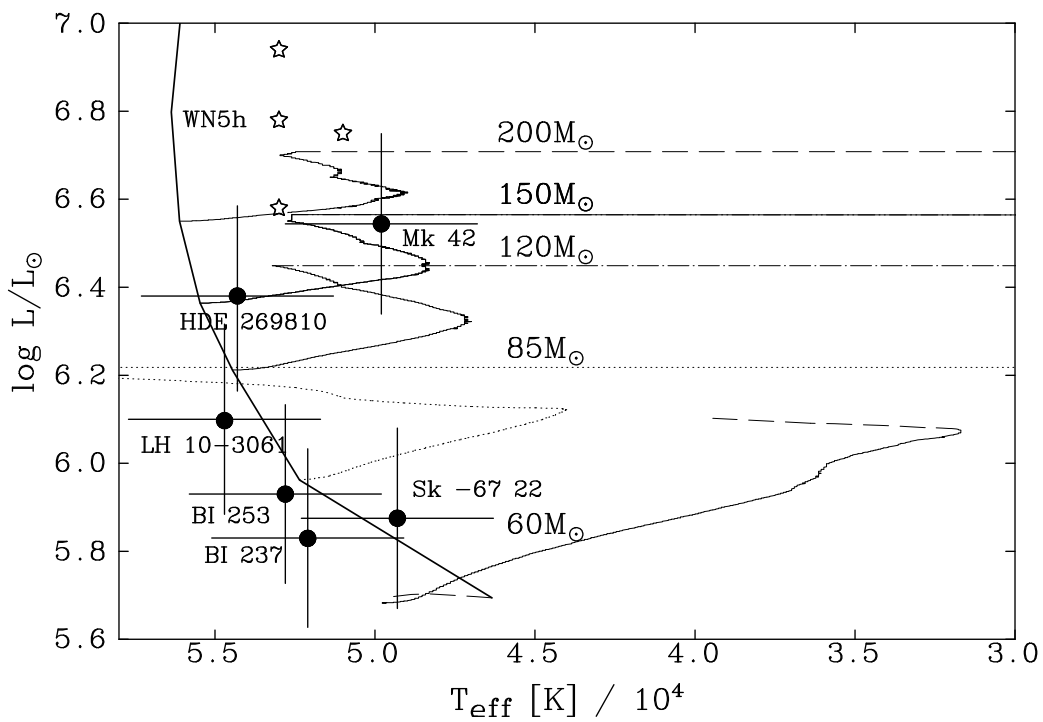


Figure 5.2: H-R diagram of O2 stars (filled circles) overlaid on Geneva evolutionary rotating tracks 60  $M_{\odot}$  (dashed-solid), 85  $M_{\odot}$  (dotted), 120  $M_{\odot}$  (dot-dashed), 150  $M_{\odot}$  (solid) and 200  $M_{\odot}$  (dashed). The thick solid line represents the ZAMS. R136 WN5 h stars from Crowther et al. (2010) have also been included (empty stars).

difference. Figure 5.3 is taken from RG12b and compares their model  $T_{\text{eff}}$  against the calibrations of Martins et al. (2005). Dwarf stars with a subtype of O4 and later showed a typical offset of  $\approx 1$  kK. Studies of additional LMC O-type dwarfs by Massey et al. (2004, 2005) showed a consistent deviation. The census therefore derived  $T_{\text{eff}}$  for dwarfs O4 and later by applying the Martins et al. (2005) calibration, with a +1 kK correction. Only limited models were available for giants and even fewer for supergiants. However, given their minimal offsets from the Martins et al. (2005) calibration, the same relation was assigned to all census giants and supergiants, subtype O4 and later. Tables 5.4-5.6 list the final  $T_{\text{eff}}$  assigned to each SpT.

In the case of O2-O3.5 subtypes, where possible,  $T_{\text{eff}}$  was based on averages from the works of RG12b, Massey et al. (2004, 2005) and the O2 models presented in Section 5.2.1. RG12b had compared their models produced by FASTWIND with equivalent CMFGEN predictions. They found good agreement in the H/He lines that would be visible in cooler stars. For the hottest stars, they deduced that CMFGEN would return a lower  $T_{\text{eff}}$  if it concentrated solely on the N IV  $\lambda 4058$  and N III triplet. Fortunately, the N V  $\lambda\lambda 4604-4620$  line can also be modelled, which appeared to be code independent although very dependent on  $T_{\text{eff}}$ . This line was used when analysing the O2 stars in Section 5.2.1 but as only preliminary fits had been made to the spectra, a double weighting was given toward the contemporary models of RG12b when calculating the  $T_{\text{eff}}$  averages of the O2-O3.5 subtypes. Interpolations were made from the Martins et al. (2005) calibrations in the case of intermediate subtypes.

### O-type star intrinsic colours and bolometric corrections

Intrinsic colours were adopted from Table 2.1 of Conti et al. (2008) and references therein. In the case of earlier giants and supergiants, where colours were lacking, a  $(B - V)_o$ -SpT relation was assumed consistent with the models of Martins & Plez (2006). Martins et al. (2005) provide a  $T_{\text{eff}} - BC_V$  calibration for O-type stars, (their equation 4). This calibration was slightly adapted to account for the subtypes earlier than O4, by combining it with the stellar parameters derived by RG12a & RG12b and in this work. Figure 5.4, plots  $BC_V$  against  $T_{\text{eff}}$  for all the dwarfs. This was fitted with a low order polynomial to give the equation:

$$BC_V = 0.482 + 1.35 \times 10^{-4} T_{\text{eff}} + 7.54 \times 10^{-10} T_{\text{eff}}^2. \quad (5.1)$$

Only very minimal variations in  $BC_V$  were evident in giants and supergiants, as can be seen in Figure 5.4. Equation 5.1 was therefore applied to all O-type stars luminosity classes.

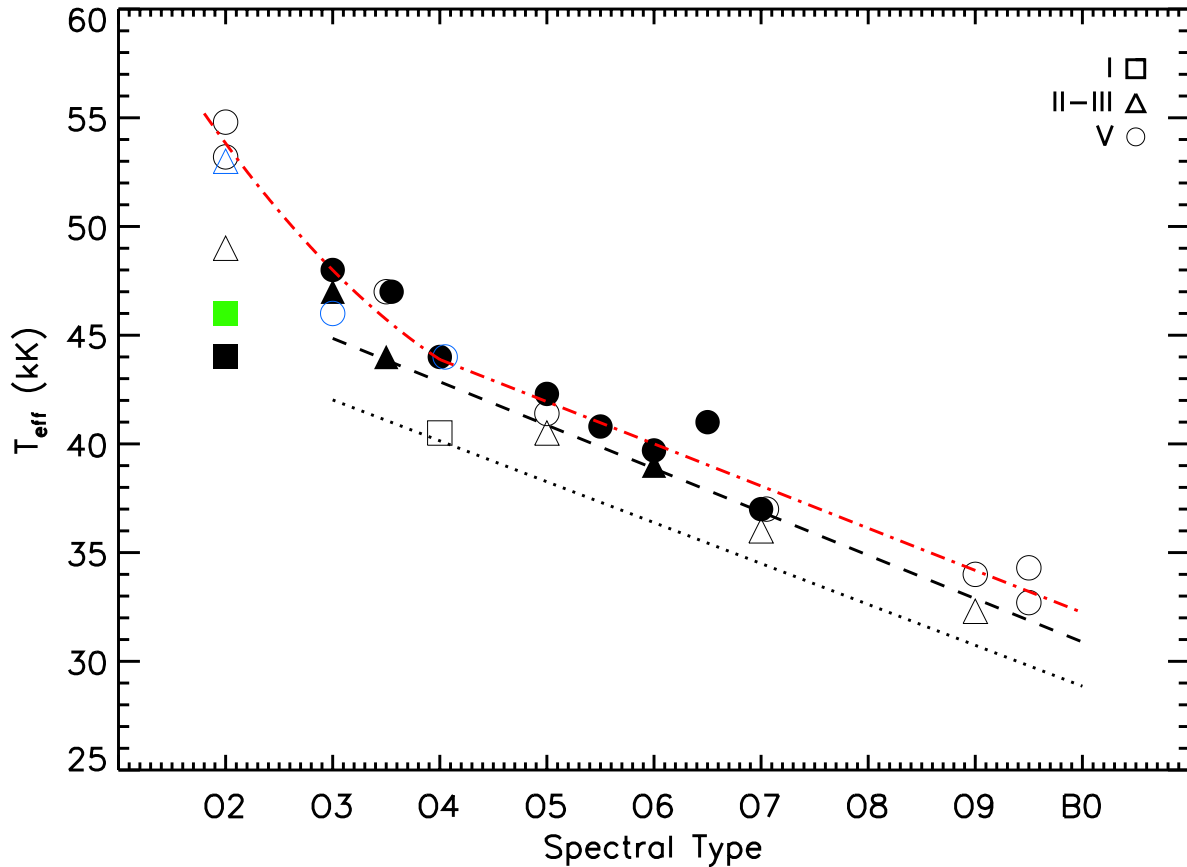


Figure 5.3:  $T_{\text{eff}}$  as a function O subtype for stars analysed by RG12a & RG12b. Black symbols: LMC objects; blue symbols: SMC objects; green symbol: Sk  $-67^\circ 22$  (O2 If\*/WN 5, LMC). Squares refer to supergiants, triangles to (bright) giants, and circles to dwarfs. Filled symbols correspond to objects with  $[N] \geq 8.0$ , and open ones to objects with  $[N] < 8.0$ . The dashed-dotted (red) line displays a least square linear and quadratic fit to all dwarfs. The  $T_{\text{eff}}$  calibration from Martins et al. (2005) for Galactic O-type dwarfs (dashed) and supergiants (dotted) is displayed for comparison. For clarity, some objects have been slightly shifted horizontally. Taken from RG12b.

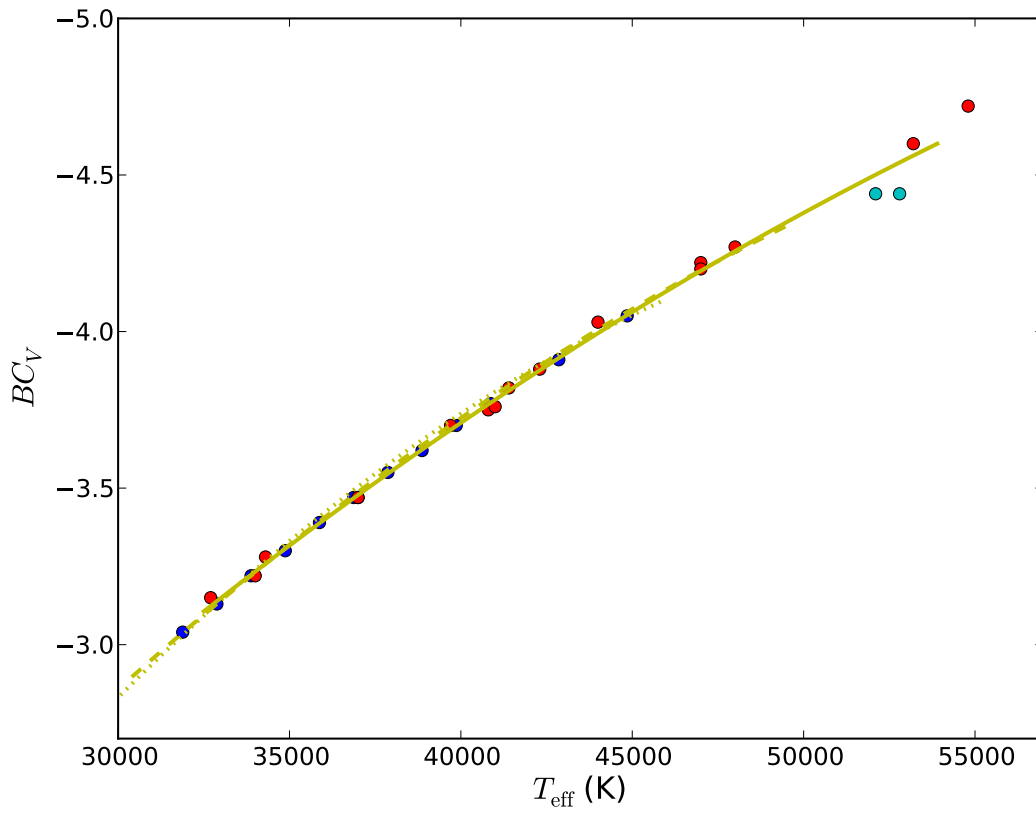


Figure 5.4:  $BC_V$  as a function of  $T_{\text{eff}}$  for O-type dwarfs. Data points are taken from Martins et al. (2005) (blue), RG12a (red) and this work (cyan). The solid line represents the calibration in Equation 5.1 plotted for the  $T_{\text{eff}}$  range assigned to dwarfs. The dashed and dotted lines represent equivalent fits to the giant and supergiant data points, respectively.

### O-type star ionising photon fluxes and luminosities

Martins et al. (2005) also derived a  $q_0(T_{\text{eff}}, \log g)$  function. As with the  $BC_V$ , their values were combined with data from RG12a & RG12b and the O2 stars in this work, as well as additional models from Smith et al. (2002) and Mokiem et al. (2004) to help sample the higher temperature range. Figure 5.5 plots  $q_0$  against  $T_{\text{eff}}$  for each luminosity class. The ionising photon flux clearly increases with  $T_{\text{eff}}$ . Low order polynomial fits were made to determine the following  $q_0(T_{\text{eff}})$  relations for dwarfs, giants and supergiants:

$$\text{Dwarfs : } \log q_0 = 3.96 + 1.21 \times 10^{-3} T_{\text{eff}} - 2.44 \times 10^{-8} T_{\text{eff}}^2 + 1.69 \times 10^{-13} T_{\text{eff}}^3; \quad (5.2)$$

$$\text{Giants : } \log q_0 = 11.2 + 7.51 \times 10^{-4} T_{\text{eff}} - 1.46 \times 10^{-8} T_{\text{eff}}^2 + 9.94 \times 10^{-14} T_{\text{eff}}^3; \quad (5.3)$$

$$\text{Supergiants : } \log q_0 = 1.33 + 6.31 \times 10^{-4} T_{\text{eff}} - 1.23 \times 10^{-8} T_{\text{eff}}^2 + 8.60 \times 10^{-14} T_{\text{eff}}^3. \quad (5.4)$$

Similarly, the luminosity of the star in the EUV, capable of ionising H atoms, the ionising luminosity, is termed  $L_{\text{EUV}}$ . Integrations were performed over the model SEDs of Martins et al. (2005) and the O2 stars from this work in order to calculate  $L_{\text{EUV}}$  as a fraction of the total bolometric luminosity,  $L_{\text{Bol}}$ . These were also plotted with respect to  $T_{\text{eff}}$  and fitted with low order polynomials as shown in Figure 5.6. As expected, hotter stars show a higher proportion of their luminosity in the EUV, reaching  $\sim 70\%$  in the earliest O2 stars and falling below 10% for the latest O-type stars. Given their consistency, the same relation was established for both dwarfs and giants while a separate one was made for supergiants:

$$\text{Dwarfs \& Giants : } L_{\text{EUV}}/L_{\text{Bol}} = -1.34 + 5.69 \times 10^{-5} T_{\text{eff}} - 3.35 \times 10^{-10} T_{\text{eff}}^2; \quad (5.5)$$

$$\text{Supergiants : } L_{\text{EUV}}/L_{\text{Bol}} = -1.71 + 8.46 \times 10^{-5} T_{\text{eff}} - 7.51 \times 10^{-10} T_{\text{eff}}^2. \quad (5.6)$$

### O-type star wind velocities and mass-loss rates

An extensive observational study of the terminal velocities of Galactic OB stars was made in the UV by Prinja et al. (1990). The  $v_{\infty}$  assigned to the different SpTs were primarily based on the mean values given in their Table 3, with slight updates made to incorporate the later work of Prinja & Crowther (1998), Massey et al. (2004) and Massey et al. (2005), who studied further O-type stars, this time in the Magellanic Clouds. Measurements did not extend to the latest subtype of O9.7, and so a value for  $v_{\infty}$  was assumed in these cases. For mass-loss rates, the theoretical prescriptions of Vink et al. (2001) were applied, using a LMC metallicity of  $Z = 0.5 Z_{\odot}$ , throughout.

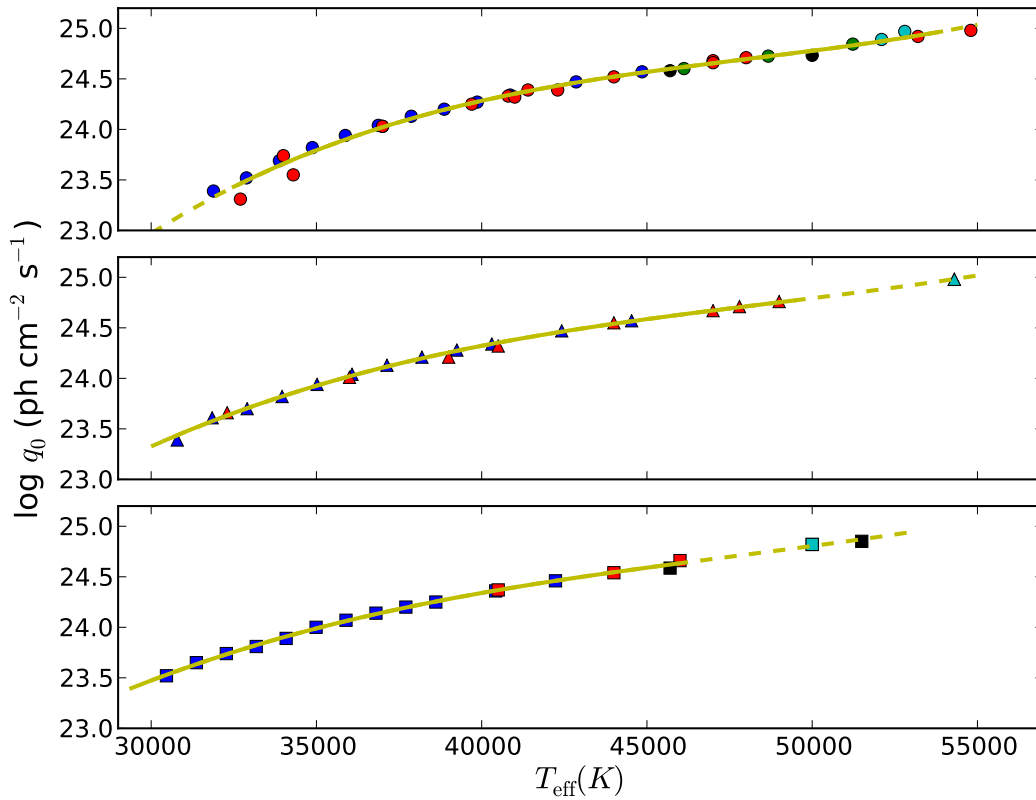


Figure 5.5:  $q_0$  as a function of  $T_{\text{eff}}$  for O-type dwarfs (top), giants (middle) and supergiants (bottom). Data taken from Martins et al. (2005) (blue), RG12a (red), Mokiem et al. (2004) (green), Smith et al. (2002) (black) and this work (cyan) plotted in cyan. The yellow dashed lines represent the calibrations in Equations 5.2-5.4 and are marked as solid lines over the  $T_{\text{eff}}$  range assigned to each luminosity class.

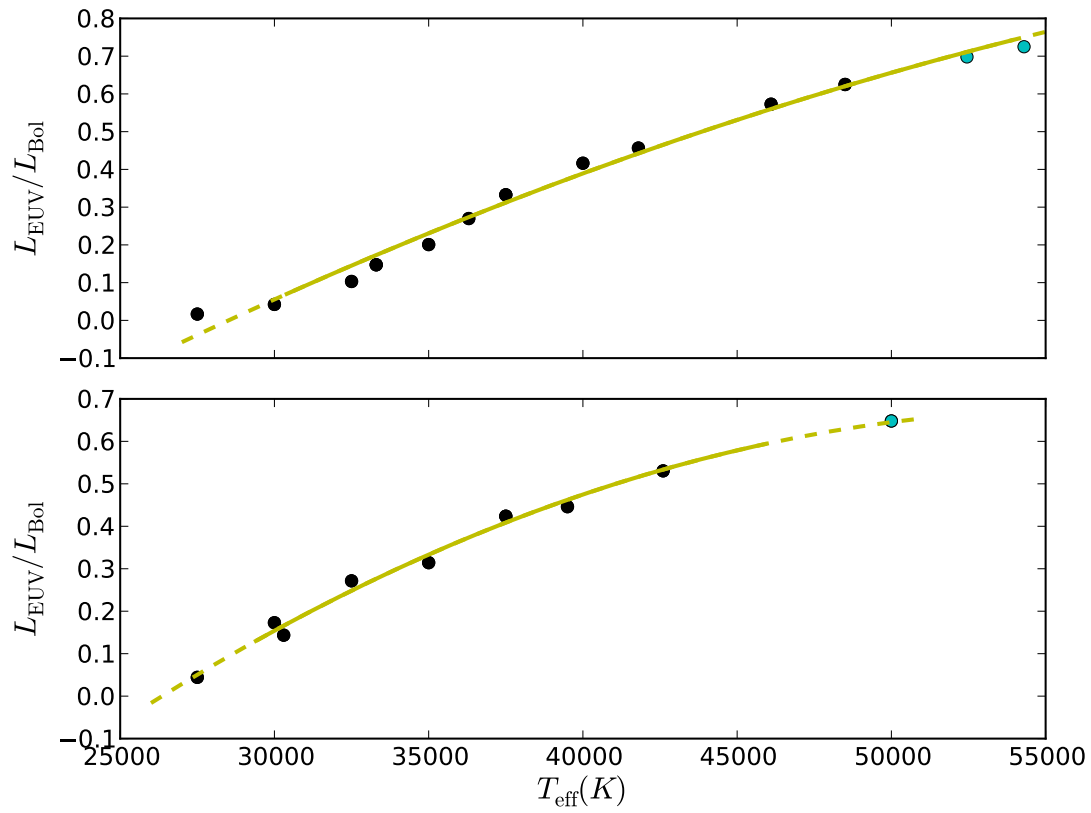


Figure 5.6:  $L_{\text{EUV}}/L_{\text{Bol}}$  as a function of  $T_{\text{eff}}$  for O-type dwarfs and giants (top), and supergiants (bottom). Data taken from Martins et al. (2005) (black) and this work (cyan). The yellow dashed lines represent the calibrations in Equations 5.5 & 5.6 and are marked as solid lines over the  $T_{\text{eff}}$  range assigned to each luminosity class.

Table 5.4: Parameters for O-type stars with luminosity class V.

SpT	$T_{\text{eff}}$ (kK)	$BC_V$ (mag)	$\log q_0$ ( $\text{ph cm}^{-2} \text{s}^{-1}$ )	$L_{\text{EUV}}$ ( $L_{\text{Bol}}$ )	$v_{\infty}$ ( $\text{km s}^{-1}$ )
O2	54.0	-4.61	24.97	0.74	3300
O3	48.0	-4.26	24.70	0.61	3000
O3.5	47.0	-4.19	24.65	0.58	3300
O4	43.9	-3.99	24.52	0.50	3000
O5	41.9	-3.84	24.41	0.44	2700
O5.5	40.9	-3.77	24.34	0.42	2000
O6	39.9	-3.70	24.27	0.39	2600
O6.5	38.9	-3.62	24.20	0.36	2500
O7	37.9	-3.55	24.11	0.32	2300
O7.5	36.9	-3.47	24.01	0.29	2000
O8	35.9	-3.39	23.90	0.26	1800
O8.5	34.9	-3.31	23.78	0.23	2000
O9	33.9	-3.22	23.64	0.19	1500
O9.5	32.9	-3.14	23.49	0.16	1500
O9.7	32.5	-3.11	23.43	0.14	1200

Table 5.5: Parameters for O-type stars with luminosity class III.

SpT	$T_{\text{eff}}$ (kK)	$BC_V$ (mag)	$\log q_0$ ( $\text{ph cm}^{-2} \text{s}^{-1}$ )	$L_{\text{EUV}}$ ( $L_{\text{Bol}}$ )	$v_{\infty}$ ( $\text{km s}^{-1}$ )
O2	49.6	-4.34	24.78	0.65	3200
O3	47.0	-4.20	24.67	0.58	3200
O3.5	44.0	-4.01	24.54	0.50	2600
O4	42.4	-3.90	24.46	0.46	2600
O5	40.3	-3.75	24.34	0.40	2800
O5.5	39.2	-3.67	24.27	0.37	2700
O6	38.2	-3.58	24.20	0.33	2600
O6.5	37.1	-3.50	24.12	0.30	2600
O7	36.1	-3.41	24.03	0.27	2600
O7.5	35.0	-3.32	23.93	0.23	2200
O8	34.0	-3.23	23.82	0.20	2100
O8.5	32.9	-3.13	23.70	0.16	2300
O9	31.8	-3.03	23.58	0.12	1900
O9.5	30.8	-2.93	23.44	0.08	1500
O9.7	30.4	-2.89	23.38	0.07	1200

Table 5.6: Parameters for O-type stars with luminosity class I.

SpT	$T_{\text{eff}}$ (kK)	$BC_V$ (mag)	$\log q_0$ (ph cm <sup>-2</sup> s <sup>-1</sup> )	$L_{\text{EUV}}$ ( $L_{\text{Bol}}$ )	$v_{\infty}$ (km s <sup>-1</sup> )
O2	46.0	-4.10	24.63	0.60	3000
O3	42.0	-3.88	24.45	0.52	3700
O3.5	41.1	-3.81	24.40	0.50	2000
O4	40.1	-3.75	24.35	0.48	2300
O5	38.3	-3.61	24.23	0.43	1900
O5.5	37.3	-3.53	24.17	0.40	1900
O6	36.4	-3.45	24.10	0.38	2300
O6.5	35.4	-3.37	24.03	0.35	2200
O7	34.5	-3.28	23.95	0.32	2100
O7.5	33.6	-3.20	23.86	0.29	2000
O8	32.6	-3.10	23.77	0.25	1500
O8.5	31.7	-3.01	23.67	0.22	2000
O9	30.7	-2.91	23.56	0.18	2000
O9.5	29.8	-2.81	23.45	0.15	1800
O9.7	29.4	-2.77	23.40	0.13	1800

### 5.2.3 B-type stars

#### B-type star temperatures

Most B-type star parameters were estimated using existing calibrations. Trundle et al. (2007) and Hunter et al. (2007) carried out atmospheric modelling on over 100 B-type stars as part of the previous VLT-FLAMES Survey of Massive Stars, many of which were in the LMC. The  $T_{\text{eff}}$ -SpT scale given in Table 10 of Trundle et al. (2007) was used to assign temperatures. It is noted that some of these values, particularly for giants, required interpolation due to the lack of certain SpTs in their sample. However, these stars compose only a small portion of the census and the hottest early B-type stars were still directly based on model results.

#### B-type star intrinsic colours and bolometric corrections

As with O-type stars, the intrinsic colours for B-type stars were adopted from Table 2.1 of Conti et al. (2008) and references therein. Interpolations were made to account for the B0.2 and B0.7 SpTs not listed. With regards to bolometric correction, Crowther et al. (2006) produced a  $T_{\text{eff}} - BC_V$  calibration based on their Galactic B-supergiant studies, along with work from Trundle et al. (2004) and Trundle & Lennon (2005), who had studied SMC B-supergiants. This was applied to all the B-supergiants in the census. In the case of the earliest B-dwarfs

and giants, the relation from Lanz & Hubeny (2003) (their equation 2) was used although as with the O-type stars,  $BC_V$  showed only small changes with luminosity class, with  $T_{\text{eff}}$  being the dominant factor.

### B-star ionising photon fluxes and ionising luminosities

Similar to the O-type stars, a  $q_0(T_{\text{eff}})$  relation was determined for the cooler B-type stars. Data were taken from RG12a, Conti et al. (2008) and Smith et al. (2002) as shown in Figure 5.7 to sample these cooler temperatures. The following relations were derived for the combined dwarf and giant luminosity classes, and the separate supergiant class:

$$\text{Dwarfs \& Giants : } \log q_0 = 21.76 + 1.83 \times 10^{-4} T_{\text{eff}} + 7.22 \times 10^{-9} T_{\text{eff}}^2; \quad (5.7)$$

$$\text{Supergiants : } \log q_0 = 18.46 + 8.33 \times 10^{-5} T_{\text{eff}} + 2.49 \times 10^{-9} T_{\text{eff}}^2. \quad (5.8)$$

As with the O-type stars, the EUV luminosities of B-type stars were obtained using Equations 5.5 & 5.6. However, the SEDs that had been integrated to derive these relations only extended down to  $T_{\text{eff}} \approx 27$  kK so would not accurately sample the coolest B-type stars in the census. The fits in Figure 5.6 showed that they could not be extrapolated for these lower temperatures. Instead, progressively cooler stars should theoretically show progressively lower  $L_{\text{EUV}}/L_{\text{Bol}}$  ratios until they no longer produce any ionising photons. On this basis, cooler stars with  $L_{\text{EUV}}/L_{\text{Bol}} < 0.01$  were taken to have negligible ionising luminosities, especially when compared to the notably hotter early O-type stars.

### B-type star wind velocities and mass-loss rates

Prinja et al. (1990) was once again used to assign  $v_{\infty}$  to the B-supergiants with Kudritzki & Puls (2000) offering values to the later SpTs. With no data sampling the early B-dwarfs and giants, they were assumed to have a similar  $v_{\infty}$  to their late O-type star counterparts. Realistically,  $v_{\infty}$  would be expected to fall for later dwarf and giant subtypes in a similar manner to the values observed for supergiants. This would arise due to later subtypes having a lower mass which would decrease  $v_{\text{esc}}$  and in turn  $v_{\infty}$ . However, with regards to the integrated wind luminosity, this difference will have a negligible effect as shown later.

Mass-loss rates were again derived using the Vink et al. (2001) prescription. An exception was made for B-supergiants, however, following a discrepancy between the prescription and empirical results (Markova & Puls 2008; Crowther et al. 2006; Trundle & Lennon 2005). The authors employed the wind-luminosity relation (WLR) of Kudritzki et al. (1999) whereby the modified wind momentum is proportional to the stellar luminosity. When separating their

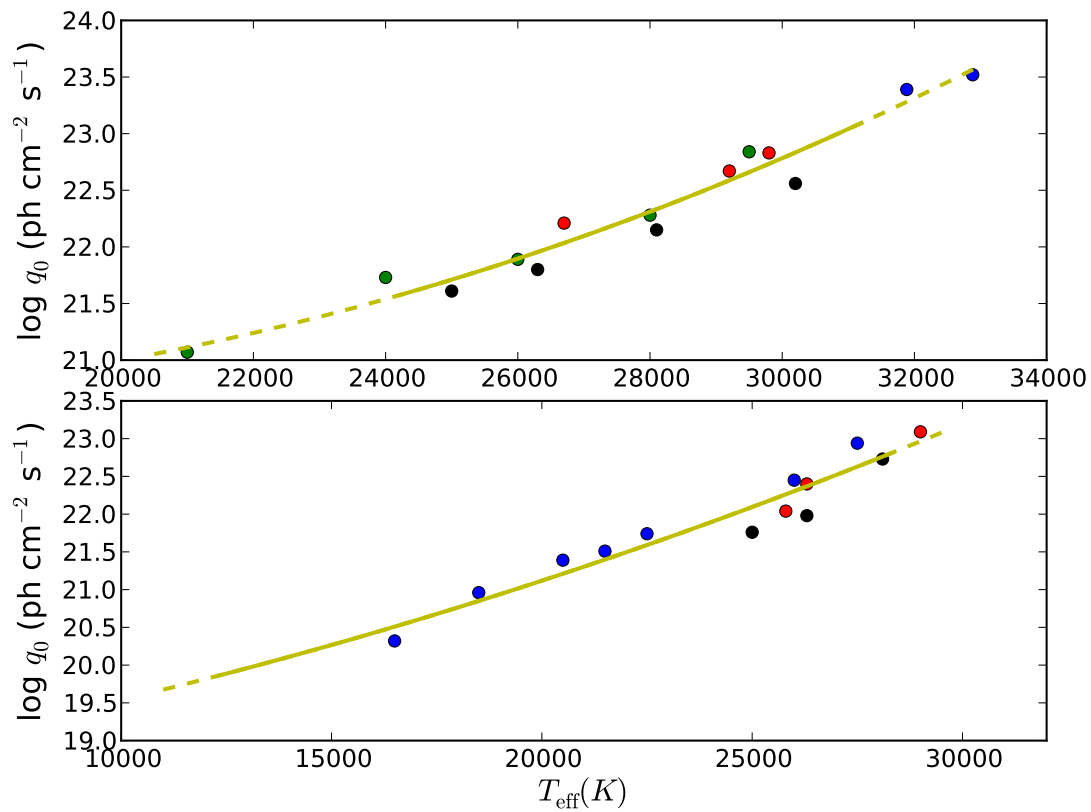
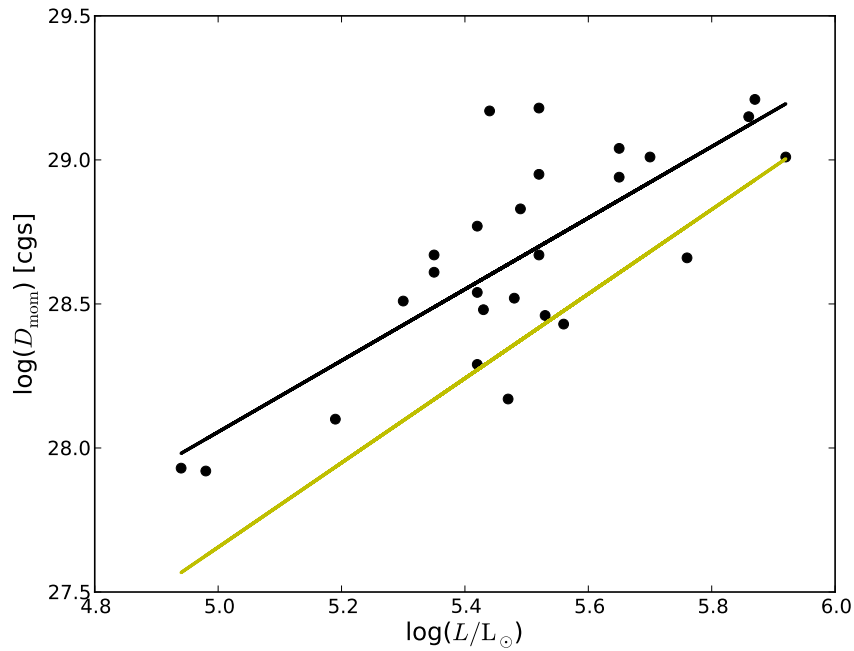


Figure 5.7:  $q_0$  as a function of  $T_{\text{eff}}$  for B-type dwarfs and giants (top) and supergiants (bottom). Data taken from Martins et al. (2005) (blue), RG12a (red), Conti et al. (2008) (green) and Smith et al. (2002) (black). The yellow dashed lines represent the calibrations in Equations 5.7 & 5.8 and are marked as solid lines over the  $T_{\text{eff}}$  range assigned to each luminosity class.

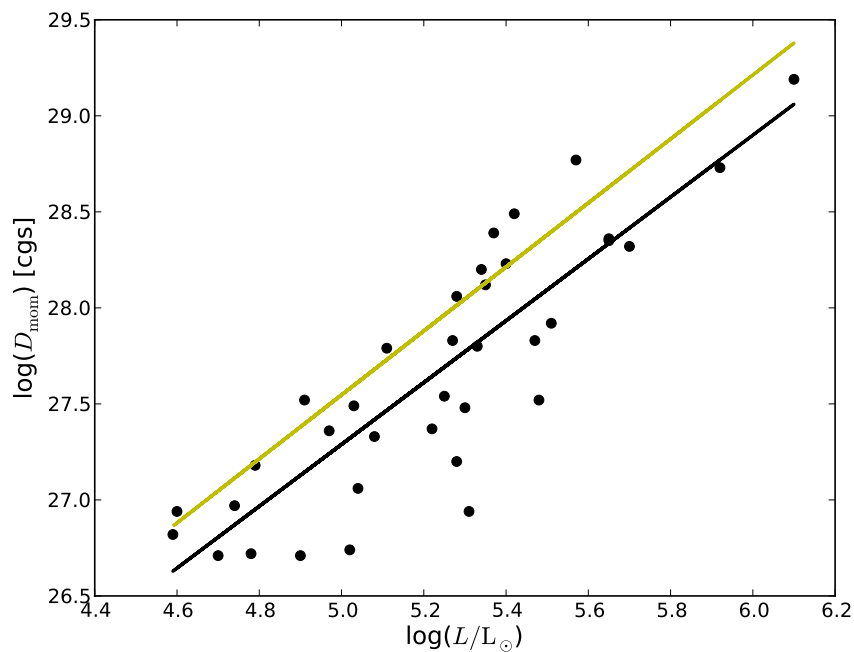
Table 5.7: B-type star parameters for all luminosity classes.

SpT	$T_{\text{eff}}$ (kK)	$BC_V$ (mag)	$\log q_0$ ( $\text{ph cm}^{-2} \text{s}^{-1}$ )	$L_{\text{EUV}}$ ( $L_{\text{Bol}}$ )	$v_{\infty}$ ( $\text{km s}^{-1}$ )
Luminosity Class V					
B0	31.4	-3.04	23.15	0.11	1000
B0.2	30.3	-2.93	22.85	0.06	1000
B0.5	29.1	-2.81	22.56	0.02	1000
Luminosity Class III					
B0	29.1	-2.81	22.56	0.02	1000
B0.2	27.9	-2.68	22.28	< 0.01	1000
B0.5	26.7	-2.55	22.02	< 0.01	1000
B0.7	25.4	-2.41	21.78	< 0.01	1000
B1	24.2	-2.26	21.56	< 0.01	1000
Luminosity Class I					
B0	28.6	-2.71	22.86	0.10	1500
B0.2	27.0	-2.58	22.51	0.03	1400
B0.5	25.4	-2.44	22.17	0.03	1400
B0.7	23.8	-2.30	21.84	0.01	1200
B1	22.2	-2.14	21.52	< 0.01	1100
B1.5	20.6	-1.97	21.22	< 0.01	800
B2	19.0	-1.79	20.93	< 0.01	800
B2.5	17.4	-1.60	20.65	< 0.01	800
B3	15.8	-1.38	20.39	< 0.01	600
B5	14.2	-1.14	20.13	< 0.01	500
B8	12.3	-0.83	19.86	< 0.01	200

samples into early (B0-B1) and mid/late (B1.5-B9) B-supergiants, they found theoretical predictions to be offset from their empirical values. This same relation can be seen in Figure 5.8 which adopts a series of B-supergiant parameters from the studies of Markova & Puls (2008); Lefever et al. (2007); Crowther et al. (2006); Kudritzki et al. (1999) and plots  $\log D_{\text{mom}}$  against  $\log L$ . The sample was split into early and mid/late type stars before a least squares fit was made. This fit was then used to calibrate the mass-loss rates for each sample. Despite the discrepancies with the Vink et al. (2001) predictions, given the relatively small number of B-supergiants in the census, the eventual integrated properties for 30 Dor should not be too dissimilar with either mass-loss rate approach.



(a)



(b)

Figure 5.8: The modified wind momentum ( $D_{\text{mom}}$ ) as a function of stellar luminosity ( $L_{\odot}$ ) for early (a) and mid/late (b) B-type supergiants. The black circles mark empirical data taken from Markova & Puls (2008); Lefever et al. (2007); Crowther et al. (2006); Kudritzki et al. (1999). The black lines represent a least squares fits to this empirical data. The yellow lines represent the fits in the case where the Vink et al. (2001) prescription is used to obtain the mass-loss rates and derive  $D_{\text{mom}}$ .

### 5.2.4 Uncertainties in calibrations

All of the stellar calibrations are open to various uncertainties. Most important to estimating an accurate ionising flux is the adopted  $T_{\text{eff}}$ -SpT calibration. Martins et al. (2005) and Trundle et al. (2007) would suggest uncertainties on  $T_{\text{eff}}$  of about  $\pm 1 - 2$  kK but these are likely to be higher ( $\pm 3 - 4$  kK) in the case of the earliest O-type stars.

The  $BC_V$  of the stars are particularly dependent on  $T_{\text{eff}}$  (Martins et al. 2005; Martins & Plez 2006). Given the low extinction of 30 Dor and renewed accuracy in its distance (Pietrzyński et al. 2013), it is the  $BC_V$  of the stars which dominate the uncertainty of their bolometric luminosity ( $L_{\text{Bol}}$ ). The uncertainty on  $\log L_{\text{Bol}}/L_{\odot}$  is found to be about  $\pm 0.15 - 0.25$  dex. With  $T_{\text{eff}}$  similarly affecting the values of  $q_0$ , the final ionising photon rates,  $Q_0$ , are expected to be within  $\sim 60\%$  in the hottest stars, although more accurate in cooler stars.

A reliable wind luminosity depends on the accuracy of  $\dot{M}$  and  $v_{\infty}$ . The assignment of  $v_{\infty}$  to each SpT was primarily based on the observational UV study by Prinja et al. (1990). It remains one of the most extensive works yet many SpTs rely on only a couple of measurements. Again, these were carried out on Galactic OB stars, but a metallicity dependence is noted for  $v_{\infty}$ , (Leitherer et al. (1992) derived  $v_{\infty} \propto Z^{0.13}$ ). With  $L_{\text{SW}} \propto v_{\infty}^2$ , the effect could be substantial, although  $\dot{M}$  is the more dominant term in this case, so that any metallicity dependence of  $v_{\infty}$  should only change the  $L_{\text{SW}}$  by up to  $\sim 10\%$ . Given the limited data for some SpTs, no attempt was made to correct for this metallicity dependence. However, in the case of the earliest stars (O2-3.5), values were supplemented by the later work of Prinja & Crowther (1998) and Massey et al. (2004) who studied further O-type stars, this time in the Magellanic Clouds.

In the case of the mass-loss rates, wind clumping is not directly accounted for by the Vink et al. (2001) prescription. The effects of clumping have been thought to potentially scale down  $\dot{M}$  by a factor of a few. However, Mokiem et al. (2007b) argued that, if a modest clumping correction is applied to empirical mass-loss rates, a better consistency is found with the Vink et al. (2001) prescription.

The uncertainties on the adopted SpT (about  $\pm 0.5$  subtype) should be insignificant when compared to those of the stellar parameters. Any SpT will naturally show a spread in parameters, however, over the entire census, such uncertainties are expected to balance out to provide first order estimates of the feedback. To test this, the properties of a selection of O2-3 type stars in 30 Dor which had been previously modelled (Rivero González et al. 2012a; Evans et al. 2010; Massey et al. 2005), were compared to those provided by the calibrations. Offsets up to a factor of two were found, but typically the calibrations estimated  $Q_0$ ,  $L_{\text{SW}}$  and  $D_{\text{mom}}$  within  $\sim 40\%$  of values obtained from tailored analyses.

### 5.2.5 Binary systems

The spectroscopic binary fraction of O-type stars in 30 Dor has been estimated to be  $0.51 \pm 0.04$  (Sana et al. 2013a): a considerable number of the stars in the census. In the case of these close binary systems, the photometric data will represent the combined light of both components, giving an absolute magnitude for the system,  $M_V^{\text{sys}}$ . For the time being, corrections were only made for a subset of the SB2 systems, whereby a robust subtype and luminosity class was known for both components. This included 27 of the 48 SB2 systems identified in the census, listed in Table 5.8. Average absolute magnitudes from the census (Table 4.8) allowed  $\Delta M_V = M_V^1 - M_V^2$  to be estimated. Absolute magnitudes for each component could then be calculated from  $\Delta M_V$  and  $M_V^{\text{sys}}$ . Separate stellar parameters were then calculated for each star following the usual calibrations. SB1 and SB2 systems where complete classification of the secondary component was unavailable, were not adjusted i.e. all light was assumed to have originated from the primary component.

### 5.2.6 Wolf-Rayet and Of/WN Stars

A total of 25 W-R and 6 Of/WN stars were identified in the census. Their properties were derived from a combination of individual and template models as described in Section 3.7. Any known W-R binaries were also corrected for as explained in Section 3.7.2.

### 5.2.7 Census of hot luminous stars with spectroscopy

Stellar parameters were derived for all the hot luminous stars with spectroscopy. These are listed in Table 5.9 which gives an extract of the full census which is accessible via anonymous ftp to [cdsarc.u-strasbg.fr](ftp://cdsarc.u-strasbg.fr) (130.79.128.5). The table lists the same identification number assigned to each candidate star in Table 4.3. The adopted SpT and accompanying reference is given for each star.

Table 5.8: A breakdown of the SB2 systems that were corrected for in the census.  $\Delta M_V = M_V^1 - M_V^2$ . The sum of the ionising photon rate and wind luminosity from the individual components was calculated and used in the final integrated values of 30 Dor.

ID #	$V$ (mag)	$B - V$ (mag)	$A_V$ (mag)	$M_V^{\text{sys}}$ (mag)	SpT <sup>1</sup>	SpT <sup>2</sup>	$\Delta M_V$ (mag)	$M_V^1$ (mag)	$M_V^2$ (mag)
56	16.91	0.28	2.1	-3.6	O9V	O9.5V	-0.3	-3.0	-2.7
63	15.56	0.23	1.9	-4.8	O8.5V	O9.5V	-0.4	-4.2	-3.8
64	16.23	0.30	2.2	-4.4	O6.5V	O6.5V	-0.0	-3.7	-3.7
73	15.15	0.22	1.9	-5.2	O8.5III	O9.7V	-1.0	-4.8	-3.8
126	16.44	0.21	1.8	-3.8	O9.7V	B0V	-0.1	-3.1	-3.0
191	15.50	0.25	2.0	-5.0	O8V	B0V	-0.6	-4.5	-3.9
194	14.78	0.03	1.2	-4.9	O6V	O9.5V	-0.8	-4.5	-3.7
206	15.81	0.22	1.9	-4.5	O9V	B0V	-0.5	-4.0	-3.5
235	13.79	-0.11	0.7	-5.4	O4V	O5V	-0.1	-4.7	-4.6
333	14.38	-0.10	0.8	-4.9	O4.5V	O5.5V	-0.2	-4.2	-4.0
422	15.71	0.18	1.8	-4.5	O7V	O7V	-0.0	-3.8	-3.8
424	14.75	0.10	1.5	-5.2	O3.5V	O5.5V	-0.3	-4.6	-4.3
439	15.86	0.44	2.7	-5.3	O7.5V	O7.5V	-0.0	-4.5	-4.5
512	14.16	-0.11	0.7	-5.0	O8V	O9.5V	-0.4	-4.5	-4.1
525	14.19	-0.08	0.8	-5.1	O6.5V	O6.5V	-0.0	-4.4	-4.4
576	14.72	-0.03	1.2	-5.0	O3V	O4V	-0.7	-4.5	-3.8
620	11.94	0.10	1.4	-7.9	O6.5I	O6.5I	-0.0	-7.2	-7.2
635	14.50	0.08	1.7	-5.7	O4V	O6V	-0.1	-5.0	-4.9
722	13.99	-0.03	0.9	-5.4	O7.5I	O9I	-0.5	-4.8	-4.3
735	15.41	0.03	1.2	-4.3	O9V	O9.7V	-0.4	-3.7	-3.3
782	15.91	0.19	1.7	-4.3	O9.7III	B0V	-0.2	-3.6	-3.4
812	14.93	0.06	1.3	-4.9	O8V	O9.7V	-0.5	-4.3	-3.8
885	16.03	0.38	2.4	-4.9	O5V	O8V	-0.3	-4.3	-4.0
906	15.13	0.08	1.4	-4.8	O6.5V	O6.5V	-0.0	-4.0	-4.0
944	16.91	0.30	2.2	-3.8	O7V	O8V	-0.3	-3.1	-2.8
1024	16.89	0.49	2.8	-4.4	O7.5V	O8.5V	-0.3	-3.8	-3.5
1058	14.06	-0.17	0.5	-5.0	O5.5V	O7V	-0.0	-4.2	-4.2

**Notes.** A total of 48 SB2 systems were identified in the census. However, in order to determine accurate feedback values of both components, only the 27 SB2 systems, for which both a subtype and luminosity class was known for the secondary component, are listed in this table.

Table 5.9: Stellar parameters of the spectroscopically confirmed hot luminous stars in the census. Absolute magnitudes are given in narrow-band for W-R stars and broad-band in all other cases. Stars are listed in order of increasing projected distance ( $r_d$ ) from star R136a1. The first 20 stars are given here, see online data for full census. References for the spectral types are as follows: ST92 - Schild & Testor (1992), P93 - Parker (1993), WB97 - Walborn & Blades (1997), MH98 - Massey & Hunter (1998), CD98 - Crowther & Dessart (1998), B99 - Bosch et al. (1999), W99 - Walborn et al. (1999), BAT99 - Breysacher et al. (1999), Paper I - Evans et al. (2011), T11 - Taylor et al. (2011), D11 - Dufton et al. (2011b), CW11 - Crowther & Walborn (2011), HB12 - Hénault-Brunet et al. (2012), Walborn - Walborn et al. (2014), McEvoy - McEvoy et al. (in prep.) and this work.

ID #	$r_d$ (pc)	Spectral Type	Ref.	$T$ (kK)	$M_v$ or $M_V$ (mag)	$\log L$ ( $L_\odot$ )	$Q_0$ (ph s $^{-1}$ )	$v_\infty$ (km s $^{-1}$ )	$\dot{M}$ ( $M_\odot$ yr $^{-1}$ )	$L_{SW}$ (erg s $^{-1}$ )	$D_{\text{nom}}$ ( $\text{g cm}^3 \text{s}^{-2}$ )
630	0.00	WN 5h	CW11	53	-8.3	6.9	6.6e+50	2600	5.0e-05	1.1e+38	1.3e+36
633	0.02	WN 5h	CW11	53	-7.8	6.8	4.8e+50	2450	5.0e-05	8.7e+37	1.0e+36
642	0.07	O2 If*	CW11	46	-6.3	6.1	7.4e+49	3000	5.0e-06	1.3e+37	9.6e+34
638	0.09	O3 III(f*)	MH98	47	-5.7	5.8	4.6e+49	3200	2.5e-06	8.4e+36	5.0e+34
640	0.12	O3 V	MH98	48	-5.5	5.8	3.9e+49	3000	2.0e-06	5.1e+36	3.0e+34
613	0.12	WN 5h	CW11	53	-7.4	6.6	3.0e+50	2200	4.0e-05	5.6e+37	6.5e+35
651	0.14	O3 III(f*)	MH98	47	-5.5	5.8	3.9e+49	3200	2.0e-06	6.8e+36	3.8e+34
614	0.15	O7 V	MH98	38	-6.2	5.8	2.5e+49	2300	1.6e-06	2.8e+36	2.7e+34
656	0.18	O3 V	CD98	48	-5.6	5.9	4.5e+49	3000	2.0e-06	6.2e+36	3.8e+34
595	0.19	O5:: V	MH98	42	-4.9	5.4	1.3e+49	2700	4.0e-07	1.0e+36	6.1e+33
602	0.22	O3 V	MH98	48	-5.9	6.0	5.6e+49	3000	3.2e-06	8.3e+36	5.4e+34
662	0.25	O9 V	MH98	34	-5.1	5.2	3.9e+48	1500	3.2e-07	2.3e+35	2.8e+33
661	0.26	O3-6 V	MH98	44	-5.5	5.7	2.9e+49	3000	1.3e-06	3.2e+36	2.0e+34
644	0.28	O3 V	MH98	48	-5.5	5.8	4.0e+49	3000	2.0e-06	5.1e+36	3.0e+34
670	0.29	O3 III(f*)	MH98	47	-5.5	5.8	3.9e+49	3200	2.0e-06	6.8e+36	3.8e+34
682	0.38	O3 If*	MH98	42	-6.1	5.9	4.7e+49	3700	2.0e-06	8.3e+36	4.8e+34
624	0.41	O3 V	MH98	48	-5.7	5.9	4.8e+49	3000	2.5e-06	6.8e+36	4.3e+34
678	0.43	O3 III(f*)	MH98	47	-5.7	5.9	4.9e+49	3200	2.5e-06	8.9e+36	5.3e+34
687	0.43	O3 III(f*)	CD98	47	-6.2	6.0	7.1e+49	3200	4.0e-06	1.4e+37	9.1e+34
648	0.44	O3 V	MH98	48	-5.6	5.8	4.4e+49	3000	2.0e-06	5.9e+36	3.6e+34

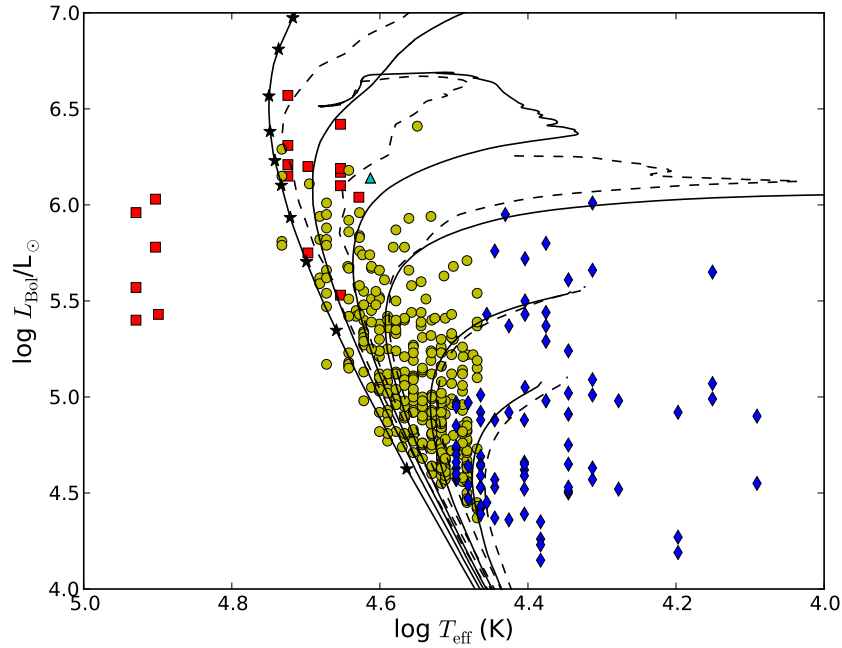
## 5.3 Stellar Census

On the basis of the inferred stellar parameters, estimates of age and mass could be made. Figure 5.9a presents an H-R diagram of all the hot luminous stars in the MEDUSA region. As discussed in Section 5.2.4 uncertainties on  $T_{\text{eff}}$  are likely to be about  $\pm 2000$  K while  $\log L_{\text{Bol}}/L_{\odot}$  is accurate to  $\pm 0.2$  dex. The zero age main sequence (ZAMS) positions are based on the contemporary evolutionary models of Brott et al. (2011) and Köhler et al. (in prep.). The accompanying isochrones are overlaid for rotating ( $v_{\text{rot}} = 300 \text{ km s}^{-1}$ ) and non-rotating ( $v_{\text{rot}} = 0 \text{ km s}^{-1}$ ) models, spanning ages from 0 to 8 Myr. The hot stars to the far left of the diagram are the evolved W-R stars. They are not covered by the isochrones as the associated evolutionary tracks only modelled as far as the terminal-age main sequence. The isochrones reveal a large age spread across more than 8 Myr. Indeed, Walborn & Blades (1997) found several distinct stellar regions of different ages within 30 Dor, suggesting a possibility for triggered star formation.

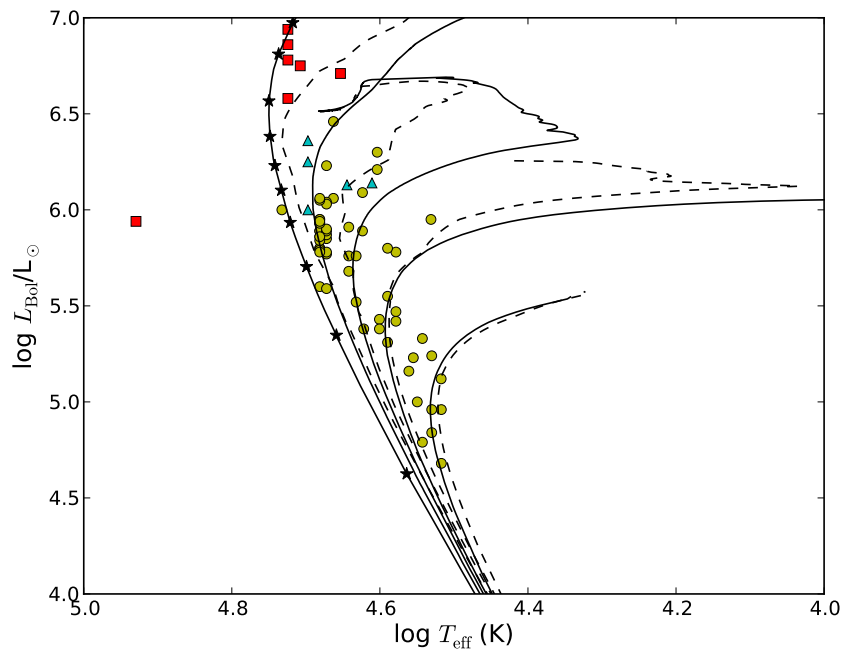
The ionising stars are, nevertheless, largely concentrated between 2 – 5 Myr. Is this consistent with the representative age that would be obtained if 30 Dor were an extragalactic star forming region? A representative age of the population was estimated using the  $\text{H}\alpha$  nebular observations of Pellegrini et al. (2010). The integrated  $\text{H}\alpha + [\text{N II}]$  emission line flux was measured and corrected for  $[\text{N II}]$  contamination (assuming  $F([\text{N II}]\lambda 6548, \lambda 6583)/F(\text{H}\alpha) = 0.15$ ) resulting in  $W_{\lambda}(\text{H}\alpha) = 1100 \text{ \AA}$  (E. Pellegrini priv. comm.).  $W_{\lambda}(\text{H}\alpha)$  will decline with age, since hot stars gradually end their lives and the hydrogen gas can no longer be ionised (Schaerer & Vacca 1998). At LMC metallicity,  $W_{\lambda}(\text{H}\alpha) = 1100 \text{ \AA}$  corresponds to an age of  $\sim 3.5$  Myr, consistent with the average stellar age.

Identifying individual age groups is difficult in more distant unresolved star forming regions, but an attempt could be made for the massive R136 region. Figure 5.9b shows a similar H-R diagram for the stars in the R136 region. The cluster represents a naturally younger population in comparison to the rest of 30 Dor. In particular, the most luminous and massive stars, including all the WN and Of/WN stars, fall between  $\sim 1 - 2$  Myr. A large scatter remains, however, with stars at lower luminosities favouring older ages up to 5 Myr and making an individual age for the cluster, hard to assign. Nevertheless, the findings are largely consistent with the work of Massey & Hunter (1998) who found ages  $\sim 2$  Myr. Sabbi et al. (2012) determined a similar 1 – 2 Myr age for R136 but also identified an older ( $\sim 2 - 5$  Myr) region extending  $\sim 5.4$  pc to the north-east. As the R136 region in the census extends to 5 pc, there is a high possibility of contamination from older non-coeval stars.

To estimate stellar masses, a mass-luminosity relation of  $L \propto M^{1.75}$  was applied to all O-type dwarfs. Yusof et al. (2013) had since derived two relations where  $L \propto M^{2.71}$  for 9 – 50  $M_{\odot}$



(a)



(b)

Figure 5.9: An H-R diagram of all the spectroscopically confirmed hot luminous stars in the MEDUSA region (a) and R136 region (b). W-R stars (red squares), Of/WN stars (cyan triangles), O-type stars (yellow circles) and B-type stars (blue diamonds). Isochrones at 1, 2, 3, & 5 Myr are overlaid in both cases, with 8 Myr also used for the MEDUSA region. The isochrones are based on rotating ( $v_{\text{rot}} = 300 \text{ km s}^{-1}$ , dashed line) and non-rotating ( $v_{\text{rot}} = 0 \text{ km s}^{-1}$ , solid line) evolutionary models of Brott et al. (2011) and Köhler et al. (in prep.). The ZAMS positions for stars with  $M_{\text{init}} = 20, 40, 60, 80, 100, 120, 150, 200, 300$  &  $400 M_{\odot}$  are marked by black stars and joined with a solid line.

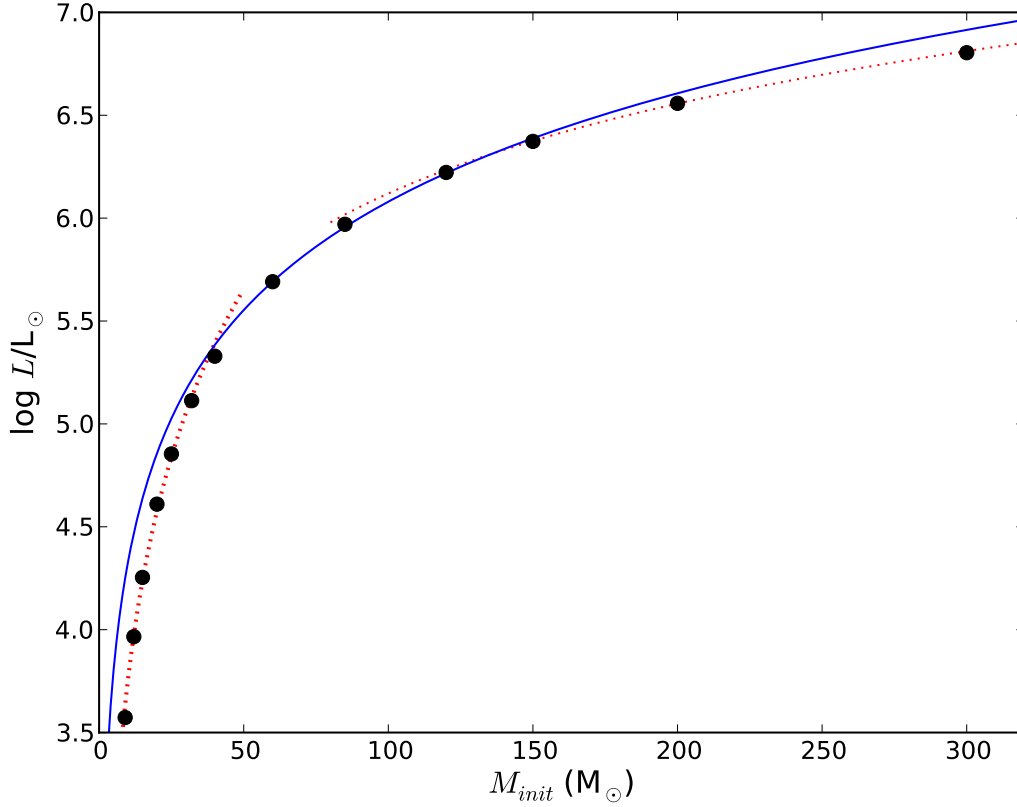


Figure 5.10: The black circles mark the stellar parameters used by Yusof et al. (2013) to fit their lower  $L \propto M^{2.71}$  ( $9 - 50 M_{\odot}$ ) and upper  $L \propto M^{1.45}$  ( $80 - 500 M_{\odot}$ ) ZAMS mass-luminosity relations plotted with a dotted red lines. The solid blue line represents the  $L \propto M^{1.75}$  relation used in the census.

and  $L \propto M^{1.45}$  for  $80 - 500 M_{\odot}$ . A fit was made to their stellar parameters showing that the  $L \propto M^{1.75}$  relation used for the census was best suited to stars with  $50 \lesssim M_{init} \lesssim 150 M_{\odot}$ . As a result, this would underestimate the masses for lower luminosity dwarfs. Conversely, more accurate masses should be obtained for the luminous dwarfs for which completeness was higher and the integrated mass would be more dependent on.

However, the relation strictly only applies to ZAMS stars such that, in the case of the O-type giants and supergiants, the  $\log g$ -SpT calibrations of Martins et al. (2005) were adopted. The stellar radius was then derived following Equation 1.1. This finally allowed the mass to be calculated via the relation:  $M = gR^2/G$ , where  $G$  is the gravitational constant. A similar approach was used for the B-type stars, only  $\log g$  averages were taken for each SpT from the works of Trundle et al. (2007) and Hunter et al. (2007). Rough mass estimates of the WC and WNC stars were obtained through the calibration of Schaerer & Maeder (1992). However, in

case of the H burning WN and Of/WN stars, due to their expected younger age, the H-burning mass-luminosity relation ( $L \propto M^{1.75}$ ) was applied once more.

Photometry suggested a further 141 hot luminous stars were present within the R136 region and 222 stars within 30 Dor (Section 4.6.4). Therefore, these stars also needed to be taken into account when deriving the mass function for each region. In this case, the SpTs for the census were obtained through a combination of spectroscopy and photometry (Sp+Ph), as opposed to relying solely on stars that had spectroscopy (Sp). The inferred mass functions for 30 Dor and the R136 region are plotted in Figure 5.11. There is consistency with the Salpeter (1955)  $\alpha = -2.3$  slope but this notably deviates at  $\sim 20 M_{\odot}$ . This will have occurred due to incomplete photometry and spectroscopy of fainter lower mass stars. Assuming the Sp+Ph stellar census to be complete above  $20 M_{\odot}$  and adopting a Kroupa (2001) IMF, the total stellar mass for each region was obtained. This produced the first direct estimate of the 30 Dor stellar mass as  $M_{30\text{Dor}} \sim 1.1 \times 10^5 M_{\odot}$ . In the case of R136,  $M_{\text{R136}} \sim 5.0 \times 10^4 M_{\odot}$ . Hunter et al. (1995) had also estimated a stellar mass for R136 but adopted a Salpeter IMF. After adapting their results to fit a Kroupa IMF, results were found to agree with the census to within  $\sim 10\%$ .

## 5.4 Integrated Stellar Feedback

For an estimate of the total stellar feedback of 30 Dor, the contributions of individual stars were combined to produce the cumulative plots presented in Figures 5.12 - 5.13. While the R136 region showed a lower completeness compared to 30 Dor, it still contained a high proportion of the brightest W-R, Of/WN and O-type stars, and is therefore considered separately. In addition, feedback estimates are also made for the stars lacking spectroscopy (Section 4.6.4). The integrated feedback at different projected radial distances can be found in Table 5.10 along with a breakdown of the contributions from the different SpTs.

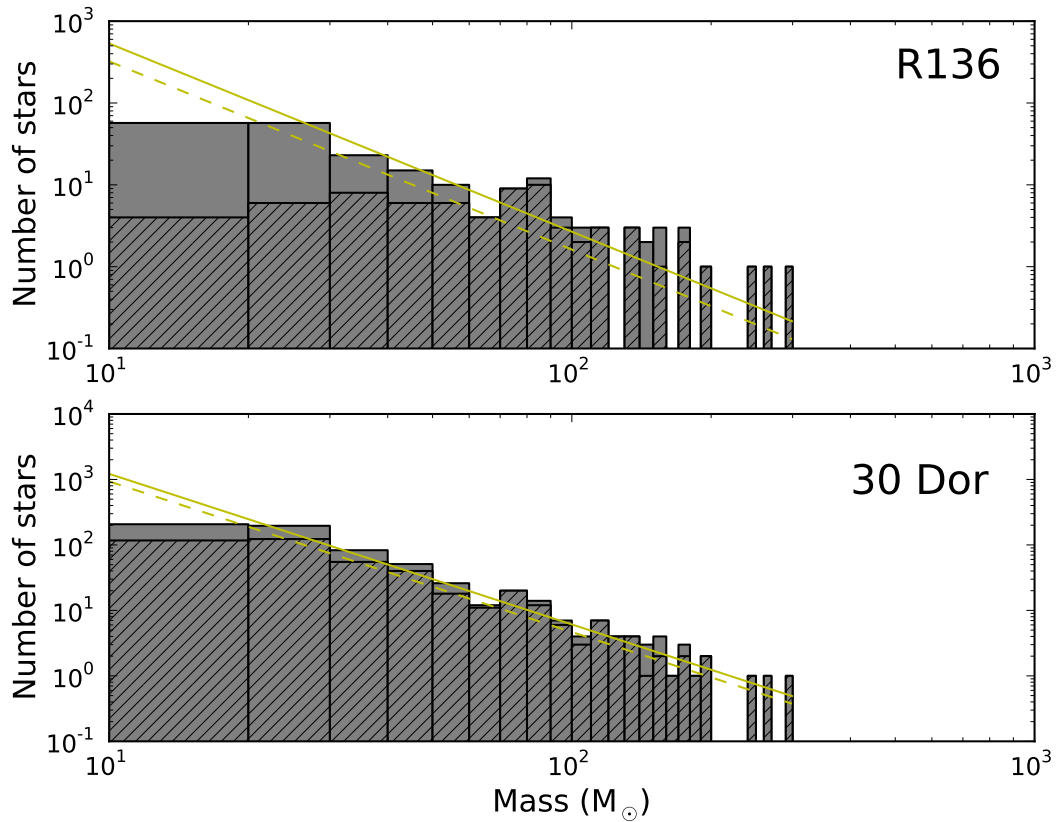


Figure 5.11: The present day mass function of all hot luminous stars classified spectroscopically and photometrically (Sp+Ph) in the R136 region (top) and in 30 Dor (bottom). Hatched regions indicate where the mass function is based solely on stars classified spectroscopically (Sp). A Salpeter  $\alpha = -2.3$  slope is overlaid with a yellow line (solid = Sp+Ph, dashed = Sp), for which the integrated mass ( $> 20 M_{\odot}$ ) is consistent with that of each region.

Table 5.10: The cumulative properties of hot luminous stars in 30 Dor for an increasing projected radius,  $r_d$ , given in (pc), from R136a1. The top half of the table gives the more robust values, based solely on the number of stars (N) classified spectroscopically (Sp). The bottom half combines both spectroscopically and photometrically classified stars (Sp+Ph). Note the contribution from the W-R and Of/WN stars remains unchanged as none of these stars were taken to lack spectroscopy.  $\log L_{\text{Bol}}$  is given in ( $L_{\odot}$ ),  $Q_0$  in ( $\times 10^{49} \text{ ph s}^{-1}$ ),  $L_{\text{SW}}$  in ( $\times 10^{37} \text{ erg s}^{-1}$ ) and  $D_{\text{mom}}$  in ( $\times 10^{36} \text{ cgs units}$ ).

Region	OB Stars						W-R and Of/WN Stars						Grand Total					
	N	$\log L_{\text{Bol}}^{\text{Sp}}$	$Q_0^{\text{Sp}}$	$L_{\text{SW}}^{\text{Sp}}$	$D_{\text{mom}}^{\text{Sp}}$		N	$\log L_{\text{Bol}}^{\text{Sp}}$	$Q_0^{\text{Sp}}$	$L_{\text{SW}}^{\text{Sp}}$	$D_{\text{mom}}^{\text{Sp}}$		N	$\log L_{\text{Bol}}^{\text{Sp}}$	$Q_0^{\text{Sp}}$	$L_{\text{SW}}^{\text{Sp}}$	$D_{\text{mom}}^{\text{Sp}}$	
5	60	7.61	242	37.6	2.72		12	7.66	334	63.9	7.69		72	7.93	576	101	10.4	
10	120	7.77	319	48.6	3.86		13	7.67	343	65.8	8.03		133	8.02	662	114	11.9	
20	191	7.88	397	59.0	4.83		19	7.74	398	85.3	9.98		210	8.12	795	144	14.8	
150	469	8.07	554	75.6	6.22		31	7.84	503	122	13.7		500	8.27	1056	197	19.9	
< $r_d$	N	$\log L_{\text{Bol}}^{\text{Sp+Ph}}$	$Q_0^{\text{Sp+Ph}}$	$L_{\text{SW}}^{\text{Sp+Ph}}$	$D_{\text{mom}}^{\text{Sp+Ph}}$		N	$\log L_{\text{Bol}}^{\text{Sp+Ph}}$	$Q_0^{\text{Sp+Ph}}$	$L_{\text{SW}}^{\text{Sp+Ph}}$	$D_{\text{mom}}^{\text{Sp+Ph}}$		N	$\log L_{\text{Bol}}^{\text{Sp+Ph}}$	$Q_0^{\text{Sp+Ph}}$	$L_{\text{SW}}^{\text{Sp+Ph}}$	$D_{\text{mom}}^{\text{Sp+Ph}}$	
5	201	7.85	388	60.3	4.54		12	7.66	334	63.9	7.69		213	8.06	723	124	12.2	
10	284	7.96	474	71.9	5.74		13	7.67	343	65.8	8.03		297	8.14	786	138	13.8	
20	374	8.04	555	82.4	6.72		19	7.74	398	85.3	9.98		393	8.22	952	168	16.7	
150	691	8.20	734	102	8.49		31	7.84	503	122	13.7		722	8.36	1237	224	22.2	

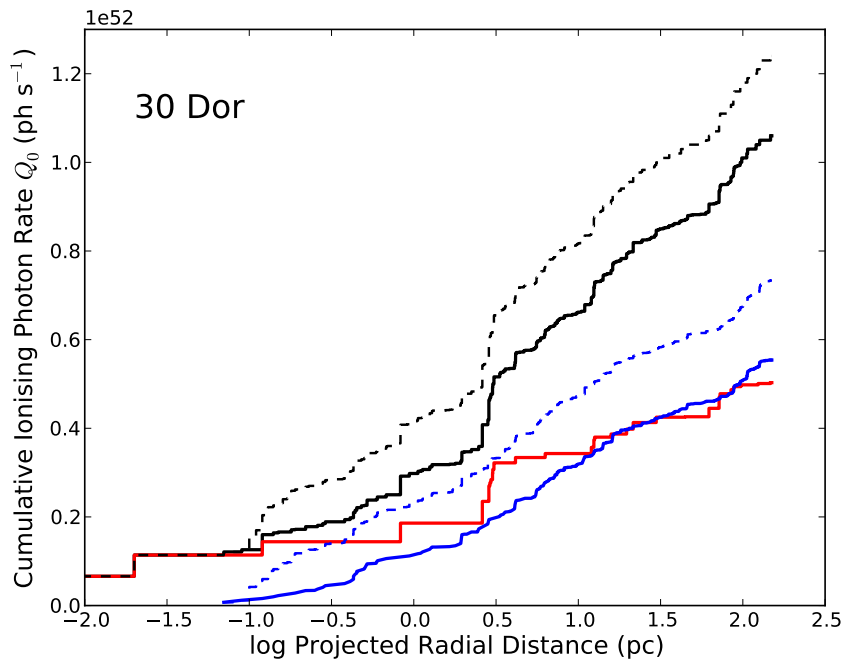
### 5.4.1 Ionising photon rate

Figure 5.12a shows the total ionising photon rate from stars with spectroscopy (solid line) to be  $Q_0^{\text{Sp}} \approx 1.0 \times 10^{52} \text{ ph s}^{-1}$ . A sharp increase is seen within the inner 20 pc (80 arcsec) of 30 Dor from which  $\sim 75\%$  of the ionising photons are produced. This relates to the large number of hot massive stars in the vicinity of R136. The increases reflect the contributions from W-R and Of/WN stars. In spite of only 31 such stars being within 30 Dor, they contribute an equivalent output to the 469 OB stars present. Taking a closer look at the feedback from the R136 region (see Figure 5.12b), it is analogous to 30 Dor as a whole. The ionising photons are shared roughly equally between the W-R & Of/WN stars and OB stars. An exception to this is seen at the very core of the cluster where the four WN 5h stars (Crowther et al. 2010) dominate the output of the cluster.

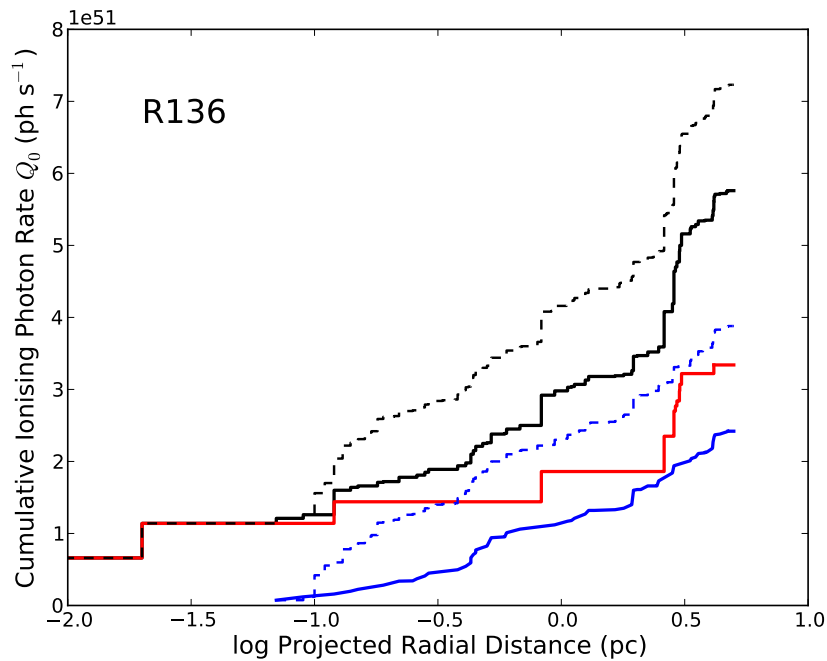
The dashed lines represent the total ionising photon rate when accounting for stars which had their SpTs estimated from photometric data ( $Q_0^{\text{Sp+Ph}}$ ). The contribution from these stars increases the total number of ionising photons by about 25% and 15%, in the R136 region and 30 Dor, respectively. While these values are less robust, it shows that the remaining hot luminous stars in 30 Dor without spectroscopy (predominantly in R136) should not be neglected. However, it also indicates that the stars with known SpT likely dominate the total output so that any uncertainties due to stars lacking spectroscopy should not be too severe.

Crowther & Dessart (1998) made earlier estimates of the ionising output of 30 Dor using this same method of summing the contribution of the individual stars. Their study extended out to  $r_d = 10 \text{ pc}$  and found  $Q_0 = 4.2 \times 10^{51} \text{ ph s}^{-1}$ . They also made SpT assumptions for some stars and so comparisons were made with  $Q_0^{\text{Sp+Ph}}$ . The revised values of the census were found to be almost 90% larger (see Table 5.10). The offset will largely be due to the higher  $T_{\text{eff}}$  calibrations and updated W-R star models used, along with the new photometric and spectroscopic coverage of the stars within the region.

Table 5.11 lists the ten stars with the highest ionising photon rates. These are all found to be W-R or Of/WN stars, except for Mk 42 (O2 If\*), and are mainly located within the R136 region. These ten stars alone produce 28% of  $Q_0^{\text{Sp+Ph}}$ . It is accepted that some less luminous stars will have been missed from the census but their impact on the integrated ionising output will be negligible in comparison to these W-R stars. For example, Figure 4.7 showed 38 subluminous VFTS O-type stars being removed from the census by the selection criteria. Their combined ionising output is estimated to be  $< 0.5\%$  of  $Q_0^{\text{Sp}}$ , which is below the output from B-type stars in the census.



(a)



(b)

Figure 5.12: Cumulative ionising photon rates of the hot luminous stars in 30 Dor (a) and the R136 region (b). Feedback from all stars (black), W-R and Of/WN stars (red) and OB stars (blue). Solid lines include the feedback from stars which were spectroscopically classified as hot and luminous (Sp) while dashed lines include feedback from photometrically classified stars (Sp+Ph).

### 5.4.2 Stellar wind luminosity and momentum

The total stellar wind luminosity of 30 Dor was estimated at  $L_{\text{SW}}^{\text{Sp}} \approx 1.97 \times 10^{39} \text{ erg s}^{-1}$ . Figure 5.13a shows the radial cumulative wind luminosity to behave similarly to the ionising photon rate: rapidly increasing within the inner 20 pc, from which  $\sim 75\%$  of the total wind luminosity is produced. W-R and Of/WN stars dominate the mechanical feedback, providing about two thirds of the total. Their higher contribution arises from their high mass-loss rates and fast winds. This behaviour is repeated in the R136 region (see Figure 5.13b), where the four WN 5h stars again provide significant mechanical feedback to the cluster. The dashed lines again represent the combined spectroscopically and photometrically classified sample.  $L_{\text{SW}}^{\text{Sp+Ph}}$  values suggest wind luminosities in the R136 region and within 30 Dor could increase about a further 25% and 15%, respectively.

Again, comparisons were made to the work of Crowther & Dessart (1998) who found  $L_{\text{SW}} = 1.61 \times 10^{39} \text{ erg s}^{-1}$  out to  $r_d = 10 \text{ pc}$ , i.e. about 15% higher than  $L_{\text{SW}}^{\text{Sp+Ph}}$  (see Table 5.10). The offset results again from the updated stellar calibrations and mass-loss rates that are corrected for wind clumping.

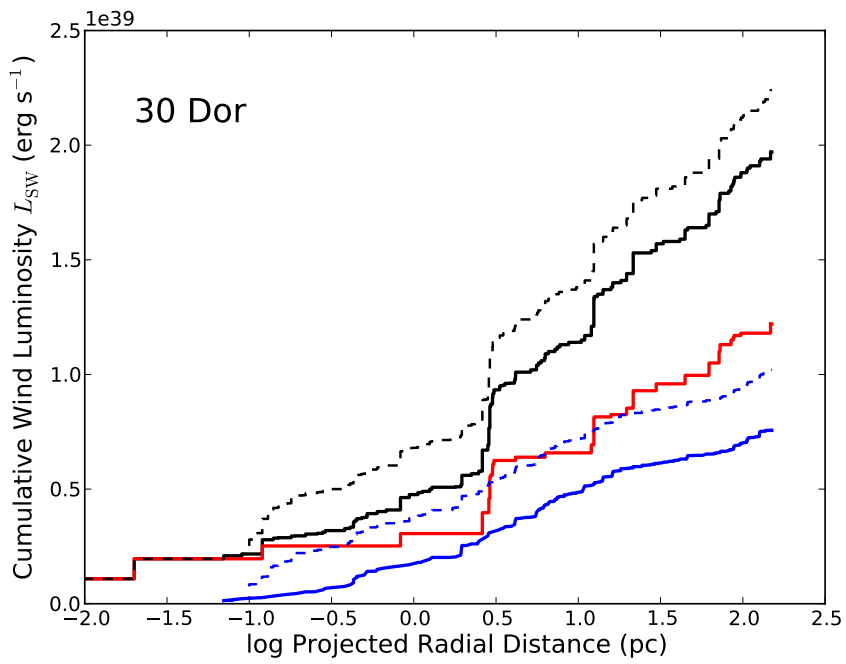
Table 5.11 also lists the ten stars with the highest wind luminosities. These are all W-R stars, most of which overlap with the dominant ionising stars and are also located within the R136 region. The importance of the W-R stars is echoed here as these ten stars alone contribute 35% of  $L_{\text{SW}}^{\text{Sp+Ph}}$ . Once again, contributions of subluminous stars become negligible, such as the VFTS O-type stars excluded from the census whose combined wind luminosity is  $< 0.05\%$  of  $L_{\text{SW}}^{\text{Sp}}$  and just a few % of the B-type star output.

The integrated modified wind momenta,  $D_{\text{mom}}$ , behave very similarly to  $L_{\text{SW}}$ . Table 5.10 shows how the W-R and Of/WN stars are again the key contributors while the contribution from OB stars is slightly reduced, likely due to the lower dependence that their high  $v_{\infty}$  play on  $D_{\text{mom}}$ .

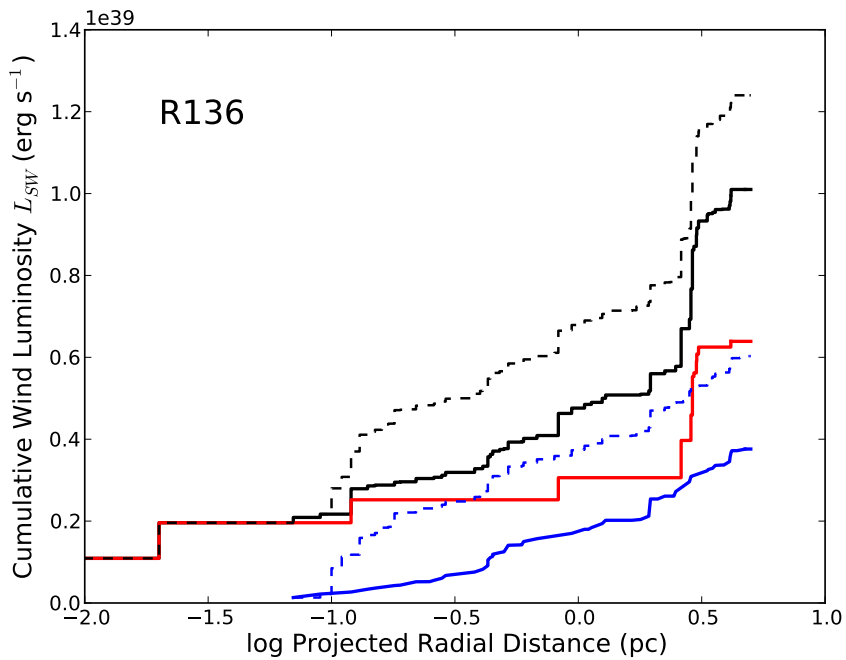
It is noted that the contribution of the W-R stars on the stellar bolometric luminosity is different to the stellar feedback. OB stars contribute  $\sim 70\%$  of the bolometric luminosity of 30 Dor (Table 5.10). W-R and Of/WN stars, while individually luminous compared to many of the OB stars, contribute  $\sim 30\%$  of the integrated luminosity of the region.

### 5.4.3 Feedback from additional sources

While the census focusses on selecting hot luminous stars, the estimates are potentially influenced by additional sources of feedback. Embedded stars, shock emission and sources outside the census could all contribute. Nevertheless, here it is argued that they will only have a limited



(a)



(b)

Figure 5.13: Cumulative stellar wind luminosities of the hot luminous stars in 30 Dor (a) and the R136 region (b). Lines are as in Figure 5.12.

impact on the integrated values and that the W-R stars still have the greatest influence.

Firstly, what is the impact of stars beyond the selected  $r_d \leq 150$  pc region of 30 Dor? Figures 5.12a & 5.13a clearly show the cumulative effect of hot luminous stars to drop off at large distances from R136. There are no significant young clusters close to the census border to provide extra feedback. To further test this, the selection criteria introduced in Section 4.4 were applied to original photometric catalogues but extended to a radius of  $r_d \leq 225$  pc (more than doubling the projected area on the sky). While, the photometric coverage of some regions would be incomplete, it is expected that only an additional  $\sim 300$  candidate hot luminous stars (25% of the census) would be enclosed. Spectral coverage is poor beyond  $r_d \sim 150$  pc but only one W-R star is known to exist within this extended 30 Dor region, namely BAT99-85/VFTS 002, WC 4+(O6-6.5 III).

A further lack of highly ionised species, such as [O IV] and [Ne V] leaves photoionisation as the dominant process in the energy budget (Indebetouw et al. 2009; Pellegrini et al. 2010). But within the  $r_d \leq 150$  pc region of 30 Dor, the selection criteria allowed for extinction as high as  $A_V = 3.92$  mag. Until now, W-R star VFTS 682 had been overlooked due to its high extinction, posing the question of whether other populations of massive stars could also have been hidden from view. As neither optical nor IR nebular emission lines show a strong correlation between high excitation regions and listed embedded stars, the ionisation structure of 30 Dor primarily arises from the optically known hot stars (Indebetouw et al. 2009).

The isochrones in Figure 5.9 show the age of massive stars within 30 Dor to extend beyond 8 Myr, with ages of 20-25 Myr derived for the Hodge 301 cluster (Grebel & Chu 2000). This clearly extends well beyond the epoch of the first SNe that would have occurred in the region and is demonstrated by the N157B supernova remnant (Chu et al. 1992). A complex structure of gas filaments and bubbles is generated by stellar winds and SNe, many of which coincide with bright X-ray sources (Townsley et al. 2006). Chu & Kennicutt (1994) identify a number of gas shells expanding at velocities up to  $200 \text{ km s}^{-1}$ . Despite the evidence for shocks, the ionising output from hot stars seems capable of keeping the shells ionised (Chu & Kennicutt 1994).

When considering mechanical feedback, however, SNe do become significant. While some of the smaller shells are thought to be wind-blown bubbles, the larger and faster moving shells are only likely to be carved by the energy input of SNe (Chu & Kennicutt 1994). An exception would be the shell surrounding R136. Taking the derived wind luminosity for the R136 region with a pre-SNe age of  $\sim 2$  Myr, the kinetic energy generated by the stellar winds could amount to a few  $10^{52}$  erg, sufficiently high to drive the bubble (Chu & Kennicutt 1994). However, determining a combined stellar/SNe energy budget for 30 Dor, awaits a better understanding of its star formation history (SFH).

## 5.5 Comparison with Population Synthesis Models

Population synthesis codes seek to mimic the combined properties of a stellar system of a given age and mass. With only a few initial parameters being required, expected observable properties of extragalactic star forming regions can be predicted. However, there are limited targets available to test the reliability of such models. R136 is one of the few resolved massive star clusters which allows an empirical study of the stars to be compared to synthetic predictions. In particular, its high mass ( $M_{cl} = 5 - 10 \times 10^4 M_{\odot}$ , Hunter et al. 1995; Andersen et al. 2009) and young age (1 – 2 Myr, Section 5.3), means that the upper mass function is well populated and any stochastic effects are minimal (Cerviño et al. 2002).

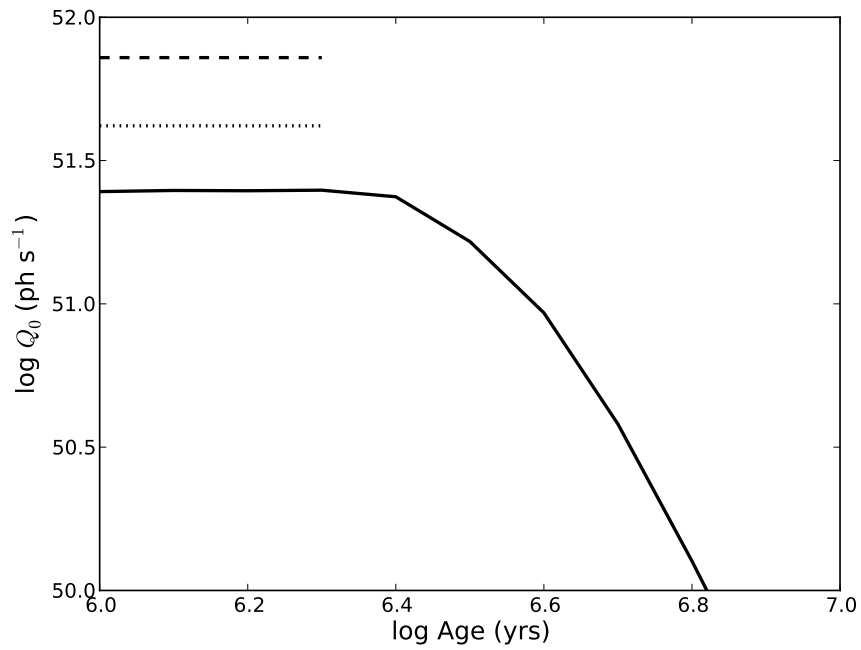
A synthetic model of a R136-like cluster was generated by the population synthesis code, *Starburst99* (Leitherer et al. 1999). An instantaneous burst model with total mass  $10^6 M_{\odot}$  and metallicity  $Z = 0.4 Z_{\odot}$ <sup>1</sup> was adopted, which was scaled to  $M_{cl} = 5.5 \times 10^4 M_{\odot}$ <sup>2</sup>, in order to mimic R136. A Kroupa IMF with an upper mass limit of  $M_{up} = 100 M_{\odot}$  was selected along with the “high mass-loss rate” Geneva evolutionary tracks of Meynet et al. (1994). The theoretical wind model was chosen, meaning that the wind luminosity produced was based on mass-loss rates and terminal wind velocities from Equations 1 & 2 of Leitherer et al. (1992), respectively. Ionising photon fluxes used the calibration from Smith et al. (2002).

The empirical feedback from R136 is compared with *Starburst99* in Figure 5.14. Here, the combined spectroscopic and photometric values ( $Q_0^{Sp+Ph}$  &  $L_{SW}^{Sp+Ph}$ ) are used in the comparison. The *Starburst99* predictions only represent contributions from stars (i.e. excluding supernovae). Their changing values, over time, reflect the different SpTs that contribute to the feedback. Comparisons to *Starburst99* are made between 1-2 Myr, given the age obtained by Massey & Hunter (1998) for the most luminous members of R136 (see also Figure 5.9b). In both cases, empirical results exceed the predictions of *Starburst99*. The predicted ionising photon rate underestimates the empirical results by a factor of two, while the wind luminosity is underestimated by a factor of nine.

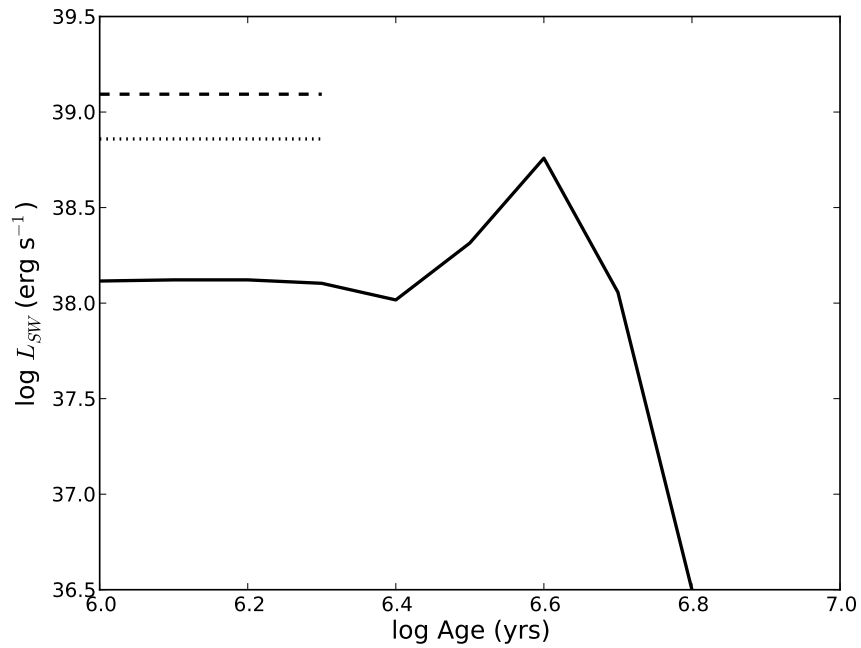
The standard feedback recipe for *Starburst99* is somewhat dated and may help explain this disagreement. In the case of the ionising photons, W-R stars have already been seen to contribute significantly to the output of R136. Recent spectral modelling of the four core WN5h stars by Crowther et al. (2010) has estimated them all to have initial masses  $M_{init} > 150 M_{\odot}$ . However, the IMF used for *Starburst99* was limited to  $M_{up} = 100 M_{\odot}$  and the incorporated evolutionary tracks only extended up to  $120 M_{\odot}$ . The *Starburst99* output would therefore have

<sup>1</sup>This is the most appropriate LMC metallicity provided by *Starburst99*, and while different to  $Z = 0.5 Z_{\odot}$  adopted for the stellar wind calibrations, this difference should have minor effects when comparing results.

<sup>2</sup>This mass was favoured as it was derived from lower mass stars  $2.8 - 15 M_{\odot}$  (Hunter et al. 1995) and then scaled to a Kroupa IMF.



(a)



(b)

Figure 5.14: The integrated ionising photon rate (a) and stellar wind luminosity (b) of the R136 region. Predictions from *Starburst99* are plotted with a solid line. Values from the census, with and without  $M_{\text{init}} > 100 M_{\odot}$  stars, are plotted in dashed and dotted lines, respectively.

excluded stars with  $M_{\text{init}} > 100 M_{\odot}$ .

In an attempt to identify other stars with  $M_{\text{init}} > 100 M_{\odot}$ , examinations were made of the latest Bonn evolutionary tracks by Köhler et al. (in prep.), which extend to  $500 M_{\odot}$ . For a LMC metallicity and an age of  $\leq 2$  Myr, the luminosity of a  $100 M_{\odot}$  star was expected to be  $\log(L_{\text{Bol}}/L_{\odot}) \gtrsim 6.3$ . Table 5.11 lists ten census stars to which this applies, of which eight are located within the R136 region. The dotted lines in Figure 5.14, show empirical results if such stars are excluded. A better agreement is obtained with *Starburst99*, with differences in  $Q_0$  reduced to  $\sim 0.2$  dex. Minimal differences were found between the  $q_0$  calibration derived for this work and the one used by *Starburst99* (Smith et al. 2002), so this remaining offset most likely arises from the higher  $T_{\text{eff}}$  that were assigned to the SpTs.

When comparing the wind luminosities, excluding stars with  $M_{\text{init}} > 100 M_{\odot}$  has less of an impact and *Starburst99* is still seen to underestimate empirical results by  $\sim 0.7$  dex. In this case, the disagreement largely arises from the different mass-loss prescriptions. *Starburst99* predictions follow Leitherer et al. (1992) and are found to differ from the Vink et al. (2001) mass-loss rates by a factor of 2 – 10, depending on SpT. Any differences in  $v_{\infty}$  should be minimal, however, (see Figure 2 in Leitherer et al. 1992).

## 5.6 Star Formation Rates

There are various methods to estimate the SFR of a region, from UV through to IR. Each have advantages and disadvantages, as they trace the fate of the ionising photons from the young stellar population (Kennicutt 1998). The census of 30 Dor now provides the total ionising photon rate produced by its stars. The UV stellar continuum is a direct probe of this emission while nebular recombination lines (e.g.  $H\alpha$ ) and the far-infrared (FIR) dust continuum are more widely used and have already been applied in Chapter 2. In this section, the findings of these different indicators are compared for both Salpeter and Kroupa IMFs. Comparing their estimates to those of the census also allows the determination of the possible fraction of ionising photons which may be escaping the region,  $f_{\text{esc}}$ .

Kennicutt (1998) provide a series of widely used calibrations to estimate the SFR from various wavelengths. They are derived from population synthesis models which predict the respective values ( $Q_0$ ,  $H\alpha$  etc.) for a given set of parameters, including the IMF, over a period of constant star formation. They were revisited in a review by Kennicutt & Evans (2012) and references therein, where changes arose from updates to the IMF and stellar population models. However, these calibrations are more applicable to galaxies and starburst regions, for which star formation has occurred for at least 100 Myr. In the case of 30 Dor, findings from

Table 5.11: The census stars with the highest ionising photon rates, wind luminosities and masses and their combined contribution to 30 Dor. Entries given in bold are based on tailored W-R analyses (see Table 3.12). Other entries rely either on the less reliable W-R star template method or the calibrations discussed in Section 5.2.

ID #	Star	SpT	$r_d$ (pc)	$Q_0$ ( $10^{49}$ ph s $^{-1}$ )	$L_{SW}$ ( $10^{37}$ erg s $^{-1}$ )
10 STARS WITH HIGHEST IONISING PHOTON RATE					
<b>630</b>	<b>R136a1</b>	<b>WN 5h</b>	<b>0.00</b>	<b>66.0</b>	<b>10.9</b>
770	<i>Mk34</i>	<i>WN 5h</i>	2.61	49.2	9.2
<b>633</b>	<b>R136a2</b>	<b>WN 5h</b>	<b>0.02</b>	<b>48.0</b>	<b>8.7</b>
<b>706</b>	<b>R136c</b>	<b>WN 5h</b>	<b>0.83</b>	<b>42.0</b>	<b>5.4</b>
493	<i>R134</i>	<i>WN 6(h)</i>	2.86	35.3	6.2
<b>613</b>	<b>R136a3</b>	<b>WN 5h</b>	<b>0.12</b>	<b>30.0</b>	<b>5.6</b>
1001	<i>BAT99-122</i>	<i>WN 5h</i>	71.71	25.0	5.5
580	<i>Mk 42</i>	<i>O2 If*</i>	1.96	18.8	4.0
<b>916</b>	<b>BAT99-118</b>	<b>WN 6h</b>	<b>62.27</b>	<b>18.2</b>	<b>5.3</b>
375	<i>BAT99-95</i>	<i>WN 7h</i>	21.56	15.8	7.6
Total (% of $Q_0^{Sp+Ph}$ or $L_{SW}^{Sp+Ph}$ ):			348.3 (28%)	68.4 (29%)	
10 STARS WITH HIGHEST WIND LUMINOSITY					
<b>630</b>	<b>R136a1</b>	<b>WN 5h</b>	<b>0.00</b>	<b>66.0</b>	<b>10.9</b>
543	<i>R140a1</i>	<i>WC 4</i>	12.43	6.6	9.7
762	<i>Mk33Sb</i>	<i>WC 5</i>	2.90	6.3	9.4
770	<i>Mk34</i>	<i>WN 5h</i>	2.61	49.2	9.2
<b>633</b>	<b>R136a2</b>	<b>WN 5h</b>	<b>0.02</b>	<b>48.0</b>	<b>8.7</b>
375	<i>BAT99-95</i>	<i>WN 7h</i>	21.6	15.8	7.6
493	<i>R134</i>	<i>WN 6(h)</i>	2.86	35.3	6.2
<b>613</b>	<b>R136a3</b>	<b>WN 5h</b>	<b>0.12</b>	<b>30.0</b>	<b>5.6</b>
1001	<i>BAT99-122</i>	<i>WN 5h</i>	71.7	25.0	5.5
<b>706</b>	<b>R136c</b>	<b>WN 5h</b>	<b>0.83</b>	<b>42.0</b>	<b>5.4</b>
Total (% of $Q_0^{Sp+Ph}$ or $L_{SW}^{Sp+Ph}$ ):			324.2 (28%)	78.2 (35%)	
STARS WITH $M_{init} > 100 M_{\odot}$					
<b>630</b>	<b>R136a1</b>	<b>WN 5h</b>	<b>0.00</b>	<b>66.0</b>	<b>10.9</b>
770	<i>Mk34</i>	<i>WN 5h</i>	2.61	49.2	9.2
<b>633</b>	<b>R136a2</b>	<b>WN 5h</b>	<b>0.02</b>	<b>48.0</b>	<b>8.7</b>
<b>706</b>	<b>R136c</b>	<b>WN 5h</b>	<b>0.83</b>	<b>42.0</b>	<b>5.4</b>
493	<i>R134</i>	<i>WN 6(h)</i>	2.86	35.3	6.2
<b>613</b>	<b>R136a3</b>	<b>WN 5h</b>	<b>0.12</b>	<b>30.0</b>	<b>5.6</b>
1001	<i>BAT99-122</i>	<i>WN 5h</i>	71.71	25.0	5.5
580	<i>Mk 42</i>	<i>O2 If*</i>	1.96	18.8	4.0
<b>916</b>	<b>BAT99-118</b>	<b>WN 6h</b>	<b>62.27</b>	<b>18.2</b>	<b>5.3</b>
375	<i>Mk35</i>	<i>O2 If*/WN 5</i>	3.07	15.6	1.7
Total (% of $Q_0^{Sp+Ph}$ or $L_{SW}^{Sp+Ph}$ ):			348.1 (28%)	62.5 (28%)	

Walborn & Blades (1997) and the census suggest stellar ages  $> 10$  Myr but information on the region's SFH is limited. Nevertheless, De Marchi et al. (2011) had used their HST/WFC3 photometry to focus on pre main-sequence stars, albeit within a smaller central region of 30 Dor compared to the census. They estimated a relatively constant SFH for 30 Dor for the past  $\sim 10$  Myr.

Based on these findings, the use of alternative SFR calibrations, tailored to 30 Dor, was favoured. Equations 5.9 - 5.13 present new SFR calibrations that were derived using *Starburst99* for this work on 30 Dor. A *Starburst99* synthetic model was set to run for 10 Myr with a continuous SFR =  $1 M_{\odot} \text{ yr}^{-1}$ . All other model parameters were identical to the R136 burst model discussed in Section 5.5, i.e. a Kroupa IMF, “high mass-loss rate” Geneva evolutionary tracks and  $Z = 0.4 Z_{\odot}$ . Different luminosities predicted by *Starburst99*, at an age of 10 Myr, were then adopted following the earlier assumption that the SFR in 30 Dor had been constant for up to  $\sim 10$  Myr. This allowed the calibrations in Equations 5.9 - 5.13 to be derived since the SFR of the model had been set to  $1 M_{\odot} \text{ yr}^{-1}$ . For example, at 10 My, *Starburst99* estimated  $\log Q_0 = 53.24$ . Since the SFR is known to be  $1 M_{\odot} \text{ yr}^{-1}$ , the coefficient in Equation 5.9 is simply derived by:  $1/10^{53.24} \approx 5.8 \times 10^{-54}$ . However, Section 5.4 showed how the exclusion of  $M_{\text{init}} > 100 M_{\odot}$  stars can lead to integrated stellar luminosities being underestimated. On this occasion, no attempts were made to adjust the coefficients in Equations 5.9 - 5.13, noting that the most massive stars could lead to SFR discrepancies. Nevertheless, they should still be more reliable than those calibrated for galaxies.

### 5.6.1 Lyman continuum from census

30 Dor offers the rare opportunity to measure the integrated Lyman continuum (LyC) ionising photon rate directly from its stars. As only massive ( $> 10 M_{\odot}$ ) and young ( $< 20$  Myr) stars significantly contribute to this quantity, it provides a nearly instantaneous measure of the SFR (Kennicutt 1998). This integrated value has already been estimated as  $Q_0^{\text{Sp+Ph}}$ . The resulting SFR for 30 Dor is then:

$$\text{SFR} (M_{\odot} \text{ yr}^{-1}) = 5.8 \times 10^{-54} Q_0 (\text{ph s}^{-1}). \quad (5.9)$$

When accounting for photometrically classified stars, the census gives a SFR of 0.105 or 0.073  $M_{\odot} \text{ yr}^{-1}$  for a Salpeter or Kroupa IMF, respectively (see Table 5.12). Having accounted for stars individually, this is one of the most direct methods of quantifying their ionising output. The following sections discuss the alternative methods available and compare their results in Table 5.12.

### 5.6.2 Far-UV continuum

Probing the young massive stars can also be achieved in the far-UV (FUV), since they will dominate the integrated UV spectrum of a star forming region. However, it is particularly sensitive to extinction (as the cross-section of dust peaks in the UV). The FUV continuum flux of 30 Dor was obtained from images taken by Parker et al. (1998) from the Ultraviolet Imaging Telescope (UIT) using its B5 (1615 Å) filter (Figure 5.15). An aperture consistent to the census region was used and corrected for a uniform extinction using the Fitzpatrick (1986) law, adopting the average census values of  $R_V \approx 3.5$  and  $E(B - V) \approx 0.4$ . The SFR calibration for 30 Dor from the FUV is:

$$\text{SFR} (M_{\odot} \text{ yr}^{-1}) = 1.2 \times 10^{-40} L_{1615} (\text{erg s}^{-1} \text{ \AA}^{-1}), \quad (5.10)$$

where  $L_{1615}$  is the continuum luminosity at 1615 Å. This gave a SFR in very good agreement with the census. As a direct tracer of the hot luminous stars, the consistency of the FUV continuum luminosity would be expected. The sensitivity of this diagnostic to extinction shows that the adoption of a uniform Fitzpatrick (1986) law is reasonable for 30 Dor.

### 5.6.3 Lyman continuum from H $\alpha$

For most giant H II regions, the ionising stars are not individually observable and H recombination lines, primarily H $\alpha$ , serve as the main indicator for a young massive population. Kennicutt et al. (1995) measured the H $\alpha$  flux from 30 Dor through a series of increasing circular apertures, centred on R136, from which a 10 arcmin radius was selected, consistent with the census region. The  $4000 \text{ \AA} + H\beta$  and dereddened H $\alpha$  fluxes were retrieved from the 30 Dor nebular study by Pellegrini et al. (2010). These were summed to give a flux ratio of  $F(\text{H}\alpha)/F(\text{H}\beta) = 4.37$ . Recalling Equation 2.5, values for  $f(\text{H}\alpha)$  and  $f(\text{H}\beta)$  according to  $R_V = 3.5$  were determined for a Cardelli et al. (1989) extinction law. The extinction in H $\alpha$  could be determined since  $A_{\lambda} = 2.5 \log(I_{\lambda}/F_{\lambda})$  thus  $A_{\lambda} = -2.5 f_{\lambda} c(\text{H}\beta)$ . It was derived as  $A_{\text{H}\alpha} = 1.20 \text{ mag}$ . The SFR for 30 Dor based on H $\alpha$  was then:

$$\text{SFR} (M_{\odot} \text{ yr}^{-1}) = 4.2 \times 10^{-42} L_{\text{H}\alpha} (\text{erg s}^{-1}), \quad (5.11)$$

where  $L_{\text{H}\alpha}$  is the H $\alpha$  luminosity. The SFR from this method is  $\sim 30\%$  lower than estimates from the census. As with the FUV, this method can be sensitive to extinction as well as the IMF. Furthermore, absorption of ionising photons by dust and their potential leakage make this SFR a lower limit.

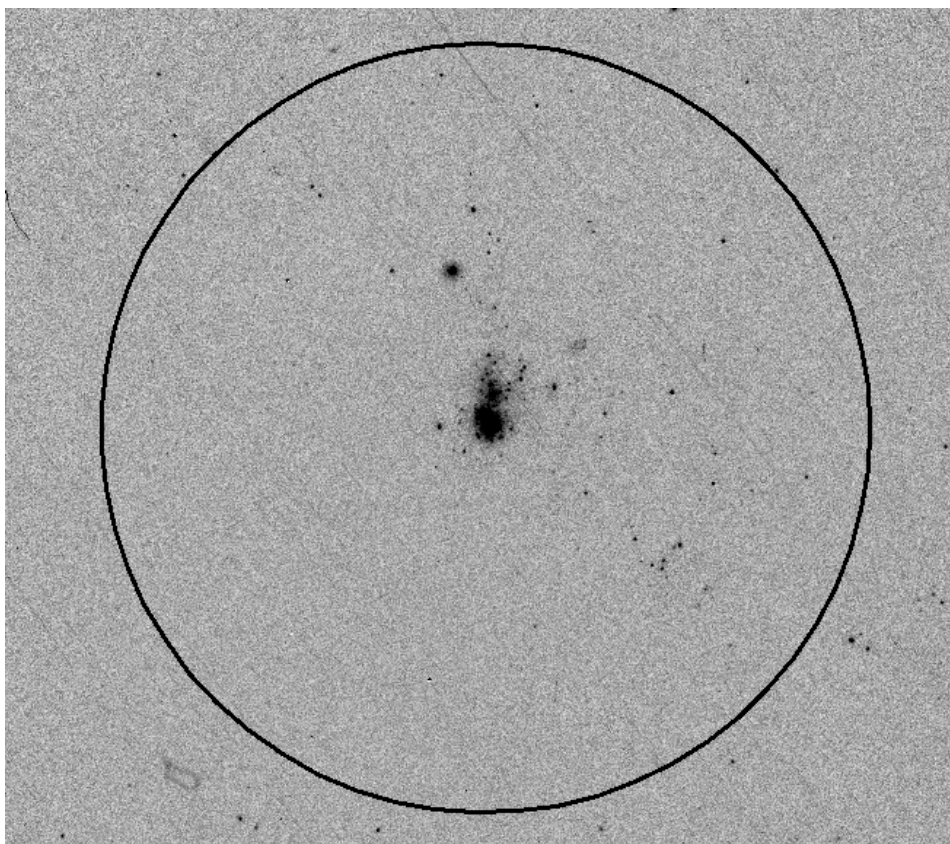


Figure 5.15: FUV image ( $25' \times 22'$ ) of 30 Dor obtained with UIT using the B5 filter. The black circle marks the  $r_d = 10$  arcmin region of the census. North is up and east is to the left.

### 5.6.4 Far-infrared continuum

Stellar UV photons may be absorbed by dust and re-emitted at FIR wavelengths. Measuring the FIR luminosity accounts for this absorption and in cases of high dust opacity, it provides a SFR tracer too. Skibba et al. (2012) recently produced dust luminosity ( $L_{\text{dust}}$ ) surface density maps of the Magellanic Clouds (Figure 5.16)<sup>3</sup>. These integrated observations from the *Spitzer* SAGE (Meixner et al. 2006) and *Herschel Space Observatory* HERITAGE (Meixner et al. 2013) surveys.  $L_{\text{dust}}$  covered 5.8-500  $\mu\text{m}$ , and while limits are not completely consistent with the FIR provided by *Starburst99* (8-1000  $\mu\text{m}$ ), the FIR peak ( $\sim 100 \mu\text{m}$ ) is well covered and the overall difference should be small. The equivalent SFR calibration for 30 Dor in the FIR is:

$$\text{SFR} (\text{M}_{\odot} \text{yr}^{-1}) = 4.2 \times 10^{-44} L_{\text{FIR}} (\text{erg s}^{-1}), \quad (5.12)$$

where  $L_{\text{FIR}}$  refers to the far infrared luminosity. The coefficient is based on the total bolometric luminosity of the stars as predicted by *Starburst99*, assuming that all of the stellar luminosity is absorbed and re-radiated by the dust. The FIR continuum implies a SFR significantly lower (factor of  $\sim 10$ ) than the census. This would indicate that only a small proportion of the ionising photons contribute to heating the dust with the remainder either ionising gas or escaping the region. It should also be noted that older stellar populations ( $> 10 \text{ Myr}$ ) are still capable of heating the dust and contributing to the FIR emission, even if they no longer produce ionising photons. Such stars are not related to the recent star formation.

### 5.6.5 Combined $\text{H}\alpha$ and mid-IR

By combining a tracer based on dust emission with one tracing ionised gas, it should be possible to account for all the ionising photons, except for those escaping the region. Calzetti et al. (2007) and Kennicutt et al. (2009) provide such a SFR diagnostic by combining the observed  $\text{H}\alpha$  and 24  $\mu\text{m}$  luminosities. The observed  $\text{H}\alpha$  luminosity was calculated from Kennicutt et al. (1995) as before, only not corrected for extinction. *Spitzer* 24  $\mu\text{m}$  observations were unfortunately saturated at the core of 30 Dor. The similar 22  $\mu\text{m}$  filter aboard the Wide-field Infrared Survey Explorer (WISE) was therefore used as a substitute. A luminosity was measured from the archival image coadd\_id=0837m697\_ab41. While the SFR calibration of Calzetti et al. (2007) is suited for  $\text{H II}$  regions (their Equation 7), for consistency, their first coefficient is replaced with the one derived in Equation 5.11. In addition, to account for the narrower bandwidth and shorter wavelength of the WISE filter, their second coefficient was

<sup>3</sup>The  $L_{\text{dust}}$  values from Skibba et al. (2012) incorporated 24  $\mu\text{m}$  MIPS images that were saturated at the very core of 30 Dor. These few pixels did not list values. To correct for this, values of neighbouring pixels were substituted in to obtain the final integrated  $L_{\text{FIR}}$  given in Table 5.12.

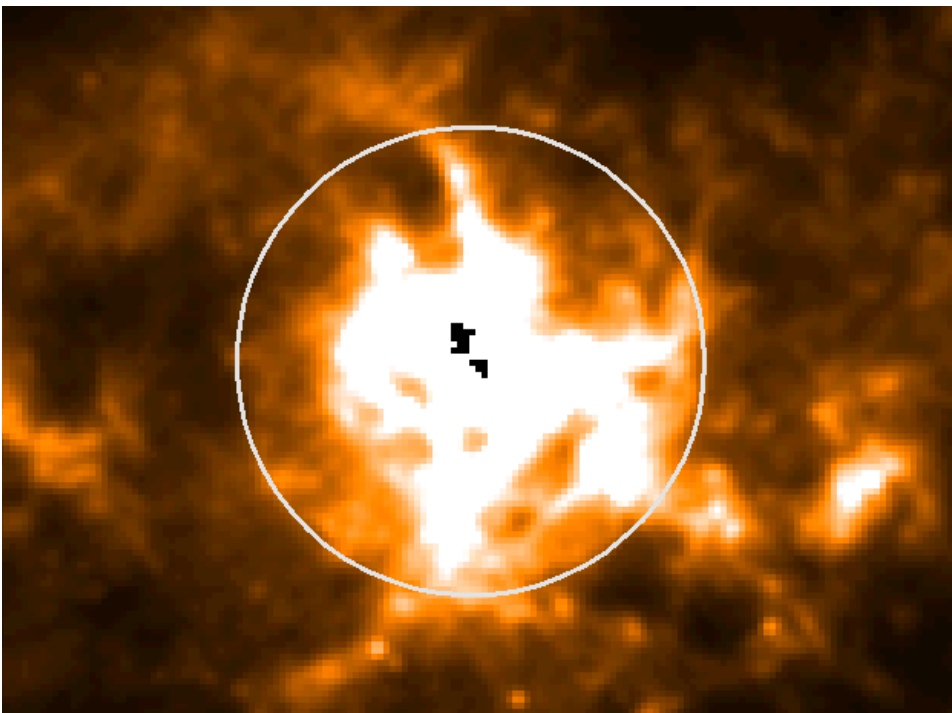


Figure 5.16: Luminosity surface density map ( $40' \times 30'$ ) of the 30 Dor region taken from Skibba et al. (2012). The maps combined fluxes from the SAGE and HERITAGE surveys and covering wavelengths  $5.8 - 500 \mu\text{m}$ . The white circle marks the  $r_d = 10$  arcmin region of the census. North is up and east is to the left.

adjusted to give:

$$\begin{aligned} \text{SFR (M}_{\odot} \text{ yr}^{-1}) = & 4.2 \times 10^{-42} [L_{\text{H}\alpha(\text{obs})} (\text{erg s}^{-1}) \\ & + 0.039 \times \nu L_{22} (\text{erg s}^{-1})], \end{aligned} \quad (5.13)$$

where  $L_{22}$  is the observed luminosity density at  $22 \mu\text{m}$  and  $\nu$  is the central frequency of the  $22 \mu\text{m}$  filter. This method also estimated a SFR lower than the empirical census, by a factor of  $\sim 2$ . However, it is noted that by substituting the extinction corrected H $\alpha$  luminosity ( $L_{\text{H}\alpha(\text{corr})}$ ) into Equation 5.13, results are much more consistent. Since most star forming regions often lack UV imaging, this approach would therefore be the recommended tracer for the SFR.

Table 5.12: Comparison of SFR tracers for 30 Dor.

SFR Tracer	SFR [ $M_{\odot} \text{ yr}^{-1}$ ]			
	Salpeter IMF	Kroupa IMF		
Lyman Continuum (Stars)	$Q_0^{\text{Sp}}$ [ $\text{ph s}^{-1}$ ]	$10.56 \times 10^{51}$	$0.088 \pm 0.053$	$0.061 \pm 0.037^c$
	$Q_0^{\text{Sp+Ph}}$ [ $\text{ph s}^{-1}$ ]	$12.37 \times 10^{51}$	$0.103 \pm 0.062$	$0.073 \pm 0.044^c$
	$F_{1615}$ [ $\text{erg cm}^{-2} \text{ s}^{-1} \text{ \AA}$ ]	$4.88 \times 10^{-11}$		
FUV Continuum (1615Å)	$I_{1615}^a$ [ $\text{erg cm}^{-2} \text{ s}^{-1} \text{ \AA}$ ]	$2.01 \times 10^{-9}$		
	$L_{1615}$ [ $\text{erg s}^{-1} \text{ \AA}$ ]	$6.02 \times 10^{38}$	$0.102 \pm 0.033$	$0.071 \pm 0.023^d$
	$F_{\text{H}\alpha}$ [ $\text{erg cm}^{-2} \text{ s}^{-1}$ ]	$1.37 \times 10^{-8}$		
Lyman Continuum ( $\text{H}\alpha$ )	$I_{\text{H}\alpha(\text{corr})}^b$ [ $\text{erg cm}^{-2} \text{ s}^{-1}$ ]	$4.12 \times 10^{-8}$		
	$L_{\text{H}\alpha(\text{corr})}$ [ $\text{erg s}^{-1}$ ]	$1.23 \times 10^{40}$	$0.075 \pm 0.018$	$0.052 \pm 0.012^e$
	$F_{22}$ [ $\text{Jy}$ ]	2800		
	$\nu L_{22}$ [ $\text{erg s}^{-1}$ ]	$1.13 \times 10^{41}$		
	$L_{\text{H}\alpha(\text{obs})}$ [ $\text{erg s}^{-1}$ ]	$4.09 \times 10^{39}$	$0.050 \pm 0.003$	$0.035 \pm 0.002^f$
Combined $\text{H}\alpha$ and MIR ( $22\mu\text{m}$ )	$L_{\text{H}\alpha(\text{corr})}$ [ $\text{erg s}^{-1}$ ]	$1.23 \times 10^{40}$	$0.100 \pm 0.018$	$0.070 \pm 0.012^f$
	$L_{\text{FIR}}$ [ $\text{erg s}^{-1}$ ]	$1.58 \times 10^{41}$	$0.010 \pm 0.001$	$0.007 \pm 0.001^g$

**Notes.** Salpeter IMF SFRs are obtained by scaling Kroupa IMF SFRs by a factor of 1.44.

<sup>a</sup>  $A_{1600} = 4.0$  mag from Fitzpatrick (1986) law.

<sup>b</sup>  $A_{\text{H}\alpha} = 1.20$  mag from integrated  $F(\text{H}\alpha)/F(\text{H}\beta)$  ratio.

<sup>c</sup> From Equation 5.9.

<sup>d</sup> From Equation 5.11.

<sup>e</sup> From Equation 5.10.

<sup>f</sup> From Equation 5.13.

<sup>g</sup> From Equation 5.12.

### 5.6.6 Star formation rate comparison

Table 5.12 compares the discussed standard extragalactic SFR tracers with the direct approach of the census. The FUV clearly showed the best agreement. All other tracers fell below the census, deviating by up to a factor of two, with the exception of the FIR continuum which underestimated by a factor of 10. Drawing conclusions from this single result could be premature given the uncertainties on the census calibrations. However, Chomiuk & Povich (2011) suggest similar discrepancies when comparing the SFR tracers available for well resolved regions and unresolved extragalactic regions. They too, recognise the importance of the most massive stars to the ionising output but also stress how the uncertainty of the adopted IMF could lead to inconsistencies. The SFR calibrations in Equations 5.9 - 5.13 were derived for compatibility with 30 Dor, particularly allowing for the region's relatively young SFH in comparison to galaxies, but there are further factors to be considered. For example, Leitherer (2008) offers alternative calibrations accounting for the effects of stellar rotation which produce even lower SFRs.

So when attempting to determine the SFR of a young unresolved star forming region, similar to 30 Dor, what might be the favoured SFR tracer? Returning to Table 5.12, the very good agreement from the FUV continuum tracer might be preferred but this approach still relies heavily on an accurate extinction law and observations in the FUV are not always readily available. Both the  $H\alpha$  and FIR continuum tracers fail to account for ionising photons absorbed by dust or ionising gas, respectively. The combined  $H\alpha$  and MIR tracer therefore might be expected to be the most accurate although it still underestimates by a factor of 2. However, if instead, the extinction corrected  $H\alpha$  luminosity ( $L_{H\alpha(\text{corr})}$ ) is used in Equation 5.13, a much better agreement with the census is achieved. In regions of relatively low amounts of dust, as suggested by  $L_{\text{FIR}}$ , the accuracy of this approach therefore depends more on the reliability of  $L(H\alpha)$  and  $A_{H\alpha}$  although it should be noted that any escaping photons would still not be accounted for.

## 5.7 Photon Escape Fraction

The leakage of ionising photons from 30 Dor might be expected given the open structure and filaments of the region. The  $f_{\text{esc}}$  for 30 Dor can only be considered by dealing in numbers of photons. The number of ionising photons emitted by its stars has already been determined,  $Q_0^{\text{Sp+Ph}}$ . The number of photons which ionise the gas ( $Q_0^{H\alpha}$ ) can be calculated from Equations 5.9 and 5.11, and is shown to be directly proportional to  $L(H\alpha)$ .

The number of photons absorbed by dust ( $Q_0^{\text{Dust}}$ ) is more complicated since both EUV

and non-EUV photons contribute to heating the dust. The  $L_{\text{EUV}}/L_{\text{Bol}}$  fraction was already calibrated for each SpT (see Tables 5.4 - 5.7). An average  $L_{\text{EUV}}/L_{\text{Bol}} \approx 0.45$  was obtained for the whole 30 Dor stellar population, representing a typical O5 V star. By applying this same fraction to the dust would give  $L_{\text{EUV}}^{\text{Dust}} \sim 0.45 \times L_{\text{FIR}}$ , where  $L_{\text{EUV}}^{\text{Dust}}$  is the dust luminosity heated by EUV photons. Of course, it has already been determined that a fraction of the EUV photons leaving the stars must ionise the gas, while variations in the dust opacity could result in further photons escaping the region. An additional test was therefore made with the dust grain models of Weingartner & Draine (2001) to calculate the fraction of ionising photons from a typical O5 V star that are absorbed by dust. These estimates suggested that  $L_{\text{EUV}}^{\text{Dust}} \approx 0.55 \times L_{\text{EUV}}$  for a variety of  $R_V$  values (M. Min, priv. comm.). Therefore, in terms of the number of ionising EUV photons:

$$Q_0^{\text{Dust}} \sim 0.55 \times L_{\text{FIR}}/L_{\text{EUV}} \times Q_0^{\text{Sp+Ph}}. \quad (5.14)$$

Table 5.13 gives a breakdown of the ionising photons. The ratio of  $(Q_0^{\text{H}\alpha} + Q_0^{\text{Dust}})/Q_0^{\text{Sp+Ph}} \sim 0.94$ , therefore  $f_{\text{esc}} \sim 0.06$ . This would suggest 30 Dor to be ‘density bounded’ with just under 6% of its ionising photons escaping the region. Unfortunately, given the uncertainties on the derived values,  $f_{\text{esc}}$  potentially ranges from 0 – 0.61. This could equally see 30 Dor as a ‘radiation bounded’ region. However, it is noted that  $Q_0^{\text{Sp+Ph}}$  is still likely an underestimate due to unaccounted contributors (see Section 4.6.3).  $Q_0^{\text{Dust}}$  is also likely to be an upper limit. This arises from the omission of luminous cool supergiants from the census due to their minimal ionising contribution. However, these older stellar populations would still have contributed to  $L_{\text{Bol}}$ , hence lowering the integrated  $L_{\text{EUV}}/L_{\text{Bol}}$  fraction.

Smith & Brooks (2007) followed the same approach as this work on the Carina Nebula and found a quarter and one third of the ionising photons to be unaccounted for when comparing to radio and H $\alpha$  fluxes, respectively. Similar work by Voges et al. (2008) showed 20-30% of their less luminous LMC H II regions to be in a similar density bounded state. A slightly different approach was made by Pellegrini et al. (2011) who implemented nebular line ratios to detect ionisation fronts around H II regions in the Magellanic Clouds. They too, concluded the regions to be density bounded with an average  $f_{\text{esc}} > 0.4$ . This escape fraction is a possible reason for the discrepancies measured between H $\alpha$  and FUV continuum tracers in nearby galaxies (Lee et al. 2009; Relaño et al. 2012) and could help to explain the offsets seen in Equations 5.9 - 5.13.

Table 5.13: Comparison of  $Q_0$  tracers for 30 Dor.

$Q_0$ Tracer			$Q_0$ [ $10^{51}$ ph s $^{-1}$ ]
LyC (Stars <sup>Sp</sup> )	$L_{\text{EUV}}$ [erg s $^{-1}$ ]	$3.49 \times 10^{41}$	$10.6 \pm 6.3^a$
LyC (Stars <sup>Sp+Ph</sup> )	$L_{\text{EUV}}$ [erg s $^{-1}$ ]	$4.01 \times 10^{41}$	$12.4 \pm 7.4^a$
LyC (H $\alpha$ )	$L_{\text{H}\alpha}$ [erg s $^{-1}$ ]	$1.23 \times 10^{40}$	$9.0 \pm 1.8^b$
FIR Continuum	$L_{\text{FIR}}$ [erg s $^{-1}$ ]	$1.58 \times 10^{41}$	$2.6 \pm 2.0^c$

**Notes.**<sup>a</sup> From census.<sup>b</sup> From equating Equations 5.9 & 5.11.<sup>c</sup> From Equation 5.14.

## 5.8 Summary

Following the census of hot luminous stars in 30 Dor discussed in Chapter 4, a range of calibrations have been derived to obtain the stellar parameters of the 500 spectroscopically classified and 222 photometrically classified stars in the region. These calibrations were based on a series of previous O and B-type star atmospheric models. Newer modelling was carried out and adopted for the more recently introduced O2-3.5 spectral classes to improve the reliability of calibrations at higher temperatures. The 31 W-R and Of/WN stars were handled differently by assigning model derived parameters to each SpT and using this as a template for equivalent stars.

These individual properties allowed estimates of the stellar mass to be made. Both 30 Dor and its central R136 cluster were found to possess a typical Salpeter IMF slope of  $\alpha \approx -2.3$ . Despite incomplete photometry and spectroscopy impeding the number of stars  $\lesssim 20 M_{\odot}$  in the census, by integrating over a Kroupa IMF the first total stellar mass estimate of 30 Dor was made at  $M_{30\text{Dor}} \sim 1.1 \times 10^5 M_{\odot}$ . Similarly,  $M_{\text{R136}} \sim 5.0 \times 10^4 M_{\odot}$  was obtained for the stellar mass of R136, agreeing within 10% of the mass found by Hunter et al. (1995) who had sampled the lower mass (2.8 – 15  $M_{\odot}$ ) stars.

Age estimates were also consistent with previous works. Comparisons to the latest isochrones showed R136 to be 1 – 2 Myr old as found by Massey & Hunter (1998). The rest of the 30 Dor population extended beyond 8 Myr but was concentrated between 2 – 5 Myr with the  $W_{\lambda}(\text{H}\alpha)$  of the nebular lines indicating a similar 3.5 Myr age for the region.

By adopting the latest distant modulus to 30 Dor with a uniform extinction law, a total bolometric luminosity of  $\log L_{\text{Bol}} \approx 10^{8.36} L_{\odot}$  was derived. The mechanical and radiative feedback was also determined for each star. The total ionising photon rate and stellar wind luminosity of the hot luminous stars in 30 Dor was estimated at  $Q_0^{\text{Sp+Ph}} \approx 12.4 \times 10^{51}$  ph s $^{-1}$  and

$L_{\text{SW}}^{\text{Sp+Ph}} \approx 2.24 \times 10^{39} \text{ erg s}^{-1}$ , respectively. While these values include stars classified from photometry, they are still likely to be lower limits given the other sources that were unaccounted for in the census. The W-R and Of/WN stars were found to be crucial to this feedback with just 31 of them providing a comparable ionising photon output, and even greater wind luminosity, than the 469 OB stars in the region. This behaviour was replicated within R136, which alone was seen to contribute over 50% of the overall ionising photons and wind luminosity of 30 Dor.

Stars with the highest initial masses, exceeding  $100 M_{\odot}$ , were also predominantly W-R stars and hence showed large contributions to the feedback. The inclusion of such massive stars is therefore crucial when attempting to determine a reliable energy budget for luminous star forming regions. This was demonstrated with comparisons to the population synthesis code *Starburst99*. The current code's inability to model stars  $M_{\text{init}} > 100 M_{\odot}$  led to the ionising photon rates and wind luminosities being underestimated by factors of  $\sim 2$  and  $\sim 9$ , respectively.

The integrated ionising photon rate offered a direct estimate of the SFR of 30 Dor at  $0.073 \pm 0.04 M_{\odot} \text{ yr}^{-1}$ , when adopting a Kroupa IMF. Further analysis of the nebular properties allowed the SFR to be estimated via conventional methods. These additional techniques largely underestimated the findings of the census. However, SFR tracers involving the FUV continuum showed good agreement as did a modified  $\text{H}\alpha$  + MIR tracer, providing the  $\text{H}\alpha$  luminosity was corrected for extinction. The discrepancies in some of these SFR tracers could be partly explained by the photon escape fraction. After accounting for gas ionisation and dust heating, estimates suggest  $\sim 6\%$  of the ionising photons in 30 Dor are free to escape the region.

To accompany the census of hot luminous stars in 30 Dor, stellar parameters are now available for all the spectroscopically classified stars as listed in Table 5.9. Despite best efforts to accurately represent the earliest stars and W-R stars in the census, uncertainties on values such as temperature still remain high and propagate on to other properties as well as the integrated estimates for the region. The calibrations used here offer a first order investigation into the stellar population of 30 Dor but are still no substitute for the individual spectral modelling of each star that will follow in the future.

# Chapter 6

## Summary and Future Work

### 6.1 A summary of this study

Chapter 2 presented new intermediate resolution spectroscopy obtained of O-type stars embedded within H II regions in the outer Galaxy. The stars were classified and from their SpTs, a range of stellar properties were estimated using contemporary calibrations, including their temperatures, luminosities and ionising photon rates. Meanwhile, spectroscopy of the surrounding nebulae was acquired, supplying details on their gas temperatures, densities and chemical abundances.

The study drew relations between the two components, particularly when attempting to understand the ionising photon budget of each region. The H $\alpha$  luminosity of the gas was used to trace the ionising photons absorbed by the gas. Similarly, supplementary IR data gave indications of the presence of dust and its role in absorbing photons. In nearly all cases, the number of ionising photons absorbed by the gas was found to be less than those emitted from the star. It was also evident that this fraction varies with time as the H II region evolves. This was due to natal dust absorbing a fraction of the photons in young regions, whilst in older diffuse regions where the dust had been destroyed, the photons were able to escape.

The remaining chapters were focussed on 30 Dor in the LMC where similar methods applied to the Galactic H II regions were transferred to the scale of this GH II region. In this case, hundreds of stars ionised the nebula but recent multi-epoch spectroscopy observations from the VFTS allowed them to be studied.

The 30 Dor stellar population covered a range of SpTs including 31 known emission line stars. Earlier studies found them to make notable contributions to the feedback in star forming regions so they were considered separately in Chapter 3. The VFTS spectra provided revised spectral classifications of the stars and revealed a previously unknown WN 5h star - VFTS 682.

The new multi-epoch data allowed spectral variations to be inspected to help determine the binary nature of the sample and test previously determined orbital parameters. An investigation was made into the reliability of different spectral lines when seeking to measure a star's radial velocity. The radial velocities produced by atmospheric models were found to be consistent with those measured directly from the stellar spectra for O2 dwarfs, giants and supergiants. Both methods proved less consistent for Of/WN and WN stars with stronger winds. However, the N v  $\lambda 4944$  line did remain reliable for a WN star. Stellar properties were estimated for all the emission line stars in 30 Dor by using a combination of new and adopted atmospheric models as templates for the sample. All the WN stars were classified as H-rich and found to have the highest luminosities and ionising outputs of stars in the 30 Dor population.

With a better understanding for the emission line stars, Chapter 4 compiled a census of the hot luminous stars within a central 10 arcmin radius of 30 Dor. It aimed to include all the stars that provided a radiative or mechanical feedback to the region through their ionising photons or strong stellar winds. Candidate hot luminous stars were selected from different photometric surveys via a number of criteria. Subsequent matching to available spectroscopic data showed 500 of these candidates to have classifications. Further classifications estimated from the photometry of the stars improved this count to 722. Thanks largely to the observations of the VFTS, it was estimated that the spectroscopic completeness of hot luminous stars in 30 Dor had reached  $\sim 85\%$ . Completeness was lower ( $\sim 35\%$ ) in the central R136 cluster due to crowding. The inner regions nevertheless showed the highest density of hot luminous stars, containing a majority of the emission line stars, and would prove to be the focal point of stellar feedback in the 30 Dor.

Chapter 5 quantified this by estimating the properties of all the stars in the census. These were determined via a series of stellar calibrations that had been adjusted to account for extreme parameters found in the earliest O subtypes. To assist this, new atmospheric modelling was carried out on a sample of LMC O2 stars and their properties were incorporated into the stellar calibrations. Further estimates were made of their stellar masses and evolutionary paths. This suggested that typical O2 stars evolve through the standard dwarf, giant and supergiant phases, while the process is much more rapid in the most massive cases and they are likely precursors to the WNh stars observed across 30 Dor.

Integrated stellar properties were obtained for 30 Dor, with focus on the ionising photon rate and wind luminosity of the stars. Results showed that the very massive stars,  $M_* > 100 M_{\odot}$ , made the largest contributions, with the ten most massive stars in 30 Dor found to contribute 28% of the feedback in both cases. For R136, comparisons were made with the population synthesis code *Starburst99*. It was found to underpredict the ionising photon rate and wind luminosity of the census by factors of  $\sim 2$  and  $\sim 9$ , respectively. These offsets were

predominantly deemed to be the result of the very massive stars not being accounted for in the synthetic code.

The census estimated the SFR rate for 30 Dor to be  $0.073 \pm 0.04 M_{\odot} \text{ yr}^{-1}$ . This was also compared to values returned by a variety of SFR tracers. Global observations of the region across a number of wavelengths were used to detect the ionised gas, the heated dust or directly sample the stars. The UV tracer showed good agreement with the census but other wavelengths returned underestimates. These discrepancies are believed to arise, in part, due to ionising photons escaping the region. It was estimated that  $\sim 6\%$  of the stellar ionising photons escape 30 Dor and hence will not have been accounted for by SFR calibrations that trace these photons.

The census was also compared to contemporary isochrones to show a wide spread of ages across 30 Dor, extending beyond 8 Myr. However, the R136 cluster was notably younger with a majority of stars falling between 1 – 2 Myr and agreeing with past studies. Finally, the integrated stellar mass of both 30 Dor and R136 was determined at  $M_{30\text{Dor}} \sim 1.1 \times 10^5 M_{\odot}$  and  $M_{\text{R136}} \sim 5.0 \times 10^4 M_{\odot}$ , respectively, with both showing a mass function consistent with a standard Salpeter function. Again, results for the R136 mass were consistent with earlier findings.

## 6.2 Expanding on this Study

### 6.2.1 Selection of stellar sources

To obtain a full understanding of the processes in a H II region, it is essential to account for all of its associated ionising stars. All of the H II regions studied in Chapter 2 were believed to be dominated by a single massive star but contributions from neighbouring stars could not be ruled out. Additional stars were observed and while those with SpTs suggested a limited ionising effect compared to the primary star, their impact on heating dust could be much larger. Perhaps more significant were stars close to the nebular borders and beyond the field of view that could add to the ionising luminosity but would not have been accounted for. The asymmetrical shapes of some of the targets suggest more than one ionising source could be at work (e.g Sh2 206), but also that multiple stellar winds are shaping the region from different directions.

To improve confidence in the derived stellar contribution, investigation begins on the primary stars. Reliable SpTs may have been obtained, but their binary nature is still open to debate without further observation. Young regions with copious amounts of dust will hinder the detection of companions and any other neighbouring stars. Studies from Lahulla (1985); Russeil et al. (2007) have helped to classify a number of stars in Galactic regions but many

remain unknown. Given the variation of extinction across a region, spectroscopic rather than photometric properties are needed to ensure that their impact on the nebula is indeed negligible.

These principles equally apply on larger scales. The VFTS has successfully managed to identify a large proportion of the massive star binaries in 30 Dor (Sana et al. 2013a). Chapter 5 only addressed the feedback from the SB2 systems, estimating the light contributions from the two components based on their SpTs. This approach could be improved by turning to the spectra of the stars and measuring their line strengths to determine their individual brightness. Better still, the separate components in the SB1 systems (for which there are even more) could also be estimated with future modelling of their SEDs.

30 Dor shows areas of high extinction, with the discovery of VFTS 682 (Section 3.5.3) being a prime example that other important high mass stars may still be hidden and undergoing formation (Walborn et al. 2013). Knowledge of the 30 Dor extinction law continues to improve (Tatton et al. 2013, MaizApellaniz:2014) so that the uniform law applied in Chapter 4 can be replaced with values on a regional basis or even individually for each star. Following the same selection criteria applied in this work, candidate stars would see fewer contaminants. A complete census of hot luminous stars could then be achieved with the support of an IR survey to uncover any young embedded stars.

### 6.2.2 New stellar properties

In this study, derivation of stellar properties has relied on various calibrations or templates, with atmospheric models supplying parameters for only a few of the W-R stars. New individual models from Hainich et al. (2014) and Bestenlehner et al. (submitted) discussed in Section 3.7.5 will supersede this approach. In addition, the spatial extent of the VFTS means the same individual modelling can be expected of the OB stars, and a substantial fraction have recently been analysed (e.g. Ramírez-Agudelo et al. 2013; Sabín-Sanjuliáin et al. submitted; McEvoy et al. in prep.). Again, properties will become more reliably constrained and take into account finer spectral details. For example, two stars of the same SpT could have a different age, rotational velocity or surface abundance but would have been assigned the same properties by the calibrations in this work. These differences and their impacts on the stellar properties will be revealed by the VFTS studies. Nevertheless, in some cases, obtaining reliable individual stellar spectra is not always possible, and such stellar calibrations are the only option of reproducing the star. It is therefore important to understand what discrepancies lie between the two methods, and how these might affect the modelling of similar massive regions.

### 6.2.3 Nebula comparisons

As with the Galactic H II regions, the spatial extent of the study is important. H $\alpha$  images of the whole LMC show that the nebulae associated with 30 Dor extend far beyond the 10 arcmin radius of the census. Kennicutt et al. (1995) observed the H $\alpha$  flux through circular apertures of a range of sizes, showing it to rise as neighbouring H II regions were included to form a 30 Dor “superassociation”. They found a clear peak in emission coinciding with the centre of 30 Dor. The census in turn showed this to be the focus of stellar ionising photons with a high density of hot young stars and a number of massive WNH stars. However, Kennicutt et al. (1995) did note further smaller peaks in the emission at radii beyond the census, as neighbouring regions became enclosed.

Section 5.6 only compared the census to observations (e.g. H $\alpha$ , FIR, UV) that had been measured from apertures of an equal radius. But this radius could be varied, potentially in both directions. At smaller radii, the census already provides information of the stellar content but greater resolution would be required to distinguish the nebular structure. Moving to larger radii, and although more SpTs are needed for completeness, could parameters such as the photon escape fraction be expected to change as the region becomes more segregated? As radio waves are unobscured by dust, they can provide another tracer for the ionising output of the stars. While not extending to the radius of the census, Israel & Koornneef (1979) had observed the central  $3 \times 3$  arcmin of 30 Dor in the radio to offer a further comparison not carried out in this work.

## 6.3 Application to Other Star Forming Regions

R136 was initially chosen as a test bed for more distant star forming regions due to its close proximity and high abundance of spatially resolved massive stars. Another region to meet these criteria is NGC 3603 shown in Figure 6.1. Lying at a distance of  $\sim 7.6$  kpc (Melena et al. 2008), it is thought to be at a similar pre-SNe age of  $< 2$  Myr (Crowther & Dessart 1998). At  $\sim 1 \times 10^4 M_{\odot}$  (Harayama et al. 2008) it is less massive than R136, but still contains over 30 O-type stars along with three WNH stars (Melena et al. 2008; Drissen et al. 1995). Do the most massive stars here play a similar importance to the stellar feedback as was found in R136 (and 30 Dor)?

An analogous study was therefore carried out on NGC 3603. On this occasion, selection of the hot luminous stars was more simplified using solely the  $K$ -band magnitude and a threshold of  $M_K < -4$  mag. As a Galactic star forming region, NGC 3603 suffers from higher levels of extinction compared to R136 and its distance is not well constrained. An average extinction

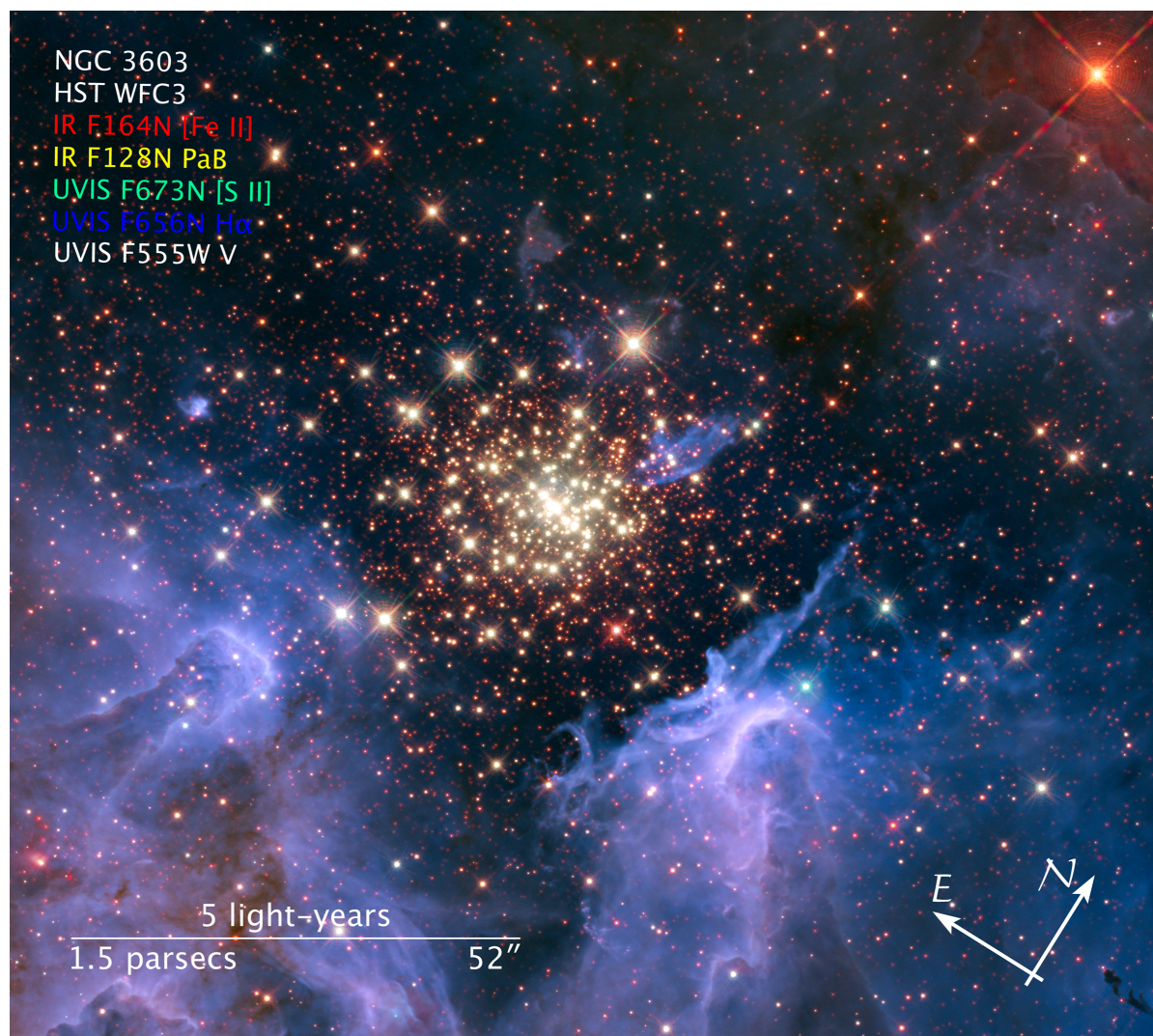


Figure 6.1: The star forming nebula NGC 3603. Composite image obtained with HST-WFC3/UVIS and WFC3/IR F128N ( $\text{Pa}\beta$ ), F164N ( $[\text{Fe II}]$ ), F555W ( $V$ ), F657N ( $\text{H}\alpha$ ), and F673N ( $[\text{S II}]$ ) filters. Courtesy of NASA, ESA. R. O'Connell, F. Paresce, E. Young, the WFC3 Science Oversight Committee and the Hubble Heritage Team.

value was obtained from the available  $H-$  and  $K-$  band photometry in the same way as was described in Section 4.3 and this was then adopted for the whole cluster. Observations by Drissen et al. (1995) and Melena et al. (2008) allowed this census to extend to a radius of  $\sim 2$  pc and gave a spectroscopic completeness of  $\sim 70\%$ .

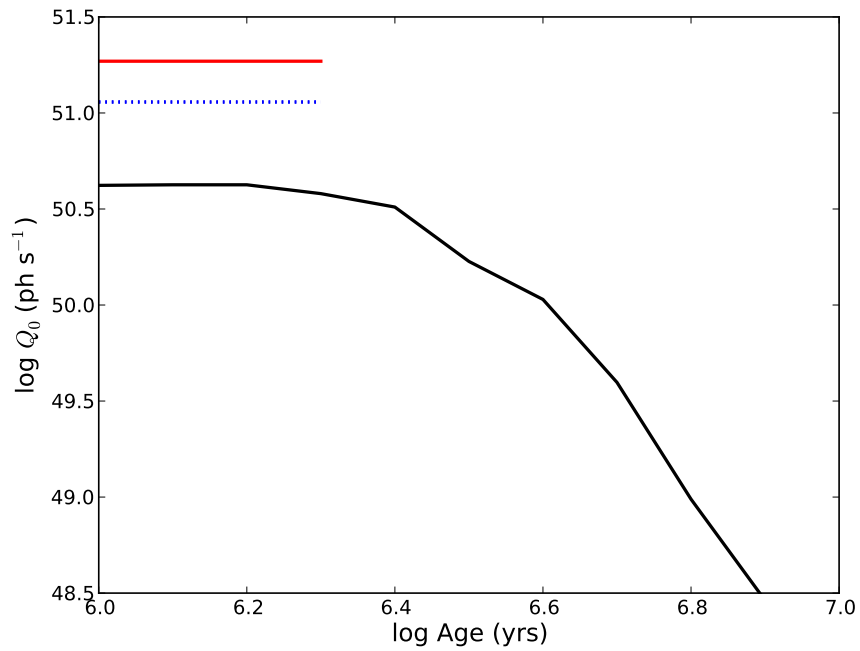
Stellar properties of the OB stars were estimated as before using various calibrations (e.g. Martins et al. 2005; Vink et al. 2001; Prinja et al. 1990). As these were typically based on Galactic stars, fewer adjustments were needed for metallicity as was the case for R136. Accurate models of all three of WNh stars had already been generated by Crowther et al. (2010) so that the integrated stellar properties of NGC 3603 were arguably more accurate than R136. The three WNh stars alone were found to contribute 40% of the ionising luminosity and 55% of the wind luminosity. This echoes the results of the R136 cluster, with the most massive stars making the largest contributions to the feedback.

This work could be continued, as it was for 30 Dor, by again comparing the stellar output with observed nebular properties. Indeed, Kennicutt (1984) already indirectly derived the  $H\alpha$  luminosity using radio maps of NGC 3603, and Drissen et al. (1995) compared these values to their partial spectroscopic sample. They found that 14 stars produced 80% of the necessary ionising luminosity and that the 21 brightest stars in the centre of the cluster should be capable of providing it all, albeit based on older calibrations. Will NGC 3603 therefore favour a similar density bounded scenario as indicated by 30 Dor?

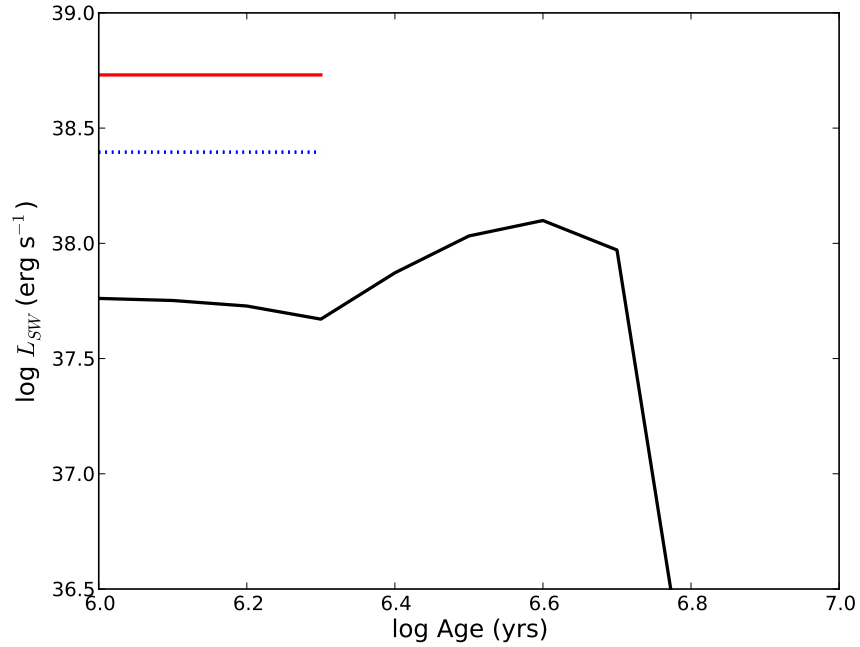
### 6.3.1 Synthetic modelling

Section 5.5 made comparisons to the widely used population synthesis code *Starburst99*. It greatly underpredicted the stellar ionising output and wind luminosities integrated from the census of R136, but showed better consistency once  $M_{\text{init}} > 100 M_{\odot}$  stars had been taken into account, as they were not included in the IMF used by the code. The same comparisons were carried out for NGC 3603, this time excluding the effects of the WNh stars (see Figure 6.2) and similar improvements were seen.

In the case of R136,  $M_{\text{init}} > 100 M_{\odot}$  stars were identified from a mass-luminosity relation indicated by contemporary evolutionary tracks. The masses of WNh stars in NGC 3603 should be more accurately known thanks to the binary nature of one of them, NGC 3603-A1. Schnurr et al. (2008a) was able to determine a mass ratio for the system (NGC 3603-A1a=116  $M_{\odot}$ , NGC 3603-A1b=89  $M_{\odot}$ ) and masses of the other stars (NGC 3603-B=132  $M_{\odot}$ , NGC 3603-C=113  $M_{\odot}$ ) have since been estimated and all their initial masses believed to be above 100  $M_{\odot}$  (Crowther et al. 2010). Forthcoming evolutionary models (Köhler et al. in prep.) which extend to 500  $M_{\odot}$  are now being included into synthetic codes to incorporate the effects of such high



(a)



(b)

Figure 6.2: The integrated ionising luminosity (a) and stellar wind luminosity (b) of NGC 3603. Predictions from *Starburst99* are plotted with a solid line. Values from the NGC 3603 census, with and without the WNh stars, are plotted in dashed and dotted lines, respectively.

mass stars. However, the overall mass of NGC 3603 raises the question as to whether the number of stars with  $M_{\text{init}} > 100 M_{\odot}$  is typical for a cluster of its mass or a stochastic effect. Such IMF fluctuations not only influence the feedback luminosities, but diagnostics such as  $W(\text{H}\beta)$  and the number ratios of stars (Cerviño et al. 2002; Jamet et al. 2004). R136 may still be one of the few reliable high mass clusters above the stochastic mass limit.

However, it is evident from both R136 and NGC 3603 that the standard *Starburst99* code needs further modifications on top of accounting for the most massive stars. Recent versions have explored several avenues including rotation (Vázquez et al. 2007; Levesque et al. 2012). They typically found that rotating models prolonged the ionising output of stars, particularly those in lower mass bins. Rotation led to increased temperatures and luminosities and hence a greater and harder ionising luminosity, especially  $> 3$  Myr in the presence of W-R stars. Rotational mixing would also increase mass-loss rates and so the wind luminosity is potentially higher as well. The situation is more complex when incorporating massive binaries, but Eldridge & Stanway (2009) indicate an increase in ionising luminosity at later ages. Discrepancies in the adopted mass-loss rates were mentioned in Section 5.5, but the Vink et al. (2001) prescription is now widely used in many of the latest codes. Despite these updates, the ability to model the most massive stars still appears crucial for accurate predictions of the feedback.

As this gap between theoretical models and observations closes, it also benefits extragalactic astronomy which relies heavily on population synthesis, but comparisons should not be restricted to the youngest clusters. Once SNe have begun, they will displace even the most massive stars as the most dominant sources of mechanical feedback. Given the age spread found for 30 Dor, SNe will have undoubtedly contributed to its global feedback. Just how the energy budget is balanced between stars and SNe, and how it changes as a region evolves, can be investigated. Indeed, Voss et al. (2012) used the stellar census of the Carina region compiled by Smith & Brooks (2007) and compared this to population synthesis models. When accounting for SNe, their results showed a consistent energy budget to that of the Smith & Brooks (2007) census.

## 6.4 Ongoing and Future Observations

Findings from the Galactic H II regions have helped to identify suitable targets for future study, where photoionisation modelling of the nebulae can be compared to atmospheric models of the star. For example, cases where the photon escape fraction is high would be less favourable as the nebula spectrum would not accurately reflect the ionising output of the star. But if the photons are bound by the system a direct comparison can be made between the two (e.g. Fur-

ness et al. 2010; Morisset et al. 2002). Future observations would aim to span all wavelengths from optical through to IR in order to optimally constrain the hardness of the radiation and the nebular parameters. This would incorporate forbidden lines such as [S III]  $\lambda 9531$  (not used in this work) and [Ne III]  $15.5 \mu\text{m}$ /[Ne II]  $12.8 \mu\text{m}$  and [S IV]  $10.5 \mu\text{m}$ /[S III]  $18.7 \mu\text{m}$ , as analysed by Furness et al. (2010), and they could even be applied to H II regions in the nearby MCs.

30 Dor remains the focus of several future surveys, and the census provides a foundation for many of these studies. Spectroscopy is still the key to determining the properties of the stellar population. The VFTS boosted the overall spectroscopic completeness of hot luminous stars in 30 Dor as high as 85% but this can still be improved. It is certainly necessary in the dense R136 region where completeness dropped to 35% and is already underway (Crowther et al. in prep.). This work uses new HST/STIS observations to obtain spectroscopy for 25 new stars, all classified in the UV as hot O-types, and will be supported by further optical data to aid the atmospheric modelling.

Section 4.6.5 discussed the benefits of the recent *Swift* UVOT imaging of the LMC. Hot luminous stars would appear as bright sources in the UV. It would be easy to identify any such stars that were currently lacking spectroscopy by checking them against stars in the census. This approach would be equally useful when extending the census to larger radii, as the brightest sources would correspond to the hottest stars that could then be targeted for future spectroscopic observation.

The census is already being matched to sources previously identified by the Chandra X-ray Observatory. The hot luminous stars are all potential X-ray sources, given their ability to produce X-rays from shocks in their winds as well as from the colliding winds of a binary systems. A new Chandra survey, The Tarantula - Revealed by X-rays (T-ReX), P.I. Townsley, offers the deepest X-ray observations of 30 Dor. They will further help to reveal the effects of winds and SNe on the ISM in the creation of superbubbles, mapping the structure of the X-ray plasma and its connection to pre-main sequence stars.

To supplement new spectroscopy, the Hubble Tarantula Treasury Project (HTTP, Sabbi et al. 2013) introduces contemporary photometry of the Tarantula Nebula from near-UV to NIR bands using the HST ACS and WFC3 instruments. This would again offer a straightforward method for identifying various SpTs in the region, and the extensive filter coverage would provide an excellent constraint on stellar SEDs.

Detecting the proper motions of the stars in 30 Dor has been assigned to another ongoing HST project (P.I. Lennon). Targets will be observed with WFC3/UVIS and ACS/WFC over a two year base line allowing proper motions with an equivalent velocity  $\gtrsim 25 \text{ km s}^{-1}$  to be detected. This will be particularly crucial in identifying runaway stars in 30 Dor (Bressert et al. 2012) and their original point of origin. It will aid the investigation into whether massive stars

such as VFTS 682 (Section 3.5.3) are capable of forming in isolation or have been influenced in the past. The central  $16' \times 12'$  region of 30 Dor is being covered such that the census and VFTS spectra can all be combined with any stars showing dynamical interest.

Looking even further ahead to future telescopes, the upcoming James Webb Space Telescope (JWST) will offer unprecedented infrared observations of the Universe. Amongst its targets will be young star forming regions like 30 Dor. It will be able to better constrain levels of extinction, detect any hidden stars and obtain an even more complete census of the region. With the ability to peer through the high dust levels of circumstellar disks, it will help reveal answers on the evolution of massive stars. JWST will help to uncover the first massive stars, detecting their supernovae and understanding their role during the reionisation of the early Universe. The forthcoming Square Kilometre Array (SKA) will offer similar groundbreaking observations in the radiowaves. SKA will be able to target UCH II regions extending to distances of up to 50 Mpc, studying their spatial distributions, morphologies and populations statistics (Johnson 2004). Furthermore, it has already been noted how the radio can serve as alternative diagnostic to  $L(\text{H}\alpha)$ , when measuring the ionised gas in H II regions. Individual stellar parameters could be also obtained as SKA provides a reliable estimate of mass-loss rates using the thermal radio continuum emission of massive stars. Needless to say, the next few years promise exciting times in the research of massive stars and their H II regions.



## **Appendix A**

### **ISIS slit orientations and ACAM H $\alpha$ aperture positions**

H6553 images of all the H II regions studied in Chapter 2. In all cases, north is up and east is to the left. The orientation of the ISIS slit is shown in (a) and the position of the aperture used to determine the nebular flux is shown in (b).

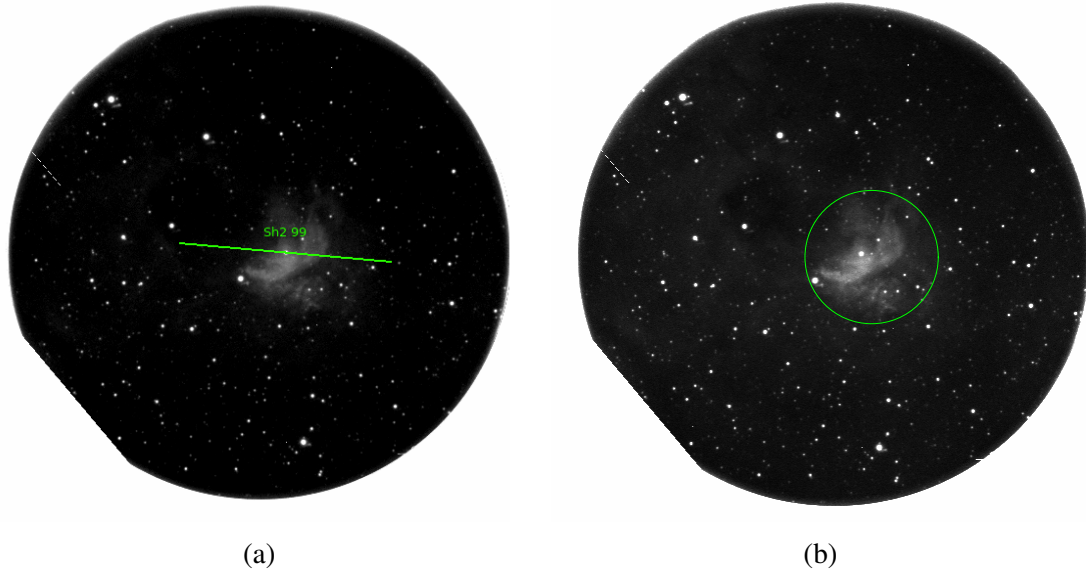


Figure A.1: Sh2 99

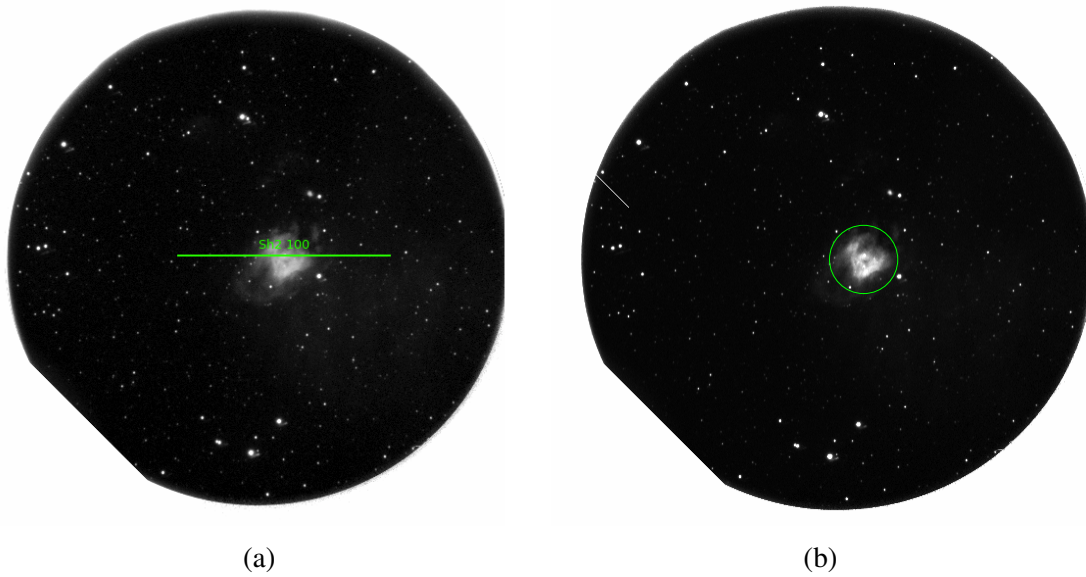


Figure A.2: Sh2 100

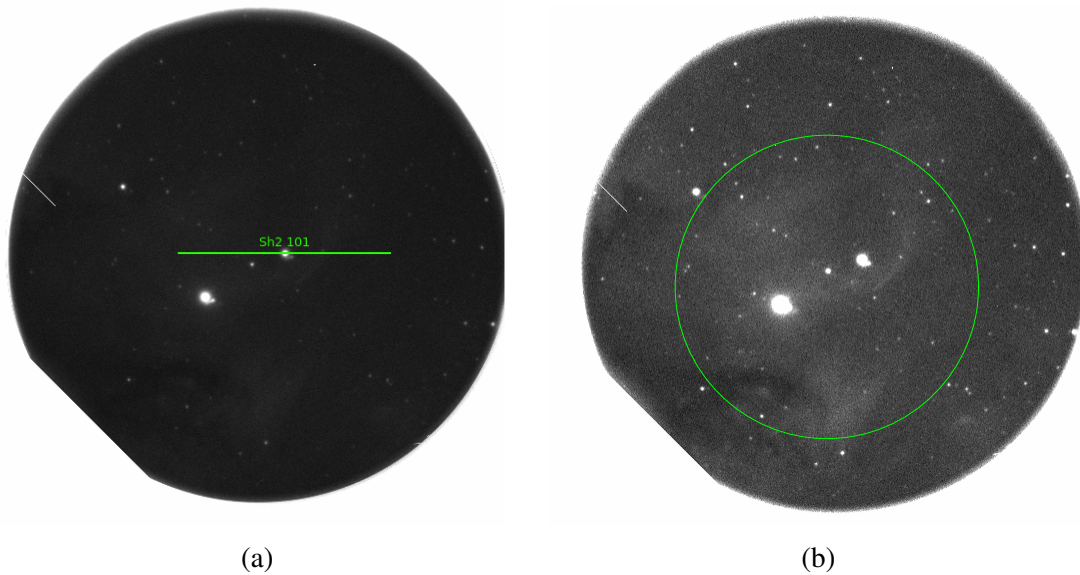


Figure A.3: Sh2 101

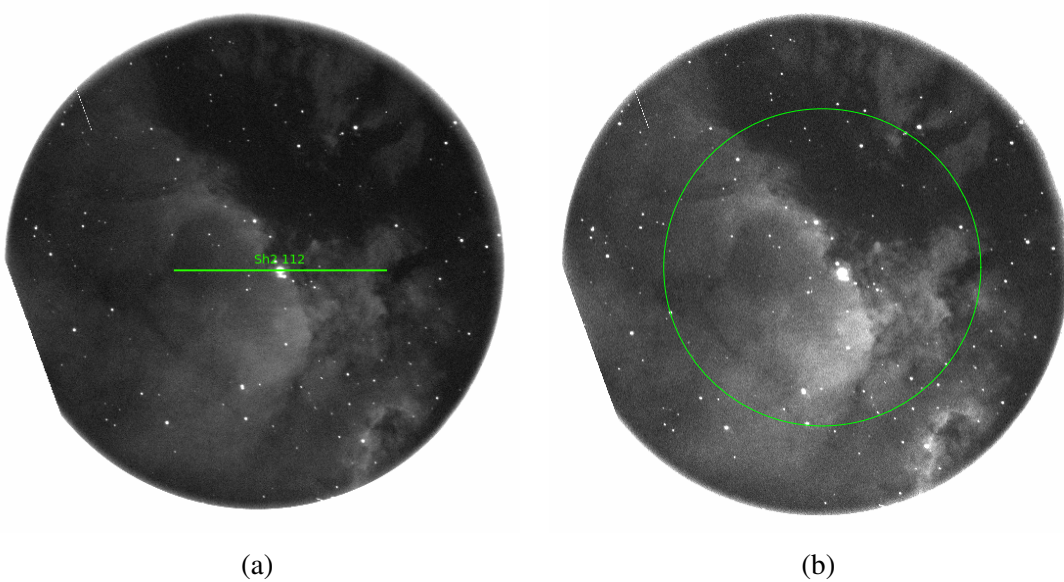


Figure A.4: Sh2 112

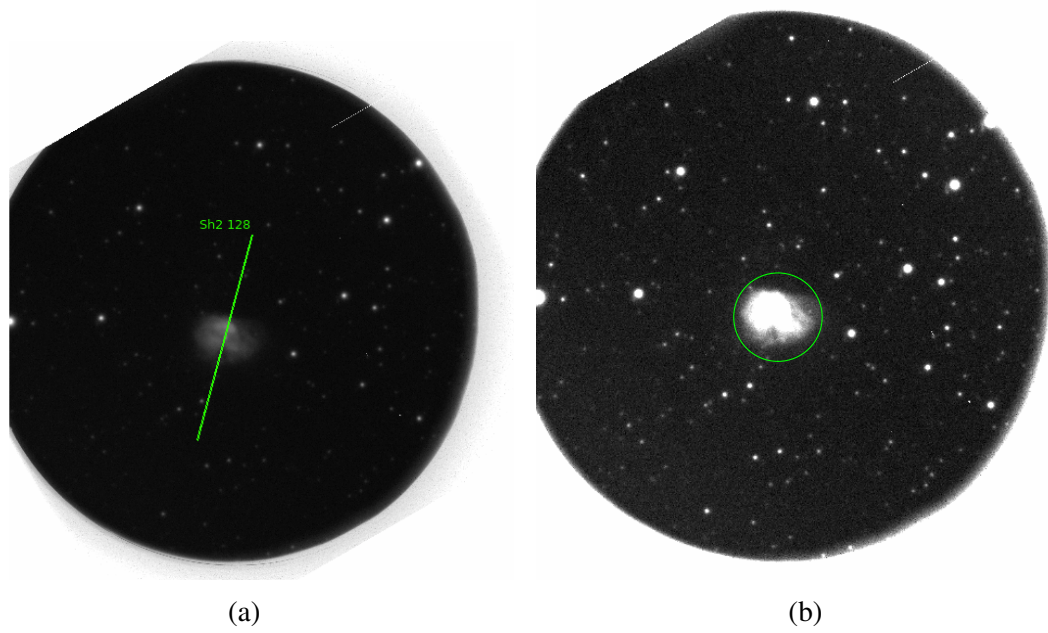


Figure A.5: Sh2 128

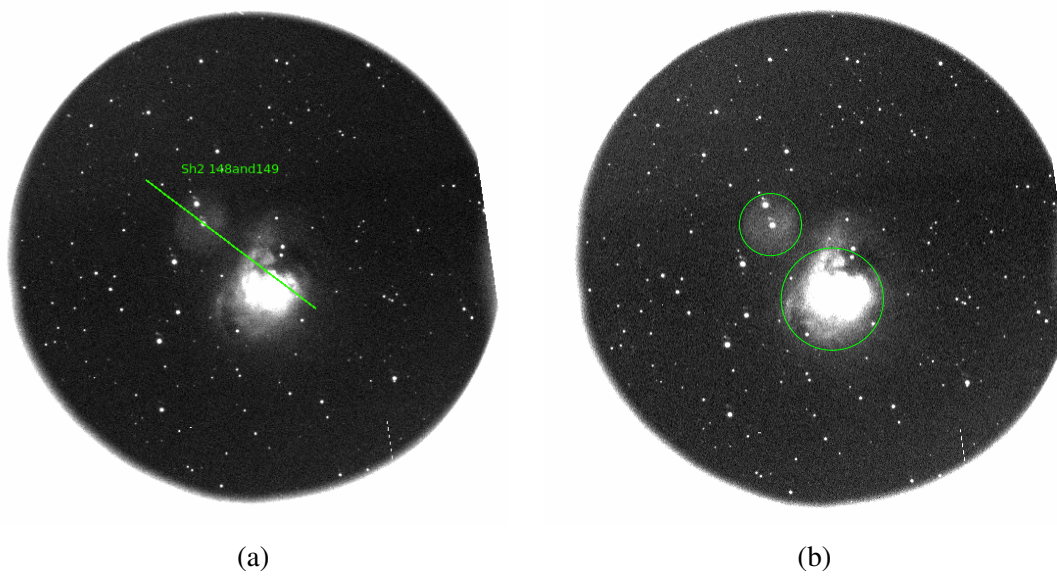


Figure A.6: Sh2 148 and Sh2 149

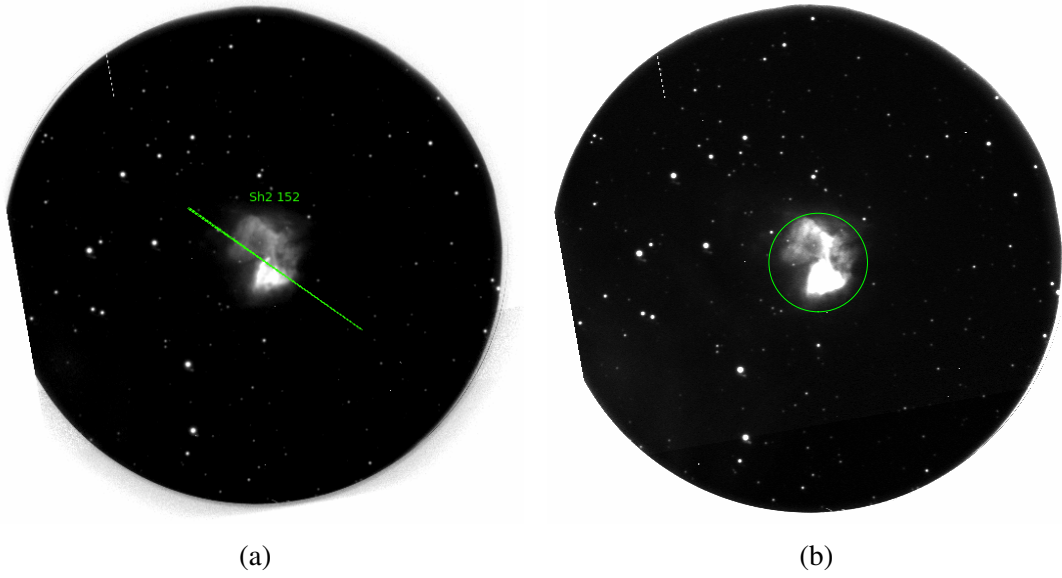


Figure A.7: Sh2 152

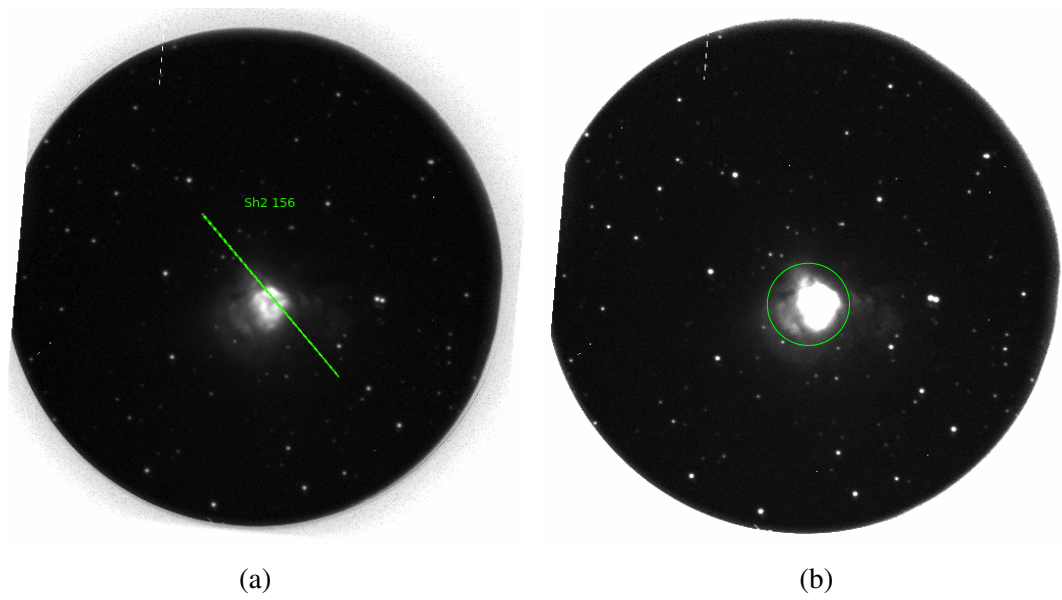


Figure A.8: Sh2 156

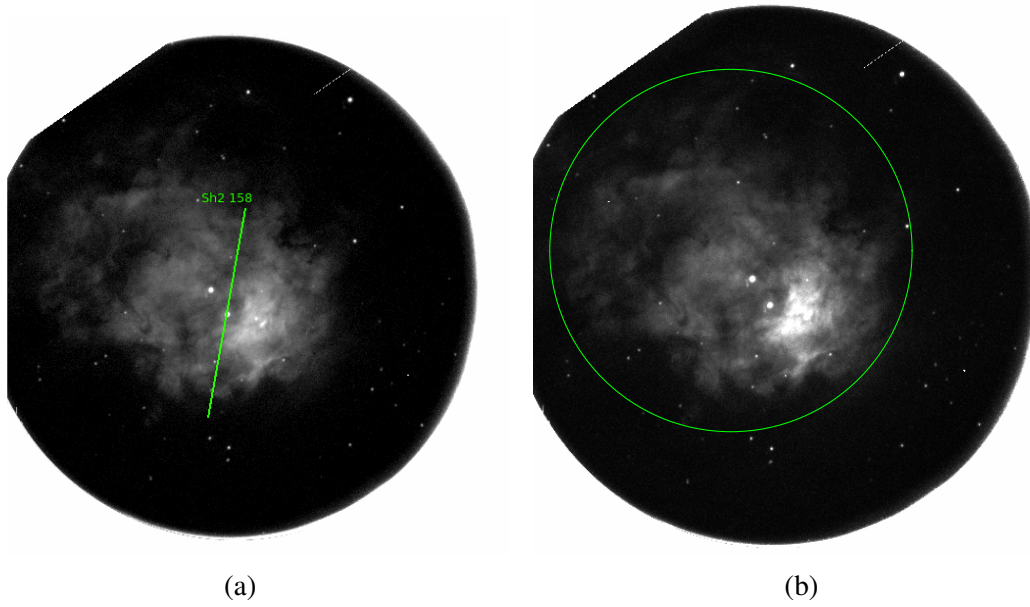


Figure A.9: Sh2 158

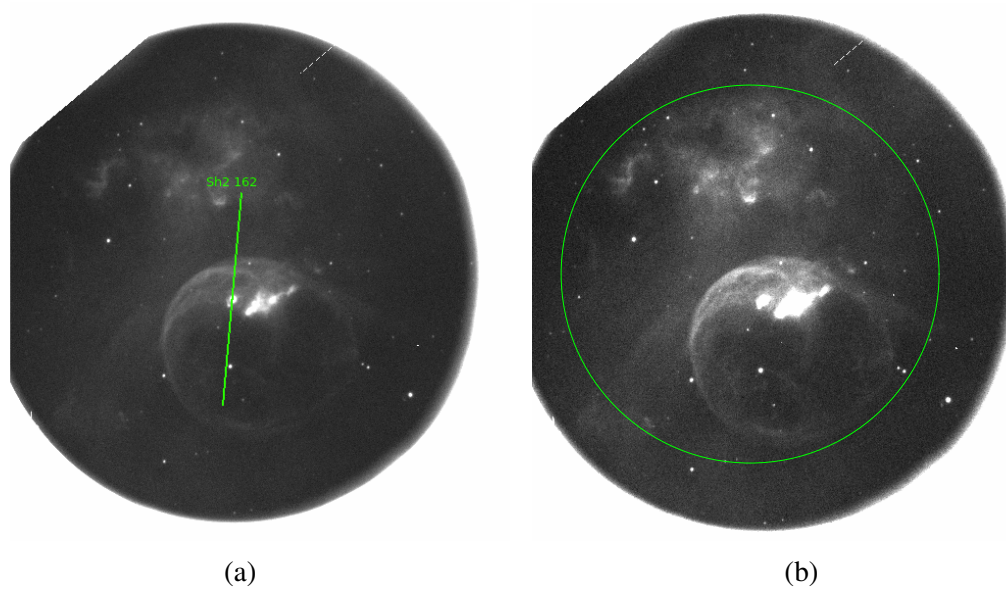


Figure A.10: Sh2 162

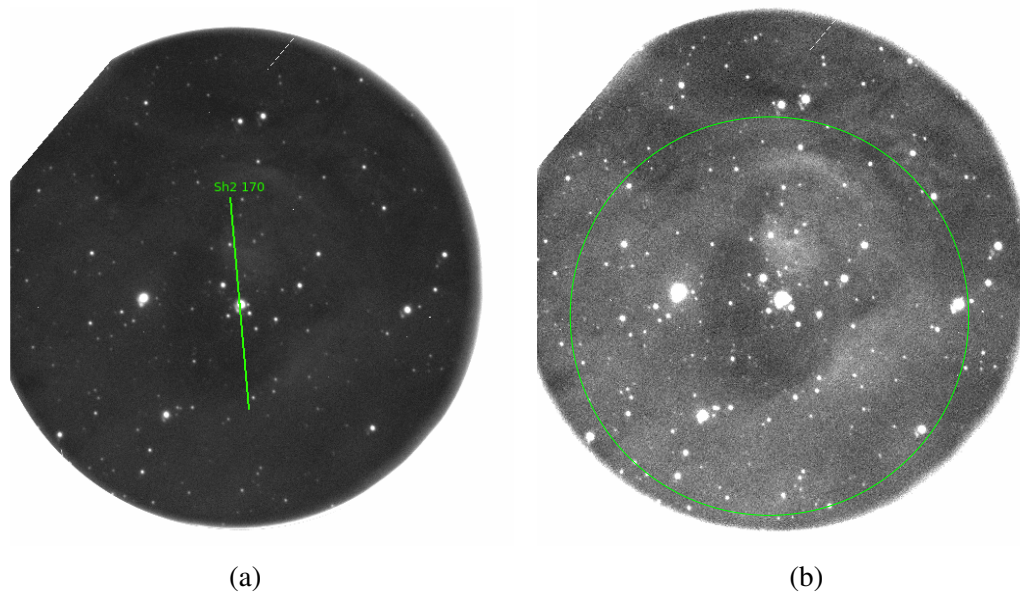


Figure A.11: Sh2 170

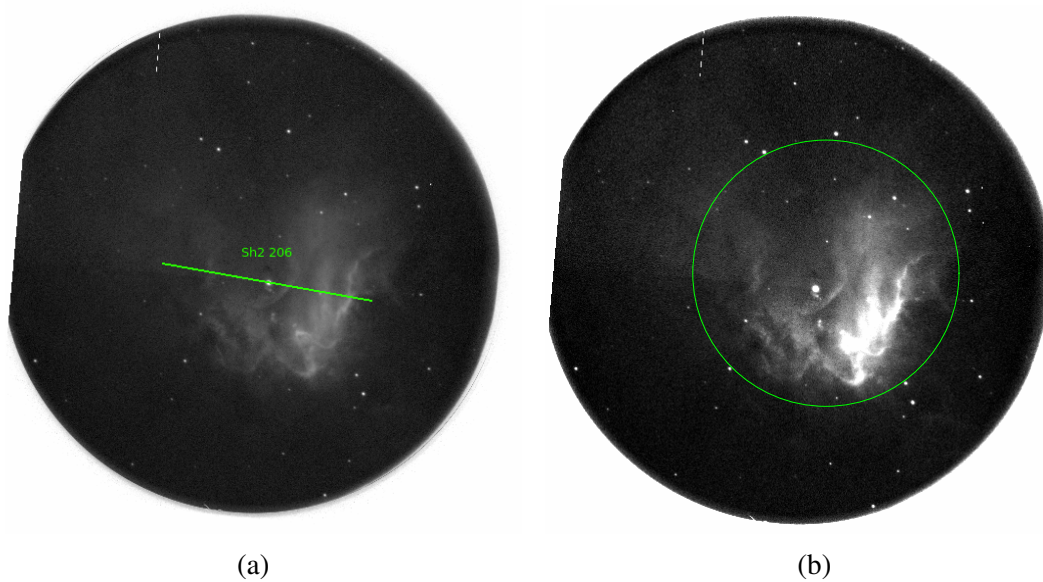


Figure A.12: Sh2 206



## Appendix B

# The VFTS MEDUSA Observational Epochs

Table B.1: Epochs for the VFTS MEDUSA observations. Each epoch was tied to an observing block which included a pair of exposures (a+b or c+d in a few cases).

Field	$\lambda$ -setting	Epoch	MJD
A	LR02	01 [a+b]	54794.187
	LR02	02 [a+b]	54794.231
	LR02	03 [a+b]	54794.328
	LR02	04 [a+b]	54798.303
		04 [c+d]	54836.146
	LR02	05 [a+b]	54836.191
		05 [c+d]	54867.058
	LR02	06 [a+b]	55108.281
	LR03	01 [a+b]	54794.279
	LR03	02 [a+b]	54795.182
	LR03	03 [a+b]	54795.228
	HR15N	01 [a+b]	54795.281
	HR15N	02 [a+b]	54796.207
	B	LR02	01 [a+b]
LR02		02 [a+b]	54804.148
LR02		03 [a+b]	54804.191
LR02		04 [a+b]	54836.239
LR02		05 [a+b]	54836.287
		05 [c+d]	54867.109
LR02		06 [a+b]	55114.320
		06 [c]	55108.318
LR03		01 [a+b]	54808.143
LR03		02 [a+b]	54808.187
LR03		03 [a+b]	54808.230

Table B.1 – continued from previous page

	HR15N	01 [a+b]	54804.247
	HR15N	02 [a+b]	54804.300
C	LR02	01 [a+b]	54774.286
	LR02	02 [a+b]	54809.098
	LR02	03 [a+b]	54809.141
	LR02	04 [a+b]	54837.182
	LR02	05 [a+b]	54867.159
	LR02	06 [a+b]	55112.264
	LR02	07 [a+b]	55459.292
	LR03	01 [a+b]	54809.191
	LR03	02 [a+b]	54809.235
	LR03	03 [a+b]	54809.290
	HR15N	01 [a+b]	54808.285
	HR15N	02 [a+b]	54819.262
D	LR02	01 [a+b]	54824.242
	LR02	02 [a+b]	54824.285
	LR02	03 [a+b]	54822.156
	LR02	04 [a+b]	54858.171
	LR02	05 [a+b]	54879.052
	LR02	06 [a+b]	55111.336
	LR03	01 [a+b]	54820.252
	LR03	02 [a+b]	54821.328
	LR03	03 [a+b]	54822.107
	HR15N	01 [a+b]	54818.189
	HR15N	02 [a+b]	54819.062
E	LR02	01 [a+b]	54822.254
	LR02	02 [a+b]	54822.298
	LR02	03 [a+b]	54822.341
		03 [c+d]	54824.333
	LR02	04 [a+b]	54858.220
	LR02	05 [a+b]	54889.052
	LR02	06 [a+b]	55114.272
	LR03	01 [a+b]	54825.240
	LR03	02 [a+b]	54825.284
	LR03	03 [a+b]	54825.327
	HR15N	01 [a+b]	54819.120
	HR15N	02 [a+b]	54819.174
F	LR02	01 [a+b]	54748.277
	LR02	02 [a+b]	54748.323

Table B.1 – continued from previous page

	LR02	03 [a+b]	54749.223
	LR02	04 [a+b]	54837.133
	LR02	05 [a+b]	54868.057
	LR02	06 [a+b]	55112.313
	LR03	01 [a+b]	54810.238
	LR03	01 [c]	54755.188
	LR03	02 [a+b]	54810.281
	LR03	03 [a+b]	54810.336
	HR15N	01 [a+b]	54749.273
	HR15N	02 [a+b]	54810.170
G	LR02	01 [a+b]	54817.223
	LR02	02 [a+b]	54817.267
	LR02	03 [a+b]	54822.058
	LR02	04 [a+b]	54860.105
	LR02	05 [a+b]	54890.041
	LR02	06 [a+b]	55112.361
	LR03	01 [a+b]	54818.243
	LR03	02 [a+b]	54818.287
	LR03	03 [a+b]	54818.330
	HR15N	01 [a+b]	54818.076
	HR15N	02 [a+b]	54818.129
H	LR02	01 [a+b]	54815.276
	LR02	02 [a+b]	54815.328
	LR02	03 [a+b]	54822.206
	LR02	04 [a+b]	54859.231
	LR02	05 [a+b]	54891.084
	LR02	06 [a+b]	55113.329
	LR03	01 [a+b]	54813.240
	LR03	02 [a+b]	54813.285
	LR03	03 [a+b]	54813.336
	HR15N	01 [a+b]	54776.268
	HR15N	02 [a+b]	54776.322
I	LR02	01 [a+b]	54767.334
		01 [c+d]	54827.283
	LR02	02 [a+b]	54828.240
	LR02	03 [a+b]	54828.284
	LR02	04 [a+b]	54860.154
	LR02	05 [a+b]	54886.127
	LR02	06 [a+b]	55114.370
	LR03	01 [a+b]	54828.332

**Table B.1 – continued from previous page**

LR03	02 [a+b]	54836.052
LR03	03 [a+b]	54836.096
HR15N	01 [a+b]	54819.323
HR15N	02 [a+b]	54827.338

---

Exposure times for LR02 and LR03 observations are all 1815 s (except the LR02-05 exposures for Field D, with an exposure time of 2000 s). All HR15N observations have exposure times of 2265 s.

# Appendix C

## W-R star Spectral Fits

The spectral fits for the W-R template stars listed in Table 3.12. Figures C.1-C.9 provide a comparison between the CMFGEN models (red) and the observed spectra (black, see Table 3.11). Photometric data is also plotted over the CMFGEN spectral energy distributions: broad band photometry (filled squares), narrow band photometry (open squares).

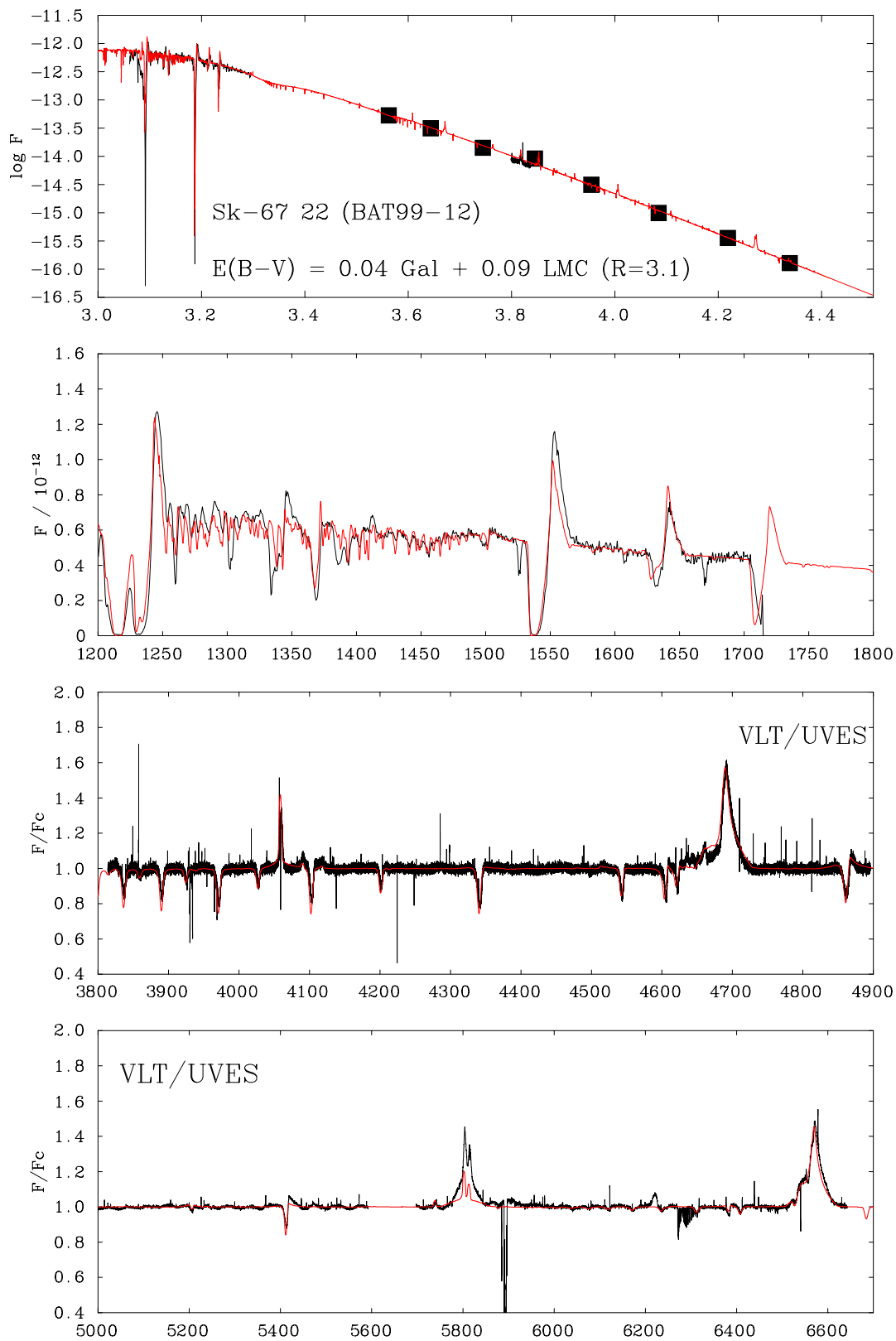


Figure C.1: Spectral fitting for the O2 If\*/WN 5 template star BAT99-12/Sk -67° 22.

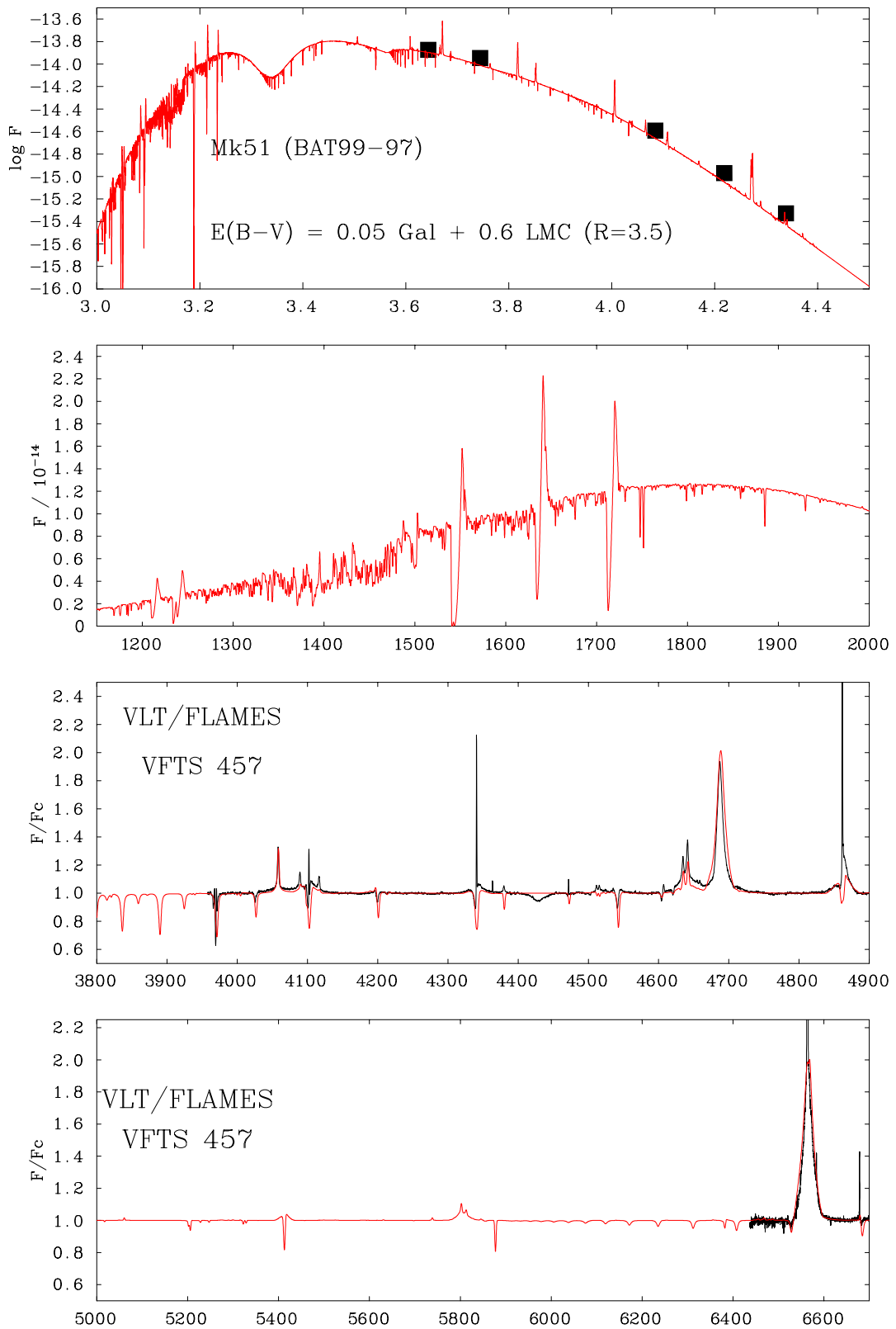


Figure C.2: Spectral fitting for the O3.5 If\*/WN 7 template star Melnick 51/VFTS 457.

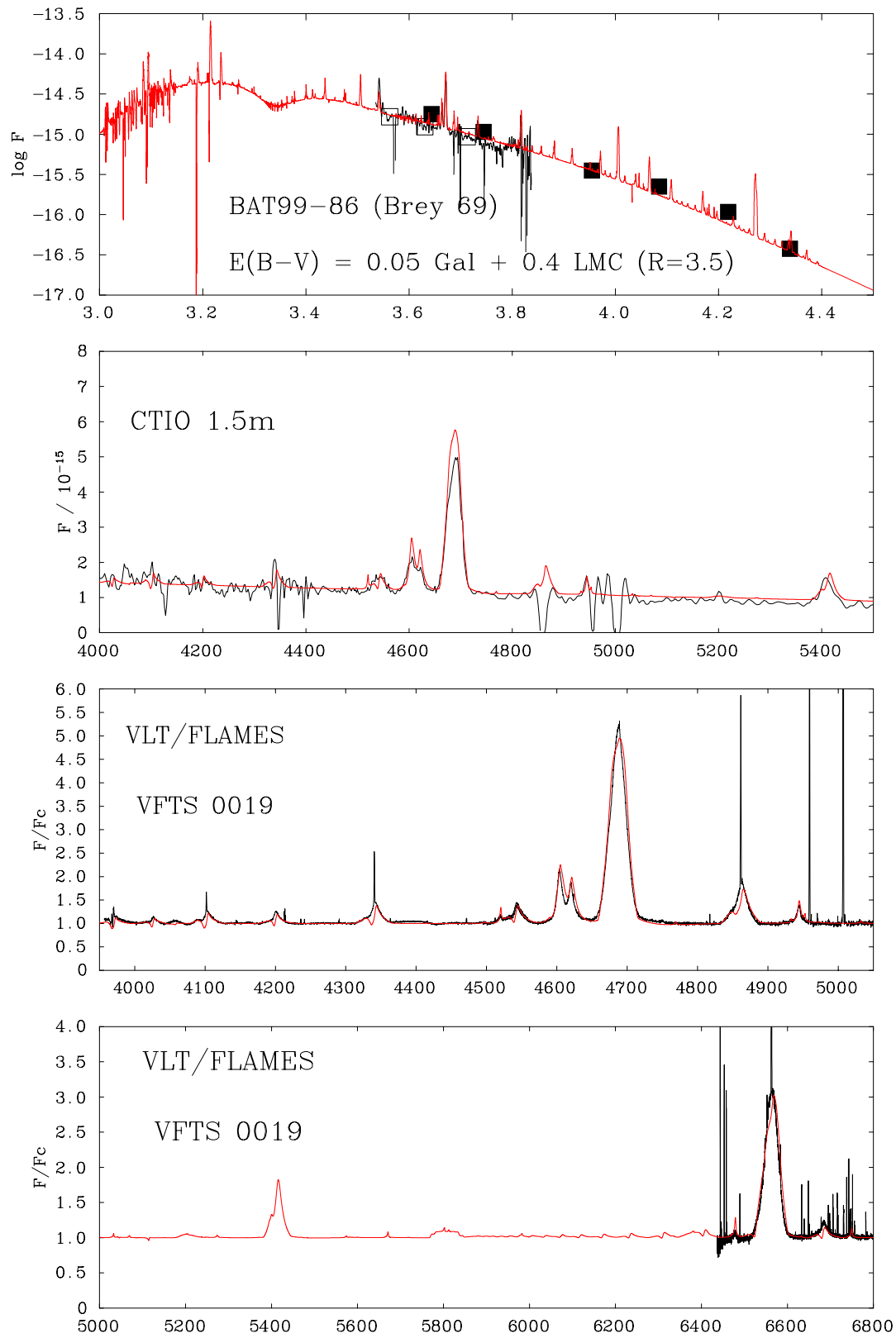


Figure C.3: Spectral fitting for the WN 3 template star BAT99-86/Brey 69/VFTS 019.

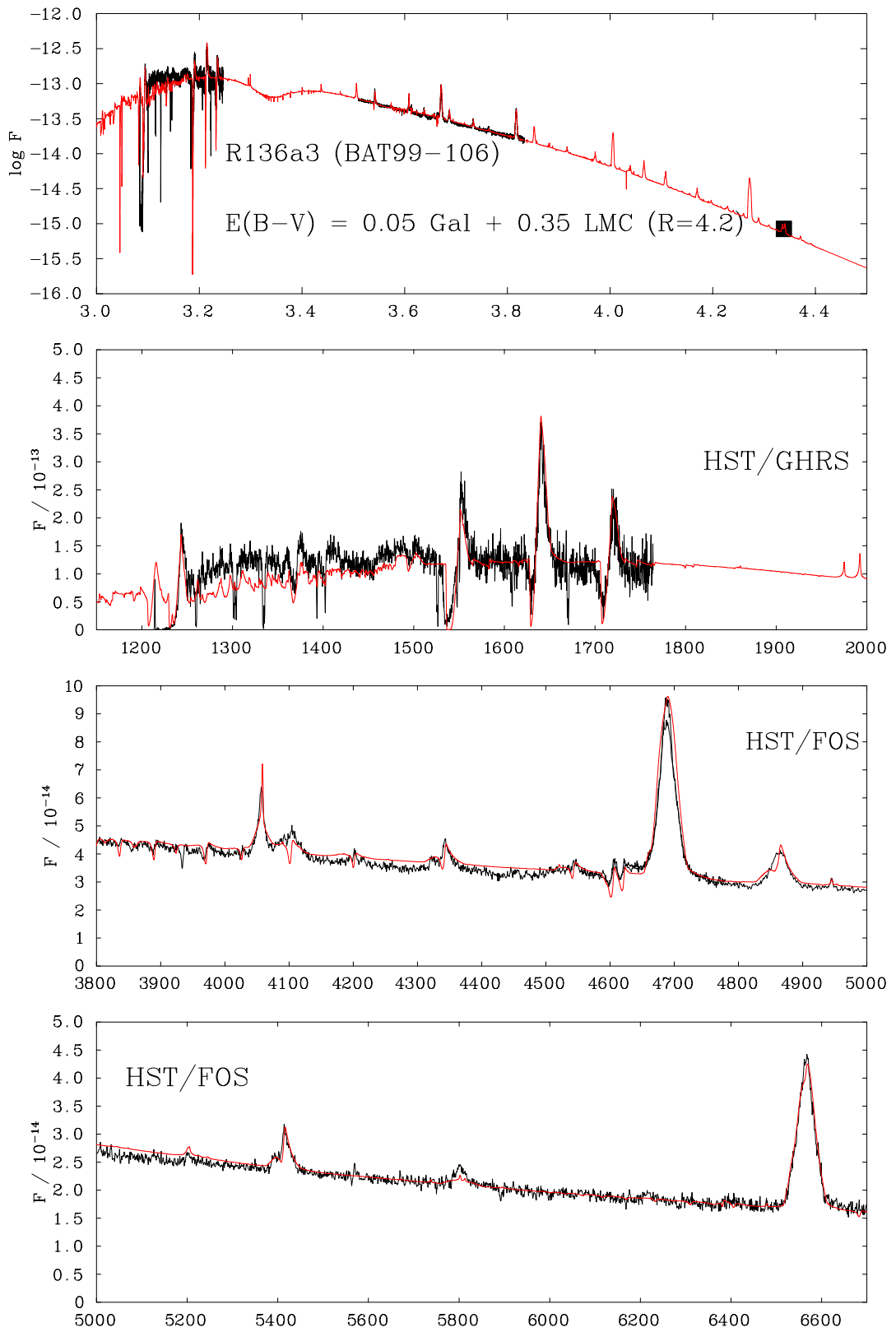


Figure C.4: Spectral fitting for the WN 5 template star BAT99-106/Brey 82/R136a3.

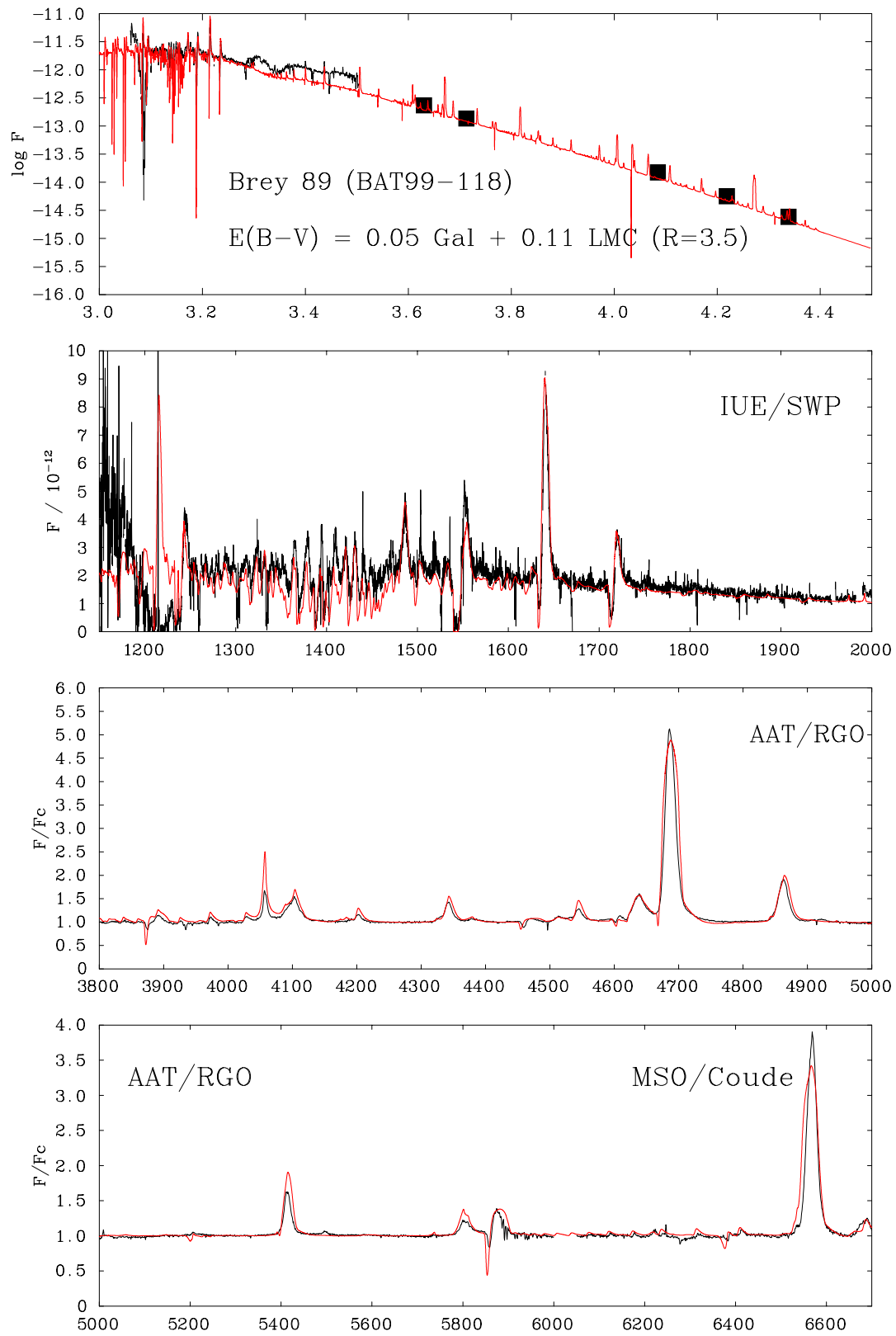


Figure C.5: Spectral fitting for the WN 6 template star BAT99-118/Brey 89.

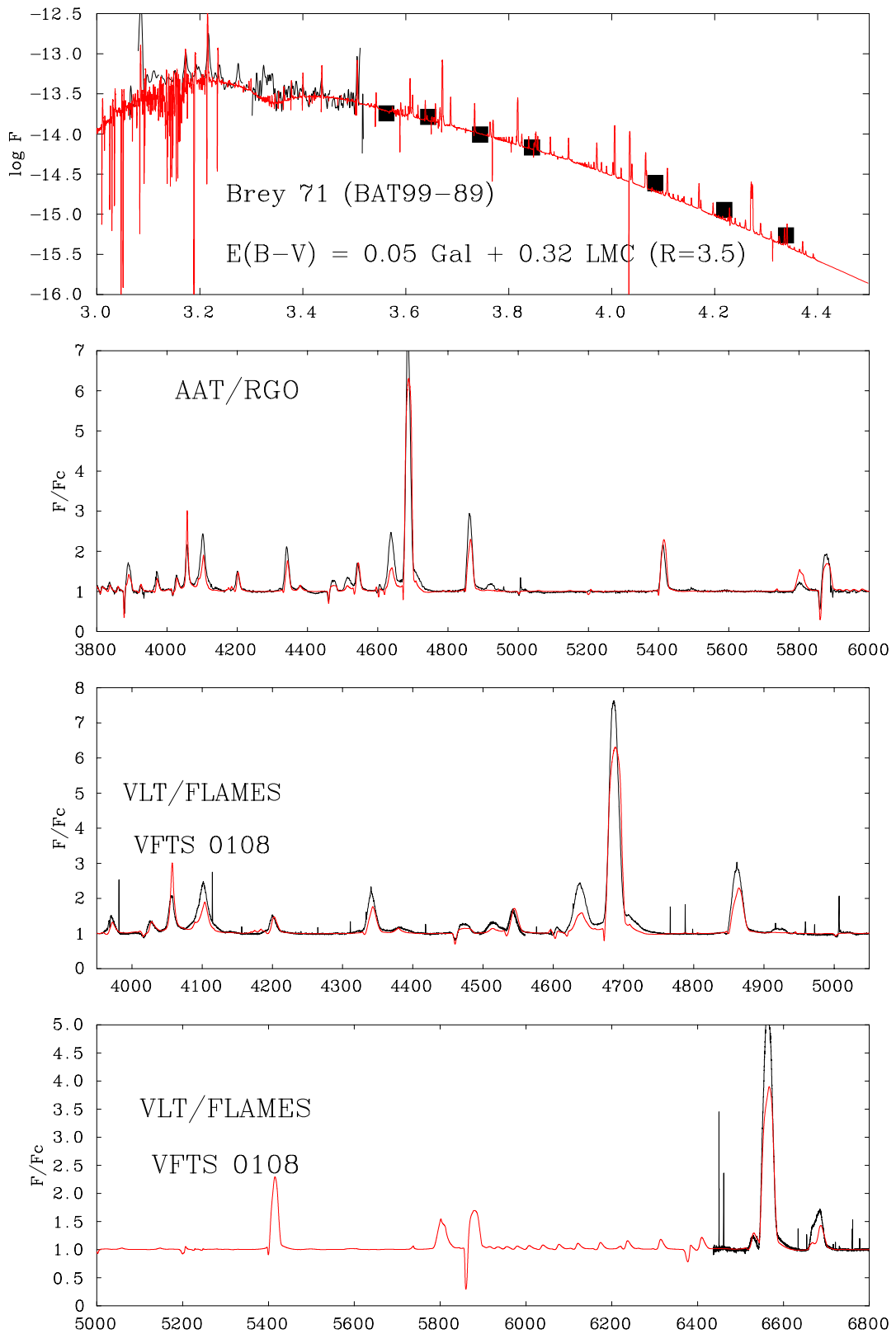


Figure C.6: Spectral fitting for the WN7 template star BAT99-89/Brey 71/VFTS 108.

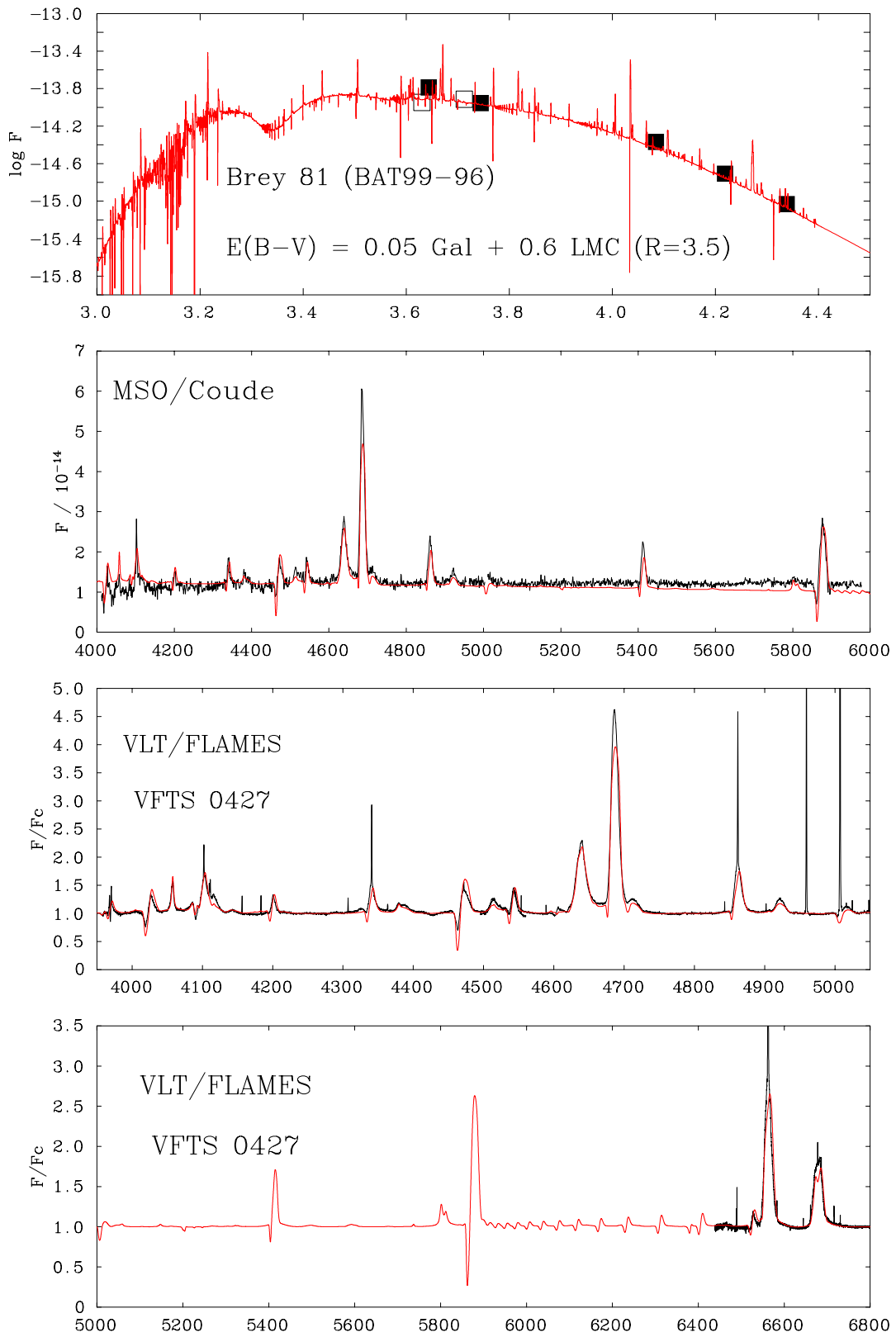


Figure C.7: Spectral fitting for the WN 8 template star BAT99-96/Brey 81/VFTS 427.

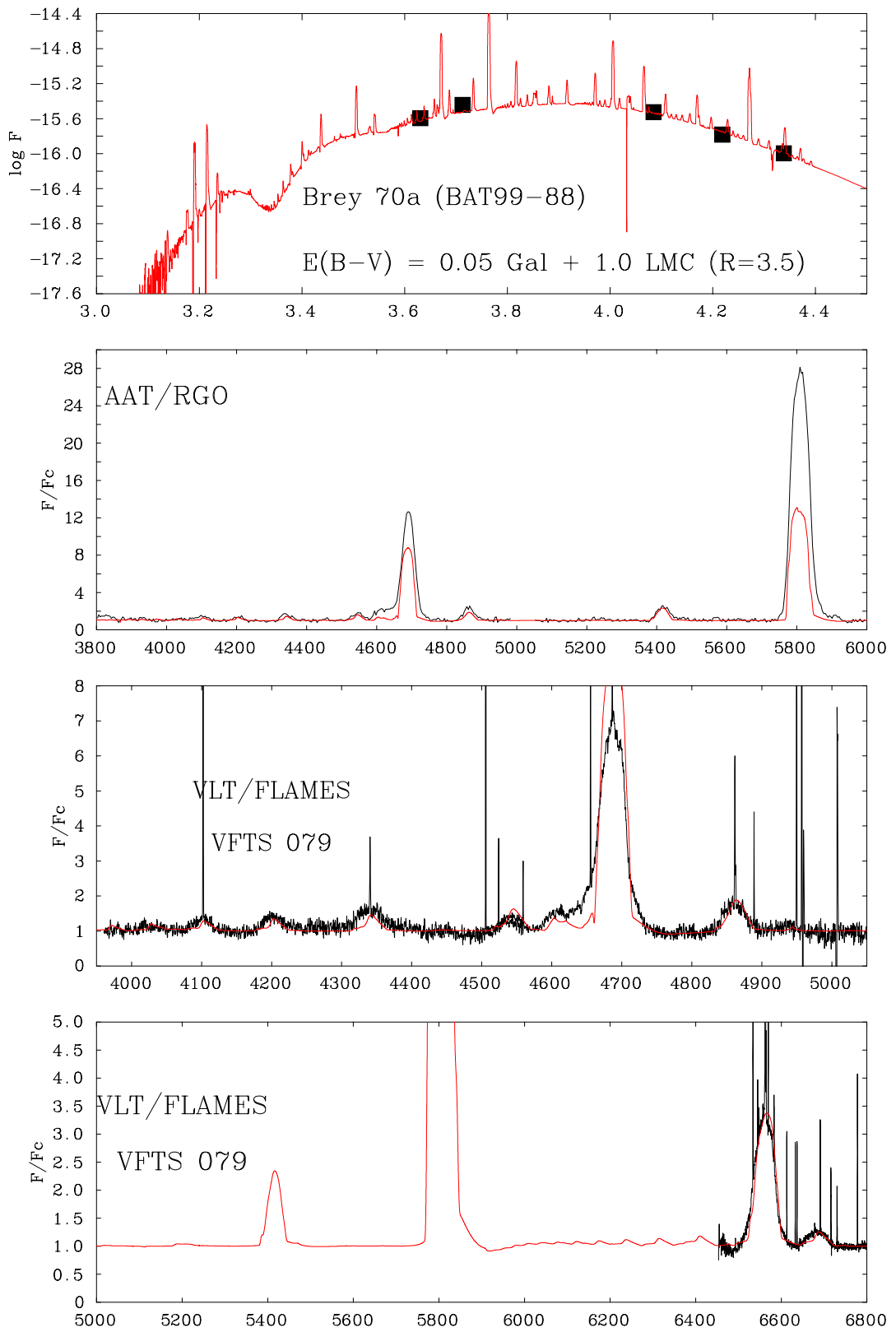


Figure C.8: Spectral fitting for the WN/C template star BAT99-88/Brey 70a/VFTS 079.

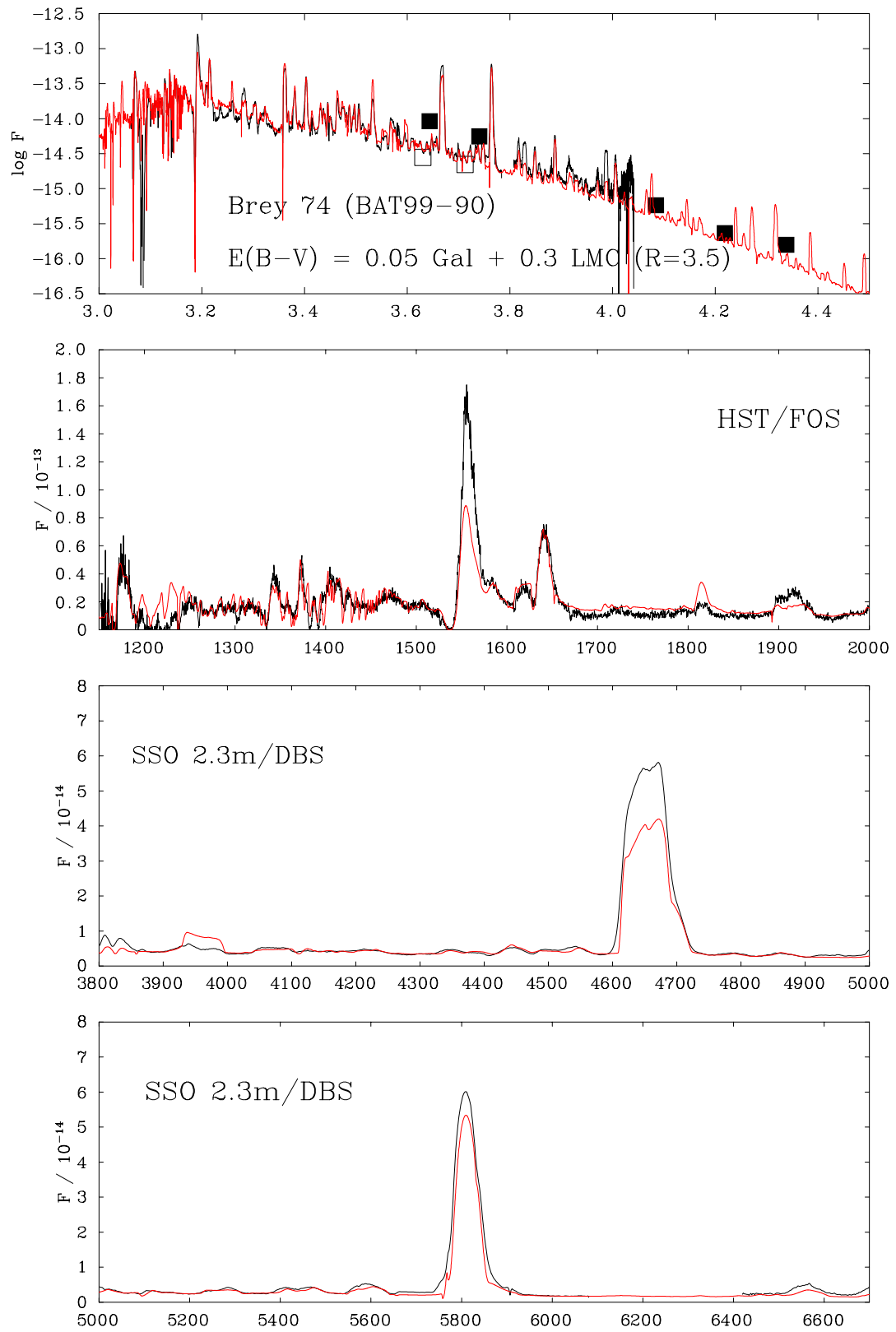


Figure C.9: Spectral fitting for the WC 4 template star BAT99-90/Brey 74.

## Appendix D

### Spectral Fits of the O2 Star Models

The spectral fits for the O2 stars listed in Table 5.1. Figures D.1-D.4 provide a comparison between the synthetic spectra returned by the CMFGEN models (red, Table 5.2) and the observed spectra (black, Table 3.5). Note that in the case of the UV data, the observed spectra are left flux calibrated and the synthetic spectra are reddened to them. This is carried out, as opposed to normalising the observed spectra as is done for optical wavelengths, because the amount of the spectral continuum that is detectable is limited.

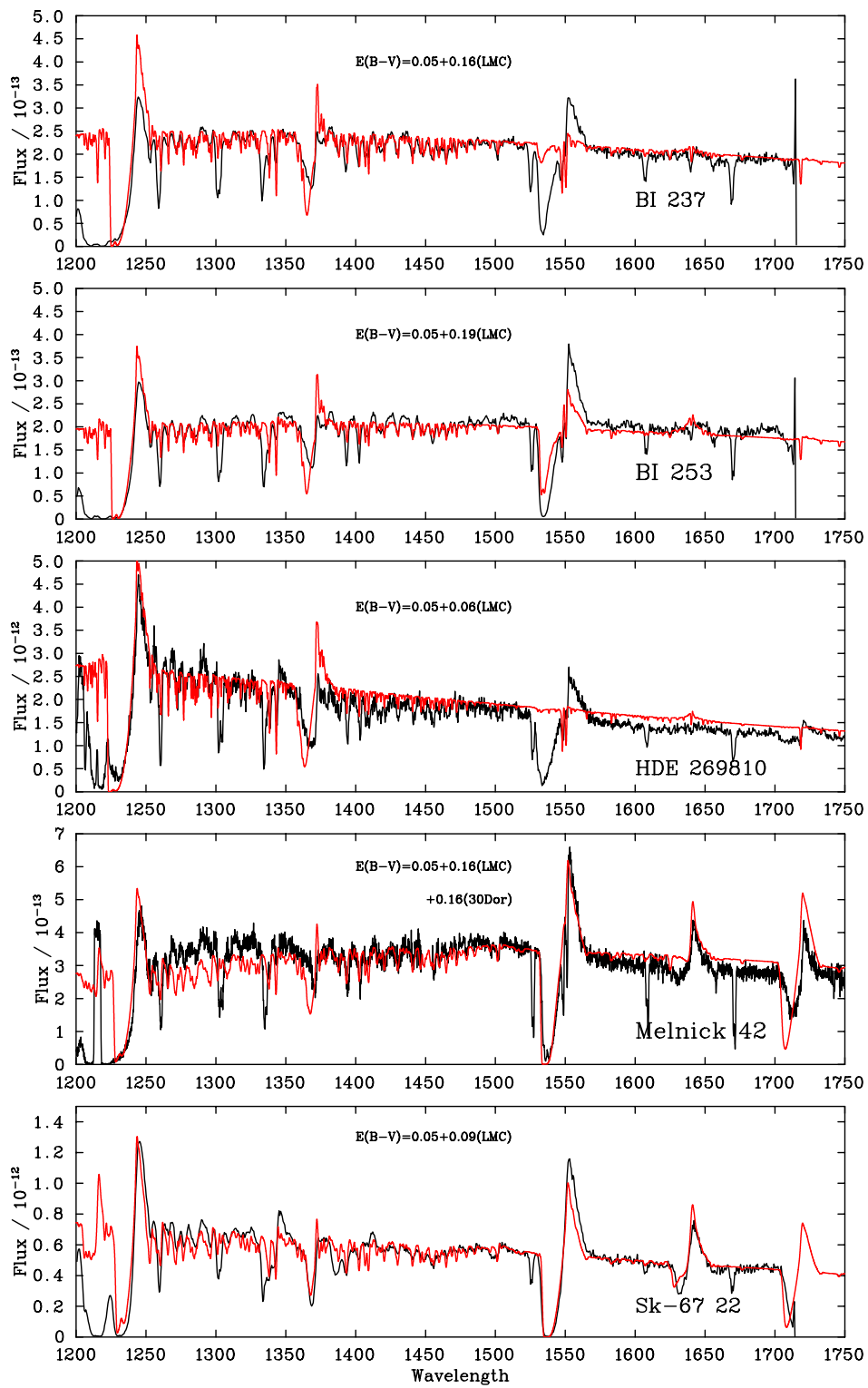


Figure D.1: Spectral fitting in the UV

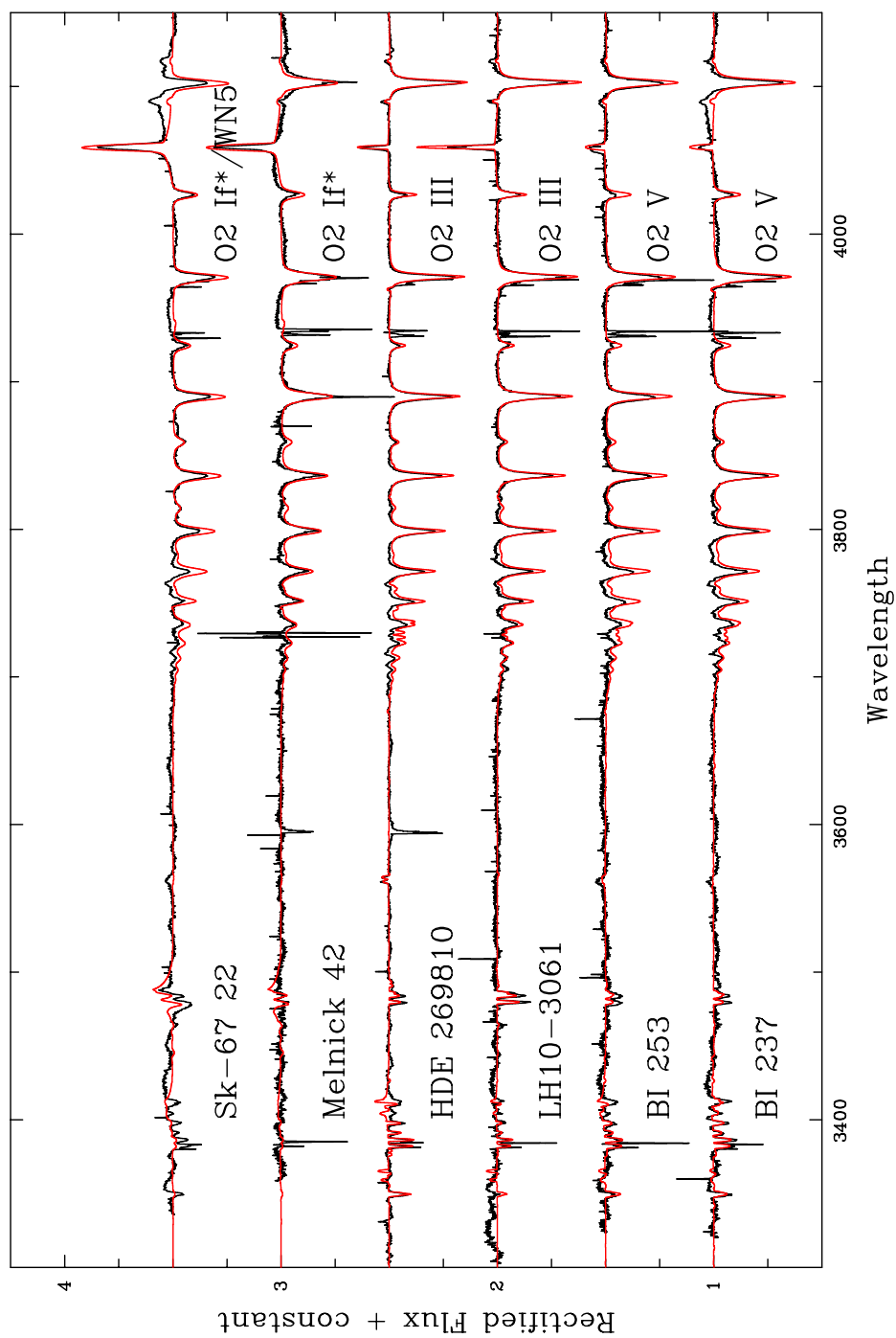


Figure D.2: Spectral fitting in the far-blue

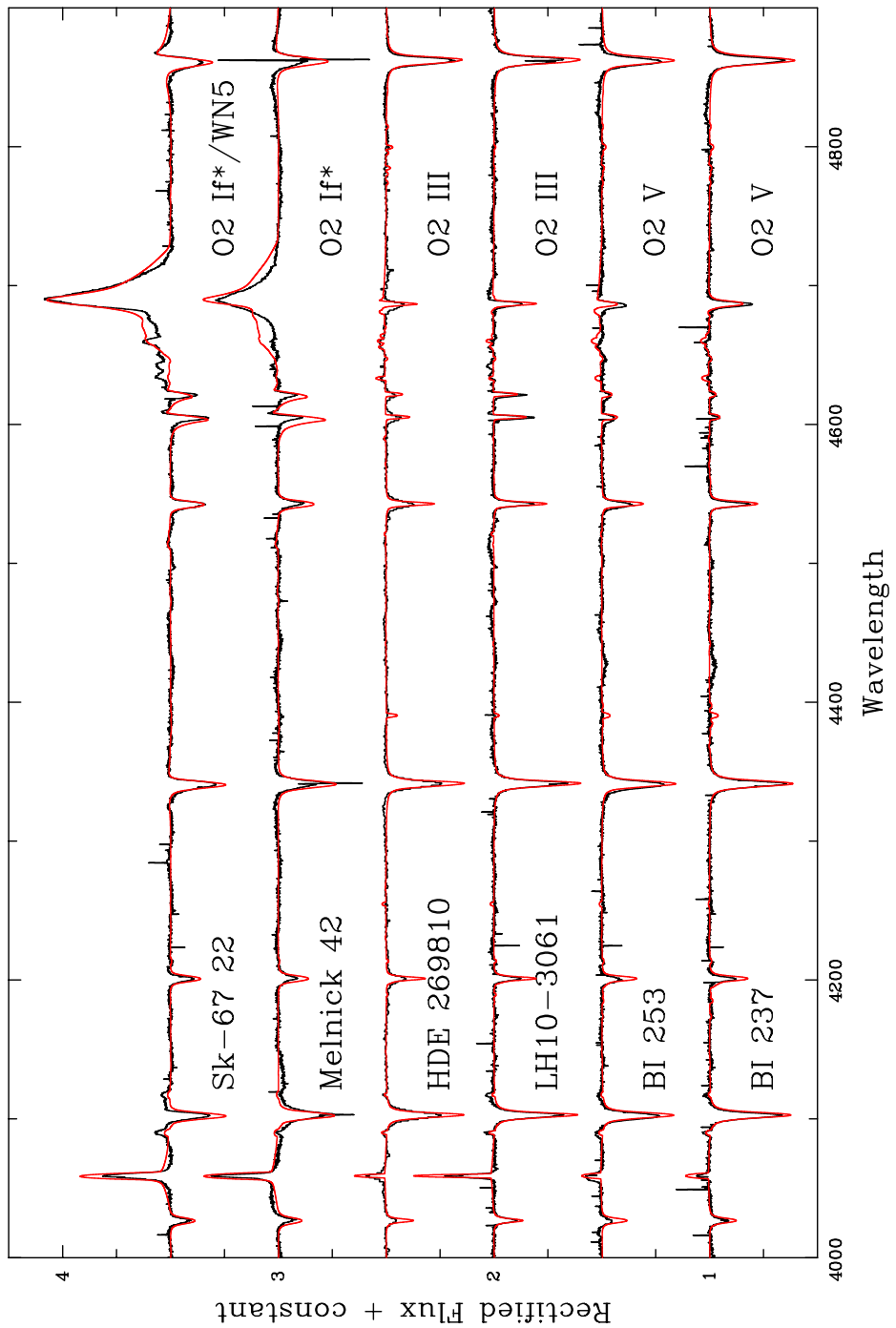


Figure D.3: Spectral fitting in the blue

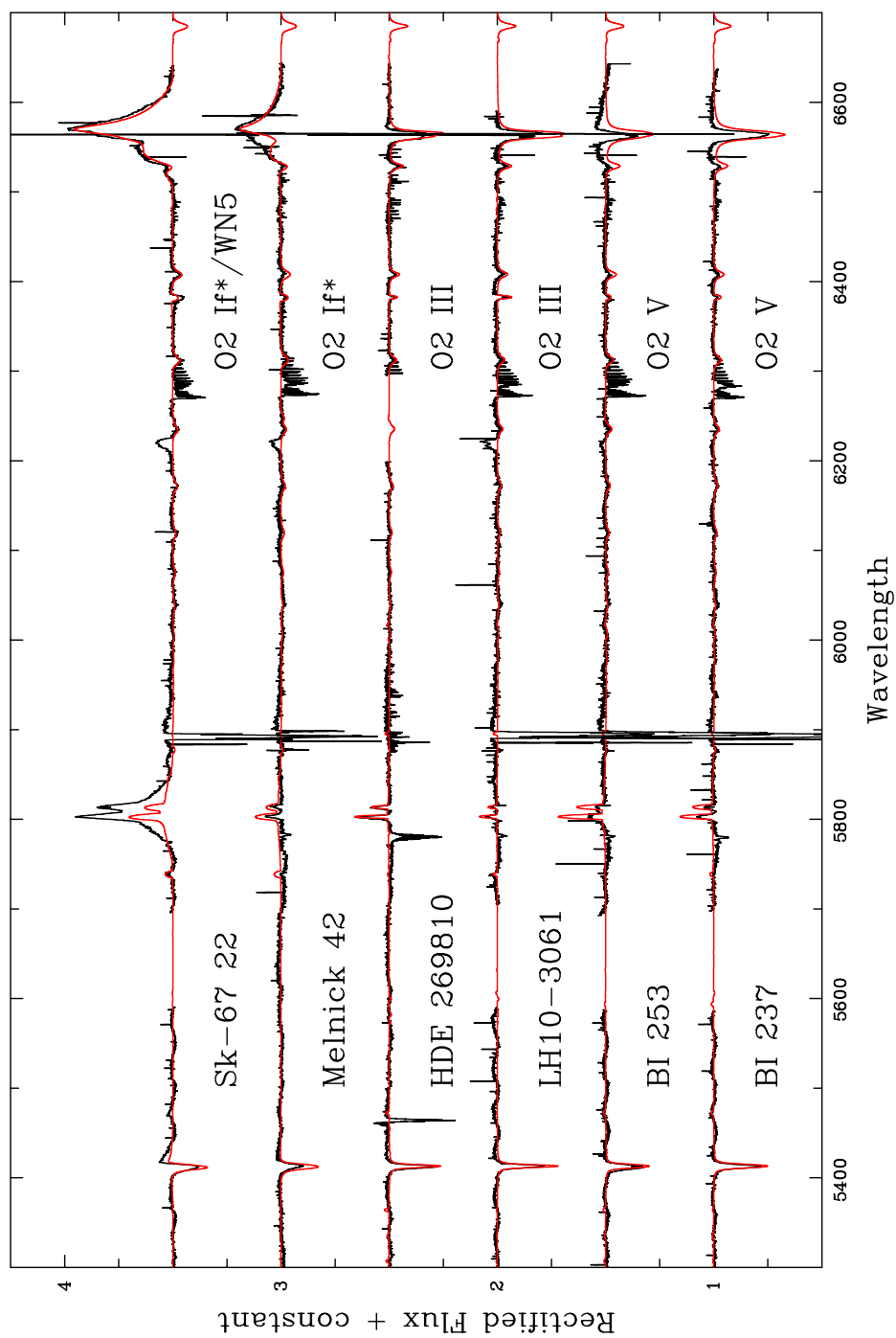


Figure D.4: Spectral fitting in the yellow-red



# Bibliography

- Afflerbach, A., Churchwell, E., & Werner, M. W. 1997, *ApJ*, 478, 190
- Andersen, M., Zinnecker, H., Moneti, A., et al. 2009, *ApJ*, 707, 1347
- Aparicio, A., Herrero, A., & Sánchez, F., eds. 1998, *Stellar astrophysics for the local group : VIII Canary Islands Winter School of Astrophysics*
- Asplund, M., Grevesse, N., Sauval, A. J., & Scott, P. 2009, *ARA&A*, 47, 481
- Auer, L. H. & Mihalas, D. 1972, *ApJS*, 24, 193
- Banerjee, S., Kroupa, P., & Oh, S. 2012, *ApJ*, 746, 15
- Bartzakos, P., Moffat, A. F. J., & Niemela, V. S. 2001, *MNRAS*, 324, 18
- Bastian, N., Covey, K. R., & Meyer, M. R. 2010, *ARA&A*, 48, 339
- Bertelli, G., Bressan, A., Chiosi, C., Fagotto, F., & Nasi, E. 1994, *A&AS*, 106, 275
- Bestenlehner, J. M., et, & al. submitted
- Bestenlehner, J. M., Vink, J. S., Gräfener, G., et al. 2011, *A&A*, 530, L14
- Blanco, V. M., Demers, S., Douglass, G. G., & Fitzgerald, M. P. 1968, *Publications of the U.S. Naval Observatory Second Series*, 21, 1
- Bohlin, R. C., Harris, A. W., Holm, A. V., & Gry, C. 1990, *ApJS*, 73, 413
- Bonnell, I. A. & Bate, M. R. 2005, *MNRAS*, 362, 915
- Bosch, G., Terlevich, R., Melnick, J., & Selman, F. 1999, *A&AS*, 137, 21
- Brandner, W., Grebel, E. K., Barbá, R. H., Walborn, N. R., & Moneti, A. 2001, *AJ*, 122, 858
- Bressert, E., Bastian, N., Evans, C. J., et al. 2012, *A&A*, 542, A49
- Bressert, E., Bastian, N., Gutermuth, R., et al. 2010, *MNRAS*, 409, L54
- Breysacher, J. 1981, *A&AS*, 43, 203
- Breysacher, J. 1986, *A&A*, 160, 185

- Breysacher, J., Azzopardi, M., & Testor, G. 1999, *A&AS*, 137, 117
- Brott, I., de Mink, S. E., Cantiello, M., et al. 2011, *A&A*, 530, A115
- Caballero-Nieves, S. M., Nelan, E. P., Gies, D. R., et al. 2014, *AJ*, 147, 40
- Calzetti, D., Kennicutt, R. C., Engelbracht, C. W., et al. 2007, *ApJ*, 666, 870
- Campbell, M. A., Evans, C. J., Mackey, A. D., et al. 2010, *MNRAS*, 405, 421
- Caplan, J., Deharveng, L., Peña, M., Costero, R., & Blondel, C. 2000, *MNRAS*, 311, 317
- Cardelli, J. A., Clayton, G. C., & Mathis, J. S. 1989, *ApJ*, 345, 245
- Castor, J. I., Abbott, D. C., & Klein, R. I. 1975, *ApJ*, 195, 157
- Cen, R. 2012, *ApJ*, 755, 28
- Cerviño, M., Valls-Gabaud, D., Luridiana, V., & Mas-Hesse, J. M. 2002, *A&A*, 381, 51
- Chan, G. & Fich, M. 1995, *AJ*, 109, 2611
- Chini, R. & Wink, J. E. 1984, *A&A*, 139, L5
- Chomiuk, L. & Povich, M. S. 2011, *AJ*, 142, 197
- Chopinnet, M., Georgelin, Y. M., & Lortet-Zuckermann, M. C. 1973, *A&A*, 29, 225
- Chu, Y.-H. & Kennicutt, Jr., R. C. 1994, *ApJ*, 425, 720
- Chu, Y.-H., Kennicutt, Jr., R. C., Schommer, R. A., & Laff, J. 1992, *AJ*, 103, 1545
- Conti, P. S. 1975, *Memoires of the Societe Royale des Sciences de Liege*, 9, 193
- Conti, P. S. & Alschuler, W. R. 1971, *ApJ*, 170, 325
- Conti, P. S., Crowther, P. A., & Leitherer, C. 2008, *From Luminous Hot Stars to Starburst Galaxies* (Cambridge University Press)
- Conti, P. S. & Frost, S. A. 1977, *ApJ*, 212, 728
- Conti, P. S. & Leep, E. M. 1974, *ApJ*, 193, 113
- Conti, P. S. & Massey, P. 1989, *ApJ*, 337, 251
- Crampton, D. & Fisher, W. A. 1974, *Publications of the Dominion Astrophysical Observatory Victoria*, 14, 283
- Crampton, D., Georgelin, Y. M., & Georgelin, Y. P. 1978, *A&A*, 66, 1
- Crowther, P. A. 2007, *ARA&A*, 45, 177

- Crowther, P. A., De Marco, O., & Barlow, M. J. 1998, MNRAS, 296, 367
- Crowther, P. A. & Dessart, L. 1998, MNRAS, 296, 622
- Crowther, P. A., Dessart, L., Hillier, D. J., Abbott, J. B., & Fullerton, A. W. 2002, A&A, 392, 653
- Crowther, P. A., et, & al. in prep.
- Crowther, P. A. & Hadfield, L. J. 2006, A&A, 449, 711
- Crowther, P. A., Kus, A., & Baker, K. 2014
- Crowther, P. A., Lennon, D. J., & Walborn, N. R. 2006, A&A, 446, 279
- Crowther, P. A., Schnurr, O., Hirschi, R., et al. 2010, MNRAS, 408, 731
- Crowther, P. A. & Smith, L. J. 1997, A&A, 320, 500
- Crowther, P. A. & Walborn, N. R. 2011, MNRAS, 416, 1311
- de Koter, A., Heap, S. R., & Hubeny, I. 1997, ApJ, 477, 792
- De Marchi, G., Paresce, F., Panagia, N., et al. 2011, ApJ, 739, 27
- de Mink, S. E., Sana, H., Langer, N., Izzard, R. G., & Schneider, F. R. N. 2014, ApJ, 782, 7
- De Robertis, M. M., Dufour, R. J., & Hunt, R. W. 1987, JRASC, 81, 195
- Deharveng, L. 1974, A&A, 35, 63
- Deharveng, L., Lortet, M. C., & Testor, G. 1979, A&A, 71, 151
- Deharveng, L., Peña, M., Caplan, J., & Costero, R. 2000, MNRAS, 311, 329
- Dessart, L. 2004, in EAS Publications Series, Vol. 13, EAS Publications Series, ed. M. Heydari-Malayeri, P. Stee, & J.-P. Zahn, 251–270
- Doran, E. I. & Crowther, P. A. 2011, Bulletin de la Societe Royale des Sciences de Liege, 80, 129
- Doran, E. I., Crowther, P. A., de Koter, A., et al. 2013, A&A, 558, A134
- Drissen, L., Moffat, A. F. J., Walborn, N. R., & Shara, M. M. 1995, AJ, 110, 2235
- Dufton, P. L., Dunstall, P. R., Evans, C. J., et al. 2011a, ApJL, 743, L22
- Dufton, P. L., Dunstall, P. R., Evans, C. J., et al. 2011b, ApJL, 743, L22
- Dufton, P. L., Langer, N., Dunstall, P. R., et al. 2013, A&A, 550, A109
- Dunstall, P. R., Fraser, M., Clark, J. S., et al. 2012, A&A, 542, A50

- Dyson, J. E. & Williams, D. A. 1997, *The physics of the interstellar medium*
- Eldridge, J. J. & Stanway, E. R. 2009, *MNRAS*, 400, 1019
- Evans, C., et, & al. in press.
- Evans, C. J., Smartt, S. J., Lee, J.-K., et al. 2005, *A&A*, 437, 467
- Evans, C. J., Taylor, W. D., Hénault-Brunet, V., et al. 2011, *A&A*, 530, A108
- Evans, C. J., Walborn, N. R., Crowther, P. A., et al. 2010, *ApJL*, 715, L74
- Eversberg, T., Lepine, S., & Moffat, A. F. J. 1998, *ApJ*, 494, 799
- Fabian, A. C. 2012, *ARA&A*, 50, 455
- Ferland, G. J., Porter, R. L., van Hoof, P. A. M., et al. 2013, *RMxAA*, 49, 137
- Ferrarese, L. & Merritt, D. 2000, *ApJL*, 539, L9
- Figer, D. F. 2005, *Nature*, 434, 192
- Fitzgerald, M. P. 1970, *A&A*, 4, 234
- Fitzpatrick, E. L. 1986, *AJ*, 92, 1068
- Foellmi, C., Moffat, A. F. J., & Guerrero, M. A. 2003, *MNRAS*, 338, 1025
- Furness, J. P., Crowther, P. A., Morris, P. W., et al. 2010, *MNRAS*, 403, 1433
- Georgelin, Y. M. 1975, PhD thesis, , Univ. Provence, Obs. de Marseille, (1975)
- Georgy, C., Ekström, S., Meynet, G., et al. 2012, *A&A*, 542, A29
- Gianninas, A., Bergeron, P., & Ruiz, M. T. 2011, *ApJ*, 743, 138
- Giveon, U., Sternberg, A., Lutz, D., Feuchtgruber, H., & Pauldrach, A. W. A. 2002, *ApJ*, 566, 880
- Grafener, G., Hamann, W.-R., Hillier, D. J., & Koesterke, L. 1998, *A&A*, 329, 190
- Gray, R. O. & Corbally, J., C. 2009, *Stellar Spectral Classification*
- Grebel, E. K. & Chu, Y.-H. 2000, *AJ*, 119, 787
- Gvaramadze, V. V., Kroupa, P., & Pflamm-Altenburg, J. 2010, *A&A*, 519, A33
- Haffner, L. M., Dettmar, R.-J., Beckman, J. E., et al. 2009, *Reviews of Modern Physics*, 81, 969
- Hainich, R., Rühling, U., Todt, H., et al. 2014, *ArXiv e-prints*

- Hamann, W.-R. & Gräfener, G. 2004, *A&A*, 427, 697
- Hamann, W.-R., Gräfener, G., & Liermann, A. 2006, *A&A*, 457, 1015
- Hanson, M. M., Conti, P. S., & Rieke, M. J. 1996, *ApJS*, 107, 281
- Harayama, Y., Eisenhauer, F., & Martins, F. 2008, *ApJ*, 675, 1319
- Heap, S. R., Altner, B., Ebbets, D., et al. 1991, *ApJL*, 377, L29
- Hénault-Brunet, V., Evans, C. J., Sana, H., et al. 2012, *A&A*, 546, A73
- Herrero, A., Kudritzki, R. P., Vilchez, J. M., et al. 1992, *A&A*, 261, 209
- Hillier, D. J. & Miller, D. L. 1998, *ApJ*, 496, 407
- Hiltner, W. A. & Johnson, H. L. 1956, *ApJ*, 124, 367
- Howarth, I. D. 1983, *MNRAS*, 203, 301
- Howarth, I. D., Murray, J., Mills, D., & Berry, D. S. 2004, *DIPSO*, Starlink User Note 50.24
- Howarth, I. D. & Schmutz, W. 1992, *A&A*, 261, 503
- Howarth, I. D. & Walborn, N. R. 2012, *MNRAS*, 426, 1867
- Hubeny, I. & Lanz, T. 1995, *ApJ*, 439, 875
- Hummer, D. G. & Storey, P. J. 1987, *MNRAS*, 224, 801
- Humphreys, R. M. & Davidson, K. 1979, *ApJ*, 232, 409
- Hunter, D. A. & Massey, P. 1990, *AJ*, 99, 846
- Hunter, D. A., Shaya, E. J., Holtzman, J. A., et al. 1995, *ApJ*, 448, 179
- Hunter, I., Brott, I., Lennon, D. J., et al. 2008, *ApJL*, 676, L29
- Hunter, I., Dufton, P. L., Smartt, S. J., et al. 2007, *A&A*, 466, 277
- Indebetouw, R., de Messières, G. E., Madden, S., et al. 2009, *ApJ*, 694, 84
- Indebetouw, R., Mathis, J. S., Babler, B. L., et al. 2005, *ApJ*, 619, 931
- Israel, F. P. & Koornneef, J. 1979, *ApJ*, 230, 390
- Jamet, L., Pérez, E., Cerviño, M., et al. 2004, *A&A*, 426, 399
- Johnson, C. O., Depree, C. G., & Goss, W. M. 1998, *ApJ*, 500, 302
- Johnson, K. E. 2004, *NAR*, 48, 1337
- Kennicutt, R. C. & Evans, N. J. 2012, *ARA&A*, 50, 531

- Kennicutt, Jr., R. C. 1984, *ApJ*, 287, 116
- Kennicutt, Jr., R. C. 1998, *ARA&A*, 36, 189
- Kennicutt, Jr., R. C., Bresolin, F., Bomans, D. J., Bothun, G. D., & Thompson, I. B. 1995, *AJ*, 109, 594
- Kennicutt, Jr., R. C., Hao, C.-N., Calzetti, D., et al. 2009, *ApJ*, 703, 1672
- Kingsburgh, R. L. & Barlow, M. J. 1994, *MNRAS*, 271, 257
- Köhler, K., et, & al. in prep.
- Kroupa, P. 2001, *MNRAS*, 322, 231
- Kudritzki, R.-P. & Puls, J. 2000, *ARA&A*, 38, 613
- Kudritzki, R. P., Puls, J., Lennon, D. J., et al. 1999, *A&A*, 350, 970
- Kuiper, R., Klahr, H., Beuther, H., & Henning, T. 2011, *Bulletin de la Societe Royale des Sciences de Liege*, 80, 211
- Kurtz, S. 2005, in *IAU Symposium, Vol. 227, Massive Star Birth: A Crossroads of Astrophysics*, ed. R. Cesaroni, M. Felli, E. Churchwell, & M. Walmsley, 111–119
- Kurucz, R. L. 1979, *ApJS*, 40, 1
- Lada, C. J. & Lada, E. A. 2003, *ARA&A*, 41, 57
- Lahulla, J. F. 1985, *A&AS*, 61, 537
- Lamers, H. J. G. L. M. & Cassinelli, J. P. 1999, *Introduction to Stellar Winds*
- Lamers, H. J. G. L. M., Snow, T. P., & Lindholm, D. M. 1995, *ApJ*, 455, 269
- Lanz, T. & Hubeny, I. 2003, *ApJS*, 146, 417
- Larson, R. B. 2003, in *Astronomical Society of the Pacific Conference Series, Vol. 287, Galactic Star Formation Across the Stellar Mass Spectrum*, ed. J. M. De Buizer & N. S. van der Blik, 65–80
- Lee, J. C., Gil de Paz, A., Tremonti, C., et al. 2009, *ApJ*, 706, 599
- Lefever, K., Puls, J., & Aerts, C. 2007, *A&A*, 463, 1093
- Leitherer, C. 2008, in *IAU Symposium, Vol. 255, IAU Symposium*, ed. L. K. Hunt, S. C. Madden, & R. Schneider, 305–309
- Leitherer, C., Robert, C., & Drissen, L. 1992, *ApJ*, 401, 596
- Leitherer, C., Schaerer, D., Goldader, J. D., et al. 1999, *ApJS*, 123, 3

- Lépine, S. & Moffat, A. F. J. 1999, *ApJ*, 514, 909
- Lépine, S. & Moffat, A. F. J. 2008, *AJ*, 136, 548
- Levesque, E. M., Leitherer, C., Ekstrom, S., Meynet, G., & Schaerer, D. 2012, *ApJ*, 751, 67
- Lumsden, S. L., Hoare, M. G., Urquhart, J. S., et al. 2013, *ApJS*, 208, 11
- Maeder, A. & Meynet, G. 2000, *ARA&A*, 38, 143
- Maíz-Apellániz, J. 2004, *PASP*, 116, 859
- Maíz Apellániz, J. 2013, in *Highlights of Spanish Astrophysics VII*, 583–589
- Maíz Apellániz, J., Evans, C. J., Barbá, R. H., et al. 2014, *ArXiv e-prints*
- Mampaso, A., Gomez, P., Sanchez-Magro, C., & Selby, M. J. 1984, *MNRAS*, 207, 465
- Markova, N. & Puls, J. 2008, *A&A*, 478, 823
- Martins, F. 2011, *Bulletin de la Societe Royale des Sciences de Liege*, 80, 29
- Martins, F., Hillier, D. J., Bouret, J. C., et al. 2009, *A&A*, 495, 257
- Martins, F. & Plez, B. 2006, *A&A*, 457, 637
- Martins, F., Schaerer, D., & Hillier, D. J. 2005, *A&A*, 436, 1049
- Massey, P. 1984, *ApJ*, 281, 789
- Massey, P. 2002, *ApJS*, 141, 81
- Massey, P., Bresolin, F., Kudritzki, R. P., Puls, J., & Pauldrach, A. W. A. 2004, *ApJ*, 608, 1001
- Massey, P. & Hunter, D. A. 1998, *ApJ*, 493, 180
- Massey, P., Puls, J., Pauldrach, A. W. A., et al. 2005, *ApJ*, 627, 477
- Mathys, G. 1988, *A&AS*, 76, 427
- Maund, J. R., Reilly, E., & Mattila, S. 2014, *MNRAS*
- Mayer, P. & Macák, P. 1973, *Bulletin of the Astronomical Institutes of Czechoslovakia*, 24, 50
- McEvoy, C., et, & al. in prep.
- McKee, C. F. & Tan, J. C. 2003, *ApJ*, 585, 850
- Meixner, M., Gordon, K. D., Indebetouw, R., et al. 2006, *AJ*, 132, 2268
- Meixner, M., Panuzzo, P., Roman-Duval, J., et al. 2013, *AJ*, 146, 62
- Melena, N. W., Massey, P., Morrell, N. I., & Zangari, A. M. 2008, *AJ*, 135, 878

- Melnick, J. 1985, *A&A*, 153, 235
- Mermilliod, J.-C. & García, B. 2001, in *IAU Symposium*, Vol. 200, *The Formation of Binary Stars*, ed. H. Zinnecker & R. Mathieu, 191
- Meynet, G., Maeder, A., Schaller, G., Schaerer, D., & Charbonnel, C. 1994, *A&AS*, 103, 97
- Moffat, A. F. J., Niemela, V. S., Phillips, M. M., Chu, Y.-H., & Seggewiss, W. 1987, *ApJ*, 312, 612
- Mokiem, M. R., de Koter, A., Evans, C. J., et al. 2007a, *A&A*, 465, 1003
- Mokiem, M. R., de Koter, A., Vink, J. S., et al. 2007b, *A&A*, 473, 603
- Mokiem, M. R., Martín-Hernández, N. L., Lenorzer, A., de Koter, A., & Tielens, A. G. G. M. 2004, *A&A*, 419, 319
- Morel, T., Marchenko, S. V., Eenens, P. R. J., et al. 1999, *ApJ*, 518, 428
- Morisset, C., Schaerer, D., Martín-Hernández, N. L., et al. 2002, *A&A*, 386, 558
- Nugis, T. & Lamers, H. J. G. L. M. 2000, *A&A*, 360, 227
- Oey, M. S. & Kennicutt, Jr., R. C. 1997, *MNRAS*, 291, 827
- Osterbrock, D. E. & Ferland, G. J. 2006, *Astrophysics of gaseous nebulae and active galactic nuclei*
- Parker, J. W. 1993, *AJ*, 106, 560
- Parker, J. W., Hill, J. K., Cornett, R. H., et al. 1998, *AJ*, 116, 180
- Pauldrach, A. W. A., Hoffmann, T. L., & Lennon, M. 2001, *A&A*, 375, 161
- Peeters, E., Martín-Hernández, N. L., Damour, F., et al. 2002, *A&A*, 381, 571
- Pellegrini, E. W., Baldwin, J. A., & Ferland, G. J. 2010, *ApJS*, 191, 160
- Pellegrini, E. W., Oey, M. S., Winkler, P. F., Smith, R. C., & Points, S. 2011, *Bulletin de la Societe Royale des Sciences de Liege*, 80, 410
- Pellerin, A., Fullerton, A. W., Robert, C., et al. 2002, *ApJS*, 143, 159
- Penny, L. R. & Gies, D. R. 2009, *ApJ*, 700, 844
- Pettini, M. & Pagel, B. E. J. 2004, *MNRAS*, 348, L59
- Pietrzyński, G., Graczyk, D., Gieren, W., et al. 2013, *Nature*, 495, 76
- Plaskett, J. S. & Pearce, J. A. 1931, *Publications of the Dominion Astrophysical Observatory Victoria*, 5, 1

- Prinja, R. K., Barlow, M. J., & Howarth, I. D. 1990, *ApJ*, 361, 607
- Prinja, R. K. & Crowther, P. A. 1998, *MNRAS*, 300, 828
- Puls, J., Kudritzki, R.-P., Herrero, A., et al. 1996, *A&A*, 305, 171
- Puls, J., Vink, J. S., & Najarro, F. 2008, *A&ARv*, 16, 209
- Quiroza, C., Rood, R. T., Bania, T. M., Balser, D. S., & Maciel, W. J. 2006, *ApJ*, 653, 1226
- Ramírez-Agudelo, O. H., Simón-Díaz, S., Sana, H., et al. 2013, *A&A*, 560, A29
- Relaño, M., Kennicutt, Jr., R. C., Eldridge, J. J., Lee, J. C., & Verley, S. 2012, *MNRAS*, 423, 2933
- Repolust, T., Puls, J., & Herrero, A. 2004, *A&A*, 415, 349
- Rivero González, J. G., Puls, J., Massey, P., & Najarro, F. 2012a, *A&A*, 543, A95
- Rivero González, J. G., Puls, J., Najarro, F., & Brott, I. 2012b, *A&A*, 537, A79
- Rosslowe, C. K., et, & al. in prep.
- Rubio, M., Barbá, R. H., Walborn, N. R., et al. 1998, *AJ*, 116, 1708
- Russeil, D., Adami, C., & Georgelin, Y. M. 2007, *A&A*, 470, 161
- Russell, S. C. & Dopita, M. A. 1990, *ApJS*, 74, 93
- Sabbi, E., Anderson, J., Lennon, D. J., et al. 2013, *AJ*, 146, 53
- Sabbi, E., Lennon, D. J., Gieles, M., et al. 2012, *ApJL*, 754, L37
- Sabín-Sanjuliáin, C., et., & al. submitted
- Salpeter, E. E. 1955, *ApJ*, 121, 161
- Sana, H., de Koter, A., de Mink, S. E., et al. 2013a, *A&A*, 550, A107
- Sana, H., et, & al. in press.
- Sana, H. & Evans, C. J. 2011, in *IAU Symposium*, Vol. 272, *IAU Symposium*, ed. C. Neiner, G. Wade, G. Meynet, & G. Peters, 474–485
- Sana, H., Gosset, E., & Evans, C. J. 2009, *MNRAS*, 400, 1479
- Sana, H., van Boeckel, T., Tramper, F., et al. 2013b, *MNRAS*, 432, L26
- Sander, A., Hamann, W.-R., & Todt, H. 2012, *A&A*, 540, A144
- Sanduleak, N. 1970, *Contributions from the Cerro Tololo Inter-American Observatory*, 89

- Santolaya-Rey, A. E., Puls, J., & Herrero, A. 1997, *A&A*, 323, 488
- Schaerer, D. & de Koter, A. 1997, *A&A*, 322, 598
- Schaerer, D. & Maeder, A. 1992, *A&A*, 263, 129
- Schaerer, D. & Vacca, W. D. 1998, *ApJ*, 497, 618
- Schaller, G., Schaerer, D., Meynet, G., & Maeder, A. 1992, *A&AS*, 96, 269
- Schild, H. & Testor, G. 1992, *A&AS*, 92, 729
- Schmutz, W., Hamann, W.-R., & Wessolowski, U. 1989, *A&A*, 210, 236
- Schmutz, W. & Vacca, W. D. 1991, *A&AS*, 89, 259
- Schnurr, O., Casoli, J., Chené, A.-N., Moffat, A. F. J., & St-Louis, N. 2008a, *MNRAS*, 389, L38
- Schnurr, O., Chené, A.-N., Casoli, J., Moffat, A. F. J., & St-Louis, N. 2009a, *MNRAS*, 397, 2049
- Schnurr, O., Moffat, A. F. J., St-Louis, N., Morrell, N. I., & Guerrero, M. A. 2008b, *MNRAS*, 389, 806
- Schnurr, O., Moffat, A. F. J., Villar-Sbaffi, A., St-Louis, N., & Morrell, N. I. 2009b, *MNRAS*, 395, 823
- Searle, L. 1971, *ApJ*, 168, 327
- Selman, F., Melnick, J., Bosch, G., & Terlevich, R. 1999, *A&A*, 341, 98
- Shara, M. M., Moffat, A. F. J., Gerke, J., et al. 2009, *AJ*, 138, 402
- Shara, M. M., Zurek, D., Kanarek, G., & Faherty, J. 2012, in *Astronomical Society of the Pacific Conference Series*, Vol. 465, *Proceedings of a Scientific Meeting in Honor of Anthony F. J. Moffat*, ed. L. Drissen, C. Rubert, N. St-Louis, & A. F. J. Moffat, 465
- Sharpless, S. 1953, *ApJ*, 118, 362
- Sharpless, S. 1959, *ApJS*, 4, 257
- Simón-Díaz, S. & Stasińska, G. 2008, *MNRAS*, 389, 1009
- Sirianni, M., Nota, A., Leitherer, C., De Marchi, G., & Clampin, M. 2000, *ApJ*, 533, 203
- Skibba, R. A., Engelbracht, C. W., Aniano, G., et al. 2012, *ApJ*, 761, 42
- Smartt, S. J. 2009, *ARA&A*, 47, 63
- Smith, L. F. 1968, *MNRAS*, 140, 409

- Smith, L. F., Shara, M. M., & Moffat, A. F. J. 1990, *ApJ*, 348, 471
- Smith, L. F., Shara, M. M., & Moffat, A. F. J. 1996, *MNRAS*, 281, 163
- Smith, L. J., Norris, R. P. F., & Crowther, P. A. 2002, *MNRAS*, 337, 1309
- Smith, N. 2006, *MNRAS*, 367, 763
- Smith, N. & Brooks, K. J. 2007, *MNRAS*, 379, 1279
- Smith, N. & Conti, P. S. 2008, *ApJ*, 679, 1467
- Smith, N., Li, W., Silverman, J. M., Ganeshalingam, M., & Filippenko, A. V. 2011, *MNRAS*, 415, 773
- Sota, A., Maíz Apellániz, J., Walborn, N. R., et al. 2011, *ApJS*, 193, 24
- St-Louis, N., Chené, A.-N., Schnurr, O., & Nicol, M.-H. 2009, *ApJ*, 698, 1951
- St-Louis, N., Dalton, M. J., Marchenko, S. V., Moffat, A. F. J., & Willis, A. J. 1995, *ApJL*, 452, L57
- Stevens, I. R., Read, A. M., & Bravo-Guerrero, J. 2003, *MNRAS*, 343, L47
- Tatton, B. L., van Loon, J. T., Cioni, M.-R., et al. 2013, *A&A*, 554, A33
- Taylor, W. D., Evans, C. J., Sana, H., et al. 2011, *A&A*, 530, L10
- Testor, G., Llebaria, A., & Debray, B. 1988, *The Messenger*, 54, 43
- Testor, G. & Schild, H. 1990, *A&A*, 240, 299
- Torres-Dodgen, A. V. & Massey, P. 1988, *AJ*, 96, 1076
- Townsley, L. K., Broos, P. S., Feigelson, E. D., et al. 2006, *AJ*, 131, 2140
- Trundle, C., Dufton, P. L., Hunter, I., et al. 2007, *A&A*, 471, 625
- Trundle, C. & Lennon, D. J. 2005, *A&A*, 434, 677
- Trundle, C., Lennon, D. J., Puls, J., & Dufton, P. L. 2004, *A&A*, 417, 217
- Turnshek, D. A., Bohlin, R. C., Williamson, II, R. L., et al. 1990, *AJ*, 99, 1243
- Vacca, W. D., Garmany, C. D., & Shull, J. M. 1996, *ApJ*, 460, 914
- Vacca, W. D., Robert, C., Leitherer, C., & Conti, P. S. 1995, *ApJ*, 444, 647
- Vázquez, G. A., Leitherer, C., Schaerer, D., Meynet, G., & Maeder, A. 2007, *ApJ*, 663, 995
- Vink, J. S., de Koter, A., & Lamers, H. J. G. L. M. 2000, *A&A*, 362, 295

- Vink, J. S., de Koter, A., & Lamers, H. J. G. L. M. 2001, *A&A*, 369, 574
- Voges, E. S., Oey, M. S., Walterbos, R. A. M., & Wilkinson, T. M. 2008, *AJ*, 135, 1291
- von Zeipel, H. 1924, *MNRAS*, 84, 665
- Voss, R., Martin, P., Diehl, R., et al. 2012, *A&A*, 539, A66
- Walborn, N. R. 1971a, *ApJL*, 167, L31
- Walborn, N. R. 1971b, *ApJS*, 23, 257
- Walborn, N. R. 1972, *AJ*, 77, 312
- Walborn, N. R. 1973, *AJ*, 78, 1067
- Walborn, N. R. 1982, *ApJL*, 254, L15
- Walborn, N. R., Barbá, R. H., & Sewiło, M. M. 2013, *AJ*, 145, 98
- Walborn, N. R. & Blades, J. C. 1997, *ApJS*, 112, 457
- Walborn, N. R., Drissen, L., Parker, J. W., et al. 1999, *AJ*, 118, 1684
- Walborn, N. R. & Fitzpatrick, E. L. 1990, *PASP*, 102, 379
- Walborn, N. R., Fullerton, A. W., Crowther, P. A., et al. 2002a, *ApJS*, 141, 443
- Walborn, N. R., Howarth, I. D., Lennon, D. J., et al. 2002b, *AJ*, 123, 2754
- Walborn, N. R., MacKenty, J. W., Saha, A., White, R. L., & Parker, J. W. 1995, *ApJL*, 439, L47
- Walborn, N. R., Sana, H., Simon-Diaz, S., et al. 2014, *ArXiv e-prints*
- Weidner, C. & Vink, J. S. 2010, *A&A*, 524, A98
- Weingartner, J. C. & Draine, B. T. 2001, *ApJ*, 548, 296
- Welty, D. E. & Crowther, P. A. 2010, *MNRAS*, 404, 1321
- Wood, D. O. S. & Churchwell, E. 1989, *ApJS*, 69, 831
- Wright, A. E. & Barlow, M. J. 1975, *MNRAS*, 170, 41
- Yusof, N., Hirschi, R., Meynet, G., et al. 2013, *MNRAS*, 433, 1114
- Zaritsky, D., Harris, J., Thompson, I. B., & Grebel, E. K. 2004, *AJ*, 128, 1606
- Zaritsky, D., Kennicutt, Jr., R. C., & Huchra, J. P. 1994, *ApJ*, 420, 87
- Zastrow, J., Oey, M. S., & Pellegrini, E. W. 2013, *ApJ*, 769, 94
- Zinnecker, H. & Yorke, H. W. 2007, *ARA&A*, 45, 481